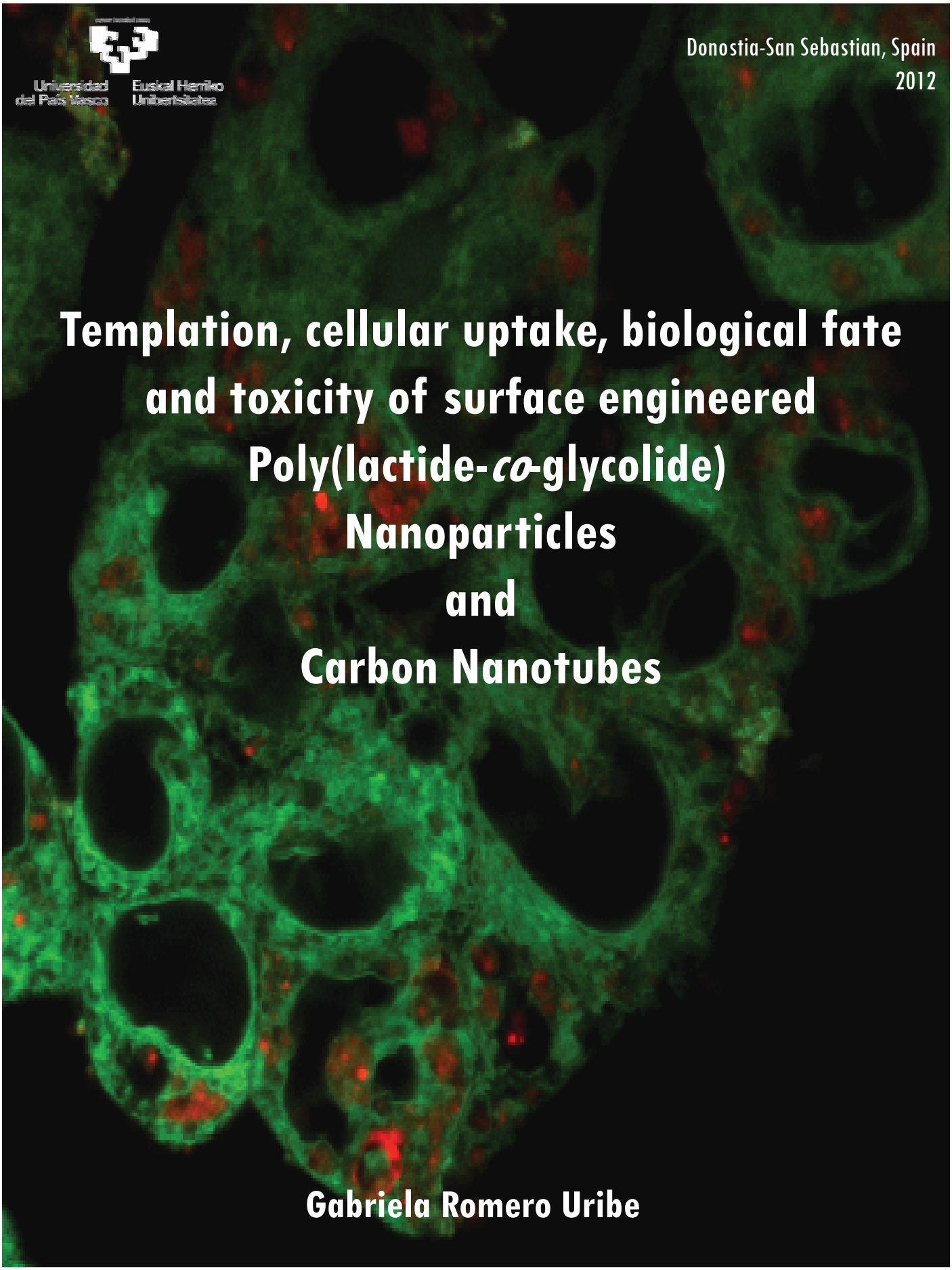

Universidad del País Vasco
Euskal Herriko Unibertsitatea

Donostia-San Sebastian, Spain
2012

Templation, cellular uptake, biological fate and toxicity of surface engineered Poly(lactide-*co*-glycolide) Nanoparticles and Carbon Nanotubes

Gabriela Romero Uribe

Templation, cellular uptake, biological fate and toxicity of surface engineered Poly(lactide-*co*-glycolide) Nanoparticles and Carbon Nanotubes

Dissertation presented to the Department of Applied Chemistry
University of the Basque Country (UPV/EHU), San Sebastian
for the degree of International Doctor
in Applied Chemistry and Polymeric Materials

Presented by

Gabriela Romero Uribe

Thesis Supervisor: Dr. Sergio E. Moya
University Tutor: Dr. José Ramón Leiza

Donostia-San Sebastian, Spain
2012

This PhD thesis has been carried out at:

CIC biomaGUNE
Biosurfaces Unit
Donostia-San Sebastian, Spain

Universität Leipzig
Institut für Medizinische Physik und Biophysik
Leipzig, Germany

Zhejiang University
Department of Polymer Science and Engineering
Hagzhou, China

Capsulution Pharma AG
Berlin, Germany

Contents

List of Figures

Introduction

Chapter 1

Chapter 2

Chapter 3

Chapter 4

Chapter 5

Appendix

Abstract

This PhD thesis is focused on the design, fabrication and surface engineering of poly(lactide-*co*-glycolide) (PLGA) nanoparticles (NPs) and carbon nanotubes (CNTs) as potential and versatile nanocarriers for drug delivery.

PLGA NPs were prepared by means of an emulsion-solvent evaporation method using polyethyleneimine (PEI) or bovine serum albumin (BSA) as stabilizers. PLGA NPs have been surface functionalized with polyelectrolytes assembled via the layer by layer (LbL) technique. The LbL coating provides functional groups for the further surface modification via covalent linking of polyethylene glycol (PEG) and folic acid (FA), or can be used as a support for the assembly of lipid bilayers. It has been proven that pegylation reduces interactions with proteins and cell uptake preventing unspecific interactions, while FA increases cell uptake by HepG2 cells due to specific interactions. It has been also demonstrated that surface modification, using biopolyelectrolyte multilayers of chitosan and alginate, generates a more biocompatible NP surface with greater antifouling properties. Finally, lipid layers composed of 1,2-dioleoyl-sn-glycero-3-choline and 1,2-dioleoyl-sn-glycero-3-phospho-L-serine assembled on top of the polyelectrolyte coated PLGA NPs have been used to engineer the NPs for targeted delivery towards the endoplasmic reticulum of the cell.

CNTs have been surface functionalized by the *in situ* synthesis of a polyelectrolyte brush made of poly(3-sulfopropylmethacrylate). The brush provides colloidal stabilization in aqueous media. The covalently bonded polyelectrolyte brushes are used as a platform to provide different functionalities to the CNTs such as the *in situ* synthesis of CdS quantum dots and magnetic iron oxide nanoparticles, or by allowing the assembly of a lipid layer on top of the CNTs.

Cellular uptake, intracellular distribution and toxicity have been study using Confocal Raman Microscopy (CRM), Flow cytometry, Confocal Scanning Laser Microscopy and MTT for both surface engineered PLGA NPs and CNTs.

Finally the potential use of PLGA NPs as carriers for drug delivery has been established by studying the encapsulation and the intracellular delivery of the antibody antitumor necrosis factor alpha (antiTNF-α), and the anticancer drug, doxorubicin. For antiTNF-α encapsulation a protocol has been developed based on the formation of a complex consisting of the antibody with alginate and the assembly of the complex on top of the PLGA NPs; while doxorubicin was encapsulated into the polymer matrix of PLGA NPs during NPs fabrication process.

Resumen

La utilización de nanomateriales (NMs) en biomedicina contribuye con nuevas perspectivas para el diagnóstico y tratamiento de muchas enfermedades, entre ellas el cáncer, el alzhéimer o la diabetes. Los nanomateriales tienen características únicas debido a la elevada relación de su superficie respecto al volumen y a los efectos cuánticos asociados a su estructura de escala nanométrica. Estas propiedades singulares son muy relevantes para las diferentes aplicaciones de los NMs orgánicos e inorgánicos en el campo de la medicina, ya sea como agentes de contraste para imagen *"in vivo"*, como sensores, como soportes para regeneración de tejidos o en el diseño de vectores para la liberación controlada de fármacos.

La liberación controlada y dirigida de fármacos constituye una metodología ingeniosa y sofisticada de liberar agentes terapéuticos en lugares específicos del organismo. Los NMs constituyen un tipo de vectores o portadores de fármacos que pueden ser modificados superficialmente con el objetivo de incorporar funciones específicas de reconocimiento que focalicen la liberación. Además, éstos NMs también trabajan como protectores del fármaco para evitar interacciones no deseadas entre éste y otras moléculas presentes en el organismo. En el diseño de sistemas de liberación controlada y dirigida se busca controlar la velocidad de liberación del agente terapéutico dentro de células, tejidos u órganos específicos, con la posibilidad de prologar el tiempo de circulación y así reducir los efectos secundarios e incrementar la eficacia y eficiencia del fármaco.

Para su utilización en sistemas de liberación controlada, los agentes terapéuticos pueden ser incorporados de dos maneras diferentes: en la superficie de los NMs o encapsulados dentro de estos. Algunos ejemplos de NMs con fármacos incorporados en la superficie pueden encontrarse en nanopartículas (NPs) de oro, dónde comúnmente el medicamento es enlazado en la superficie de oro a través tioles; o en cápsulas de polielectrolitos,

donde el fármaco queda atrapado entre las capas de polímero durante el proceso de fabricación. El medicamento puede ser incorporado dentro de los NMs siguiendo diferentes rutas de encapsulación, dentro de las NPs orgánicas algunos ejemplos de encapsulado son la emulsión al utilizar NPs de látex o la sonicación utilizando vesículas lipídicas.

Para focalizar la liberación de un agente terapéutico, es necesario proveer a los NMs con funciones específicas. La incorporación de funciones específicas puede llevarse a cabo a través de enlaces covalentes, autoensamblado o interacciones supramoleculares. Un ejemplo interesante sobre autoensamblado e interacciones supramoleculares es la técnica de capa a capa, del inglés Layer by Layer (LbL), que se basa en el ensamblado alternante de polielectrolitos con carga opuesta por interacciones electrostáticas. Por medio de LbL se construyen capas o películas de polímero muy delgadas a las que posteriormente, se les puede unir covalentemente proteínas, anticuerpos, polietilenglicol (PEG), etc. Además de direccionar la liberación, el enlace de una función específica también puede utilizarse para incrementar el tiempo de circulación de los NMs en el organismo, y la técnica más usual para ello es la inclusión de PEG o pegilación. Resumiendo, la modificación superficial los NMs es fundamental para controlar su interacción con moléculas biológicas y su localización a nivel celular y dentro del organismo.

Los NMs de origen orgánico han recibido especial atención en la búsqueda de sistemas la liberación controlada. Los NMs orgánicos pueden encontrarse de forma natural como son los agregados de proteína, los cuerpos lipídicos, las emulsiones, o en forma de estructuras más complejas como los virus. Sin embargo, los NMs orgánicos más utilizados como vectores, son aquellos sintetizados como las NPs poliméricas, las micelas, las cápsulas, los dendrímeros, los liposomas e incluso los nanotubos de carbono (CNTs).

Esta tesis doctoral está enfocada en el diseño de vectores para la liberación controlada y direccionada utilizando dos tipos diferentes de NMs altamente representativos: las NPs de ácido poli (láctico-*co*-glicólico) (PLGA) y los nanotubos de carbono (CNTs). El diseño de éstos NMs se basa en su modificación superficial con moléculas de polielectrolitos fabricadas mediante la técnica de LbL o con la síntesis *in situ* de cepillos poliméricos; así como el estudio de su asimilación celular, su co-localización dentro de la célula, y su posible uso como vectores para la liberación controlada de el anticuerpo contra el factor de necrosis tumoral (antiTNF-α) y del anticancerígeno doxorubicina.

El trabajo realizado en esta tesis, está organizado en seis capítulos que se resumen a continuación:

- En el **Capítulo 1**, se detallarán los materiales y los métodos necesarios para la realización del trabajo experimental presentado en esta tesis.

- En el **Capítulo 2** se presentará la fabricación de las NPs de PLGA mediante técnicas de emulsión, junto con diferentes enfoques para su funcionalización. Las NPs de PLGA fueron preparadas utilizando como estabilizadores, el polielectrolito sintético polietilenimina (PEI), o la proteína albumina de suero bovino (BSA). La superficie de las NPs de PLGA se modificó mediante recubrimientos de polielectrolitos con el objetivo de proveer a la superficie con grupos funcionales aminos o carboxílicos. Posteriormente, estos grupos funcionales sirvieron para unir covalentemente PEG o ácido fólico (FA). Alternativamente se depositaron vesículas de lípidos sobre las multicapas. Finalmente, se estudió la interacción de las NPs de PLGA funcionalizadas con proteínas y su asimilación celular, utilizando la línea derivada de un carcinoma hepatocelular humano HepG2.

Los resultados obtenidos muestran que la pegilación por si sola reduce la interacción de las NPs con proteínas y por consiguiente su asimilación celular previniendo interacciones no específicas, mientras que el recubrimiento de las NPs con PEG y FA, reduce también la interacción con proteínas, pero al mismo tiempo incrementa su asimilación celular debido a interacciones específicas con las células hepáticas. La modificación superficial de las NPs de PLGA mediante la técnica de LbL utilizando biopolielectrolitos sirvió para generar NPs con superficies biocompatibles y con baja interacción con proteínas. Finalmente, las modificaciones superficiales con capas de lípidos en base a los fosfolípidos 1,2-dioleoil-sn-glicero-3-colin y 1,2-dioleoil-sn-glicero-3-fosfo-L-serina, se utilizaron para controlar la distribución intracelular de las NPs y su direccionamiento al retículo endoplásmico de las células.

- En el **Capítulo 3** se mostrará una estrategia para funcionalizar la superficie de los CNTs utilizando la síntesis *in situ* de un cepillo del polielectrolito poli (3-sulfopropilamino metacrilato) (PSPM), con el objetivo de estabilizar los CNTs en medio acuoso. Los CNTs recubiertos covalentemente con el cepillo de PSPM sirvieron como plataforma para la síntesis, también *in situ*, de puntos cuánticos de CdS o de NPs magnéticas de óxido de hierro. Éste tipo de sistemas híbridos duales compuestos por NPs y CNTs, no había sido sintetizado antes utilizando un cepillo polimérico como base.

  La capa de PSPM que recubre a los CNTs, se utilizó también para ensamblar una capa de lípidos sobre la superficie. La estrategia de funcionalización con lípidos pude ser utilizada para el recubrimiento de superficies donde los CNTs están presentes como parte de un material compuesto y se requiera de cierta biocompatibilidad.

- El **Capítulo 4** está dirigido al estudio de la asimilación celular, la distribución intracelular y la toxicidad de las NPs de PLGA y los CNTs modificados

superficialmente haciendo uso de la Microscopía Raman Confocal (CRM). La CRM se utilizó para estudiar la localización de los nanomateriales dentro de las células. Los espectros Raman de células expuestas a los NMs contienen bandas correspondientes a la señal de los NMs, y a las de señales de moléculas propias de la célula, como proteínas, ADN y lípidos, lo que permite la identificación de la región celular donde se localizan los NMs: núcleo, citoplasma y región de cuerpos oleosos.

Se muestra que las NPs modificadas con PEI tienen una cinética de asimilación más lenta que las que presentan las NPs estabilizadas con BSA. Tanto las NPs de PLGA estabilizadas con PEI como las estabilizadas con BSA, se localizaron en la región de los cuerpos lipídicos de la célula. Los estudios de viabilidad celular revelaron que las NPs de PLGA estabilizadas con BSA son más biocompatibles que las NPs con PEI.

En el caso de los CNTs modificados superficialmente, se demuestra que el recubrimiento con lípidos reduce de forma significativa el efecto tóxico de las CNTs. Los CNTs recubiertos con lípidos pueden ser utilizados para aplicaciones biológicas, liberación de fármacos o cómo sensores, en dónde una respuesta tóxica "*in vitro"* moderada sea aceptable.

- El **Capítulo 5** se centra en el estudio de las NPs de PLGA como posibles vectores para la liberación controlada de agentes terapéuticos. Se investigó la capacidad de las NPs de PLGA como vectores de agentes terapéuticos con diferentes pesos moleculares. El anticuerpo antiTNF-α se depositó sobre la superficie de las NPs de PLGA mediante el autoensamblado "capa a capa", mientras que el fármaco anticancerígeno doxorubicina, se encapsuló dentro de las NPs de PLGA durante su fabricación. En ambos casos, se caracterizaron los perfiles de liberación dentro y fuera de la célula, a través de las técnicas apropiadas para casa caso.

La encapsulación de antiTNF-α se llevó a cabo en base a la formación de un complejo de antiTNF-α con exceso de alginato, y después mediante el ensamblado del complejo en multicapas de polielectrolitos. Se demostró que mediante el encapsulado del anticuerpo por el método propuesto es posible controlar la dosis de antiTNF-α a través del número de capas depositadas sobre la superficie de las NPs de PLGA. La liberación del anticuerpo, tanto en PBS como dentro de la célula, se asemeja a un perfil de liberación de primer orden.

La droga anticancerigena doxorubicina se encapsulo dentro de la matriz polimérica de las NPs de PLGA. La liberación de la doxorubicina dentro de las células HepG2 fue estudiada mediante técnicas de fluorescencia como citometría de flujo y microscopía de fluorescencia. Además, se confirmó la liberación de la doxorubicina de las NPs de PLGA a través de la disminución en la proliferación celular como resultado de la intercalación del anticancerígeno en las cadenas de ADN.

- Finalmente, en el **Capitulo 6** se resumen detalladamente las conclusiones obtenidas en este trabajo de tesis doctoral sobre el uso de las NPs de PLGA y los CNTs en el campo de la nanomedicina.

Introduction

The uses of nanomaterials for biomedical applications are allowing novel approaches in the diagnosis and treatment of diseases to be developed. Nanomaterials have unique features stemming from their nanoscale structure, large surface area to volume ratio, and quantum effects. Indeed in recent years, organic and inorganic nanomaterials have been proposed for several applications in the medical field. For example, quantum dots *[1-3]* or gold nanoparticles (NPs) *[1-4]*, gadolinium NPs *[3, 5, 6]*, iron oxide NPs *[2, 6, 7]* and polymer based hybrid nanostructures *[3, 5, 7]* have been extensively studied as contrast agents for *"in vivo"* imaging. Metal oxide NPs *[8-11]*, carbon nanotubes *[12-14]* and graphene *[12, 15-18]* due to their excellent electrical properties, either alone or incorporated into different matrices have received special attention for the fabrication of sensors. A wide range of nanomaterials including nanoceramics (alumina, titania or hydroxyapatite) *[19-21]*, metallic NPs (gold, iron or titanium) *[22-24]*, polymeric NPs *[24, 25]* and carbon nanotubes *[26-28]* have been employed in the design of composites for tissue regeneration, being most frequently, incorporated into scaffolds made of different biopolymers. Finally, various nanomaterials such as metallic NPs *[29-33]*, polymeric NPs *[34-37]*, micelles *[38, 39]*, dendrimers *[40-43]*, liposomes *[44-46]*, capsides *[47, 48]* or carbon nanotubes *[49-52]* have been proposed as vectors for drug delivery.

Targeted drug delivery can be defined as the "smart way" to deliver therapeutic agents into specific damaged cells in the body. Targeted drug delivery is based on the use of carriers that contain the desired drugs. These carriers are usually nanomaterials that can be further surface engineered in order to attach specific recognition functions. In addition to the targeting properties, the carrier also works as a protector of the drug, helping to avoid undesired interactions with other molecules. Targeted drug delivery systems are designed to control the release rate of the therapeutic agent into specific targeted cells with the possibility of prolonging the circulation time and as such, reduce the side effects and increase efficacy and efficiency of drugs *[53-56]*.

In targeted delivery applications the therapeutic agent can be incorporated into the cargo either by, attachment to the nanomaterials surface or by encapsulation. Examples of carriers with attached therapeutics can be found in gold NPs, where the cargo is linked to the gold core through thiols *[57-59]*, or in polyelectrolyte capsules, where the cargo is assembled between polyelectrolyte layers *[60-62]*. Organic NPs offer several routes for encapsulation: the cargo can be incorporated in latex NPs during emulsion preparation, entrapped in vesicles through sonication, etc.

The surface engineering of NPs and nanomaterials is fundamental to control their interaction with biomolecules and their translocation at both the cellular and body level. Covalent chemistry, self assembly and supramolecular interactions can be applied to endow nanomaterials with specific functions for targeting or to increase their circulation time in the body. The surface engineering with polyethylene glycol (PEG), known as pegylation *[63]*, is the most used among the surface modifications to increase circulation time. An interesting approach of surface functionalization via self assembly and supramolecular interactions is given by the Layer by Layer technique (LbL). LbL is based on the alternative assembly of polyelectrolytes of opposite charge by electrostatic interactions, to form a thin polymer film. LbL assembly can also be combined with covalent chemistry to attach proteins, antibodies, PEG, etc.

This dissertation is focused on the design, fabrication and surface engineering of poly(lactide-*co*-glycolide) (PLGA) NPs and carbon nanotubes (CNTs) as potential and versatile nanocarriers for drug delivery, the study of their fate and intracellular localization, as well as their use for the delivery of the antitumor necrosis factor alpha (antiTNF-α), and the anticancer drug doxorubicin.

Organic Nanoparticles for drug delivery

Organic nanomaterials have received special attention for drug delivery. Organic nanomaterials are templated upon natural or synthetic organic molecules. Nature provides a wide range of examples of organic NPs such as protein aggregates, lipid bodies, milk emulsions, or more complex organized structures like viruses to name a few. There is also a wide range of organic synthesized nanomaterials such as polymeric NPs, micelles, dendrimers, liposomes or even CNTs (*Figure 1*) that have been proposed as carriers for delivery in different fields since they offer relatively simple routes for the encapsulation of materials.

Organic NPs differ conceptually from inorganic NPs in terms of the principles of fabrication. Inorganic NPs are normally formed by the precipitation of inorganic salts, which are linked in a matrix. The nature of the binding among atoms can be different: covalent, metallic, etc., but in any case, the inorganic structure forms a three dimensional arrangement with linked atoms. Most of the organic NPs are formed by several organic molecules, which are driven together by self organization or chemical binding. For the synthesis of organic NPs, with the exception of dendrimers and some other polymer NPs and CNTs, organic molecules that can arrange themselves three dimensionally are needed as interactions between molecules are sometimes not strong as in the case of micelles and vesicles. Self assembly and the presence of zwitterionic molecules, with polar and non-polar regions, as the main components of NPs or the means to encapsulate other organic molecules, are key elements for the fabrication of many of the organic NPs.

Some of the organic NPs, due to the weak nature of the interactions holding them together, have dynamic behavior. Micelles and vesicles can self aggregate and generate larger particles. The continuous addition of surfactant to a micellar solution can indeed increase size and force the micelle to change shape from spherical to cylindrical over the so called second critical micellar concentration. Sizes can also not always be truly

nano for organic NPs as for inorganic NPs, in which the formation of the NPs sometimes needs only the clustering of few atoms. In the case of the organic NPs, the size and geometry of the organic molecules impose, in many cases, the limits to go to nano scale. In micelles, which are among the smallest organic NPs, size is controlled by the length of the surfactant, with the smallest size that can be achieved being a sphere with a radius equal to the length of the surfactant in the micellar phase, typically, around 15-20 Å. The lipids forming a vesicle assemble into bilayers because of the relation of their hydrophilic and hydrophobic volume. Bilayers must close in on themselves to form a vesicle, this results in an internal volume that can be used for encapsulation but also establishes limits for the smallest attainable size. For organic NPs, like polymer latexes, it is incredibly difficult to obtain NPs below a certain size threshold. For latexes, the polymeric core is stabilized by a surfactant. The size of the NP is then the combination of the core and the stabilizing surfactant. Dendrimers, as single molecule NPs are an exception and can have a controllable size below 10 nm.

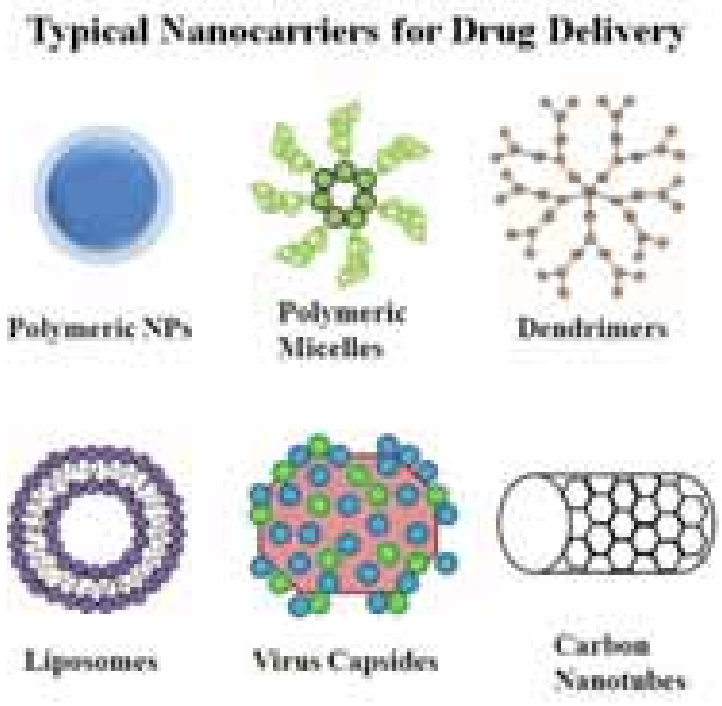

Figure 1. *Schematic representation of the typical nanocarries used for drug delivery*

Organic NPs can be fabricated by both, "top-down" and "bottom-up" approaches. In the "top-down" techniques the most common fabrication method is mechanical milling *[64]*; although, recently, other more complicated techniques involving microfluidics and lithography *[65, 66]* have been used to produce organic nanomaterials. The "bottom-up" techniques are based on the building up of NPs via physico-chemical processes, starting with single molecules. In contrast to the "top-down" approaches, in "bottom-up" techniques, NPs are fabricated from atoms or molecules via synthetic chemistry and self-organization. The "bottom-up" techniques are used for the generation of a wide range of nanomaterials such as micelles *[67-70]*, vesicles and liposomes *[71-76]*, polymersomes *[77-79]*, polymer conjugates *[80-84]*, dendrimers *[85-88]*, capsules *[89-95]* and polymeric NPs *[96-103]*.

Poly(lactide-*co*-glycolide) Nanoparticles

Polymeric NPs, also known as polymeric nanospheres, are usually defined as submicron-sized solid polymer particles with a matrix type structure *[104]*, in which a cargo can be encapsulated within the polymer matrix but also absorbed through the surface. Polymeric NPs can be easily synthesized and in most cases, the protocols for drug encapsulation are performed in parallel with fabrication. Furthermore, polymeric NPs are normally suitable to be functionalized for targeted delivery by multiple procedures. During the last three decades, synthetic biodegradable polymers, for example, poly(amino acids), poly(alkyl-2-cyanoacrylates), polyesters, polyorthoesters, polyanhydrides and polyurethanes, have been employed in the fabrication of nanocarriers for drug delivery. Among them, the polyester lactic acid (PLA) *[101, 105]* and its copolymer, poly(lactide-*co*-glycolide) (PLGA) *[106-112]*, are commonly used to fabricate NPs for a wide variety of pharmaceutical and biomedical applications.

PLGA plays an important role as a carrier because it displays controllable biodegradability, excellent biocompatibility and good degradation kinetics and mechanical properties. In addition to all the properties suitable for biotechnology

applications, micro and nanoparticles fabricated with PLGA are authorized by the Food and Drug Administration (FDA) for drug delivery applications. In *Figure 2* is shown the chemical structure of PLGA.

The degradation of PLGA NPs takes place by hydrolysis of the ester linkages *[113]*, resulting in the original monomer molecules (lactic acid and glycolic acid). The degradation products are easily metabolized and eliminated by the body *[114]* and consequently there is almost no systematic toxicity caused by PLGA NPs. Another advantage of PLGA NPs as drug delivery carriers is their ability to avoid endolysosomal degradation. In the design of delivery systems for therapeutic proteins such as DNA, the protection that the NPs can bring to the cargo from enzymatic degradation is crucial *[115]*.

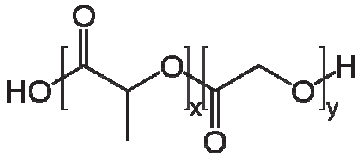

Figure 2. *Chemical structure of poly(lactide-co-glycolide) (PLGA). The subscript "x" refers to the number of units of lactic acid and the subscript "y" to the number of units of glycolic acid.*

In the design of a drug delivery system, it is also very important to control the drug release rate. Targeted delivery systems offer the possibility to design carriers for prolonged drug release, and in most cases a sustained release is preferred as opposed to a burst release *[108, 116, 117]*. Similarly for many other polymeric NPs, a cargo can be released from PLGA NPs either by diffusion through the polymeric matrix as a response to an environmental stimulus, or during the NPs degradation process. The release kinetics of PLGA NPs can be accurately controlled by the physicochemical properties of the copolymer such as molecular weight, copolymer ratio, polydispersity index, hydrophobicity and crystalinity *[118]*.

Several techniques have been developed for the preparation of PLGA NPs, the emulsion solvent evaporation method is probably the most commonly used to fabricate NPs.

Here, the polymer is dissolved in an organic solvent and emulsified in an aqueous solution containing a surfactant. Then, the organic solvent is evaporated inducing the precipitation of the polymer NPs. A cargo molecule can be added into the polymer solution for encapsulation. Using this method, it is possible to encapsulate both hydrophobic and hydrophilic drugs *[102, 119-121]*. The particle size can be controlled by the emulsification rate, time and by the nature of the polymer and surfactant. Besides emulsion techniques, there are other methods applied in the fabrication of PLGA NPs like in situ polymerization *[122]*, emulsification solvent diffusion *[123, 124]*, nanoprecipitation *[125, 126]* and the salting out method *[127]*.

PLGA NPs have been used in drug delivery as carriers for many drugs and proteins in particular in cancer diagnosis and treatment. The poor water solubility of many of the most popular anticancer drugs limits their efficiency to penetrate and kill cancer cells. PLGA NPs have been successfully used to encapsulate some of the most typical anticarcinogenics such as paclitaxel *[128-130]*, docetaxel *[131, 132]*, cisplatin *[133]*, doxorubicin *[134, 135]*, curcumin *[136, 137]*, etc., enhancing high encapsulation efficacy especially when the drug is encapsulated in parallel with NPs fabrication. By loading anticancer drugs into PLGA NPs it is possible to control the drug release rate, to detect higher drug concentrations in cancer cells with longer retention times and as a consequence, increase the efficiency of the anticancer drugs *[111, 138]*. PLGA NPs have also been used to encapsulate photosensitizing agents for photodynamic therapies like hypericin *[139]* or zinc (II) phthalocyanine *[140]*, which were reported to be more photoactive than when used as free drugs.

A remarkable fact about polymeric NPs such as PLGA NPs, is their capacity to load molecules either by conjugation on the surface or in the core, or by physical encapsulation. In addition, PLGA NPs are suitable for surface modification in order to provide biocompatibility or specific recognition functions. Those properties make them appealing systems for the delivery of molecules and more specifically for targeted drug delivery and biomedical applications.

Carbon Nanotubes

Carbon has the tendency to form strong bonds with other carbon atoms, this unique property allows the formation of different carbon network structures *[141]*. In addition to their well known allotropes, diamond and graphite; carbon molecules can also form stable nanostructures such as fullerenes, carbon nanotubes and graphene *[142]*. Carbon nanostructures have amazing chemical and physical properties and for this reason, during the past decade, carbon science has become very attractive for different potential applications in electronics, optics, materials science, energy research and biomedicine *[143-145]*.

Since Sir Harry Kroto from the University of Sussex, and Richard Smalley from Rice University in Houston published, in 1985 in Nature, the discovery of a new closed cluster formed by 60 carbon atoms, with unique stability and symmetry *[146]*, known nowadays as fullerene, the field of carbon nanotechnology has seen hugely impressive development. In 1991 Sumio Iijima from NEC laboratories of Japan, discovered the carbon nanotubes (CNTs), described by himself as "molecular carbon fibers that consist of tiny cylinders of graphite" *[147]*. CNTs, either multiwalled (MWCNTs) or single wall (SWCNTs) (*Figure 3*), have been the subject of enormous interest because of their multiple and unique physical properties, alone or in composite materials. Moreover, in 2004, a new nanostructure of carbon, a mono layer sheet, "graphene", was discovered by Novoselov K. S. and co-workers *[148]*.

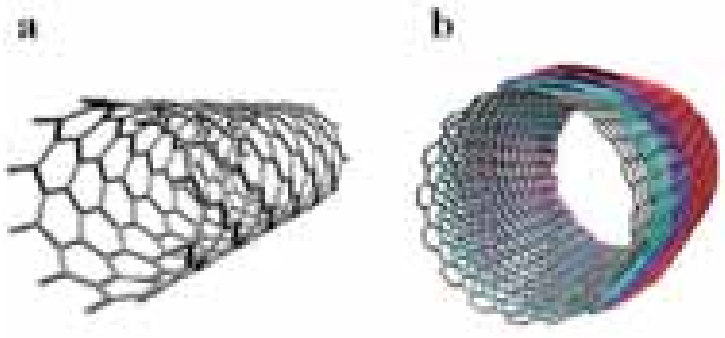

Figure 3. *Schematic representation of (a) single walled carbon nanotubes (SWCNTs) and (b) multiwalled carbon nanotubes (MWCNTs) [149].*

CNTs have unique electrical and mechanical properties which make them highly interesting for nanofabrication alone or in combination with other nanostructures, as well as for the fabrication of composite materials. The addition of CNTs to polymer mixtures generates materials with unique properties, i.e electrical and mechanical.

There are several difficulties concerning the practical usage of CNTs; for example, there is almost no solvent in which CNTs can be easily dispersed. CNTs display a high Hamaker constant *[150]*, resulting in a strong association among themselves, which leads to their precipitation. It is also not always easy to arrange CNTs in an organized way that could be fundamental for their application in electronics and device fabrication. Another drawback, and potentially the most controversial, is the questionable safety of CNTs that has created the need of deeper studying to understand their toxicity *[151-155]*. Despite these issues, CNTs have been proposed for many applications including biomedical, as sensors *[156-159]*, profiting from their unique electronic and mechanical properties or as drug delivery systems *[143, 160-162]*.

For most of the multiple applications of CNTs, the highly purified nanomaterial is required, and therefore, surface functionalization is needed in order to improve CNTs properties. The surface modification of CNTs is normally carried out post synthesis, and can be achieved by both, covalent and non-covalent methods. For example, it has been proved that solubility of CNTs can be enhanced by simply providing functional groups on their surfaces like –COOH, -OH, $-NH_2$ and others *[163]*; while CNT purification is usually achieved by strong oxidizing agents *[164, 165]*, that in addition to improving CNT solubility and facilitating their exfoliation, the oxygen groups in the surface of CNTs open up the possibility of further surface modification.

Polymers have been extensively used for the modification of CNTs due to the high colloidal solubility that polymer chains bring to CNTs. Polymers can be covalently attached to CNT surfaces by either, the direct covalent binding of a pre-synthesized polymer molecule or by the in situ polymerization or propagation of the monomers from the surface of the CNTs.

Polyelectrolyte chains attached to the surface of CNTs, due to their many monomers in the chains, have a significant impact on the colloidal solubility of CNTs and are a good means to disperse CNTs in aqueous media. Nevertheless, covalent surface modification of CNTs involves strong treatments that in most cases changes the hybridization of the carbon from sp^2 to sp^3 *[145, 166]* altering their mechanical and electric properties. Nevertheless, quite often the chemical treatment irreversibly damages the walls of the CNTs. The non-covalent surface modification of CNTs provides alternative routes for tailoring CNTs without affecting carbon hybridization and retaining the original properties of the CNTs.

The unique properties of CNTs combined with their difficulty to disperse and integrate in other materials, makes the surface functionalization of CNTs a topic of enormous interest in science and technology. Polyelectrolyte synthesized or self assembled on top of the CNTs provides good aqueous stability to CNTs. Non covalent functionalization of CNTs has the advantage of unaffecting the properties of the CNTs. CNT surface engineering can be used also to provide biocompatibility and to attach specific target molecules for the use of CNTs as carriers in gene and drug delivery.

Layer by Layer technique (LbL)

The Layer by Layer technique (LbL) was developed by Decher G., et. al., in 1992 *[167, 168]* as a versatile tool for non covalent surface modification. The LbL technique involves the electrostatic interaction between oppositely charged polyelectrolytes, which are stepwise assembled on top of a planar of curved charged surface to form a thin polymer film of a few nanometers in thickness *[169-172]*. *Figure 4* shows the LbL assembly on top of charged colloidal surfaces. The assembly of polyelectrolyte multilayers (PEMs) via LbL starts with the immersion of the charged surface in a solution of a polyelectrolyte with an opposite charge to that of the surface to be coated. Polyelectrolyte molecules attach to the surface and form the first polyelectrolyte monolayer. Polyelectrolyte assembly is followed by rinsing with a salt solution or water which removes the non attached polyelectrolyte chains. Then, the surface is immersed in the second polyelectrolyte solution, now oppositely charged to the first

polyelectrolyte coating, followed again by its corresponding rinsing. The cyclical repetition of the process leads to the formation of a thin PEM film onto the charged surface. Both synthetic and natural polyelectrolyte molecules have been used for the LbL assembly. Natural polyelectrolytes are useful in these scenarios, where biocompatibility is required such as in the fabrication of delivery devices *[173, 174]*.

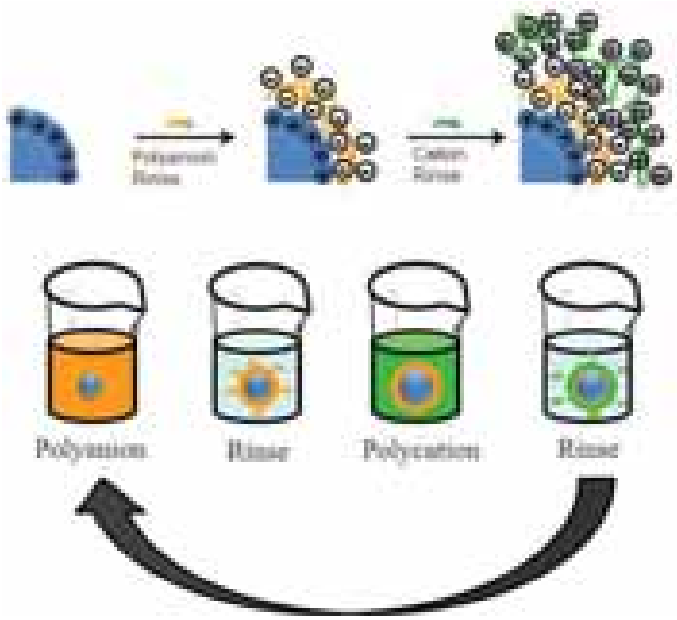

Figure 4. *Schematic representation of the Layer by Layer process on positively charged colloids surfaces*

The LbL technique can also be used for the templation of capsules for drug delivery. Capsule fabrication via LbL is based on PEM assembly on sacrificial colloidal templates that can be later destroyed by dissolution *[175, 176]*, leading to the formation of hollow polyelectrolyte nanocapsules. Different polyelectrolyte combinations and colloidal templates have been used to fabricate nanocapsules via the LbL technique, for example in *[177]* where Moya S. and co-workers fabricated PEM capsules using polystyrene sulfonate (PSS) and polyallylamine hydrochloride (PAH) on human red blood cells and melamine formaldehyde followed by template removal by dissolving in hypochlorite solution and by reducing pH respectively. Typical colloids used as templates in this technique are particles made of polystyrene *[178]*, silica *[60, 179]*,

calcium carbonate *[180, 181]*, cadmium carbonate *[182]* or gold *[183]*. Recently, the use of surfactant vesicles as templates has also been reported *[184]*. For each type of particle used as a template, the route to removing the template without dissembling the polyelectrolyte layer is different. The film thickness of the polyelectrolyte multilayers (PEMs) can be controlled by the number of layers deposited, while the shape and size of the nanocapsules can be engineered by choosing the appropriate template. The stability and surface functionality of the capsules can be controlled by the nature of the polyelectrolytes.

The LbL technique can not only be applied for the fabrication of capsules, but also for the surface engineering of drug delivery carriers. LbL allows the specific design by tuning the surface chemistry, size, permeability and degradability of the carrier. PEMs can be deposited via LbL on top of particles with encapsulated materials as barriers for release control, or as a functionalization tool to achieve specific targeting within the cell by attaching specific recognition molecules via electrostatic interactions, or by covalent binding, such as PEG *[97, 98]* or lipids *[185]* that have been proven to protect the carriers from non specific interactions. Moreover, to decrease toxicity, biocompatible polyelectolytes are used to fabricate the PEMs like chitosan/alginate *[98]*, dextran sulfate/protamine *[184]*, chondroitin sulfate/poly(L-arginine) *[186]*, poly (L-lysine)/poly(glutamic acid) *[179]*, etc. In addition, besides the loading of a therapeutic inside the particles, different cargos i.e. DNA or proteins, can be incorporated within the PEMs fabricated via LbL. The loaded material will be released from the PEM, or the PEMs will be eventually “peeled off” liberating the entrapped material *[60]*.

Polymer brushes

Surface modification via the LbL technique involves the non covalent surface engineering using polyelectrolytes. Polyelectrolytes can also be bonded to surfaces via covalent methods. When long polymer chains are covalently attached to a surface from one of their sides, the sterical repulsions between neighbouring chains force them to

stretch away from the surface forming "polymer brushes" *[187]*. Polymer brushes are interesting for many applications, for example in surface chemistry to stabilize suspensions of colloidal particles.

The grafting of polymer brushes onto surfaces can be done either via the "grafting to" or "grafting from" approach. "Grafting to" involves the direct covalent binding of a pre-synthesized polymer molecule to the surface. The active groups at the end of the polymer chain react with the functional groups on the surface. In general polymer chains bonded "to" a surface are voluminous and therefore the access between the attached polymer chains is limited.

On the other hand, the "Grafting from" approach is based on the initial covalent immobilization of polymer initiators on the surface followed by the *in situ* polymerization or propagation of the monomers from the surface. By this approach it is possible to form thick and highly dense polyelectrolyte brushes which are of special interest in solid surface engineering.

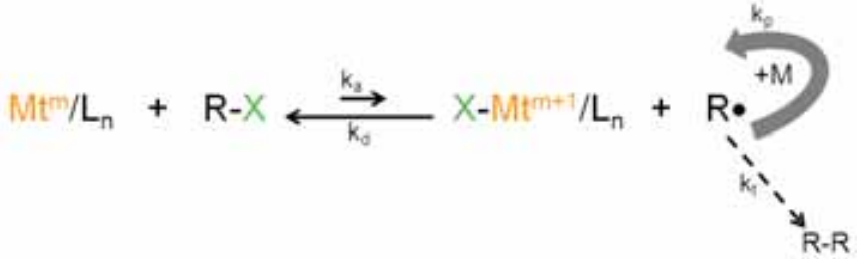

Figure 5. *Schematic representation of the ATRP reaction mechanism. Where Mt^m is a transition metal, L_n the complexing ligand, R represents the polymer chain and X the halogen Br or Cl.*

Among the polymerization methods typically used for "grafting from", atom transfer radical polymerization (ATRP) has received significant attention due to its living/controlled character, which allows the control of the molecular weight and polydispersity of the synthesized polymer brush *[188, 189]*. The polymer synthesized by ATRP is a result of the formation of radicals that can grow, but are reversibly deactivated to form dormant species. Reactivation of the dormant species allows the

polymer chains to grow again, only to be deactivated later. Such a process results in a polymer chain that slowly, yet steadily, grows and has a well-defined end group. Shown n *Figure 5* is the schematic representation of ATRP reactions. Although other controlled radical polymerization systems have been reported, ATRP remains the most powerful, versatile, simple, and most inexpensive.

Objectives and aim of this thesis

Although the design of targeted drug delivery systems is rapidly developing, there are several issues that still require further investigation, such as the biological fate *"in vitro"* and *"in vivo"*, or the toxicity of the carriers. In the case of PLGA, little is known about the degradation process inside the cells which, is fundamental in understanding the cargo release mechanism, and moreover, is crucial to ensure the expulsion of the copolymer from the cell and thus, allow disregarding any complications associated with long-term retention. Also for PLGA NPs, there is a need to find a means to target specific cell cultures and specific intracellular regions. In the case of CNTs, it is essential to fully characterize the controversial toxic effects when used as pristine CNTs and also as functionalized nanomaterials. In addition, more studies are needed in order to control CNT uptake and localization within cells, which is not a trivial task as tracking of CNTs is particularly difficult.

This PhD thesis is focused on the design of carriers for targeting delivery using two different and highly representative nanomaterials: poly(lactide-*co*-glycolide) (PLGA) nanoparticles (NPs) and carbon nanotubes (CNTs), their surface engineering on the basis of polyelectrolyte molecules through Layer by Layer films and polyelectrolyte brushes, the study of their interaction with cells, uptake, localization and biological fate; and their use for the delivery of therapeutics. The delivery of therapeutics will follow two strategies, both based on the use of PLGA NPs: small molecules, in this case doxorubicin, will be encapsulated in the core of the NP; while large molecules, in this case antiTNF-α, will be assembled in the PLGA multilayer coating, and its release will take place through the degradation of the multilayer. More specifically, the objectives of this thesis are:

- The fabrication and surface modification of PLGA NPs using polyelectrolytes, combined with covalent chemistry and/or the assembly of lipid bilayers in order

to create biocompatible coatings with specific recognition functions. It will be shown that the LbL technique combined with the covalent attachment of polyelethylene glycol and folic acid can increase uptake by cancerous cells, and that lipid layers on top of carriers with a proper lipid composition, can direct the NPs towards the endoplasmatic reticulum.

- The surface engineering of CNTs with polyelectrolytes and lipid layers in order to increase solubility and reduce toxicity for the application of CNTs in drug delivery or sensing.

- The study of the cellular uptake and intracellular distribution of engineered PLGA NPs and CNTs at the singular cell level by means of Raman Confocal Microscopy. The possibilities of Confocal Raman Microscopy as a label free technique for the intracellular localization of nanomaterials will be explored. Raman Confocal Microscopy will also be applied to study the cellular response in the presence of nanomaterials, investigating the changes in signals coming from proteins and nucleotides in the cell nucleus.

- The use of PLGA NPs for the encapsulation of different therapeutic drugs and the study of their *"in vitro"* release rate. It is demonstrated the versatility of the use of PLGA NPs to encapsulate the anticancer drug doxorubicin into the PLGA NPs core, as well as the encapsulation of high molecular weight molecules, like antiTNF-α that is intercalated between the polyelectrolyte multilayer coatings on top of PLGA NPs.

This thesis has been organized into six chapters:

- **Chapter 1**: Materials and methods used in this thesis will be detailed.

- **Chapter 2**: Fabrication of PLGA NPs by emulsion techniques will be presented together with the different approaches for their proper surface functionalization. PLGA NPs stabilized either by the synthetic polyelectrolyte polyethyleneimine (PEI) or by the protein bovine serum albumin (BSA) will be prepared. PLGA NPs will be surface functionalized via LbL coatings in order to provide functional groups for the further modification via covalent linking of polyethylene glycol (PEG) and folic acid (FA), or via self assembly of lipid bilayers.

  The interaction of the PLGA NPs with proteins and their uptake by HepG2 cells will be presented for the different surface coatings. It will be shown that pegylation alone reduces the interaction with proteins and cellular uptake, preventing unspecific interactions, while the coating with PEG and FA decreases the interaction with proteins, while at the same time increasing cellular uptake by HepG2 cells due to specific interactions. The surface modification using biopolyelectrolyte multilayers generates a more biocompatible NP surface that has antifouling properties. Finally, the assembly of lipid layers on top of the polyelectrolyte coated PLGA NPs will be used to control the intracellular distribution of the NPs toward the endoplasmic reticulum of the cell.

- **Chapter 3**: Details a strategy of surface functionalization of CNTs to provide colloidal stabilization in aqueous media. CNTs will be functionalized by the *in situ* synthesis of a polyelectrolyte brush of poly(3-sulfopropylmethacrylate) onto the surface of CNTs. The covalently bonded polyelectrolyte brushes on the surface of CNTs will be used as a platform for the *in situ* synthesis of CdS quantum dots and also for magnetic iron oxide nanoparticles. This type of dual-

particle CNT hybrid assembly was not previously synthesized by use of a covalently bonded polyelectrolyte brush. The synthesized nanoparticles can provide either magnetic or fluorescence properties to the CNTs.

The polyelectrolyte shell surrounding the CNTs will be also used for the assembly of a lipid layer on top of the CNTs. The choice of a spherical brush ensures the stability of the CNTs in aqueous solutions and also reduces the number of steps required in layer by layer to obtain a polymer cushion for coating with the lipid vesicles.

- **Chapter 4**: Addresses the cellular uptake, distribution and toxicity studies of the surface engineered PLGA NPs and CNTs by means of Confocal Raman microscopy (CRM). CRM will be used to study the localization of nanomaterials inside the cells, taking advantage of the fact that the entire Raman spectrum is recorded. The latter thus contains bands coming from the nanomaterials and from representative cell molecules: proteins, DNA and lipids; which allow identifying the region of the cell where the nanomaterials are located. It will be demonstrated that PEI stabilized NPs are uptaken by cells over a longer period of time compared with BSA stabilized PLGA NPs; although both kinds of PLGA NPs will be shown to be found in the region of the lipid bodies of the cell. Cell viability studies show that BSA stabilized NPs display better biocompatibility than PEI stabilized NPs. In the case of surface engineered CNTs it will be demonstrated that the lipid coating significantly reduces the toxic effect of CNTs, suggesting the use of lipid coated CNTs for biological applications, delivery or sensing, where a moderate toxic response *"in vitro"* is acceptable.

- **Chapter 5**: Details the study of potential uses of PLGA NPs as carriers for drug delivery. The antibody anti tumor necrosis factor (antiTNF-α) will be encapsulated in the PLGA NPs surface via LbL assembly, while the anticancer drug doxorubicin (Dox) will be loaded into PLGA NPs during NPs fabrication.

In both cases, the release profiles will be characterized in PBS and within the cell by different techniques. For the encapsulation of antiTNF-α, a strategy has been developed on the basis of the complexation of antiTNF-α with an excess of Alginate, and the assembly of this complex in the polyelectrolyte multilayers (PEMs). It will be demonstrated that by this encapsulation method it is possible to control the antiTNF-α doses by adjusting the number of layers deposited onto PLGA NPs surface. For both cases, in PBS and intracellular, the antibody delivery resembles a first order release profile.

It will also be proven that the intracellular delivery in HepG2 cells of Dox encapsulated in PLGA NPs by means of fluorescence methods such as flow cytometry and fluorescence life time microscopy. And moreover, Dox release will be confirmed by decreasing cell proliferation as a result of Dox intercalation into DNA strands.

- **Chapter 6:** Contains a summary of the results obtained in this PhD work. Conclusions and the potential future uses of PLGA NPs and CNTs in nanomedicine field will be detailed.

Chapter 1
Materials and Methods

1.1. Materials

Poly(D,L-lactide-co-glycolide) (PLGA) (D,L-lactide 85: glycolide 15 and D,L-lactide 65: glycolide 35), average molecular weight of 100 kDa, were purchased from the China Textile Academy. Multi-walled CNTs were purchased from Proforma (USA).

Dichloromethane (99%) from Aldrich was dried using molecular sieves 4 °A (microwave activated). Poly(acrylic acid) (PAA, Mw ~10 kDa), branched polyethyleneimine (PEI, Mw ~25 kDa), poly(allyl amine hydrochloride) (PAH, Mw ~15 kDa), poly(styrenesulfonate sodium salt) (PSS, Mw ~70 kDa), bovine serum albumin (BSA), folic acid (FA), amino terminated polyethylene glycol (PEG Jeffamine ED-2001, Mn ~1.9 kDa), phosphate buffer saline (PBS), ethylcarbodiimide hydrochloride (EDC), N-hydroxysuccinimide (NHS), 3-aminopropyltris(trimethoxy)silane (APTS), ethanol acetic acid (99.8%), 2-bromo-2-methylpropionic acid (98%), p-(dimethyl-amino)pyridine (99%, DMAP), 1,3-dicyclohexyldicarbodiimide (99%, DCC), copper chloride (I, 99.99%), 3-sulfopropyl methacrylate potassium salt (99%), 2,2'-bipyridil (99%, bpy), sodium sulfide, cadmium nitrate pentahydrate (99.99%), dimethylformamide (99%, DMF), PIERCE BCA Protein Assay Kit, Dulbecco's Modified Eagle's Medium (DMEM), fetal bovine serum (FBS), amiloride HCl, amantadine HCl, genistein and cytochalasin D were purchased from Sigma–Aldrich. Chitosan (Chi, Mw 100–300 kDa), sodium alginate (Alg, Mw ~25 kDa) were purchased from ACROS. Ethanol (99.95%) was purchased from Sharlau (Spain), (1-tetradecyl)trimethyl ammonium bromide (98%) and potassium permanganate (99%) from Alfa Aesar.

The phospholipids 1,2-dioleoyl-sn-hlycero-3-[phospho-L-serine] (DOPS), 1,2-Dioleoyl-sn-glycero-3-phosphocholine (DOPC) and 1-oleoyl-2-(6-[(7-nitro-2-1,3-benzoxadiazol-4-yl)amino]hexanoyl)-*sn*-glycero-3-phosphocholine (DOPC-NBD) were obtained and used as received from Avanti Polar Lipids, Inc.

5-Dodecanoylaminolfluorescein (DAF), 4',6-diamidino-2-phenylindole dihydrochloride (DAPI) and ER-Tracker™ Green (BODIPYL® FL glibenclamide) were obtained from Invitrogen. The cell line HepG2 was purchased from the American Type Culture Collection (ATCC). All chemicals were used as received.

1.2. Methods

1.2.1. ζ-Potential

When charged particles are dispersed into an aqueous solution containing ions, the ions with opposite charge will be attracted to the particle surface forming the so called electrical double layer. The electrical double layer comprise two regions, the first one, also known as "Stern layer", is formed by ions directly absorbed onto the particle surface (oppositely charged ions). The second region is then, composed by ions attracted to the particle surface via Coulomb force and is called "diffuse layer". The diffuse layer is loosely associated with the charged particle because is formed by free ions that move under the influence of electric attraction and thermal motion. Between the ions of the diffuse layer, the ones which are closer to the particle surface will remain attached, while those ions that are further away will move under the influence of tangential stress; the motional boundary that separates the mobile ions from the attached ones in the diffuse layer is usually known as "slipping plane".

The zeta potential (ζ-potential) is the electrokinetic potential at the slipping plane *[190, 191]*, and gives information about the charge density at the particle surface. In *Figure 1.1* is represented the ions distribution of a charged particle suspend in an ionic solvent.

The ζ-potential value of a particle is strongly dependent on the pH and ionic concentration of the solution. One way to quantify the ζ-potential is by measuring the electrophoretic mobility, which is the velocity of the motion of the particles in the solvent under the influence of an electric field. Electrophoretic mobility and ζ-potential are related by Henry's equation *[192]*:

$$\mu_e = \frac{\varepsilon\zeta}{6\pi\eta} f(k_a) \qquad (Eq.\ 1.1)$$

where ε is the dielectric constant of the media, η is the viscosity, ζ is the ζ-potential and $f(k_a)$ is Henry´s factor. The value of $f(k_a)$ depends on the ratio between the particle radius (a) and the thickness of the double layer (1/k). When the particle is much smaller than the double layer $f(k_a)$=1 (Hückel limit); and when particle is much layer than the double layer, $f(k_a)$=1.5 (Smoluchowsky limit).

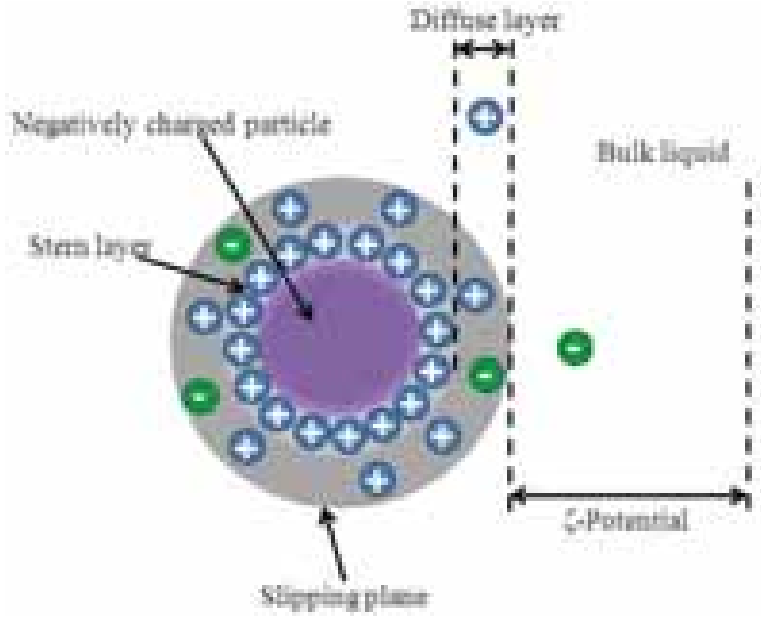

Figure 1.1. *Schematic representation of a charged particle dispersed in a solvent.*

ζ-potential measurments were used in this work to follow the different surface modifications applied on Poly(lactide-*co*-glycolide) nanoparticles and carbon nanotubes. Measurements were performed with a NanoSizer (MALVERN Nano-ZS, U.K.) instrument at 25 °C and with a cell drive voltage of 30 V, using a monomodal analysis model.

1.2.2. Dynamic Light Scattering (DLS)

Dynamic light scattering (DLS), known as well as photon correlation spectroscopy, is a widely used technique to determine the size of particles in solution. When a monochromatic and coherent laser hits a particle, the scattered intensity will show time dependent fluctuations caused by the random collisions of the particles with the molecules of the solvent that are constantly changing. This particle movement is known as the Brownian motion. DLS measures Brownian motion and relates this to the size of the particles suspended within a liquid. The frequency and the amplitude of the Brownian motion depend on the particle size and the viscosity of the solvent. The diameter that is measured in DLS is a value that refers to how a particle diffuses within a fluid, in other words, DLS measures the hydrodynamic diameter. The velocity of the Brownian motion is defined by a property known as the translational diffusion coefficient (D), and can be determined by the Stokes-Einstein equation *[191, 193]*:

$$D = \frac{k_B T}{6\pi\eta R_H} \quad (Eq.\ 1.2)$$

where D is the diffusion coefficient, k_B is Boltzmann's constant, T is the temperature, η is the viscosity of the medium and R_H is the hydrodynamic radius of the given particle.

The hydrodynamic size of surface engineered Poly(lactide-*co*-glycolide) nanoparticles was measured using a NanoSizer (MALVERN Nano-ZS, U.K.) instrument.

1.2.3. Transmission Electron Microscopy (TEM)

Transmission electron microscope (TEM) operates on the same basic principles as the light microscope but using electrons as light source. Electrons have much lower wavelength than light, which makes possible to get resolution of thousand times better than with a light microscope. By means of TEM it is possible to observe objects of the size of few angstrom (10^{-10} m) and for this reason electron microscopy is a powerful technique in medical, biological and materials science *[194, 195]*. After electrons are emitted from the electron gun, they travel over a vacuum column and pass through electromagnetic lenses that focus the electrons into a very thin beam that then travels to the sample. The objective lenses and the projector lenses magnify the transmitted beam and project it onto the fluorescent viewing screen. Impact of electrons excites the screen and produces a visible magnified image of the sample. This image is recorded with a CCD camera.

The morphology and size of surface modified poly(lactide-*co*-glycolide) nanoparticles and carbon nanotubes were characterized with a JEOL JEM-2100F electron microscope, EM-20014 model.

1.2.4. UV-Vis-NIR Spectrophotometry

Ultraviolet-Visible-Near Infrared Spectrophotometry is a technique used to measure the reflection or transmission properties of a substance in the ultraviolet (UV), visible and infrared range (IR). The absorption of UV, visible or IR light depends on the molecular structure of each substance and all the substance can absorb energy. Absorbance measurements are typical from analytical chemistry and material science since by absorbance it is possible to determine thickness and concentration of a sample *[196]*.

The commercial Varian Cary 5000 UV-Vis-NIR spectrophotometer (Varian GmbH, Australia Pty Ltd.) was employed to perform absorption spectra. The light sources of the instrument are a deuterium lamp (185–350 nm) and a halogen lamp (350–3300 nm). The absorption spectra can be collected on a wavelength range of 175 to 3300 nm.

1.2.5. Fluorescence Spectroscopy

Fluorescence occurs when a substance that has absorbed light or other electromagnetic radiation, emits light with different wavelength. The emission process can be explained on the basis of the different electronic states of the molecules called energy levels. If light is absorbed by a substance, the electronic state of the molecule changes from the ground electronic state (low energy state) to a one of the various vibrational states in the excited electronic state. Excited molecule can collide with other molecules causing as a result lose of energy until the molecule reaches the lowest vibrational state of the excited electronic state, and finally, as consequence of collisions, the molecule drops again into one of the various vibrational levels of the ground electronic state, emitting a photon in the process. Because the molecules can drop in any of the different vibrational levels of the ground state, the emitted photos will have different energies and in consequence, different frequencies *[197]*. Among their applications, fluorescence spectroscopy is often used for the biochemical, medical, and chemical analysis of organic compounds, and also has been reported to be useful for differentiating malignant tumors, in the detection of heavy metals, etc *[197, 198]*. In this work, fluorescence spectroscopy was used to characterize the functionalization of different materials with fluorescent species using a fluorometer Fluorolog® -3 HORIBA JOBIN YVON.

1.2.6. Quartz Crystal Microbalance with Dissipation (QCM-D)

The quartz crystal microbalance (QCM) is a high resolution mass sensing technique that consists of a thin quartz disk placed between a pair of electrodes. As quartz has piezoelectric properties, when an alternating electric field is applied across the device, an oscillation that propagates through the crystal is induced. The frequency of such oscillation is determined by the thickness of the crystal and the speed of shear waves in quartz. When a mass is loaded on top of the quartz crystal the mobility of the sensor becomes more limited and the oscillation frequency decays *[199, 200]*. *Figure 1.2* displays a schematic view of the different frequency responses obtained from a single quartz sensor monitored by QCM-D.

QCM technique has a resolution down to ng/cm^2 and it has been extensively used for the monitoring of thin films deposition onto surfaces. In addition to sensitively measure mass changes QCM can also characterize energy dissipative or viscoelastic behavior of the material deposited on the quartz sensor.

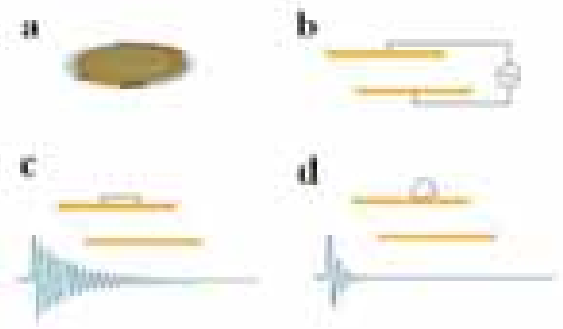

Figure 1.2. *Scheme of quartz crystal (a), electric circuit applied onto a: bare quartz sensor (b), a quartz sensor with a rigid mass deposited on top (c) and soft mass on top (d) (taken from Q-Sense, www.q-sense.com).*

The relationship between the frequency decay and the mass attached onto the quartz crystal of QCM was reported in 1959 by Günter Sauerbrey *[201]* (*Eq. 1.3*).

$$m_{QCM} = -C\frac{\Delta fi}{i} \qquad (Eq.\ 1.3)$$

where m_{QCM} represents the absorbed mass per unit area, the mass sensitivity constant C, is equal to 18.06 ± 0.15 ng /(cm^2 Hz) for sensors with a resonance frequency of 4.95 ± 0.02 MHz, and the letter "i" indicates the overtone number. The applicability of the Sauerbrey's equation is limited to rigid films. For soft and dissipative films, more complex models would be required that account for the viscoelastic properties of the film.

1.2.7. Raman Spectroscopy

Raman effect was discovered in 1928 by the Indian scientist C.V. Raman *[202]*. When light encounters a molecule, the majority of photons are elastically scattered, and this is what we know as Rayleigh scattering; the scattered light has the same wavelength as the incident light. However, a small proportion of the photons, less than 0.001%, will be inelastically scattered, where the scattered light undergoes a shift in energy, and that effect is called Raman scattering.

Raman effect is complementary to infrared spectroscopy *[203]*. Infrared spectroscopy requires a dipole moment change through the vibration, whilst Raman requires a change in polarisability. That is, the distortion of the molecule's electron cloud during the vibration must cause the molecule to interact differently with the electric field of the incoming photon *[203, 204]*.

Figure 1.3 illustrates the transitions accompanying Raman scattering. The electric field of the incident light distorts the molecule's electron cloud, causing it to undergo electronic transitions to a higher energy virtual state, which is not a true quantum mechanical state of the molecule. Raman scattering results when the scattered photon is released to a ground state with different energy that the incident photon. The change in energy between the original state and the new state causes an up-shift or down-shift frequency of the emitted photon different from the excitation wavelength. The Stoke

Raman scattering is then defined as the situation when the excited molecule generates a photon at a downshifted frequency. In contrast, anti-Stoke Raman scattering happens when the emitted photon has an up-shifted frequency. The change or shift in energy indicates molecular information and its photon mode in the target. This vibrational-reach information that supports Raman spectroscopy has become a commonly used tool in chemistry because of its specificity to the chemical bonds or symmetry of molecules.

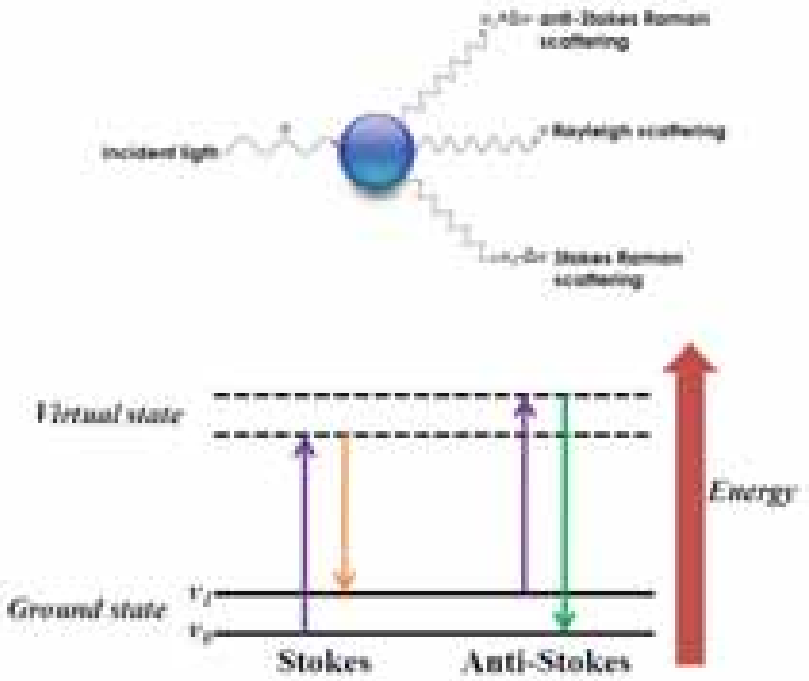

Figure 1.3. *Scheme of the Raman scattering process and its energy transitions.*

In this work Raman spectroscopy analyses were performed using a Renishaw inVia Raman microscope. The laser excitation wavelength was 532 nm with a grating of 1800 mm^{-1}. The microscope was equipped with interchangeable objective lenses with magnifications of 10×, 50×, and 100×. Most measurements were conducted using the 40× water immersion and 50× objectives. The size of the focal spot was approximately 1 μm. Raman spectra were recorded in the region from 100 to 3200 cm^{-1} with a spectral resolution of around 7 cm^{-1}. Around ten to fifteen accumulation scans at different sample points were used to reduce the spectral noise and to account for possible sample

heterogeneities. The system was calibrated to the spectral line of crystalline silicon at 520.7 cm^{-1}. All spectra were baseline corrected.

1.2.8. Confocal Laser Scanning Microscopy (CLSM)

Confocal Laser Scanning Microscopy (CLSM) is a powerful technique, that allows to obtain fluorescent images from a specific confocal plane in a sample *[205, 206]*. In other words, by CLSM is possible to discriminate the interference of light or fluorescence coming from planes different to the confocal plane, in order to generate images with high resolution and contrast. CLSM also offers the possibility to generate the three dimensional reconstruction of a sample by imaging at different focal planes.

In CLSM, coherent light emitted by the laser system passes through a pinhole aperture that is situated in a certain focal plane with a scanning point on the specimen and a second pinhole aperture positioned in front of the detector, which is a photomultiplier tube. As the laser is reflected by a dichromatic mirror and scanned across the specimen to excite it in a defined focal plane, secondary fluorescence emitted from points on the specimen in the same focal plane, pass back through the dichromatic mirror and are focused as a confocal point at the detector pinhole aperture (*Figure 1.4*) *[207]*.

The significant amount of fluorescence emission that occurs at points above and below the objective focal plane is not confocal with the pinhole and forms extended airy disks in the aperture plane *[208]*. The small fraction of the fluorescence emission that is out of the focal plane is not detected by the photomultiplier and does not contribute to the resulting image. The pinhole aperture determines the working confocality or plane thickness. By different filters placed in front of the photomultiplier, it is possible to select the desired emission wavelength. Finally, the optical signal is converted into electronic and then translated as images in a computer.

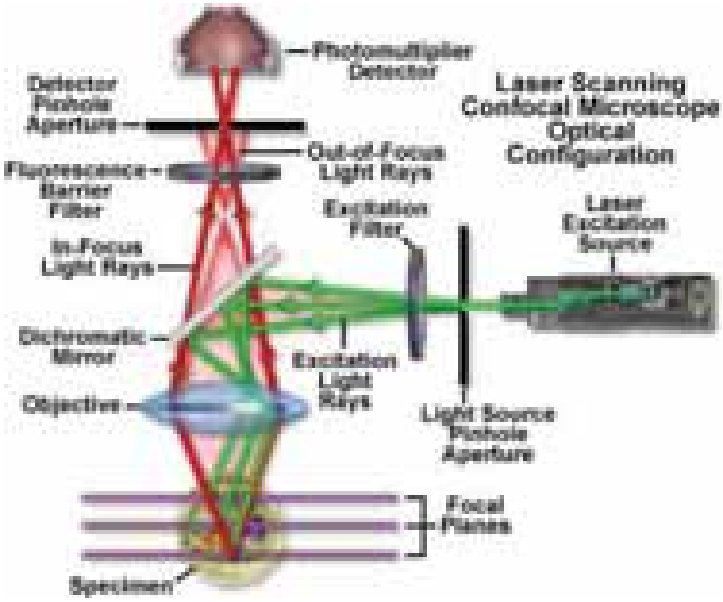

Figure 1.4. *Schematic representation of a Confocal Laser Scanning Microscope [206].*

In this work, a CLSM from Zeiss, the LSM 510-META was used for cell imaging. The microscope is equipped with Argon/2 laser for 558, 477, 488 and 514 nm; a DPSS laser for 561 nm; a HeNe laser for 633 nm and an external laser of 405 nm.

1.2.9. Fluorescence Lifetime Imaging Microscopy (FLIM)

Fluorescence lifetime imaging microscopy (FLIM) is an imaging technique that produces spatially resolved images of fluorophore lifetime (τ) from an exponential decay rate of fluorescence, providing another dimension of information for visualizing fluorophores and an additional source of contrast *[197]*. The life time of a fluorophore is affected by the environment in which it is located, changes in pH, ionic strength, polarity can be sensed through the life time.

In this work, for FLIM studies, a modular FLIM system from Becker & Hickl GmbH, adapted to the CLSM (Zeiss, LSM 510-META) was used with a 405 nm laser.

1.2.10. Flow Cytometry

Flow cytometry is an analysis technique that measures fluorescence and light scattering of individual particles in suspension, such as cells. In flow cytometry, the flow of the particles in suspension is such that never more than one particle pass through the laser light at the same time (hydrodynamic focus). The fluorescence and the scattered light generated from particle passage through the laser, is collected by detectors and converted into electronic signals. The analysis occurs simultaneously for signals, fluorescence and scattering *[209, 210]*.

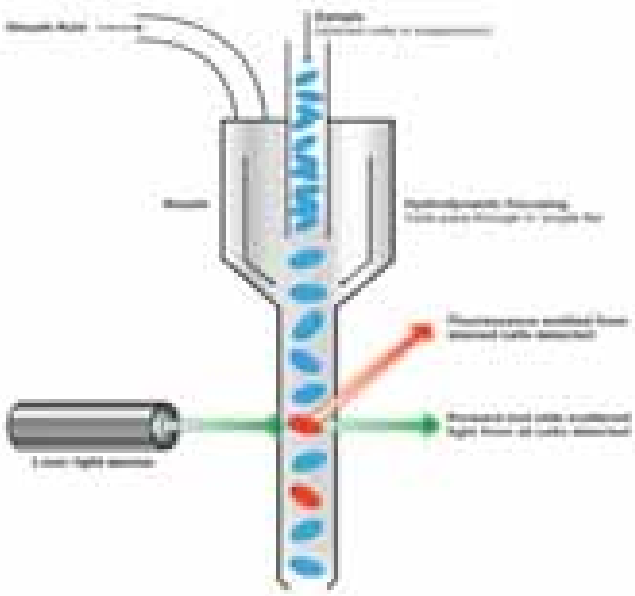

Figure 1.5. *Scheme of the working principle of the flow cytometer. (Image taken from www.abcam.com)*

Light scattering occurs when the incident light is scattered by the particle generating a change in the direction of the light. Light scattering gives information about the morphology of the particle under study. When the scattered light divert a small angle from incident light (0 to 10º), the scattering is called "forward scatter" (FSC) and this

diversion is proportional to the particle size. If the scattering is in right angle, is known as “side scatter” (SSC) and provide information about the complexity of the particle *[210]*. *Figure 1.5* shows the flow cytometer working principle. Hydrodynamic focus is applied in the particle suspension flow in front of the laser. The sample is injected into the center of the flow. Then, the flow is reduced in diameter, forcing the particles into a stream, in which only one particle at a time passes in front of the laser. Also it is possible to observe the fluorescence and light scattering processes. Herein, a flow cytometer BD FACS, Canto II model was used for the quantification of cellular uptake or fluorescence in particles.

1.2.11. Plate Reader

The plate reader is and instrument designed to detect biological, physical or chemical events from culture microplates. A high intensity light source throws light in each and every well of the microplate, and then the absorbed or emitted light coming from each well is quantified by a detector *[211]*. A plate reader can detect absorbance, fluorescent intensity, luminescence, fluorescence along time or fluorescent polarization.

In this work, a TECAN GENios Pro plate reader in the absorbance detection mode was used to quantify different biologic assays like toxicity and cellular viability by MTT assay, protein concentration via BCA assay or antibody concentration using an ELISA based test.

1.2.12. MTT assay

The MTT standard colorimetric assay that measures enzymatic activity in cell culture and is usually employed to determined cellular survival and proliferation. MTT assay is based in the metabolic reduction of 3-(4,5-Dimethylthiazol-2-yl)-2,5-diphenyltetrazolium bromide (MTT) by the mitochondrial enzyme dehydrogenase. As a result of the MTT reduction, a purple compound known as formazan is generated *[212]*. The number of cells alive is proportional to the amount of formazan produced, that can be quantified by measuring the absorption at 570 nm. Therefore, cellular viability can be calculated with the *Eq. 1.7*.

$$CellViability(\%) = \frac{Absorption_{sample}}{Absorption_{control}} \times 100 \qquad (Eq.\ 1.7)$$

1.2.13. BCA assay

The bicinchoninic acid assay (BCA assay) is a biochemical assay for determining the total concentration of protein in a solution. There are several advantages of BCA assay over other protein quantification assays like the formation of a stable complex, the low susceptibility to detergents and they applicability for broad protein concentrations.

BCA assay relies on two reactions principally. Firstly, the peptide bonds in the protein reduce Cu^{2+} ions from the cupric sulfate to Cu^{+} (a temperature dependent reaction). The amount of Cu^{2+} reduced is proportional to the amount of protein present in the solution. Next, two molecules of bicinchoninic acid chelate with each Cu^{+} ion, forming a purple-colored product that strongly absorbs light at a wavelength of 562 nm *[213]*. The amount of protein present in a solution can be quantified by measuring the absorption spectra and comparing with protein solutions with known concentrations.

1.2.14. Q-ADA ELISA assay

Q-ADA ELISA assay is an enzyme immunoassay for the quantitative determination of adalimumab (Humira®) in serum and plasma. Adalimumab is a recombinant human IgG1 monoclonal antibody specific for human tumor necrosis factor alpha TNF-α, and consists of 1330 amino acids with molecular weight of approximately 148 KDa.

Adalimumab binds specifically to TNF-α and blocks its interaction with the p55 and p75 cell surface TNF receptors. TNF is a naturally occurring cytokine that is involved in normal inflammatory and immune responses. Q-ADA assay is basically a solid phase enzyme-linked immunosorbent assay (ELISA) based on the sandwich principle. Standards and diluted samples, in either serum or plasma, are incubated in the culture microplate coated with the reactant for adalimumab. After, a horse radish peroxidase (HRP) conjugated probe is added and binds to adalimumab captured by the reactant on the surface of the wells. Finally, the bound enzymatic activity is detected by addition of chromogen-substrate *[214]*. The color developed is proportional to the amount of adalimumab in the sample or standard. Results of samples can be determined directly using the standard curve.

Chapter 2

Poly(lactide-*co*-glycolide) Nanoparticles: Synthesis and Layer by Layer Modification

2.1. Motivation

Polymeric Nanoparticles (NPs) in the submicro size are promising carriers for controlled drug delivery. Size, amount of loaded material, and release features can be well controlled for these NPs. Besides that, polymeric NPs can be further endowed to target specific organs and tissues, and in many cases are capable of overcoming certain biological barriers such as the blood–brain barrier *[215-217]*.

The lactic acid (LA) homopolymer (PLA) *[101, 105]* and its glycolic acid (GA) copolymer, poly(D,L-lactide-*co*-glycolide) (PLGA) *[107-110]* are among the most frequently used polymers for the templation of drug carriers because of their good biocompatibility, biodegradability degradation rate. The degradation of PLGA can be used for the release of drug encapsulated in the NPs, .Degradation in PLGA can be easily manipulated by adjusting the ratio LA to GA *[107]* in the copolymer.

The scope of this chapter is to show the design of PLGA NPs for targeted delivery by their surface modification via the LbL technique in combination with covalent chemistry and lipid assembly, as well as to study the *"in vitro"* cellular uptake.

The possibilities of the LbL technique for the surface modification of NPs for delivery will be explored. The LbL technique has several advantages for surface

functionalization of organic NPs. First, by means of LbL the surface of the NPs can be sequentially modified without affecting their stability. In principle, if the NPs are over 100 nm, the only requirement for self assembly is that the NPs surface must be charged. The assembled polyelectrolyte multilayers provide chemical groups, to which functional molecules can be covalently immobilized, as it will be showed for polyethylene glycol (PEG) and folic acid (FA). In this way a protocol of non covalent functionalization followed by covalent chemistry will be developed. This protocol brings multiple possibilities for the modification of NPs and can be employed for any charged surface. In addition, the LbL coating can be composed of biopolymers like proteins or charged carbohydrates, providing biocompatibility to the NPs and protecting them from the interaction with proteins.

Polyelectrolyte multilayers fabricated by means of the LbL technique are a good support for lipid layers. The surface modification of NPs with lipid layers can help to increase NP circulation time inside the cells. Moreover, the lipid coating also can be useful to control the intracellular location of NPs.

In the first part of the chapter the fabrication of PLGA NPs by emulsion techniques will be presented. PLGA NPs will be stabilized by either the synthetic polyelectrolyte polyethyleneimine (PEI) or the protein bovine serum albumin (BSA). The use of charged macromolecules for stabilization of the NPs will be important for the LbL coating. BSA was chosen to provide the NPs with a biocompatible coating.

Then, the coating of the NPs with model multilayers of synthetic polyelectrolytes, poly acrylic acid (PAA) and polyethyleneimine (PEI) will be presented. PEG and FA will be covalently linked to the carboxilate groups of PAA. The LbL assembly and covalent chemistry will be characterized on top of the PLGA NPs by ζ-potential measurements and in planar model layers with the quartz crystal microbalance. The interaction of the PLGA NPs with proteins and their uptake by the immortalized HepG2 cell line will be presented for the different surface functionalizations steps: LbL coating, PEG and FA covalently linked to PEG. It will be shown that the pegylation alone reduces the

interaction with proteins and cell uptake by the cell line preventing unspecific interactions, while the coating with PEG and FA still decreases the interactions with proteins but at the same time increases cell uptake by HepG2 cells due to specific interactions.

The same methodology will be applied using a multilayer purely based on biopolymers chitosan (Chi) and alginate (Alg). PEG and FA will be also covalently linked with to the polyelectrolytes. The interaction with proteins and cells of the polyelectrolytes assembly and the PEG and FA grafting on top of PLGA NPs will be studied as for other coatings. The scope of using these biopolymers is to generate a more biocompatible NPs surface. It will be shown in addition, that the Chi/Alg coating has itself antifouling properties.

Finally, the assembly of lipid layers on top of the polyelectrolyte coated PLGA NPs will be studied. Lipid vesicles composed of DOPC and DOPS at different molar ratios will be assembled on top of the polyelectrolytes via electrostatic interactions. The relation of DOPS and DOPC in the lipid membranes affects significantly the cellular uptake of the NPs and therefore, by adjusting the lipid composition in the NPs coating, it is possible to control NPs internalization in the cell. Moreover, it will be shown that the lipid coating results in the localization of the NPs in the endoplasmic reticulum (ER) of the cell. These NPs, that preferentially translocate in the ER could have applications for the treatment of antiviral human pathogens *[218]*, such as human immunodeficiency virus (HIV) *[219]*, hepatitis C virus (HCV) *[220]* or hepatitis B virus (HBV) *[221]*, and also in other diseases such as anticancer vaccinations *[222]*.

To resume, the LbL coating of PLGA NPs will be used to generate NPs for targeted delivered towards hepatic cancer cells, to diminish protein-NPs interactions and to achieve intracellular targeted delivery.

2.2. Poly(lactide-*co*-glycolide) nanoparticles synthesis

Poly(D,L-lactide-*co*-glycolide) (PLGA) NPs were prepared by means of an oil/water (O/W) emulsion-solvent evaporation method *[109]*. Firstly, 1 mL of 20 mg/mL of PLGA dichloromethane solution (organic phase) was added to 4 mL of a 5 % PEI solution or of a 2 % BSA solution (water phase) and then emulsified with an ultrasonicator (Sonics VCX 500) for 20 s. This emulsion was poured into 100 mL of distilled water, and stirred for 3 h with a magnetic stirrer until the organic solvent was totally evaporated. The PLGA NPs were collected by centrifugation at 10 000 g for 5 min, and washed with milliQ water five times to remove the free PEI or BSA initially presented in the water phase. The PLGA NPs preparation process is illustrated in *Figure 2.1*. PLGA NPs containing rhodamine 6G (Rd6G) were similarly prepared by addition of 0.5 mg/mL of Rd6G into the PLGA solution before mixing with the stabilizer solution.

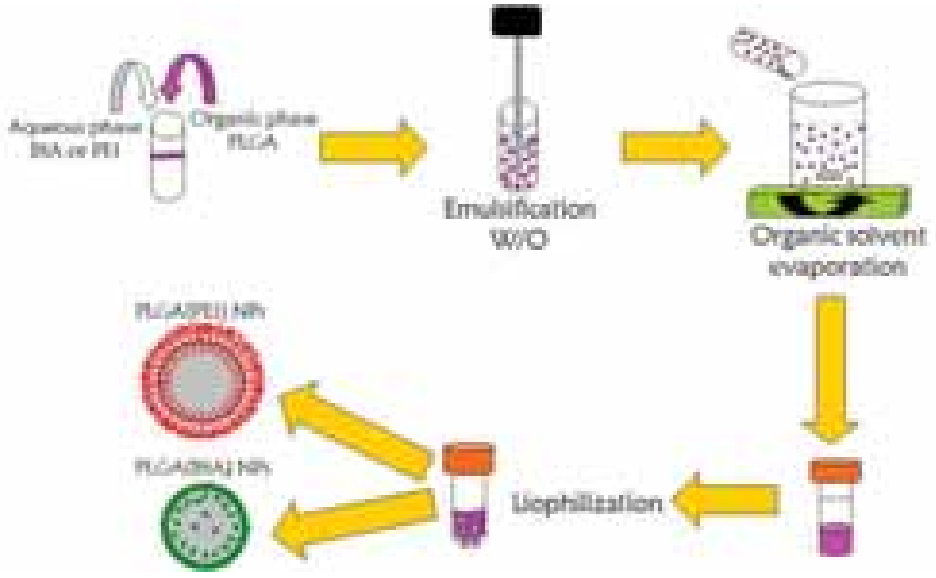

Figure 2.1. *PLGA NPs Preparation by means of the O/W emulsion-solvent evaporation method.*

The size and morphology of PLGA NPs prepared with either PEI or BSA were characterized by transmission electron microscopy (TEM) and dynamic light scattering

(DLS). PLGA NPs were observed to have spherical shape for both cases, stabilized with PEI or BSA. The average size of the particles with PEI as stabilizer is around 350 nm with a narrow distribution in the wet state as shown in *Figure 2.2a,* and around 250 nm in a dry state (*Figure 2.2b*). In the case of the NPs prepared with BSA as stabilizer the diameter observed by TEM was around 200 nm (*Figure 2.2d*). DLS show that PLGA NPs stabilized with BSA display a narrow distribution, being the average diameter measured around 400 nm (*Figure 2.2c*). For both stabilizers, the difference in the NP size observed in wet and dry state is due to the fact that in wet state PEI and BSA hydrate occupying a higher volume, and these has an impact in the measure of the NPs hydrodynamic ratios.

PLGA NPs stabilized with PEI are positively charged with ζ-Potential around 35 mV, while PLGA NPs with BSA as stabilizer have negative ζ-Potential of -27 mV.

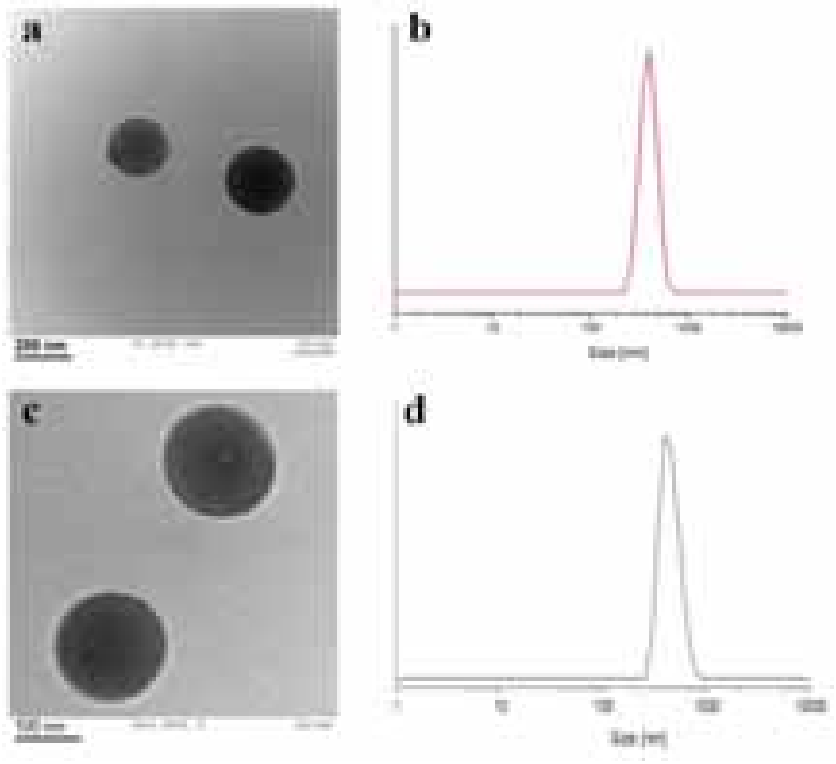

Figure 2.2. *TEM morphology of PLGA NPs stabilized with PEI (a) and BSA (c) and their respective DLS size distribution (b and d).*

2.3. PLGA NPs surface modification does selective cell targeting

One of the most important aspects in the design of a carrier for drug delivery is the control of the release site, generally recognized as the targeting site, in order to enhance the pharmaceutical efficiency while side effects are reduced. The targeted delivery of the drug carriers is usually realized by attaching specific recognition functions to the particles, e.g., specific monoclonal antibodies (mAB) *[132, 223-226]* or ligands specific to certain cell membrane receptors *[110, 227-229]*. To minimize the unspecific interactions, molecules with anti-fouling properties such as poly(ethylene glycol) (PEG) are often used as a spacer between the particle surface and the recognition function *[132, 228, 229]*. Folic acid (FA) shows extremely high affinity to the folate receptors. Compare with antibodies, molecules like FA are more stable against harsh preparation conditions, and thereby are easier to handle and more convenient for many applications. FA is a kind of vitamin B necessary for the production and maintenance of new cells. It is well known that a low level of folate receptors on the cell membrane is expressed by normal tissues, but the folate receptors are over expressed by many human tumors. Therefore, the FA grafted NPs can be used to specifically target tumor tissues.

The layer-by-layer (LbL) assembly, which is well know technique for the non-covalent surface modification, was used to engineer the surface of the PLGA NPs prepared with PEI in the water phase as stabilizer. Then, the multilayer coated PLGA NPs were further modified with FA attached to a PEG spacer.

2.3.1. Synthesis of folic acid grafted poly(ethylene glycol)

First, 65 mg (0.15 mmol) FA was dissolved in 2.5 mL dimethylsulfoxide (DMSO) by overnight stirring. Then, 38 mg NHS (0.33 mmol) and 30 mg EDC (0.17 mmol) were added into the solution to activate COOH groups of FA. The final molar ratio of FA/NHS/EDC was 1:2.2:1.1. The reaction was left for 18 h and afterwards 300 mg of amino group terminated PEG (0.15 mmol) were added to the solution. After 24 h, the product of reaction was dialyzed against water for 1week in a dialysis bag with a cut off MW of 1 000, replacing water every 24 h. The final product was lyophilized with a

lyophilizer. The FA grafted PEG (PEG-FA) was characterized by FTIR and 1 H NMR at 500 M in D_2O *(Appendix Figure A and B respectively)*.

2.3.2. Layer by Layer assembly and folic acid immobilizing on nanoparticles

The surface modification of PEI stabilized PLGA NPs was performed using 1 mg/mL of PAA and PEI solutions in 0.5 M NaCl for the LbL coating. The pH of the solution was adjusted to 7.4 by addition of either 1 M HCl or NaOH. For the LbL assembly on PLGA NPs surface, the incubation time for each polyelectrolyte layer was 15 min, and the NPs were washed with a 0.5 M NaCl solution three times between each layer . After five layers of PAA and PEI (PAA as the outmost layer) were deposited, the multilayers were either only crosslinked or crosslinked and grafted with PEG following the method described by Meng F., et al *[230]*. The NPs with multilayers were suspended in 10^{-2} M EDC and 10^{-2} M NHS solution (pH 5.6) 30 min to activate carboxylic groups, and then in a 10^{-2} M EDC and 10^{-2} M NHS (pH 8.6) or 10^{-2} M EDC, 10^{-2} M NHS and 5 mg /mL of amine terminated PEG or PEG-FA solution (pH 8.6) for crosslinking, pegylation or PEG-FA immobilization, respectively. 40 h later, the NPs were rinsed with MilliQ water.

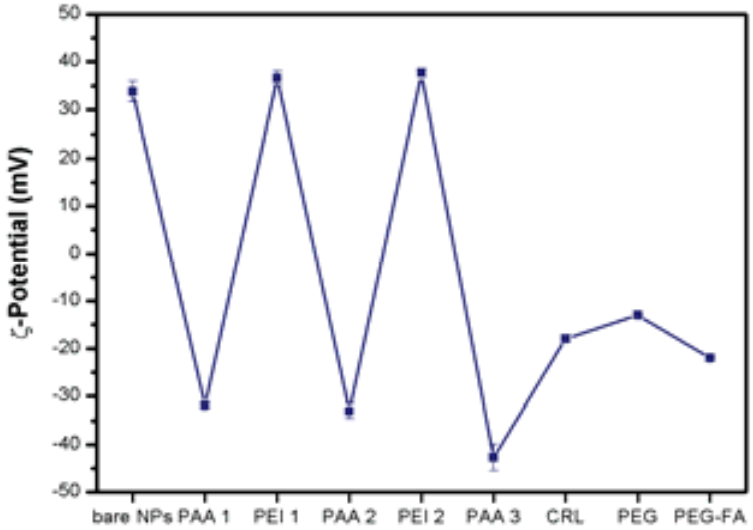

Figure 2.3. *Changes in the ζ-Potential of PLGA NPs during PEI/PAA LbL assembly and subsequent crosslinking and pegylation.*

The ζ -potential of the NPs was measured in 10 mM NaCl (pH 7.4) with a measuring potential of 60 V, ζ -potential measurements were conducted to prove polyelectrolyte assembly and the covalent binding of PEG and PEG-FA on the PLGA NPs. The alternative assembly of polyelectrolytes of opposite charge induces surface recharging and the consequent change in the sign of the potential. During the LbL assembly of PEI/PAA the ζ-potential oscillated between +35 ± 5 mV and -35 ± 5 mV for either PEI or PAA as outmost layer. After crosslinking or pegylation, the ζ-potentials changed to -20 mV and -11 mV, respectively *(Figure 2.3)*. This is understandable since the negatively charged carboxylic groups were used for the crosslinking. The further decrease in the value of the potential observed after pegylation is brought by the hydrodynamic screening effect of the PEG molecules *[231]*. After PEG-FA grafting, however the ζ-potential varied to -22 mV again. We attribute this value to the additional carboxylic groups brought to the NPs surface by the FA molecules.

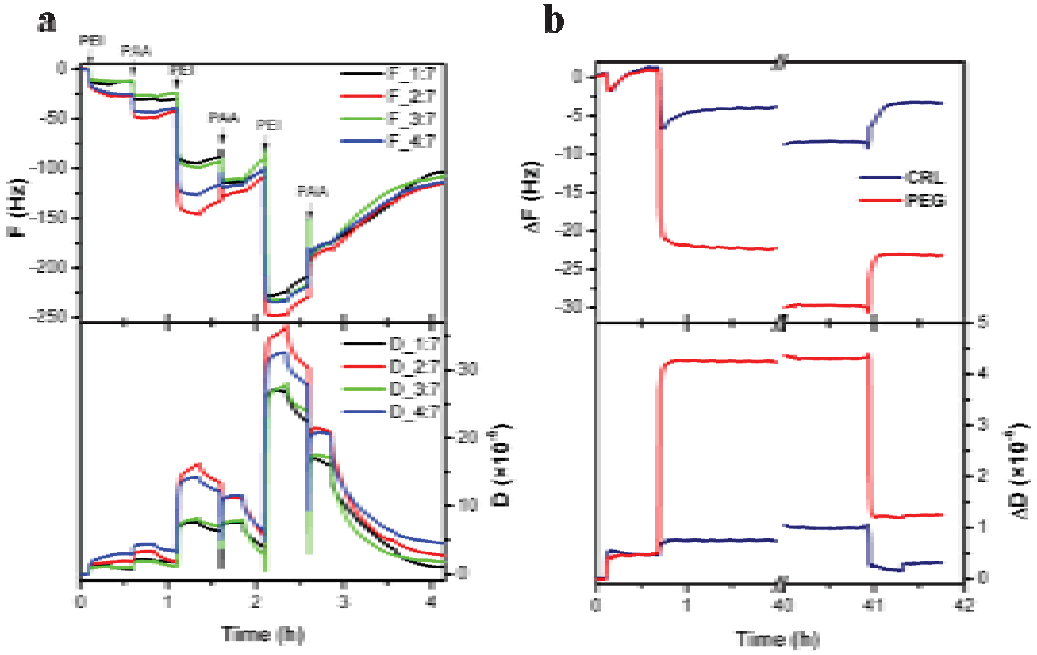

Figure 2.4. *Frequency and dissipation changes during the assembly of PEI/PAA multilayer (a), and after the crosslinking and pegylation of the multilayers (b) as followed by QCM-D.*

To have an additional proof of the covalent binding on the multilayers we followed the crosslinking and condensation reactions on planar multilayers by means of the quartz crystal microbalance with dissipation (QCM-D). Multilayers of PEI and PAA were previously assembled on top of a silica coated QCM-D crystal; the assembly is shown in *Figure 2.4a*. In *Figure 2.4b* we can observe the changes in frequency and dissipation during crosslinking and pegylation.

PEI/PAA multilayers were first stabilized in water for 5 min. Then, water was exchanged by the activation solution compose of 10^{-2} M EDC and 10^{-2} M NHS solution (pH 5.6). During activation, before crosslinking and pegylation, the frequency did almost not change. Half an hour after addition the activation, the solution was exchanged by either the crosslinking solution (CRL) or the pegylation solution. In both cases the samples were incubated for 40 h. Following incubation in the CRL, a final decrease in 5 Hz was recorded for the frequency and a dissipation increase of only 0.4 units. The crosslinking did not induce a significant change in the multilayer mass. The slight increase in mass could be due to an increase in the water entrapped in the layers as result of polyelectrolyte reorganization during the crosslinking. After pegylation a decrease in 25 Hz in frequency and an increase in 4 units in dissipation was observed. The decrease in frequency is higher than for crosslinking and can be associated with a mass increase in the multilayer as result of the binding of PEG. QCM-D confirms, therefore, that pegylation takes place on the model planar multilayer.

2.3.3. Protein adsorption on the Layer by Layer coated nanoparticles

In the case of target drug delivery, it is very important to increase circulation time after the NPs are injected into the blood in order to reach their targeted tissues or organs. Protein adsorption is an important aspect to be studied taking into consideration the possible application of NPs for drug delivery. NPs will inevitably interact with serum proteins upon contact with blood or body fluids. The circulation time of the NPs and their uptake by cells will be significantly affected by the nature and amount of proteins deposited on their surface Normally, after the injection of the NPs, there are some proteins in serum including apolipoprotein E *[232]* or complement C3 *[233]*, that are unspecifically adsorbed on those NPs which can trigger macrophage recognition and

uptake. By decreasing the interaction of the NPs with these specific proteins it is possible to increase their circulation time and reduce unspecific uptake of NPs.

We detected protein adsorption on the PEI/PAA multilayers coated PLGA NPs using the BCA method. To determine the amount of proteins adsorbed on the NPs, 3 mg of PLGA NPs were accurately weighted and incubated in 1 mg/mL BSA in PBS for 2 h or in DMEM culture media with 10 % FBS for 2 h and 16 h at 37 ºC, respectively. The supernatant was discarded after centrifugation and the particles were washed three times with 10 mM PBS, followed by the addition of 1 mL of 5 % SDS. The system was sonicated 40 min at 40 ºC. The amount of adsorbed proteins was measured from the supernatant by the BCA protein assay kit. The ζ-potential of the NPs after protein adsorption was also measured.

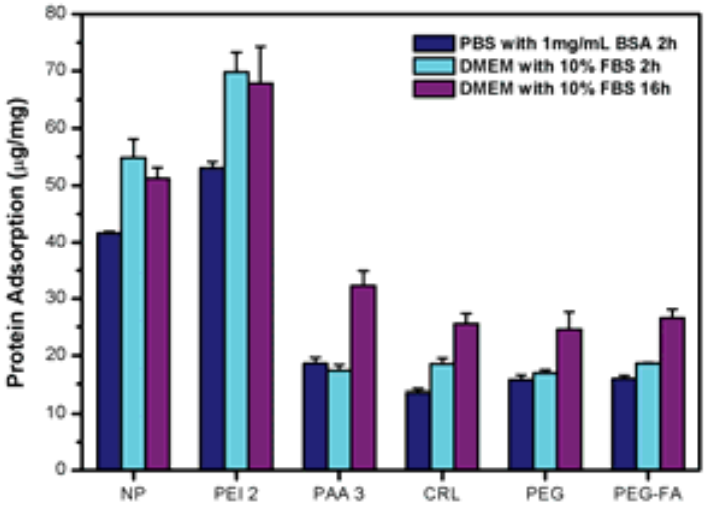

Figure 2.5. *Protein adsorption amount of the PLGA NPs with different properties at variable conditions.*

Figure 2.5 shows that the NPs covered with the $(PAA/PEI)_2$ multilayers had the largest protein adsorption amount, 50–70 μg /mg NPs, regardless of the composition of the medium. Protein adsorption for the $(PAA/PEI)_2$ coating was even larger than that of the control NPs, 40–55 μg /mg NPs, which also had PEI on their surface. The amount of adsorbed proteins on the $(PAA/PEI)_2$/PAA coated NPs with crosslinked multilayers pegylated and PEG-FA covered NPs largely decreased to around 20–30 μg /mg NPs. In

the DMEM/FBS medium generally more proteins adsorbed regardless of the structures of the NPs than in the pure BSA protein medium. On the control NPs and on the $(PAA/PEI)_2$ coated NPs, the amount of adsorbed proteins slightly decreased when extending the incubation time from 2 to 16 h. For all the samples, the longer incubation times resulted in an obviously higher amount of adsorbed proteins. In particular, the protein amount on the $(PAA/PEI)_2/PAA$ coated NPs was almost doubled and finally reached a value of 32 μg /mg NPs after 16 h incubation. These results imply that although the protein components on the NPs surface might be changing all the time during the incubation, the overall adsorption of the proteins on the positively charged surfaces is rapidly equilibrated, due to charge attraction. The protein adsorption on the negatively charged surface is a process, which requires a relatively longer time than for the positive charged surfaces, though the adsorption process can be similar for both surfaces.

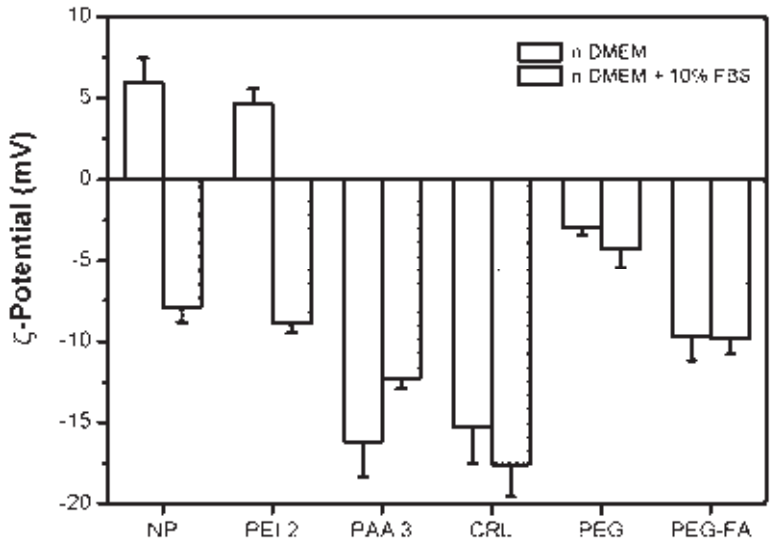

Figure 2.6. *ζ-Potential of the PLGA NPs with different polyelectrolyte coatings, pegylated and modified with PEG-FA in protein solutions.*

ζ-Potential measurements further confirmed the protein adsorption on the PLGA NPs. *Figure 2.6* shows that after incubation in DMEM, for all the samples measured the absolute value of the ζ-potential decreased compared with their initial values due to the

increase in ionic strength. After incubation in DMEM/FBS, however, the surface charge changed to negative values, confirming undoubtedly the adsorption of serum proteins, which are usually negatively charged. This is consistent with the previous results, since the most abundant and negatively charged albumin (~36–50 g /L) are adsorbed in less than 5 min on the surface *[234]*. For all the other NPs, the ζ-potentials remained negative with very minor changes. Actually, proteins can be adsorbed on the NPs surface even if they are negatively charged or pegylated, because of the non uniform distribution of charges in the proteins and existence of other forces such as hydrogen bonding and van der Waals forces.

2.3.4. Cellular uptake

The HepG2 cell line, a kind of human liver cell lines, was cultured in DMEM with 10 % FBS and 1000 U penicillin, 10 mg/mL streptomycin at 37 ºC and in 5 % CO_2. When the cell confluence was around 70 %, all the cells were trypsinized. 300 000 cells were seed into each well of a 24-well plate. 24 h later, PLGA NPs with encapsulated Rd6G and different surface coatings were added into the culture medium. The final concentration was adjusted to 100 mg/mL. Following different incubation times: 0.5, 1, 2, 4, 8, 12, and 24 h, the cells were washed with PBS twice, trypsinized and studied with flow cytometry.

The cellular uptake ratio was calculated from the dotplot graph of forward scattering (FCS) versus fluorescence intensity (PE-A) employing the WinMDI 2.9 program of data analysis. Firstly, a threshold of fluorescence was generated using a control sample, i.e., the HepG2 cells without exposure to the NPs. All dots corresponding to the control sample are located at intensities below this threshold (*Appendix Figure C1*). The number of cells carrying fluorescently labeled NPs is obtained from the dots located at higher intensities than the threshold (*Appendix Figure C2*). The cellular uptake ratio was calculated as:

$$Cellular\ uptake\ ratio = \frac{No.of\ the\ dots\ over\ the\ threshold}{No.of\ all\ the\ dots}\ X\ 100\% \qquad (Eq.2.1)$$

The fluorescence intensity is defined here as the mean fluorescence intensity of all the dots in the dotplot, which reflects the amount of fluorescent NPs associated to each cell.

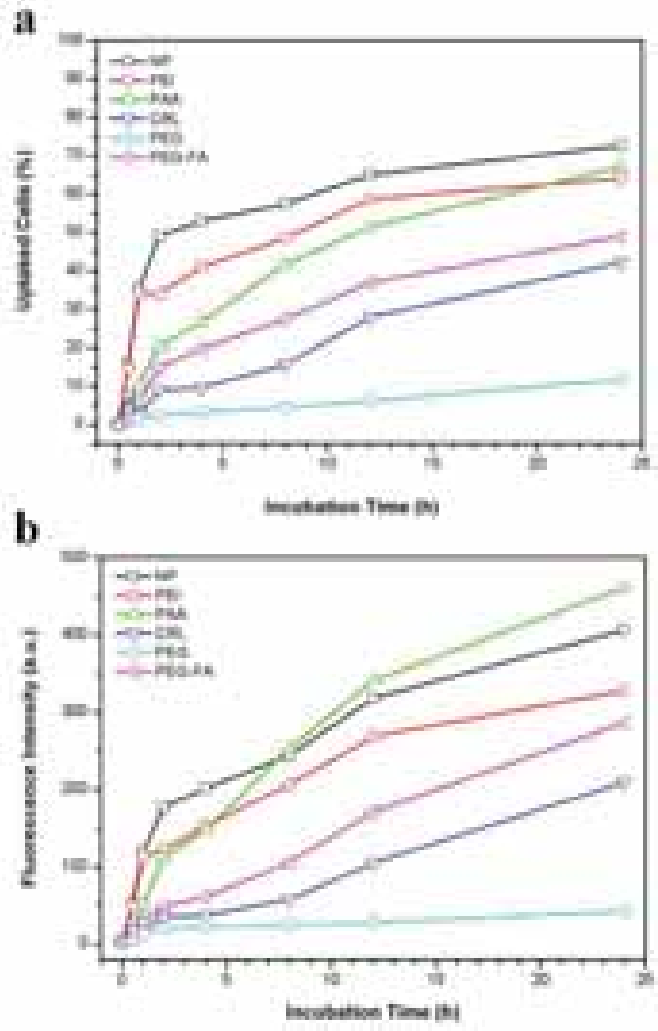

Figure 2.7. *(a) Cellular uptake ratio and (b) mean fluorescence intensity for PLGA NPs with PEI/PAA multilayer coatings, crosslinked and pegylated as a function of the incubation time.*

Quantitative cellular uptake of the NPs was then investigated as a function of the incubation time. In *Figure 2.7a* the percentage of cells displaying uptake of NPs has been plotted as a function of the time, for the different surface modified NPs, while in *Figure 2.7b* the mean fluorescence per cell has been displayed as a function of the incubation time. *Figure 2.7* shows that both the cellular uptake rate and the final amount

of assimilated NPs are greatly dependent on the surface chemistry of the NPs. For example, the uptake rates of the NPs with positively charged surface (bare NPs and $(PAA/PEI)_2$ coated NPs) were much faster at the beginning with an uptake ratio of ~40 % within 1 h incubation. Then, the uptake rate became slower and only after incubation for 24 h reached finally an uptake ratio of the 60 %.

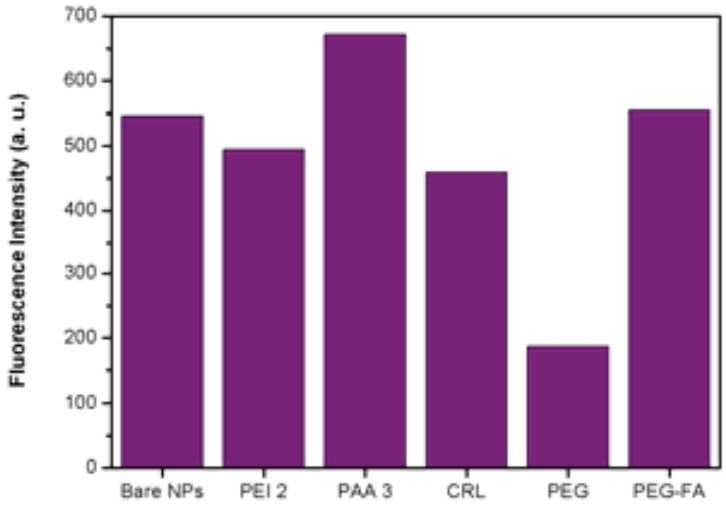

Figure 2.8. *Mean fluorescence intensity per cell after exposed to different PLGA NPs for 24 h.*

The fluorescence intensity displayed the same behavior (*Figure 2.7b*). The NPs with PAA as the outmost layer showed a more sustainable increase in both of the uptake ratio, which increased ~20 % during the first hour and then 45 % in the following 23 h, and the fluorescence intensity, which increased around 100 a.u. during the first hour and ~380 a.u. in the following 23 h. Although the final uptake ratios of these three NPs were all around 60–65 %, the mean fluorescence intensity of the $(PAA/PEI)_2/PAA$ coated NPs was 50 a.u. higher than the others. On the other hand, NPs covered with pegylated multilayers showed the slowest uptake rate, lowest cellular uptake ratio and mean fluorescence intensity. Actually, in the first hour no cellular uptake could be detected, and the final uptake ratio was only 11 % with the fluorescence intensity of 40 a.u. after 24 h incubation. It was unexpected that after crosslinking, the cellular uptake of the NPs also significantly decreased to be less than that of their precursors, i.e., the $(PAA/PEI)_2/PAA$ coated NPs, and was only higher than that of the pegylated NPs.

Immobilization of FA on the multilayers (PEG-FA NPs), however, could significantly enhance the cellular uptake compared with the PEG NPs. For example, the cellular uptake ratio after 24 h incubation improved to a 45 %, i.e., 3 times of the pegylated NPs. In *Figure 2.8* is plotted the mean fluorescence intensity in the fluorescence distribution against number of cells after 24 h incubation of the NPs with the cells. The highest uptake was obtained by the control and PAA/PEI coated NPs; crosslinked NPs and PEG-FA modified NPs show an intermediate uptake. PEG coated NPs show the lowest uptake.

Confocal laser scanning microscopy (CLSM) was also used to study the uptake of PLGA NPs by imaging the cells after incubation with NPs. 100 000 cells were seeded on a coverslip which was placed in a 3.5 cm culture plate. 24 h later, PLGA NPs with different surface coatings and encapsulated Rd6G were added into the culture medium with a final concentration up to 50 mg/mL. After incubation for another 12 h, the culture medium was removed and the cells were rinsed three times with sterilized PBS. The cells were subsequently fixed with 3.7 % formaldehyde solution in PBS for 30 min. Finally, the coverslip was sealed with Mounting Medium for fluorescence with DAPI (Vector H-1200) and observed under CLSM employing a 63 X oil objective.

In *Figure 2.9* CLSM images of NPs taken up by HepG2 cells are shown; all images were taken from the middle planes of the cells in z direction. The number of labeled NPs and their distribution in the cell varied according to the surface composition of the NPs and were consistent with flow cytometry measurements (*Figure 2.7 and 2.8*). *Figure 3.9* shows that the $(PAA/PEI)_2$ coated NPs (red spots) could be observed both in the cytoplasm and on the cell surroundings (*Figure 2.9a*), whereas most of the $(PAA/PEI)_2$/PAA NPs were internalized into the cytoplasm (*Figure 2.9b*). Very few PEG NPs can be observed in *Figure 2.9c*, where almost no fluorescence coming from rhodamine 6G can be detected. In *Figure 2.9d* we observe that the amount of PEG-FA NPs increased again. In all the cases, no particles could be found in the cell nuclei. It must be said that is not always easy to distinguish between NPs attached to the cell membranes and internalized NPs. It is though clear that some NPs are closer to the nucleus and can be thus postulated to be in the cytoplasm. Most likely, there are NPs both at the surface of the cells and in the cytoplasm. It is noticeable that negatively

charged NPs tend to be found more in the cytoplasm and that the PEG coated NPs are present in a much lower amount than when the NPs are charged. The addition of FA increases the presence of NPs in the cytoplasm and the cell membrane, providing a qualitative confirmation of the behavior observed by flow cytometry.

The cellular uptake is an important cell function, which is influenced by many factors such as the chemistry of the particle surface including charge *[235]*, ligands *[110, 223-226]*, proteins *[232, 233, 236]*, etc., particle size *[237]*, temperature, and also the particular cell type involved *[237]*. Considering similar cellular uptake ratios for the positively charged control and PAA/PEI_2 coated, and negatively charged $(PAA/PEI)_2PAA$ coated NPs (*Figure 2.7*), the surface charge does not provide an appropriate explanation for the observed phenomenon. Indeed, ζ-potential measurements reveal that in the cell culture medium containing serum, all the particles became negatively charged regardless of their initial surface characteristics, implying protein adsorption occurs nevertheless as demonstrated in *Figure 2.5*. Moreover, it is known that the surface properties of the NPs will change along with time because the binding strength between the NP surfaces and the molecules in the medium. The particular proteins adsorbed play an important role in the cellular uptake *[232, 233, 236, 238]*. However, the adsorption dynamics, the adsorbed amount of proteins and the particular proteins adsorbed must be different on the positive and on the negative NPs. On the positively charged surface, albumin, the most abundant protein in serum, adsorbs immediately to form a comparatively dense layer due to the charge attraction. Subsequently, other proteins in the serum, e.g., apolipoprotein E, may further adsorb or replace part of the albumin after 10 min incubation, and then the surface composition does not change too much after 30 min *[234]*. The adsorbed protein apolipoprotein E has been proved to bind to a specific receptor located in the liver *[236]*. On the negatively charged NPs such as the $(PAA/PEI)_2/PAA$ coated and crosslinked NPs, although all were negative, their absolute ζ-potentials were apparently higher, conveying the difference in structures and amount of adsorbed proteins. It is conceivable that due to the negative surface, electrostatic adsorption of serum proteins with the same charge will take more time, so that the protein configuration can change to achieve the adsorption. As a result of the weaker binding, during the incubation the surface protein components are easily changing too *[234, 238]*. These differences

should be responsible for the faster uptake of the control and $(PAA/PEI)_2$ coated NPs at the initial stage but after 24 h similar uptake ratios can be observed.

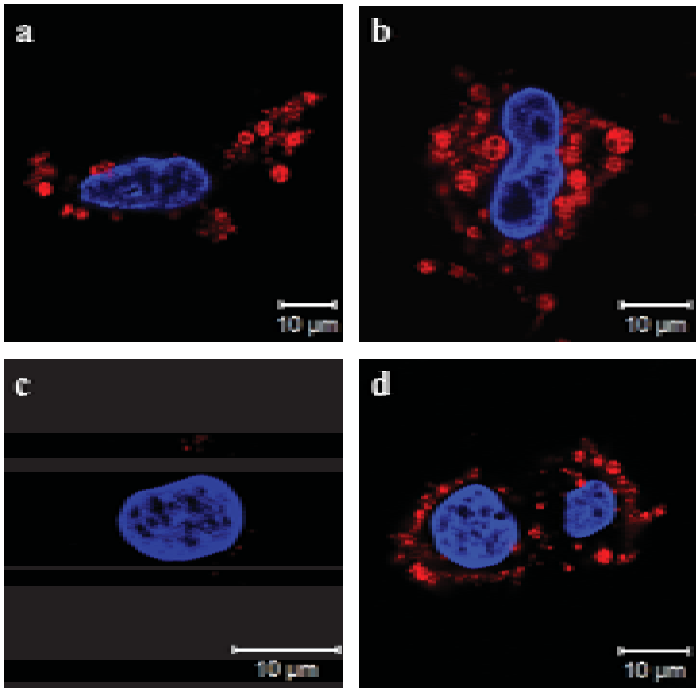

Figure 2.9. *Confocal laser scanning microscopy (CLSM) images of HepG2 exposed to (a) $(PAA/PEI)_2$, (b) $(PAA/PEI)_2PAA$, (c) PEG, (d) PEG-FA coated PLGA NPs for 12 h.*

The critical low uptake ratio of the pegylated NPs can be explained by the volume exclusion effect of the PEG molecules, which prevent nonspecific protein adsorption. Indeed, it has been proved that the apolipoprotein E is not present on the PEG covered PLA NP surface *[232]*. ζ-Potential measurements confirm the very low adsorption of serum proteins. The same low adsorption for the serum protein was observed for the crosslinked particles. The FA immobilization onto the pegylated NPs can, however on one hand, repel the nonspecific protein adsorption, and on the other hand, enhance significantly the cellular uptake of the NPs. Therefore, the PEG-FA grafted NPs can be effectively delivered to the HepG2 cells while they retain the good antifouling property.

2.4. PLGA NPs surface modification for antifouling protection

Polyelectrolyte multilayer (PEMs) fabricated by means of the LbL technique provide a very versatile tool for the noncovalent engineering of surfaces *[167, 168]*, as it has been shown in the surface modification above (section 2.3). Both synthetic and natural polyelectrolyte molecules have been used for the LbL assembly. Natural polyelectrolytes are fundamental to provide biocompatibility *[173, 174]*. PLGA NPs stabilized with the protein bovine serum albumin (BSA) were coated with the biodegradable pair of polyelectrolytes alginate (Alg) and chitosane (Chi). Besides the aim of making a purely biocompatible carrier the coating of the NPs with a chitosane/alginate PEM has two additional scopes: first, the creation of a multilayer with antifouling properties, and then, the reduction of the unspecific cell uptake of PEM coated NPs.

2.4.1. Layer by layer assembly on planar surfaces and NPs

Chitosan and alginate were assembled in a concentration of 1 mg/mL in 0.5 M NaCl. The pH value of the polyelectrolyte solution was adjusted to 5 by addition of either 1 M HCl or NaOH. For the assembly of Chi/Alg multilayers on the PLGA NPs the incubation time of each polyelectrolyte layer was 15 min. NPs were centrifuged after each polyelectrolyte deposition and washed in 0.5 M NaCl 3 times before deposition of the next layer.

The assembly of chitosan and alginate was first monitored on planar substrates by means of QCM-D. Chitosan and alginate layers were alternatively deposited on gold coated quartz crystals. For the coating, the incubation time was 15 min for each layer, followed by washings with 0.5 M NaCl for 15 min. On total, up to three bilayers of Alg/Chi were assembled on the crystals. The mass deposited on the crystal was calculated using the Sauerbrey equation as mention in Chapter 1.

Figure 2.10 shows the assembly of Chi/Alg PEM followed with QCMD. 3 bilayers of chitosan and alginate were assembled following the LbL procedure. Previous to the Chi/Alg coating a layer polyethyleneimine (PEI) was assembled since it results on a

good coating of a gold surface and then on top of PEI BSA was deposited. BSA was assembled to reproduce the surface of the BSA stabilized PLGA NPs. When the first layer of chitosan was assembled, frequency almost did not change but after assembling the next alginate layer a prominent frequency change could be observed (*Figure 2.10a*). The second layer of Alg showed a decrease in frequency of 40 Hz and the third layer of 50 Hz while for the Chitosan only a shift of 20 Hz was observed. The assembly of alginate always induced a bigger frequency shift than chitosan. Also, dissipation was always larger after alginate adsorption than after chitosan, hinting that more water molecules entrapped in the alginate layer than in the chitosan one. After the last chitosan layer was deposited, the frequency decreased ~22 Hz, which would correspond to 0.39 μg/cm^2 chitosan according to Sauerbrey equation, assuming that the mass increase comes from the chitosan alone and there is no water entrapped. This would represent a maximal possible density of amino groups of 2.4 nmol/cm^2. These amino groups are reactive for further modification through carbodiimine chemistry.

FA or PEG–FA was immobilized on the PEMs with chitosan as the outmost layer as previously described. The immobilization process was monitored with QCM-D (*Figure 2.10b*). In a first step, the carboxylic groups of FA in a 1 mg/mL FA or 5 mg/mL PEG–FA were activated with 10 mM NHS and 10 mM EDC at pH 5.3 for 30 min, then the pH value of these solutions were adjusted to 8.6. The solutions were subsequently injected into the different QCM-D chambers, which were initially stabilized for 5 min in MilliQ water. After incubated for 40 h the samples were rinsed with MilliQ water until the all the frequencies became stable.

At the end of the reaction and the rinsing with MilliQ water, final frequency changes of -6 Hz and -10 Hz were observed for the binding of FA and PEG–FA, respectively. Since only small changes in dissipation were observed after grafting FA and PEG–FA it is possible to apply the Sauerbrey equation to calculate the density of the grafted molecules. A density of 0.24 nmol/cm^2 and 0.08 nmol/cm^2 were observed for FA and PEG–FA respectively. Assuming that the density of the amine groups of the chitosan is 2.4 nmol/cm^2, a grafting yield of 10 % for FA and of 3.3 % for PEG–FA can be calculated.

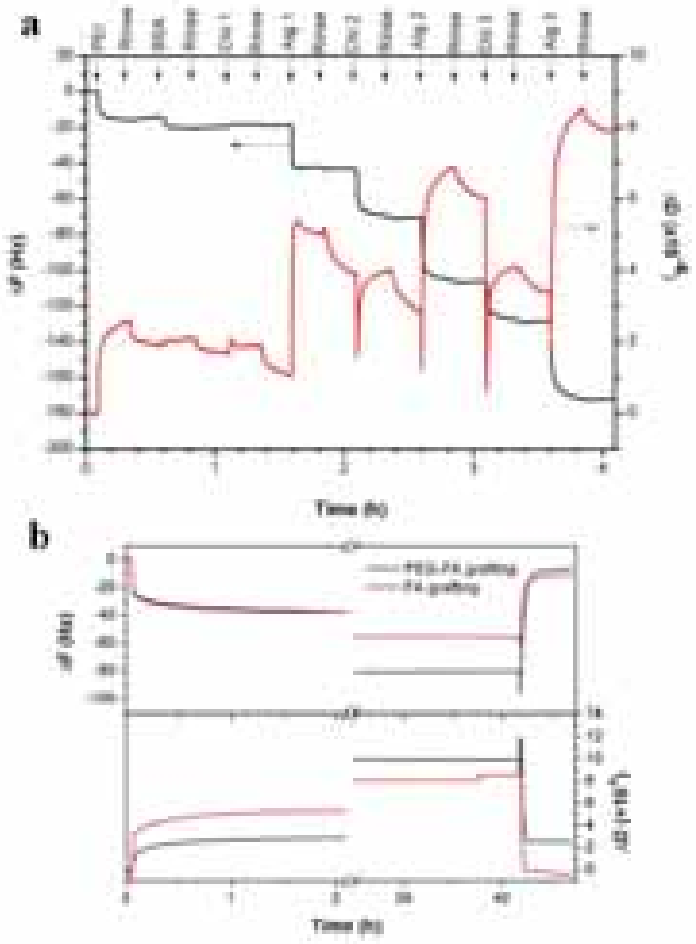

Figure 2.10. *Frequency and dissipation changes monitored by QCM-D for (a) the layer by layer assembly of chitosan and alginate and (b) FA and PEG-FA covalent binding.*

The differences in the grafting yield must be due to the changes in the chemical structure of FA after being conjugated with PEG. For PEG–FA the available number of carboxylic acid decreases even though the feeding molar ratio is almost the same. Moreover, the PEG chain may also bring a certain spatial hindrance, which reduces the reactivity of the carboxylic acid, being unfavorable for the immobilization of the PEG–FA.

The layer by layer assembly of Chi/Alg multilayers and the binding of FA or PEG-FA was performed also on glass slides to measure UV absorbance. Glass slides coated with $(Chi/Alg)_2/Chi$ were used as control sample. The absorbance between 350 and 600 nm

of the glass slides covered with FA or PEG–FA grafted $(Chi/Alg)_2/Chi$ was recorded between 350 and 600 nm. The absorbance of FA was measured in solution using a quartz cuvette.

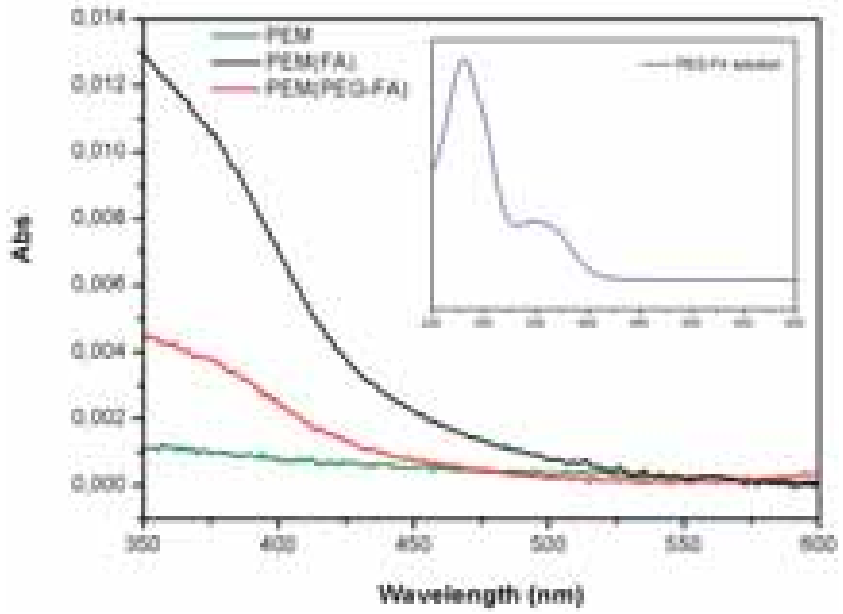

Figure 2.11. *UV-Vis spectra of chitosan/alginate PEMs after FA and PEG-FA grafting. Inset corresponds to the absorbance spectrum of the FA solution.*

UV–Vis spectra (*Figure 2.11*) further confirmed the immobilization of the FA on the multilayers. The spectra in *Figure 2.11* shows absorbance in the region of 350–400 nm after immobilization of FA and PEG–FA, which is missing in the Chi/Alg multilayer (control). This region of the spectra can be assigned to the FA (*Figure 2.11, inset*) confirming the attachment of the molecule to the PEMs. The absorbance was higher after FA immobilization than after PEG–FA immobilization. For example at 360 nm an absorbance of 0.012 was measured for FA while for PEG–FA the absorbance value was only of 0.004. These differences in absorbance are roughly consistent with the QCM-D results and indicate a higher efficiency for the FA immobilization on the PEMs.

PEMs assembly and FA or PEG–FA attachment to the PEMs on PLGA NPs were followed by ζ-potential measurements using 10 mM NaCl with pH 7.4 as medium (*Figure 2.12*). The PLGA NPs with BSA as stabilizer show a negative charge with a ζ-

potential of -27 mV due to the low pKa value of BSA (pKa: 4.7–4.9). After chitosan assembling, a ζ-potential of -15 mV was measured. Although the potential of the NPs remained negative, its absolute value decreased, hinting chitosan deposition but not a complete coverage of the NPs surface. This is consistent with QCM-D results (*Figure 2.10a*). The adsorbed chitosan cannot form a layer dense enough to hide the influence of the charges from the surface beneath. For the next assembled layers the ζ-potentials oscillated between ~-45 mV and ~0, after alginate and chitosan assembly respectively. After immobilization of FA and PEG–FA, the potential dropped to ~-15 mV, revealing the partial consumption of the amino groups. After immobilization of the FA and PEG–FA, the NPs suspension became pale yellowish. This color remained even after three rinses with MilliQ water, indicating the presence of FA groups on the NPs surface.

DLS experiments show that Chi/Alg coated NPs, as well as the particles modified with PEG and PEG–FA, have narrow size distributions (*Appendix Figure D*). The coating of PLGA NPs with polyelectrolyte multilayers does not induce changes in the morphology of the NPs neither induces substantial aggregation as observed in TEM *[239]*.

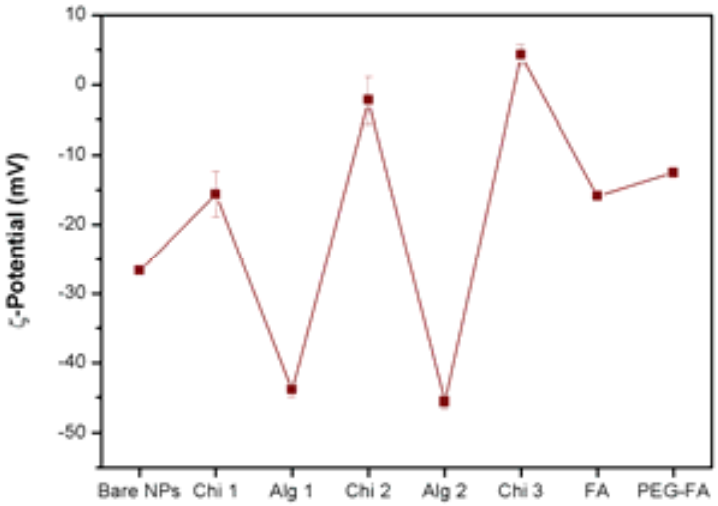

Figure 2.12. *Changes in ζ-potential during layer by layer assembly of Chi and Alg and covalent surface modification on PLGA NPs.*

2.4.2. Protein adsorption on Chi/Alg PEMs

As before for the PAA/PEI coatings BSA protein (1 mg/mL in 10 mM PBS) was used as model protein to study protein adsorption on the PEMs by means of the QCM-D. PEMs of the following composition were assembled on the QCM crystals following the above mentioned protocols: $(Chi/Alg)_2$/Chi, $(Chi/Alg)_3$, $(Chi/Alg)_2$/Chi-FA and $(Chi/Alg)_2$/Chi-PEG–FA. The QCM-D chamber was initially incubated with MilliQ water for 5 min, and then replaced with PBS. The BSA solution was injected into the QCM chambers. Five minutes later, the injection was stopped and the PEMs were incubated in the BSA solution for 1 h. Finally, the BSA solution was sequentially replaced by PBS and water.

In *Figure 2.13* we observe the adsorption behavior of BSA on multilayers of $(Chi/Alg)_2$/Chi, $(Chi/Alg)_2$/Chi-FA, $(Chi/Alg)_2$/Chi-PEG–FA and $(Chi/Alg)_3$. For all the curves the frequency decreases when passing from water to the phosphate media but then the subsequent addition of BSA does not induce a change in frequency. Finally, after rinsing with water the values of frequency and dissipation returned to their original values in water, except for the dissipation of $(Chi/Alg)_2$/Chi. These results reveal that almost no BSA was adsorbed on all of the PEMs. In the case of the $(Chi/Alg)_2$/Chi, the phosphate molecules will probably remain attached to the PEM even after water rinsing. When alginate was the outmost layer, i.e. $(Chi/Alg)_3$, the high hydrophilicity of alginate and the repulsion between alginate and BSA should be responsible for the lack of BSA adsorption *[227, 240]*. The absence of BSA adsorption on PEMs with chitosan as the outmost layer is rather surprising, since it is known that BSA can interact with chitosan by electrostatic attraction. Indeed, Yang M., et al., found that the human serum albumin adsorption was higher than 30 μg/ cm^2 on chitosan grafted polysulfone *[241]*. Sonvico F., et al., observed that almost 100 % BSA adsorbed after 1 mg/mL BSA solution was filtered through a membrane made by chitosan *[242]*. On the other hand, Rowley J. A., et al., found that chitosan deposited on alginate microcapsules did not affect the concentration of BSA in solution if there was no BSA ligand-blue dextran encapsulated *[243]*.

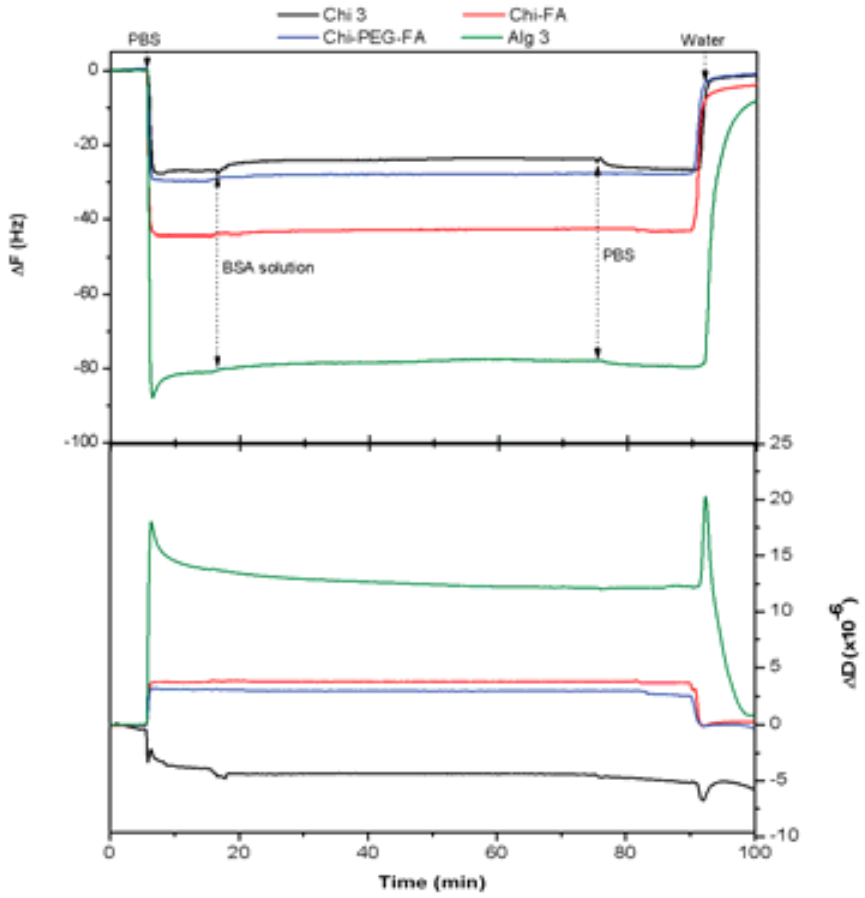

Figure 2.13. *Frequency and dissipation changes during BSA adsorption on Chi/Alg PEMs monitored by QCM-D.*

From electrophoretic mobility measurements we know that the coating with chitosan resulted in a value of ζ-potential around 0 at pH 7.4. Therefore, it is likely that there is a limited electrostatic interaction between BSA and the PEMs. In a multilayer of the LbL type the properties of the surface are not independent of the layers underneath and there is always a certain degree of interdigitation between layers. For chitosan as top layer with alginate below the properties of the surface may be substantially different from those of a pure chitosan monolayer. In other words, the alginate layer assembled before the top layer of chitosan may be protruding partially into the surface helping to prevent the deposition of BSA. It is also possible that the phosphate groups in PBS screen the charge of the amines of chitosan. It is known that phosphates have a specific interaction with primary amines. For PEMs this screening of the amine groups of the last layer may induce a recharge of the surface with the charge of the underlying polyelectrolyte layer.

For the Chi/Alg with Chi as last layer the phosphate binding may be causing a more significant influence of the alginate on the antifouling properties of the PEM. The binding of FA or PEG–FA to the chitosan does not change the adsorption of BSA. The grafting of FA, approximately a 10 % of the binding sites of the chitosan brings additional charges to the multilayer but they do not imply the accumulation of BSA. The Chi/Alg coatings could therefore be used as an alternative for pegylation to prevent protein adsorption on surfaces or particles. The influence on the antifouling properties of a polycation by the presence of a layer of alginate below are subject of further investigation.

2.4.3. Cellular uptake

As same as it is described above in section 3.3.4, cellular uptake studies were performed by flow cytometry using HepG2 cells and the different surface modified PLGA NPs labeled with Rd6G. In *Figure 2.14* we observe the cell uptake ratio (*Figure 2.14a*), the fluorescence intensity as the mean fluorescence intensity of all the cells (*Figure 2.14b*) or only from the cells internalized with the NPs (*Figure 2.14c*).

Two types of uptake profiles can be found in *Figure 2.14a*. The first profile is evidenced by bare NPs, whose uptake ratio increased rapidly in the first 1–2 h and reached the highest value, ~90 %. For all the engineered NPs the cell uptake ratio increased continuously during the first 8 h, and remained constant afterwards. Nevertheless, the uptake ratio changed significantly with the nature of the surface functionalization. The uptake ratios of $(Chi/Alg)_2$/Chi-FA, $(Chi/Alg)_2$/Chi-PEG–FA were 10–20 % higher than those of the $(Chi/Alg)_2$/Chi and $(Chi/Alg)_3$ coated NPs. The average fluorescence intensity per cell (*Figure 2.14b*) shows some differences with the uptake ratio, although all the values increased initially along the culture time as well. A highest value of intensity was also reached after 2 h incubation for the bare NPs, while the highest values for the $(Chi/Alg)_2$/Chi-FA and $(Chi/Alg)_2$/Chi-PEG–FA coated NPs were reached 8 and 4 h, respectively. For the NPs covered with $(Chi/Alg)_3$ multilayers, like for the uptake ratio, the fluorescence intensity was also the lowest, conveying the low interaction of the NPs having alginate as the outmost layer with the cells *[244]*. In contrast, the NPs covered with $(Chi/Alg)_2$/Chi-PEG–FA showed the highest

fluorescence intensity with an value of around 450 a.u., which is 150 a.u. higher than that of the $(Chi/Alg)_2$/Chi-FA coated NPs, and 3.5 times and 10 times of the bare NPs or $(Chi/Alg)_2$/Chi and $(Chi/Alg)_3$ coated NPs, respectively. After 24 h incubation, the fluorescence intensity decreased significantly for $(Chi/Alg)_2$/Chi-FA and $(Chi/Alg)_2$/Chi-PEG–FA coated NPs. The reason is not clear at present.

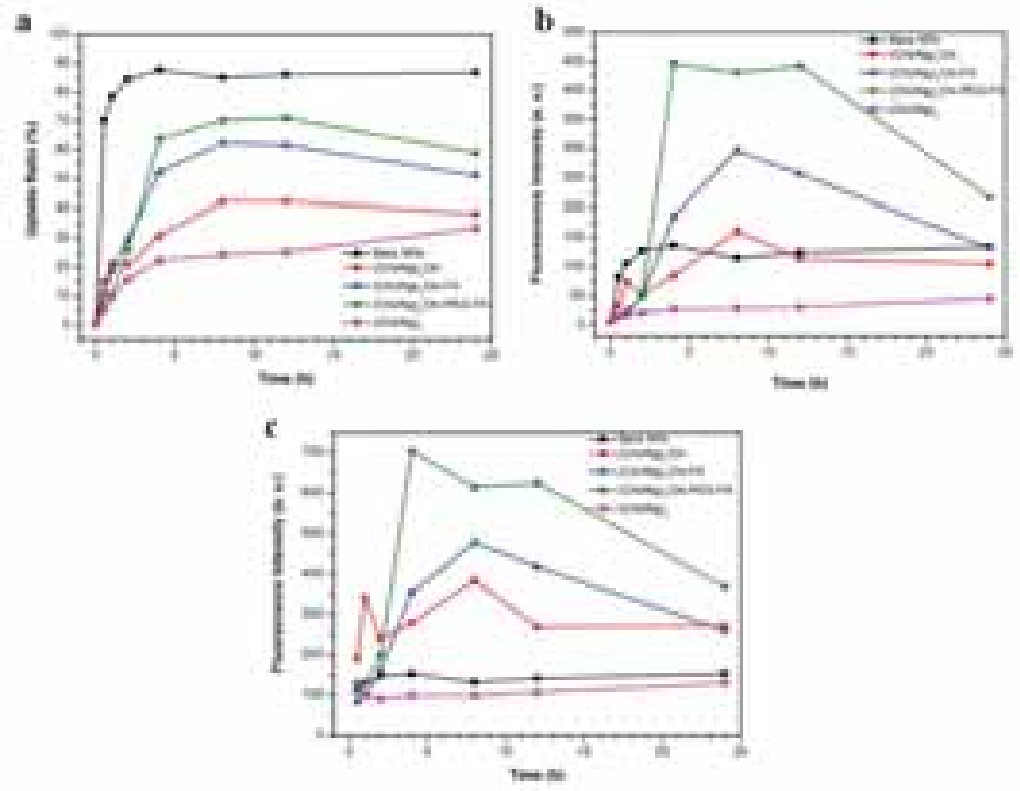

Figure 2.14. *(a) Cell uptake ratio, (b) average fluorescence intensity normalized to all cells in a population, and (c) fluorescence intensity normalized to cells with NPs as a function of incubation time.*

Exocytosis and the release of the Rd6G dye as a result of partial degradation of the PLGA NPs can also cause the decrease in fluorescence intensity. *Figure 2.14c* shows that more NPs coated with $(Chi/Alg)_2$/Chi-PEG–FA are associated to the HepG2 cells than the ones coated with $(Chi/Alg)_2$/Chi-FA. The use of PEG as spacer seems to be favorable for FA recognition. When the NPs were coated with $(Chi/Alg)_2$/Chi, the mean fluorescence intensity was also higher. An interesting feature here is that the mean fluorescence intensity for the cells incubated with the bare NPs and $(Chi/Alg)_3$ coated

NPs was almost the same, although from the *Figure 2.14a* the uptake ratio was so different.

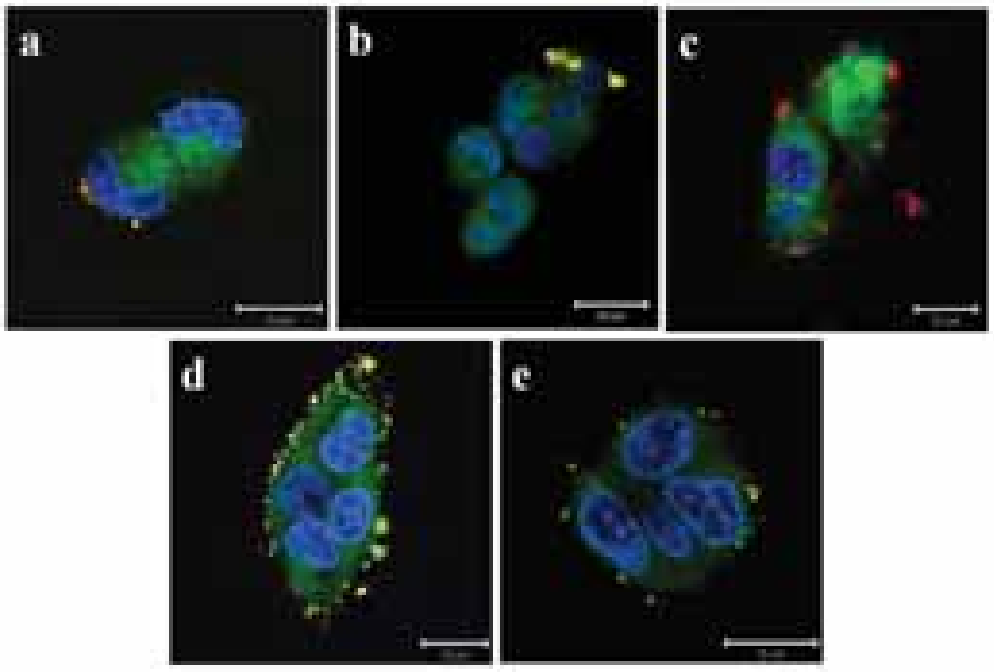

Figure 2.15. *CLSM images of HepG2 cells after co-cultured with: (a) bare NPs, (b) $(Chi/Alg)_2$/Chi, (c) $(Chi/Alg)_2$/Chi-FA, (d) $(Chi/Alg)_2$/Chi-PEG-FA and (e) $(Chi/Alg)_3$ covered NPs for 12 h .*

Finally, CLSM was employed to observe the distribution of the NPs in cells, following the same procedure detailed in section 2.3.4. The images in *Figure 2.15* were taken from the middle plane of the cells in the z direction. The bare NPs (*Figure 2.15a*) and $(Chi/Alg)_3$ coated (*Figure 2.15e*) NPs have similar appearance. Only a few NPs could be recognized on the cell membranes. This is consistent with the results from flow cytometer, few NPs clusters were found on the cell membranes when they were covered by $(Chi/Alg)_2$/Chi (*Figure 2.15b*). This is probably caused by the very weak surface charge of the NPs (*Figure 2.12*), which is further screened by phosphate salts in the culture medium. As expected, more NPs coated with $(Chi/Alg)_2$/ Chi-FA (*Figure 2.15c*) or $(Chi/Alg)_2$/Chi-PEG–FA (*Figure 2.15d*) were attached onto the HepG2 cell membranes. Moreover, the $(Chi/Alg)_2$/Chi-FA coated NPs showed aggregation on the

membrane, but the $(Chi/Alg)_2$/Chi-PEG–FA covered NPs uniformly distributed with neglectable aggregation.

The cellular uptake of the PLGA NPs can be controlled by the proper engineering of their surface. While the alginate covered surface can significantly reduce the particle attachment onto the HepG2 cells and cellular uptake, the binding of FA alone or PEG–FA to the multilayers can, on the other hand, increase both of the uptake ratio and the number of NPs per cell. The strategy of stepwise modification of the PLGA NPs is successful in achieving NPs with selective recognition functions.

2.5. PLGA NPs surface modification with lipids for the control of their intracellular distribution

Lipid vesicles play an important role in research as model systems for biological membranes, and in industry, especially in pharmaceuticals *[245-247]*, cosmetics *[247]* and food *[248, 249]*, for encapsulation or as carriers for drug delivery.

In cells, biological membranes are normally supported on a network of proteins and carbohydrates (cytoskeleton). A drawback of vesicles as models for biological membranes is that they are free standing membranes. Several models have been proposed to account for the support, such as biomembranes *[250-252]*. A strategy to mimic the support of biomembranes was shown by S. Moya, et al *[185, 253]*, employing polyelectrolyte multilayers as a membrane support. Lipid vesicles were assembled on top of empty polyelectrolyte capsules fabricated via Layer by Layer (LbL) from fixed erythrocytes. The lipid coating results in a supported membrane on the colloidal domain with the topological characteristics of natural membranes. It was also shown in *[253]* that this lipid membrane can control capsule permeability in analogy with cell membranes. The assembly and properties of lipids membranes on top of polyelectrolyte cushions fabricated by LbL have been studied in detail on both, colloidal particles and planar surfaces. The conditions to achieve a bilayer, avoiding the formation of lipid multiayers or the presence of entire vesicles, have been established

and are dependent on the lipid composition *[155]*. Bilayers were observed for lipid composition entailing approximately 25% of charged lipids, with the remainder being zwitterionic. In addition, it has been shown that the supported membrane can be used as a template for the assembly of other biological entities, i.e virus like nanoparticles, which can fuse onto the supported membrane following the mechanism that they use on cells *[48, 254-257]*.

The coating of colloidal particles with lipid membranes offers many possibilities as tools for functionalization to generate a biocompatible coating or to avoid unspecific interactions between the capsules and biomolecules, as well as to prolong circulation of drug carriers *[98, 99]*.

For this system, we will show a new application of the use of lipids to coat NPs. We will demonstrate that targeted delivery towards the endoplasmic reticulum (ER) by PLGA NPs can be achieved by means the deposition of lipid vesicles on the top of the NPs surface. Moreover, by varying the proportion of DOPS to DOPC it is possible to increase the amount of NP uptake by the cells. These results provide a simple route to control NP uptake in cells as well to target the delivery to different intracellular regions.

2.5.1. Lipid vesicles formation

Lipid vesicles were formed via sonication. First, the lipids 1,2-dioleoyl-*sn*-glycero-3-phosphocholine (DOPC) and 1,2-dioleoyl-*sn*-glycero-3-[phospho-L-serine] (DOPS) were dissolved in chloroform. Four mixtures of DOPC/DOPS with the following molar ratios: 65:35, 75:25, 85:15 and 95:5, were prepared adjusting the total final amount of lipids to 1 mg. Chloroform was evaporated from the lipid mixtures using an Argon stream first and then, placing the lipid mixture under vacuum for 1 h. After complete removal of the organic solvent, the lipid films were immediately hydrated using a filtered 150 mM NaCl solution as buffer, and applying gentle agitation with a vortex to form lipid suspensions. The lipid suspensions in NaCl were then sonicated in an ice bath

in order to form lipid vesicles. The ultrasonicator was operated in the intermittent pulsed mode with 5 seconds ON and 20 seconds OFF for 10 minutes at 20% power. After sonication, vesicles were mildly centrifuged in order to remove impurities, titania particles from the sonicator for example. To prepare fluorescent vesicles, DOPC was substituted with 1-Oleoyl-2-(6-[(7-nitro-2-1, 3-benzoxadiazol-4-yl)amino]hexanoyl-*sn*-glycero-3-phosphocholine (DOPC-NBD) following the same vesicle preparation method in order to obtain fluorescent lipid vesicles with different molar ratios of fluorescent DOPC/DOPS (65:35, 75:25, 85:15 and 95:5).

2.5.2. Polyelectrolytes and lipid vesicles assembly on PLGA NPs

Polyelectrolyte multilayer (PEM), of poly(styrenesulfonate sodium salt) (PSS) and poly(allyl amine hydrochloride) (PAH) were assembled via Layer by Layer on top of the PEI stabilized PLGA NPs using 1 mg/mL PSS and PAH solutions in 0.5 M NaCl for coating. The pH of the solution was adjusted to 7.4 by addition of either 1M HCl or NaOH. The incubation time for each polyelectrolyte layer was 15 min, and the NPs were washed with a 0.5 M NaCl solution three times between each layer assembly. After four layers of PSS and PAH (PAH as the outermost layer) DOPC/DOPS vesicles in 150mM NaCl were deposited on top of the PEMs resulting in a lipid layer. PLGA NPs coated with lipids at the four different molar concentrations of DOPC/DOPS vesicles (65:35, 75:25, 85:15 and 95:5) were prepared. This pair of polyelectrolytes was chosen on the basis that they are known to provide a good support for lipid assembly. The whole idea of depositing a PEM here is to facilitate the spreading of the lipids on the surface of the PLGA NPs.

The ζ-potential of the PLGA NPs was measured in 10mM NaCl (pH 7.4) with 60V, to monitor polyelectrolyte and lipid assembly on the PLGA NPs. The alternative assembly of polyelectrolytes of opposite charge induces surface recharging and a consequent change in the sign of the potential. PEI stabilized PLGA NPs showed a ζ-potential of +45 mV. During the LbL assembly of PSS/PAH the ζ-potential oscillated between -35 ± 3 mV and +12 ± 2 mV respectively for PSS or PAH as the outermost layer (*Figure*

2.16a). After the lipid assembly, on top of PAH, the ζ-potential dropped to negative values according with the molar composition of the DOPC/DOPS vesicles as can be seen in *Figure 2.16b.* There, we can observe that with increasing concentration of DOPS in the lipid vesicles the ζ-potential becomes more negative.

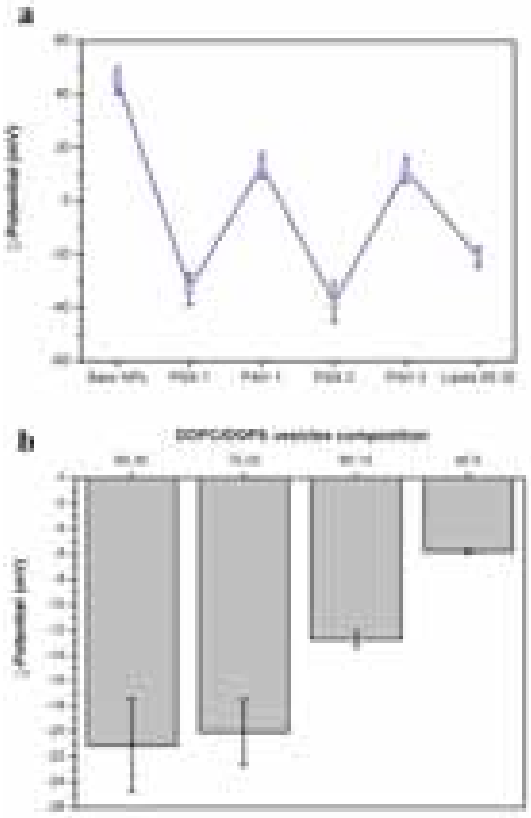

Figure 2.16. *(a)Variation of the ζ-Potential of PLGA NPs during PSS/PAH LbL assembly and subsequent lipid vesicles assembly, and (b) final ζ-potential of the lipid coated PLGA NPs according to the composition of the DOPC/DOPS vesicles assembled.*

2.5.3. Cellular uptake

The uptake of NPs by cells can take place through several different pathways depending on the physicochemical characteristics of the NPs and the nature of the target cells. From the endocytotic uptake mechanism, phagocytosis can occur only in those cells which can remove pathogens, such as macrophages, neutrophils, or monocytes *[258]*. On the other hand, pinocytosis can occur in all kind of cells via different pathways:

macrophinocytosis, clathrin-mediated, caveolae-mediated endocytosis and other independent endocytosis pathways *[259-261]*. Macropinocytosis has been seen in a wide variety of cells from multicellular animals, in macrophages and in almost all tumor cells; clathrin-mediated endocytosis is the major internalization route in most cell types; caveloae-mediated endocytosis occurs as well in the majority of cell types and unlike clathrin-mediated, caveolae assisted endocytosis involves triggering and signaling processes.

Cellular uptake studies were performed by flow cytometry using HepG2 cells and the different lipid coated PLGA NPs labeled with Rd6G, following the same procedure described above (section 2.3.4).

The cellular uptake of the NPs was quantitatively evaluated as a function of the incubation time of HepG2 cells with the NPs via flow cytometry. In *Figure 2.17a* the cellular uptake ratio has been plotted as a function of the incubation time with the lipid coated NPs for each lipid mixture. In *Figure 2.17b* the mean fluorescence per cell has been plotted as a function of the incubation time. *Figure 2.17* shows that both, the cellular uptake rate and the final amount of assimilated NPs, are strongly dependent on the ratio of DOPC to DOPS. Indeed, those PLGA NPs with a higher composition of DOPS in the lipid coating show more cellular uptake. PLGA NPs with DOPC/DOPS coating composition of 65:35 can reach an uptake ratio of ~90 % after 24 h, while only ~70 % of NPs with lipid composition 95:5 are assimilated after the same incubation time. The uptake rates for lipid coated NPs are always higher than for PEI stabilized NPs, these reached less than 70 % of uptake after 24 h of incubation.

The fluorescence intensity (*Figure 2.17b*) varied with the proportion of DOPC to DOPS in the lipid coating displaying the same tendency as observed for the cellular uptake ratio. PLGA NPs with higher concentration of DOPS (65:35) showed the highest value for the fluorescence intensity, around 700 a.u. during the first hour and ~1150 a.u. in the following 23 h. When the molar ratio of DOPS in the lipid coating decreased the fluorescence intensity also decreased, After 24 h incubation fluorescence intensities of ~700 a.u. for the NPs with 75:25 DOPC/DOPS ratio, ~600 a. u. for 85:15 DOPC/DOPS and ~300 a. u. for the 95:5 DOPC/DOPS.

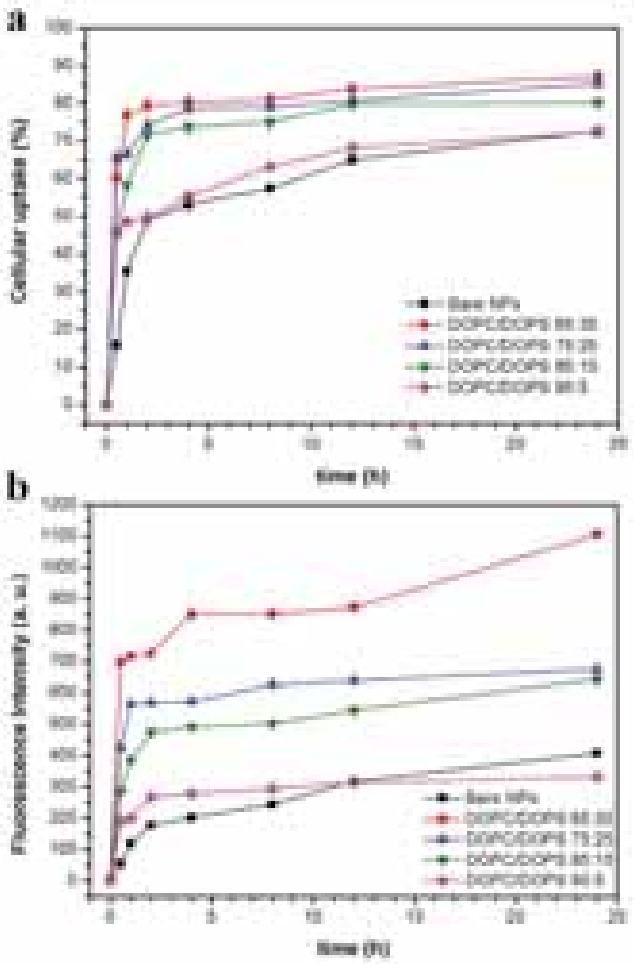

Figure 2.17. *(a) Cellular uptake ratio and (b) mean fluorescence intensity for lipid coated PLGA NPs with different DOPC/DOPS composition in their coatings as a function of the incubation time with the HepG2 cell line.*

Following the same procedure described in section 2.3.4, the results from flow cytometry were corroborated with CLSM as shown in *Figure 2.18*. Surprisingly, lipid coated PLGA NPs were found in the cell cytoplasm very close to the nucleus. With decreasing composition of DOPS in the lipid coating, below 25 %, the NPs are more prone to forming large, rounded aggregates in the proximity of the nucleus. For NPs with a lipid coating of 65:35 DOPC/DOPS (*Figure 2.18b*) it is possible to observe well distributed NP aggregates in the cytoplasm. When the lipid coating of the NPs has a composition of 75:25 DOPC/DOPS (*Figure 2.18c*) it can be seen that the NPs start to

form aggregates that resemble large vesicles in close proximity to the cell nucleus. At a DOPC/DOPS molar ratio of 85:15 (*Figure 2.18d*) or 95:5 DOPC/DOPS (*Figure 2.18e*), the formation of large aggregates of NPs in the proximity of the nucleus is more evident. The tendency to form large, rounded aggregates in the proximity of the cell nucleus seems to be characteristic of the lipid coated NPs. PEI stabilized PLGA NPs does not form vesicle-like aggregates, these NPs are well distributed in the cell cytoplasm, far from the nucleus (*Figure 2.18a*).

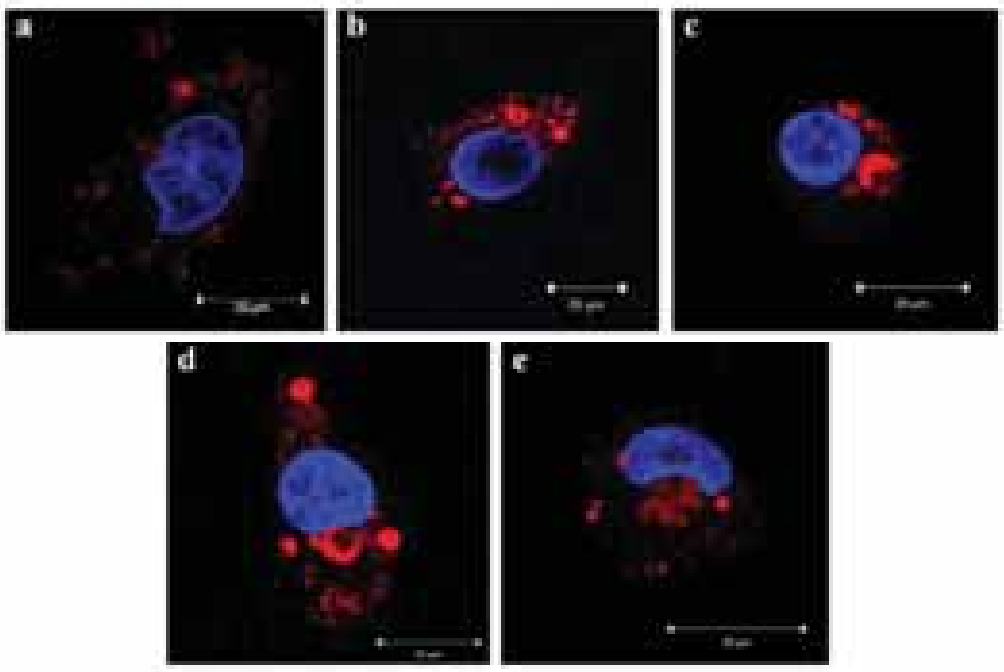

Figure 2.18. *CLSM images of HepG2 cells after incubation with (a) unmodified PLGA NPs and lipid coated NPs with molar ratios of DOPC/DOPS: (b) 65:35, (c) 75:25, (d) 85:15 and (e) 95:5. Incubation lasted 12 h. Images were taken from the mid-plane of the cells in the z direction.*

The localization of the lipid coated PLGA NPs in the close vicinity of the nucleus indicates a possible association of the lipid coated NPs with the endoplasmic reticulum (ER). In order to investigate this possibility, we perform CLSM studies of the NPs taken up by HepG2 cells using a specific green stain for ER. *Figure 2.19* displays the CLSM images of stained ER of HepG2 cells after co-incubation with PEI and lipid coated

PLGA NPs. In all images in *Figure 2.19*, the ER of HepG2 cells are clearly visible as a well defined green network. In the case of PLGA NPs without a lipid coating (*Figure 2.19a*), it can be observed that the NPs are situated in the cytoplasm of the cell but they are not co-localized within the ER since both fluorescence emissions, from the ER (green) and from the PLGA NPs (red), can be easily distinguished from each other without any spectral overlapping. Instead, for the lipid coated PLGA NPs, there is a clear overlapping in the fluorescence emission from the ER and that of the lipid coated PLGA NPs. The superposition of the fluorescence coming from the NPs and from the ER can be seen in the corresponding images as a yellowish color (*Figure 2.19b-e*). The overlapping in the fluorescence suggests that lipid coated PLGA NPs are preferentially associated in the ER of the cells. In addition, in the CLSM images is also possible to see that for those PLGA NPs with higher DOPC proportion the association within ER is higher although the number of NPs taken up by the cell is obviously lower.

In a typical endocytic pathway, the internalization of a cargo occurs from the cell membrane through endosomes, and then, the trafficking inside the cell continues from endosome to lysosome and to ER or other organelles *[262]*. Therefore, the co-localization of the lipid coated PLGA NPs within the ER of the cell suggests that those NPs were able to escape from endosomes and reach the ER with apparently no degradation, which is a significant achievement for a carrier since one of the major problems in the design of a drug delivery system is to protect the cargo from enzymatic degradation during lysosomal trafficking *[263]*. Co-localization studies previously published for bare PLGA NPs *[264]* and PLGA NPs stabilized with PVA *[265]*, also reveal the tendency of these NPs to escape or avoid endo-lysosomal degradation, but in both cases NPs were found to be associated within the endosomes and the Golgi apparatus of different epithelial cells. Moreover, targeting in the ER of HeLa cells was achieved in *[222]* using PLGA NPs decorated with a peptide that contain specific ER targeting moieties.

Co-localization of lipid coated PLGA NPs within the ER of the cell can be due to fusion between the lipid coating of the NPs and the ER membrane, this fusion has been

previously studied with liposomes of a similar composition *[218]*. Some intracellular organelles related to the ER are the lipid droplets that act as storage for lipids *[266]*; it is also possible to consider that lipid coated NPs may tend to accumulate inside these lipid droplets.

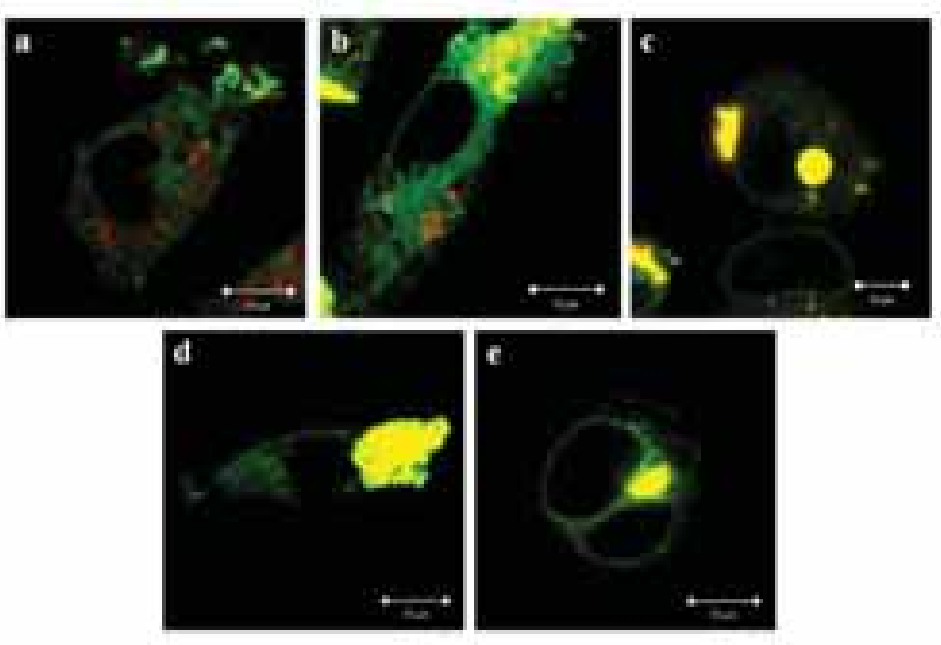

Figure 2.19. *CLSM images of HepG2 cells with stained ER (green) after co-cultured with (a) PEI stabilized PLGA NPs (red) and lipid coated PLGA NPs with lipid molar ratios DOPC/DOPS: (b) 65:35, (c) 75:25, (d) 85:15 and (e) 95:5 incubated for 12 h.*

2.5.4. Uptake pathways

It is reasonable to think that maybe the vesicle-like NP aggregates are formed during the internalization of the NPs through the fusion of the lipid coating of the PLGA NPs with the cell membrane. In order to study this possibility, fluorescent PLGA NPs were surface modified using NBD labeled DOPC, following the same procedure for vesicles preparation (section 2.5.1) and self-assembly (section 2.5.2) described above. The main reason to use a fluorescent lipid is to track the lipid coating of the NPs while they are taken up by the cell. If the lipid on top of the NPs fuses with the cell membrane, it

should be possible to observe fluorescence coming from DOPC labeled with NBD in the cell membrane.

CLSM was employed to observe the cellular uptake of the lipid coated NPs in HepG2 cells (*Figure 2.20*). Lipid coated PLGA NPs were found in the cell cytoplasm in the proximity of the nucleus forming vesicle-like aggregates, similar to those observed in *Figure 2.18*, no trail coming from labeled DOPC was observed in the cell membrane. The red and green fluorescence emitted by the particles and the lipid coating respectively showed always the same spatial localization. These results suggest that the lipid coating of PLGA NPs does not fuse with the lipids of the cell membrane but remains attached to the NPs surface.

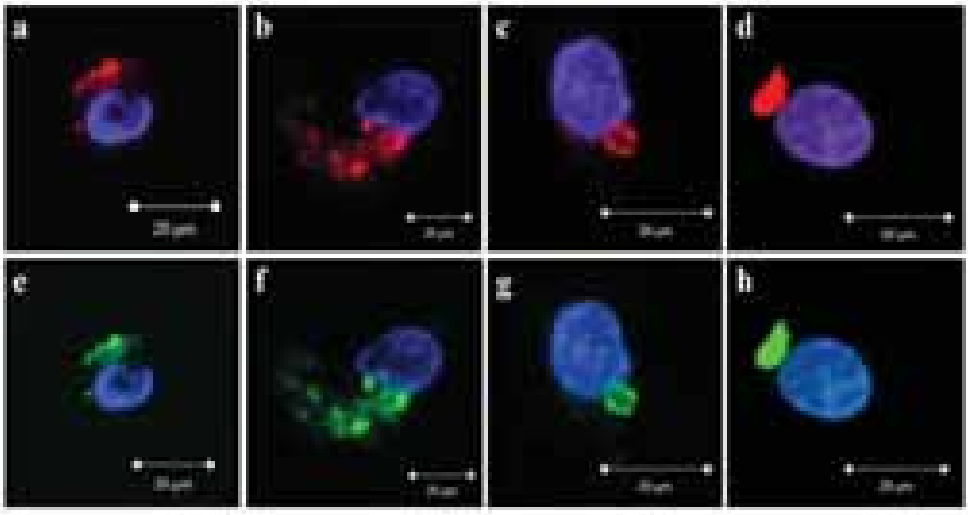

Figure 2.20. *CLSM images of HepG2 cells after co-cultured with lipid coated NPs with lipid composition of DOPC-NBD/DOPS: (a and e) 65:35, (b and f) 75:25, (c and g) 85:15 and (d and h) 95:5 incubated for 12 h. The cell nucleus was stained with DAPI (blue), PLGA NPs (a-d) are labeled with Rhd6G (red) and DOPC on PLGA NPs (e-h) is labeled with NBD (green). Images were taken from the mid-plane of the cell in the z direction.*

The energy dependent uptake pathways were studied for the lipid coated PLGA NPs using different pharmacological inhibitors, including amiloride HCl, which inhibits

uptake via macropinocytosis; amantadine HCl that blocks the clathrin-mediated endocytosis, genistein, which prevents the caveolae-mediated endocytosis and cytochalasin D that blocks the uptake through the cell cytoskeleton.

The HepG2 cell line was cultured in DMEM with 10% FBS and 1000 U penicillin, 10 mg/ml streptomycin at 37 ºC and in 5% CO2. When the cell confluence was around 70%, all the cells were trypsinized and 100 000cells were seed into each well of a 24-well plate. 12 h later, the corresponding inhibitor was incubated for 1 h adjusting the final concentration to: 2mM Amiloride HCl, 1 mM Amantadine HCl, 100 µM Genistein or 10 µg/mL Cytochalasin. PLGA NPs with Rd6G and different lipid surface coatings were added into the culture medium at final concentration of 50 µg/mL. After 4h of incubation the cells were washed with PBS twice, trypsinized and studied with flow cytometry.

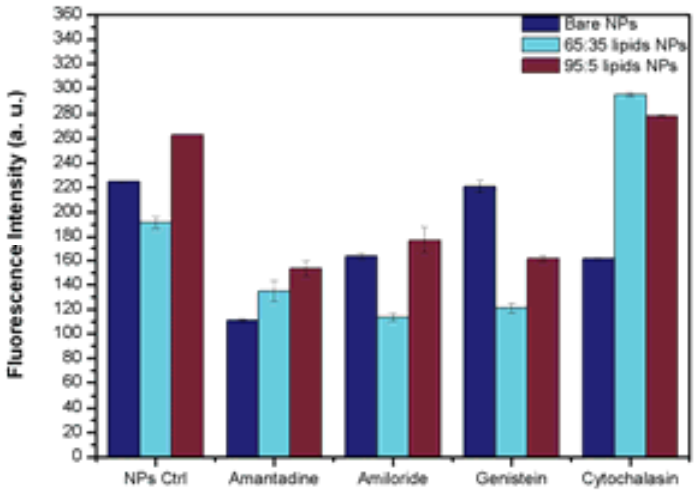

Figure 2.21. *Influence of pharmacological inhibitors on the cellular uptake of lipid coated NPs with different DOPC/DOPS composition.*

Cellular uptake of unmodified PLGA NPs and lipid coated NPs, with 65:35 and 95:5 DOPC/DOPS ratios were quantified via flow cytometry after 4 h of incubation with HepG2 cells. *Figure 2.21* shows the mean fluorescence intensity per cell of the different PLGA NPs as a function of the uptake inhibitors. Uptake of bare PLGA NPs was

significantly blocked by amiloride HCl, amantadine HCl and cytochalasin D, while genistein appears not to have any influence on the uptake. Therefore, internalization of the PEI stabilized PLGA NPs can be assigned to several cellular uptake mechanisms: clathrin-mediated endocytosis, macropinocytosis and internalization through the cell cytoskeleton. For the PLGA NPs coated with lipids either with 65:35 or 95:5 DOPC/DOPS macropinocytosis, clathrin-mediated and caveolae-mediated endocytosis are the main pathways of NPs uptake. For the lipid coated PLGA NPs with DOPC/DOPS molar ratio of 65:35 it seems that the largest amount of NPs were taken up via clathrin-mediated endocytosis, while for the 95:5 lipid ratio NPs are mainly taken up through macropinocytosis. Caveolae-mediated endocytosis was also observed to contribute to the uptake of the lipid coated NPs. It is worth mentioning that for polymeric NPs the caveolae-mediated pathway is only followed by NPs up to 100 nm in diameter *[103, 267]*.

Endocytosis through the caveolae-mediated uptake pathway is a promising cell internalization mechanism in drug delivery since the internalized material is not trafficked through endosomes and lysosomes. Our uptake pathway experiments suggest caveolae-mediated endocytosis as a possible cellular internalization mechanism for the lipid coated PLGA NPs, while unmodified PLGA NPs are not taken up via caveolaes. Moreover, the fact that lipid coated PLGA NPs co-localize within the ER of the cells, suggests a cell internalization mechanism different to the classical endocytic pathways in which endo-lysosomal trafficking is involved *[263]*. Nevertheless, we cannot discard the possibility that lipid coated PLGA NPs are internalized by the cell via specific receptors such as scavenger receptors or LDL, which are known to be involved in the uptake of PS-containing liposomes in human liver cells *[218]*.

Chapter 3
Surface Functionalization of Carbon Nanotubes

3.1. Carbon Nanotubes surface modification with polyelectrolyte brushes

Due to their characteristic electrical and mechanical properties, such as electric conductivity *[268-270]*, high tensile strength and elasticity *[271-273]*, carbon nanotubes (CNTs) *[147]*, either multiwalled (MWCNTs) or single wall (SWCNTs), are highly interesting nanomaterials for nanofabrication alone or in combination with other nanostructures, as well as for the fabrication of composite materials that enhance their performance through the incorporation with CNTs, i.e. polymer coatings, textiles, fibers, packing etc.

Nevertheless, there is a strong limitation for the practical usage of CNTs, and is that they precipitate in almost any solvent. CNTs show a high Hamaker constant *[274]*, that results in a strong association among themselves. Of particular difficultly is their solubilization in aqueous media, which is fundamental if the CNTs are to be used for biomedical applications, i.e. drug delivery. An additional limitation for the practical usage of CNTs is the difficulty in arranging them in an organized manner that could be fundamental for their application in electronics and for device fabrication.

Several strategies have been followed to increase the CNTs dispersibility, mostly by the use of surfactants to wrap the CNTs, which can lead to their stabilization in the desired phase, or by using the covalent bonding of stabilizing molecules on their surface. One appealing way to stabilize the CNTs in a selected solvent and enhance their

dispersibility is to covalently bond polymers to the surface that contain several units in the polymer chain that interact directly with the solvent *[275]*. In this regard, polyelectrolyte molecules provide a practical means to stabilize aqueous dispersions of CNTs. Their multiple charges along each polymer chain ensure the colloidal stability necessary for the suspension of the CNTs. Polyelectrolyte molecules can be assembled noncovalently or synthesized directly on the CNTs. Regarding functionalization through self-assembly, there are good examples of using zwitterionic block co-polymers with charged and non charged segments *[276]*. The non charged block attaches to the CNT walls through van der Waals interactions with the polyelectrolyte block facing the water media. Another example of stabilization of CNTs through polyelectrolyte self assembly is the use of layer-by-layer (LbL) films deposited on oxidized or surfactant-wrapped CNTs *[277]*, where the LbL films are stepwise assembled on the charged nanotubes. The main drawback of using LbL films is that each layer deposited requires several centrifugations, especially for the first assembled layers, which leads to aggregation during the assembly. To overcome this aggregation it is necessary to strongly sonicate the system, which, however, can reduce the length of the CNTs.

Polyelectrolytes can also be anchored to the surface of CNTs by a covalent reaction *[278]* or synthesized from initiator molecules attached to the surface *[279]*. In this case, the attachment of the initiator can be done by bonding silanes bearing an initiating function to oxidized CNTs *[280, 281]*. The oxidation of the CNTs provides surface hydroxide and carboxylate groups that can react with the SiOH groups of the silane to form a covalent bond and thus form a dense polymer arrangement around the tubes. This arrangement of polymers forms a brush, where one end of the polymer chains is attached to the carbon tube walls, while the other end of the chains is free. The covalent bonding of the polymer chains to the CNT walls ensures a strong and lasting stabilization of the nanomaterial.

In order to provide colloidal stabilization in aqueous media, poly(3-sulfopropylmethacrylate) (PSPM) brush has been *in situ* synthesized on CNTs surface by employing atomic transfer radical polymerization (ATRP) from initiating silanes attached to the CNTs before the polymerization.

3.1.1. *In situ* polymerization of Poly(3-sulfopropylmethacrylate) brush on CNTs surface

The strategy of the functionalization leading to the brush synthesis around the CNTs is shown in *Figure 3.1*.

In the first step, the CNTs were oxidized as described by Zhang N., et al *[281]*. A mixture of 12 mg of CNTs, 2.5 mL methylene chloride (CH_2Cl_2), and 0.5 mL acetic acid was first ultrasonicated for 15 min. Around 100 mg of (1-Tetradecyl) trimethylammonium bromide was added to the mixture, followed by the slow addition of 180 mg of powdered potassium permanganate. The mixture was then stirred vigorously overnight at room temperature. After, the mixture was filtered and washed with acetic acid, CH_2Cl_2, hydrochloric acid and water. Finally, after drying, oxidized CNTs were obtained.

The oxidation generated the necessary OH groups to achieve the CNT silanization with 3-aminopropyltris(trimethoxy)silane (APTS). 8 mg of oxidated CNTs were resuspended by ultrasonic vibration for 5 s 3 times in 2 mL of CH_2Cl_2. APTS (0.12 ml, 0.30 mm mol) in 4.5 mL of CH_2Cl_2 was added to the suspension. The mixture was then placed in the shaker for 1 h and sonicated in a water bath for 15 min. The mixture was centrifuged and resuspended in ethanol several times at 8000 rpm for 45 min to eliminate the reaction leftovers *[282]*.

Then, the amine groups of the silane were used to attach 2-bromo-2-methylpropionic acid through a condensation reaction *[283]*. Silanizated CNTs (4 mg), 2-bromo-2-methylpropionic acid (33.4 mg, 0.2 mmol) and dimethyl aminopyridine (6 mg, 0.05 mmol) in 10 mL of CH_2Cl_2 were placed in a three-necked flask and cooled down to 0 ºC while stirred magnetically. 1,3 Dicyclohexylcarbodiimide (51.6 mg, 0.25 mmol) was added after which the reaction was allowed to reach room temperature slowly and was stirred overnight. Purification was achieved by centrifugation and resuspension first in dichloromethane twice, then in acetone twice and finally in water twice as well. The 2-bromo-2-methylpropionic acid will act as initiator for the synthesis of PSPM *[284]*.

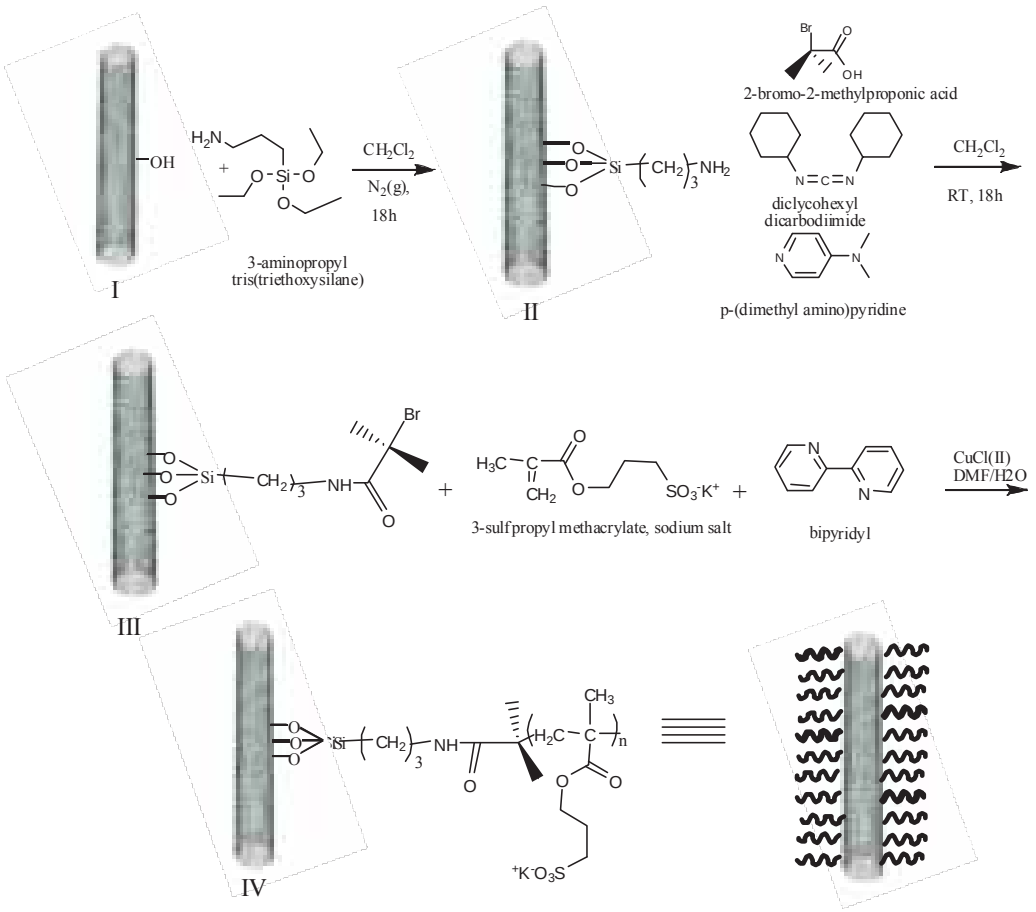

Figure 3.1. *Scheme of the brush synthesis on CNTs, starting from silane attachment to PSPM polymerization.*

PSPM was in situ synthesized on CNTs surface employing atom transfer radical polymerization (ATRP). For the polymerization, 3.5 mg of CNTs-initiator resuspended in 0.2 mL of water was added to a mixture of 3-sulfopropylamino methacrylate, SPM (0.7 g, 2.8 mmol), 2,2'-bipyridil (0.3 g, 1.9 mmol) and $CuCl_2$ (0.3 g, 2 mmol) in a previously degassed mixture of dimethylformamide/water (3:2) 4 mL. The mixture was allowed to react overnight at room temperature. The functionalized CNTs were then washed with dimethylformamide/water 3 times, acetone 3 times, ethanol 3 times and water by centrifugation and resuspension. Finally, they were placed in pleated dialysis tubing (3.500 MWCO) against millipure water. After 3 days of dialysis, the sample was freeze dried to yield 3 mg of CNTs functionalized with poly(3-sulfopropylmethacrylate) (CNTs-PSPM).

3.1.2. Characterization of the PSPM CNTs coating

The entire process of surface modification of the CNTs, from the oxidation of the CNTs and the attachment of the silanes to the PSPM synthesis, was followed by ζ-potential measurements. The ζ-potential was measured at 25 ºC and a cell drive voltage of 30 V using a monomodal analysis model, and all samples were measured at constant ionic strength in 10 mM NaCl.

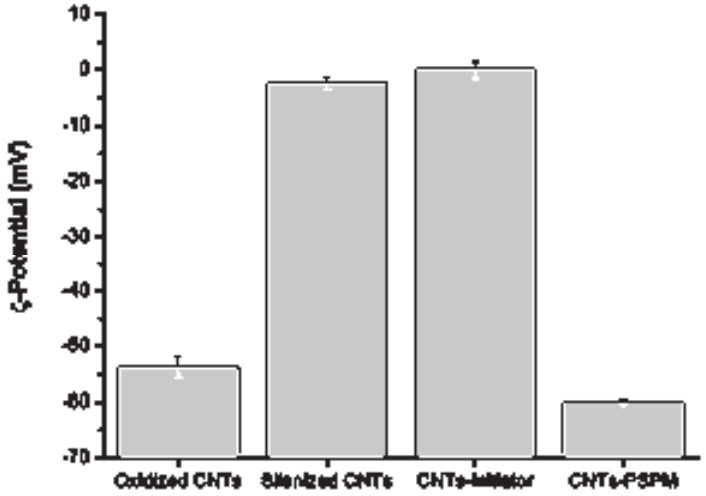

Figure 3.2. *ζ-Potential of the stepwise surface modified CNTs from oxidation to PSPM synthesis.*

The results of the ζ-potential measurements are summarized in *Figure 3.2*. The ζ-potential of the oxidized CNTs was ∼−54 mV. The ζ-potential of non oxidized CNTs could not be measured in water since it was not possible to obtain a stable aqueous dispersion of the untreated CNTs. Nevertheless, it has been shown that the ζ-potential of untreated CNTs can be measured in organic solvents, giving positive ζ-potential values that could also change to negative values, due to a charge transfer process *[277]*. However, untreated CNTs ζ-potential in organic solvents cannot be extrapolated to aqueous media. After attachment of the APTS silane the ζ-potential changed to −2.5 mV. Since this ζ-potential value is approximately zero, it reflects a compensation of the charge of the CNTs by the amine groups, which should provide at least a slightly positive charge. In view of the non positive charge, it is likely that the negatively

charged carboxylates and/or hydroxyls present on the surface of the CNTs are not completely bonded to the silanes.

After the reaction of the amine silane with 2-bromo-2-methylpropionic acid, the ζ-potential decreased to 0 mV. It is possible to observe that, in agreement with the change in ζ-potential, the attachment of the silanes decreased the solubility of the CNTs. The synthesis of PSPM, however, increased the water solubility of the CNTs and resulted in a ζ-potential of ~−60 mV for PSPM coated CNTs. The observed negative charge can be assigned to the presence of sulfonate groups from the synthesized PSPM. Such ζ-potential value is compatible with a stable colloidal dispersion and indeed, after the PSPM synthesis, the CNTs remained dispersed in water solution for longer than a month.

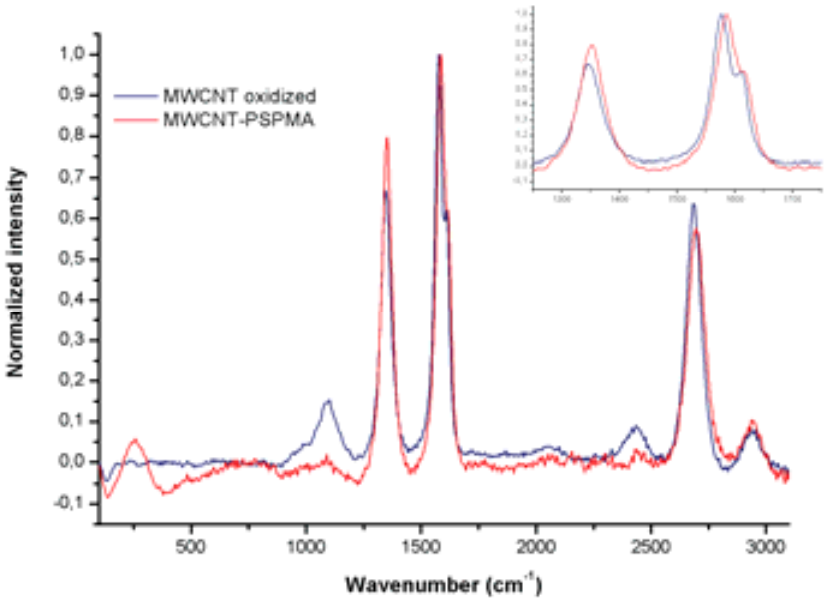

Figure 3.3. *Raman spectra of oxidized CNTs and PSPM coated CNTs.*

Raman spectroscopic data of functionalized and unfunctionalized CNTs was obtained for comparison (*Figure 3.3*). For the unmodified CNTs the Raman band corresponding to the allowed tangential mode, called the G mode, can be observed at 1580 cm^{-1}. This band is typical for graphite. The peak appearing at 1354 cm^{-1} is the so-called disorder-

induced band, or D mode. This band displays a second-order harmonic *[285]*, which can be seen at 2688 cm^{-1}.

It is possible to observe that polymer-coated CNT does not broaden the bands in the spectra. There is, however, after the PSPM synthesis, an increase in the intensity ratio of the D and G bands. The increase in the ratio of these band intensities is indicative of sp^3 hybridization *[279]*, which is consistent with the functionalization of the MWCNTs. For oxidized MWNCTs, the ratio is 0.6716, while for MWCNT–PSPM, the ratio of the normalized intensities increases to 0.7963. Also the maximum of the D band shifts for MWCNT–PSPM 15 cm^{-1} with respect to the unfunctionalized system. The displacement of the maximum as well as the observed broadening of the D band can be explained as a result of the covalent bonding of the polymer chains of PSPM to the CNT walls as previously reported by Gao C., et al *[286]*, were they associated such a displacement with the influence of the graft polymers in the electronic structure of the CNTs.

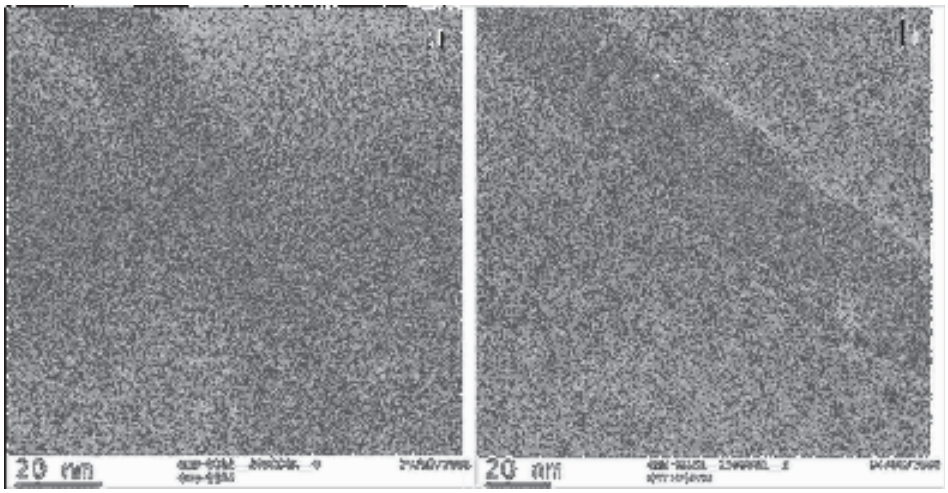

Figure 3.4. *TEM images of (a) unmodified CNTs and (b) PSPM coated CNTs, the PSPM shell thickness is around 2nm.*

TEM was employed for a direct visualization of the PSPM on the CNTs surface. TEM images were obtained by dropping dilute solutions on a copper grid. *Figure 3.4a* shows a representative TEM image of an uncoated CNT used in the study. The multi-walled structure of the CNTs can be well appreciated in the image. The thickness of the CNT

walls is approximately 20 nm. For the visualization of the polymer coating, the sample was treated with uranyl acetate. In *Figure 3.4b* it is possible to observe a thin, soft white shell around the CNTs, which was absent in the uncoated CNTs. The shell had a thickness of 2 nm. Since the TEM measurements must be of dry samples, the polymer brushes are in a collapsed state. In the hydrated state, the shell must result in a thicker film. Nonetheless, the 2 nm thick polymer shell in the dry state suggests a low density polymer shell, probably consisting of spaced polymer chains, which spread on the surface of the CNTs when the brush collapses.

3.2. Polyelectrolyte brushes coated Carbon Nanotubes endowed with quantum dots and metal oxide nanoparticles through *in situ* synthesis

In addition of provide colloidal dispersion in aqueous media, the polyelectrolytes could be used to provide other functionalities to the CNTs, for example, as shown for the tailoring of the CNTs with nanoparticles synthesized *in situ* from charged groups present in block copolymers attached to the CNTs *[276]*. Additionally, charged quantum dots and other nanoparticles have been assembled on CNTs based on electrostatic interactions *[287, 288]*.

Therefore, covalently bonded polyelectrolyte brushes were used as a platform for the *in situ* synthesis of nanoparticles and show the feasibility of this approach to incorporate CdS quantum dots or magnetic iron oxide nanoparticles in the CNT–brush assembly. This type of dual-particle CNT hybrid assembly was not previously synthesized by use of a covalently bonded polyelectrolyte brush. The approach provides a general route for the fabrication of water dispersible, core–shell-type CNT/nanoparticle structures via the polyelectrolyte brush.

3.2.1. CdS quantum dots i*n situ* synthesis on CNTs-PSPM

For the *in situ* synthesis of CdS quantum dots first, 0.5 mg of CNTs-PSPM were resuspended in 200 μL of 0.1 M $Cd(NO_3)_2$ solution and allowed to dialyze for 2 days

against millipure water, changing water every 8 h. Before each exchange of the dialysis solution a UV spectrum of this solution was measured to assess the presence of Cd(II). After dialysis, 200 μL of Na_2S 0.1 M solution were added to the sample. The mixture was sonicated and dialyzed against a membrane with a 5000 MW cutoff for 3 days.

It is known that Cd(II) has a higher binding affinity towards sulfonates than potassium ions. Therefore, a relatively high concentration of the exchanging ions was employed to ensure total displacement of the potassium ions. When the removal of free ions was completed, 0.1 M Na_2S was added to the CNTs-PSPM and Cd suspension. The pH was then adjusted to 12–13 with NaOH to induce the precipitation of nanoparticles within the PSPM brush. The reaction with Na_2S precipitated CdS in the polymer matrix. The scheme of the reaction for the CdS CNT synthesis is shown in *Figure 3.5*.

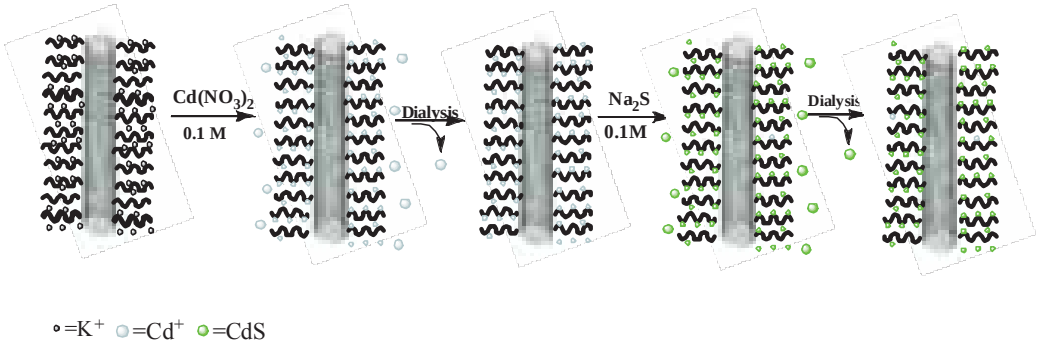

Figure 3.5. *Scheme of synthetic strategy followed for CdS quantum dot formation into PSPM attached to CNT surfaces.*

TEM images of the CNTs-PSPM with CdS attached to the surface of the CNTs are shown in *Figure 3.6*. The CdS particles are crystalline with a size between 5 and 8 nm (*Figure 3.6b*) and are located on the surface of the CNTs in a non uniform distribution. The density of the quantum dots is therefore higher in some areas and rather low in others. This is very likely due to the fact that the density of the brush varies over the length of CNTs. The thickness and density of the brush are key parameters in order to control the density and number of quantum dots around the CNTs since they will determine the number of active sites (monomers) for the nanoparticle synthesis and the distance between neighboring sites, which is also an important point for successful nanoparticle preparation and also for controlling the size of the synthesized

nanoparticle. No nanoparticles could be detected or observed outside the CNTs in large-area imaging studies of the sample.

After the synthesis of the quantum dots, the water solubility of the CNTs decreased as did the corresponding ζ-potential from ∼−60 to −9.5 mV. This is probably due to a change in the density of charged monomers at the tips of the brush after the nanoparticle synthesis. The presence of the nanoparticles among the brush chains could affect the conformation or arrangement of the polymer, possibly inducing some collapse and chain splitting.

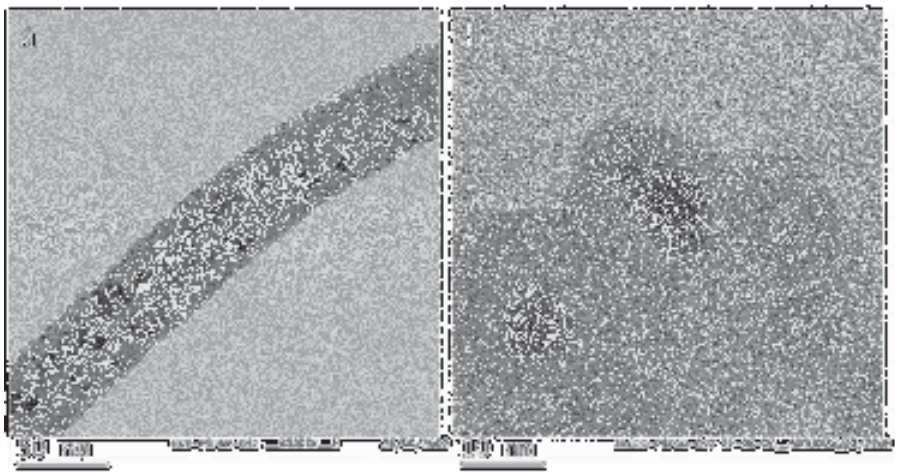

Figure 3.6. *CNTs with CdS quantum dots embedded in a PSPM shell, average size 5-8 nm (a) and its corresponding higher magnification image (b).*

The UV–vis absorption spectra recorded are shown in *Figure 3.7* for the CNTs, CNT–PSPM, PSPM–CdS and CNT–PSPM–CdS materials. The absorption spectra for the CNTs are typical while that for the CNT–PSPM shows an additional band at about 310 nm associated with the PSPM moiety. The absorption spectra of CdS, which was synthesized in a free PSPM aqueous solution, showed an adsorption band with an edge onset at about 480 nm and another one at 270 nm, with the latter similar to that observed for CdS block co-polymer-coated CNTs *[276]*. The characteristic shoulder in the CdS absorption band (*Figure 3.7c*) is blue shifted from that of bulk CdS (520 nm) and suggests quantum confinement. Furthermore, the absorption spectrum is not inconsistent with the CdS quantum dot size range of 4–5 nm *[289, 290]* as observed

from TEM data for both the PSPM–CdS and CNT–PSPM–CdS systems. No such shoulder is observed on the absorption band present in the CNT–PSPM–CdS spectrum, which may be due to the broad absorption features of both the CdS and CNTs, which extend through the near-IR or to energy transfer processes such as suggested in the fluorescence emission data discussed below.

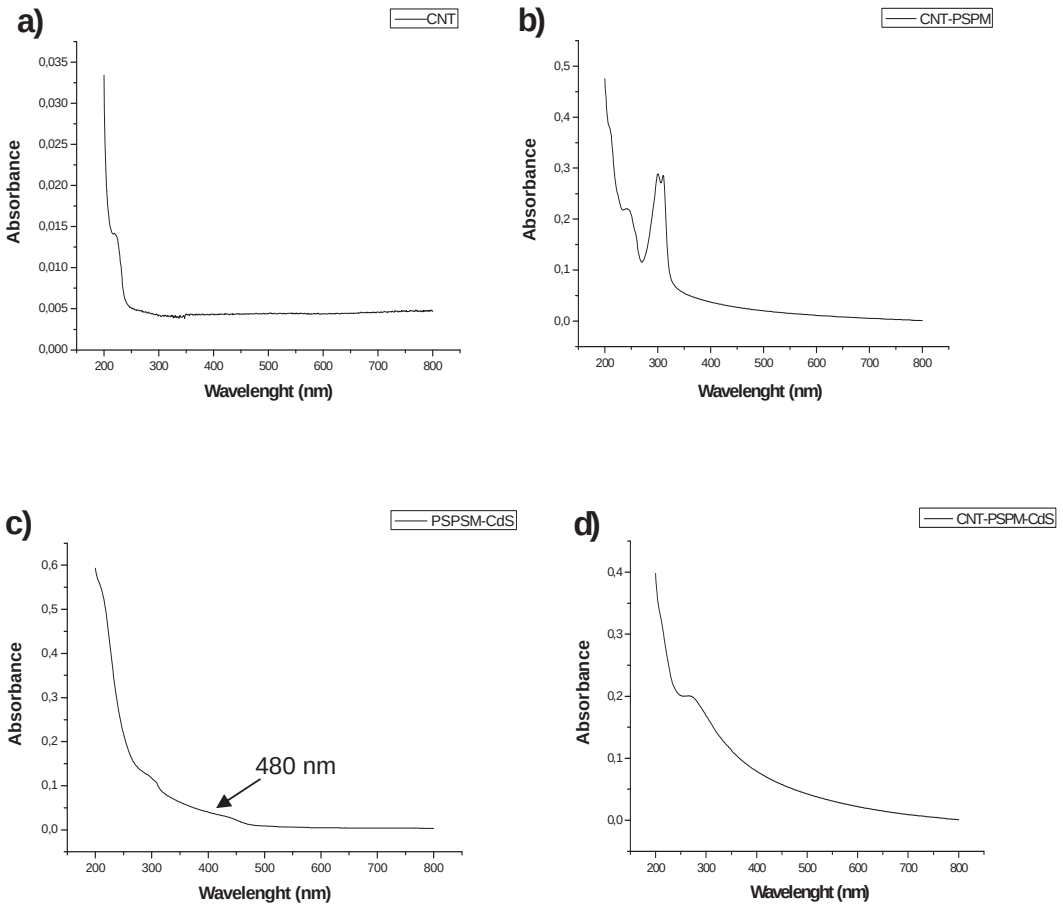

Figure 3.7. *UV-vis absorption spectra for diluted aqueous suspensions of (a) CNTs, (b) CNTs-PSPM, (c) PSPM-CdS and (d) CNTs-PSPM-CdS.*

The fluorescence emission spectra of the PSPM–CdS and CNT–PSPM–CdS samples were obtained in nanopure water exciting at 270 nm. The spectrum showed a broad band centered at 660 nm, attributed to the emission of the quantum dots *[291-293]*, as observed in *Figure 3.8*. This band is not observed for the untreated and oxidized CNTs

nor for the polymer functionalized CNTs. The band is, however, not very intense as it may be quenched by the energy transfer of the quantum dots with the CNTs.

It is possible to observe complete fluorescence quenching in the CNT–PSPM–CdS system, as was observed previously when the quantum dots were attached electrostatically to charged CNTs *[276]*. This observation may be attributed to the intervening PSPM network, which allows for a variable CdS–CNT distance normal to the CNT wall. Since the dots are synthesized along the polyelectrolyte shell, some will be synthesized closer to the CNT wall while others may be generated in the outer region of the PSPM shell. These variable distances could possibly include dots located at distances from the CNT walls where transfer is no longer effective, although the TEM revealed a thin polymer shell. However, it cannot be ruled out contributions from extraneous CdS not in the brush even though none could be detected with extensive TEM analysis.

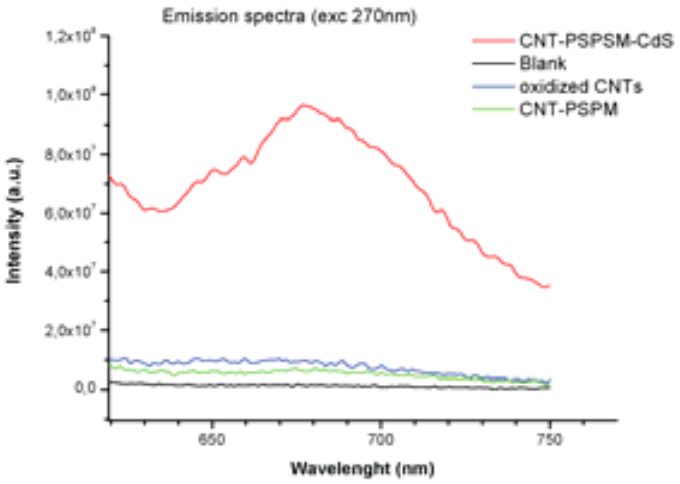

Figure 3.8. *Fluorescence emission spectra of the CNTs-PSPM-CdS.*

3.2.2. Magnetic iron oxide nanoparticles i*n situ* synthesis on CNTs-PSPM

In order to demonstrate the potential versatility of the present synthetic procedure and to extend its usefulness, CNT–PSPM systems containing metal oxide nanoparticles were

prepared, in particular, those of a magnetic iron oxide. Such a system, for example, could allow for manipulation of the CNT–PSPM-NP with electromagnetic fields *[294, 295]*. A general requirement of the present synthetic system is that the intended nanoparticles involve cations that are exchangeable with the cations of the polymer brush and that they can be precipitated or condensed within the PSPM network, as has been shown for the synthesis of quantum dots.

Magnetic iron oxide nanoparticles were *in situ* synthesized on the CNTs-PSPM as is following described. 0.5 mg of CNTs-PSPM were resuspended in 200 μL of 0.1 M $FeCl_2$. The samples were purified by extensive dialysis against millipure water, changing water every 8 h. A piece of iron bar was placed outside the membrane to avoid oxidation of the iron ions. Samples were then centrifuged, resuspended in water and centrifuged again. The water washing was repeated three times to eliminate any remaining Fe(II) in solution. The centrifugation was performed at 13 000 rpm for 15 min each time with a rotor of 22 065 × g. The samples were then dispersed in NaOH solution of pH 12 or 13 under stirring, centrifuged and washed with water three times.

The iron oxide (IO) nanoparticles in the CNT–PSPM were detected by TEM as shown in *Figure 3.9*. The synthesized iron oxide nanoparticles form a dense coating on the CNTs surface. It can be noted that a narrow distribution in size of nanoparticles can be observed, of 2–4 nm attached to the CNTs surface. As for the quantum dots no particle could be detected outside the CNTs by means of TEM. The preparative conditions, black color and observable magnetism of the CNT–PSPM–IO hybrid nanocomposite suggest the magnetic phase to be magnetite or a solid solution of magnetite and maghemite.

The detailed procedure provides a general route for the preparation of nanoparticles in the polymer matrix surrounding the CNTs and for a relatively high concentration of such particles proximal to the CNTs. Thus, CNTs endowed with nanoparticles external but proximal to the tube may be prepared to provide stable aqueous dispersions of magnetically or fluorescently responsive carbon nanotubes. The aqueous dispersibility of the CNTs could be used to process or incorporate these modified tubes into other structures through assembly, like layer-by-layer films.

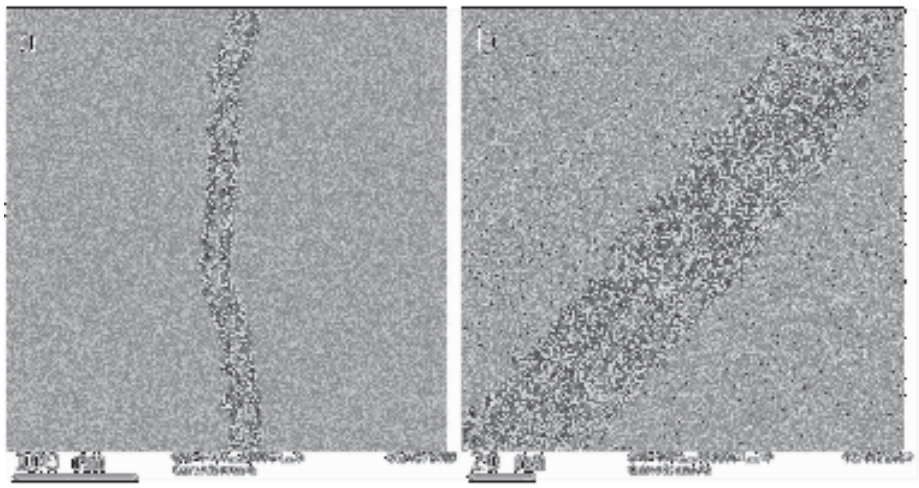

Figure 3.9. *TEM images of CNTs-PSPM-IO.*

3.3. Surface tailoring of Carbon Nanotubes with polyelectrolyte brushes and lipid layers

The low aqueous dispersibility of bare CNTs can be increased, as was mentioned above, by means of surfactants, polymer coatings, or just by charging CNTs by oxidation. Oxidation and coating of the CNTs often affect the properties of CNTs as such but increase considerably their colloidal stability in water. Perhaps, the biggest drawback for the application of CNTs is not technical, but their questionable safety, that must be ensured in those CNTs applications that imply their exposure to humans and the environment, such as in textiles or packing, or for biomedical applications (e.g.: sensors, drug delivery) *[154, 155, 296-298]*.

The unique structural characteristics of CNTs have been explored for their use as carriers for single DNA molecules *[299, 300]* or other therapeutics once stabilized in aqueous solutions. But the use of CNTs in nanomedicine requires a deeper knowledge of the toxicity of the CNTs, which is to a certain extent still missing. The special arrangement of the carbon sheets in CNTs, their high polarizability, even in some cases after surface modification, and the presence of impurities in the material can interfere

with the biochemical processes at the cellular level and therefore CNTs may appear toxic for living cells. For the toxic action of CNTs it may not be necessary that the CNTs are incorporated into cells. CNTs could interfere with the plasma membrane stability and function just by touching the membrane from outside. This is another point which raises concern on the use of CNTs in complex materials containing CNTs, with which cells could get in contact when such novel materials are being used in medical devices.

In some situations in nanomedicine it may be advantageous to be able to control the CNTs uptake and localization within cells. A biocompatible surface functionalization may be quite helpful for this purpose.

The polyelectrolyte shell surrounding the CNTs (CNTs-PSPM) can also be used for the assembly of a lipid layer on top of the CNTs in a similar fashion as shown by Artyukhin A. B., et al. *[179]* with layer by layer films, where CNTs modified with polyelectrolyte multilayers were deposited on a surface and then coated with lipids. Herein, the polyelectrolyte synthesis and the lipid assembly will be performed on CNTs dispersed in aqueous solution, following well established protocols for the formation of lipid bilayers on top of polyelectrolyte layers *[185, 301]*. The choice of a spherical brush ensures the stability of the CNTs in aqueous solutions and also reduces the number of steps required in layer by layer to obtain a polymer cushion for the coating with the lipid vesicles.

3.3.1. CNTs-PSPM surface modification with a lipid bilayer

Vesicles composed of 1,2-dioleoyl-*sn*-glycero-3-choline/1,2-dioleoyl-*sn*-glycero-3-phospho-L-serine (DOPC/DOPS) in a molar ratio 3:1 were prepared following the procedure described in section 3.5.1 from chapter 3, that detail the formation of lipid vesicles.

Figure 3.10. *Scheme of polyelectrolyte and lipid assembly on top of the CNTs.*

On top of CNTs-PSPM, a layer of poly(allyl amine hydrochloride) (PAH) was assembled taking advantage of the electrostatic interaction between the cationic PAH and the anionic PSPM. PAH provides the support for the following lipid assembly *[185, 301]*. Lipid vesicles composed of DOPC/DOPS were added and readily adsorb on PAH as a result of the specific interaction of the PAH amino groups with the carboxyl and phosphate groups of the phospholipids. The vesicles rupture and spread over the polyelectrolyte support located at the surface of the CNTs. The strategy of the functionalization leading to the polymer coating and lipid layers around the CNTs is sketched in *Figure 3.10*.

3.3.2. Characterization of the surface modified CNTs with lipids

The entire process of surface modification of the CNTs, from the oxidation of the CNTs, PSPM synthesis, PAH coating and lipid coating, was followed by ζ-potential measurements. The ζ-potential was measured at 25 ºC and a cell drive voltage of 30 V using a monomodal analysis model, at constant ionic strength in 10 mM PBS. The results of these measurements are summarized in *Figure 3.11*.

The oxidized CNTs display a negative surface potential around -54 mV. The ζ-potential decreases furthermore to ~-60 mV after the synthesis of PSPM. The assembly of a PAH layer reverses the potential to positive values, ~+6 mV. This proves that the PAH is coating the surface of the CNTs. Finally, the lipid assembly recharges the surface of the CNTs again to negative values, resulting in a ζ-potential of ~-11 mV, in accordance with the negative charge of the vesicles containing DOPS.

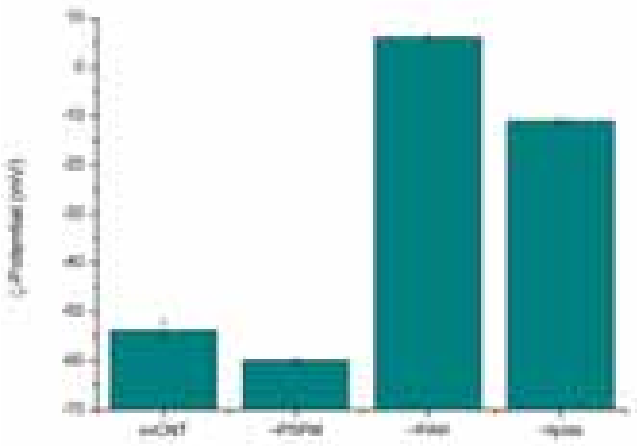

Figure 3.11. *Variation in the ζ-potential of CNTs after polymer and lipid assembly.*

TEM was then applied for a direct visualization of the polyelectrolyte and lipid coatings on the CNTs. TEM images were obtained by dropping dilute solutions on a copper grid. *Figure 3.12a* shows a representative TEM image of bare CNTs stained with uranyl acetate for comparison. The multi-walled structure of the CNTs can be well appreciated in the image. The thickness of the CNT walls corresponds approximately to 5 nm and the complete diameter of multi-walled CNTs is around 20 nm. For the visualization of the polymer coating, the samples were treated with uranyl acetate (0.01%). In *Figure 3.12b* can be observed a thin, soft shell around the CNTs, which was absent in the uncoated CNTs when treated with this substance. The shell had a thickness of 3 nm. Since the TEM measurements are performed on dry samples, the polyelectrolyte brushes are in a collapsed state. In the hydrated state, the shell has to be considerably thicker.

To visualize properly the lipids by TEM in dry state, a thin layer of PEI was deposited on top of the lipid coated CNTs. Otherwise, during drying the lipid would detach from the surface of the CNTs. The treatment with uranyl acetate did not provide a clear evidence of the lipid formation on the CNTs (*Figure 3.12c*). For this reason the lipid coated CNTs were also stained with sodium tungstate, which stains phosphate groups. In *Figure 3.12d* can be appreciated that after this treatment a shell close to 5 nm thickness can be visualized around the CNTs; 3 nm can be attributed to the polyelectrolytes coating and 2 nm due to the lipid bilayer in dry state.

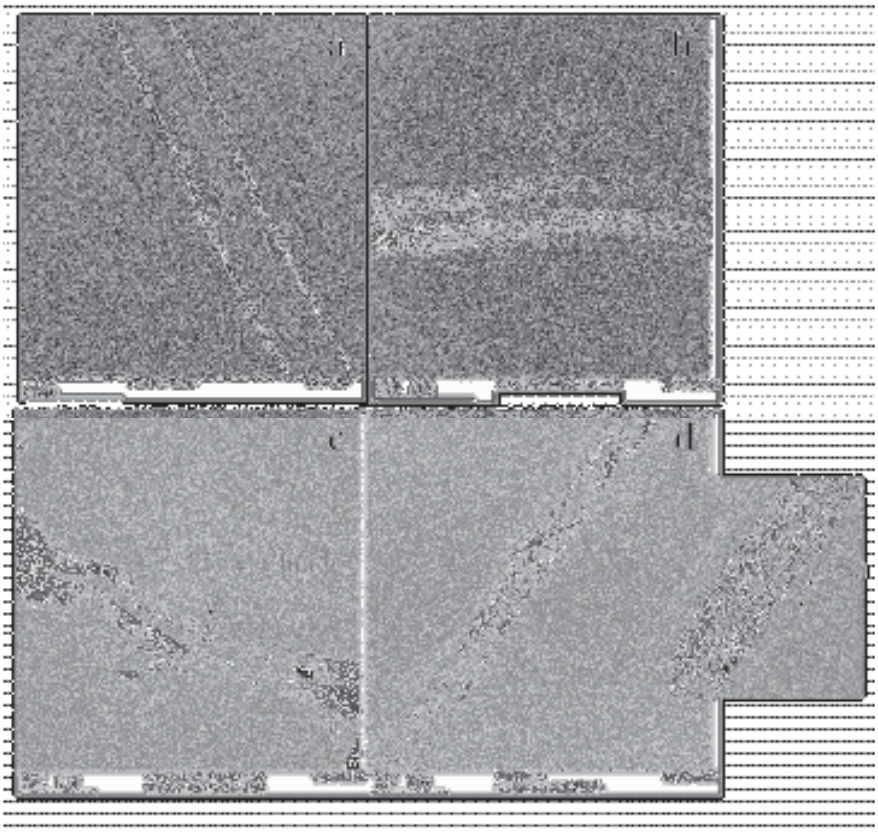

Figure 3.12. *TEM images of CNTs stained with uranyl acetate: (a) oxidized, (b) PSPM coated, (c) lipid coated, and (d) lipid coated CNTs stained with sodium tungstate.*

Chapter 4

Uptake, intracellular distribution and cytotoxicity of Poly(lactide-*co*-glycolide) Nanoparticles and Carbon Nanotubes

---

The use of NPs in medicine as drug delivery vectors, sensors or contrast agents is among the most promising areas in nanotechnology research. For the application of nanotechnology in medicine, '*in vitro*' work is of paramount importance, especially regarding the assessment of possible toxicological consequences of the nanomaterials/NPs. It is a key issue to study the effects of 'nano' in the cellular machinery and to understand how the nanomaterials are processed in the cell, their distribution and fate after being taken up by the cells.

CLSM is often applied for uptake studies, but its application for NPs is not all the times feasible since the size of the NPs falls well below optical resolution. Also, a main drawback of CLSM is that, for most of the cases, both the NPs and cellular compartments, must be fluorescently labelled and this is not always an easy task. Besides that, labelling of NPs may in some cases require complex chemical routes including, for example, silanization, assembly of polymers, etc. As a result, the labelling can induce significant changes in the structure and properties of NPs, which may in turn affect uptake and toxicity. TEM can be used to study the uptake and localization of NPs and nanomaterials when the NPs have enough contrast, avoiding their labelling. The drawback of TEM for this application is that it requires complex and time-demanding preparations that also may affect the localization of the nanomaterials within the cell. In addition, due to their nature, organic NPs, with the exception of CNTs, are not easy to visualize within cells by TEM.

Other label-free techniques for the study of the localization of nanostructures within cells are spontaneous Raman microscopy and coherent anti-stokes Raman (CARS) microscopy. In CARS, a single Raman band coming from the nanomaterial is scanned throughout the cell. A mapping of the cell is obtained showing the intensity distribution of the chosen Raman band *[260]*. Drawbacks of CARS are that only selected bands can be mapped, and that spectral overlapping may cause problems.

Confocal Raman microscopy (CRM) combines spontaneous Raman emission with confocal detection. CRM can be used to study the localization of nanomaterials in the cells, taking advantage of the fact that every spot of the whole Raman spectrum is recorded. The latter thus contains bands coming from the nanomaterials and from representative cell molecules: proteins, DNA and lipids; which allow to identify the region of the cell *[302]* where the nanostructures are located. In this chapter, the spontaneous Raman emission of Poly(lactide-*co*-glycolide) (PLGA) NPs and carbon nanotubes (CNTs) inside the cells, is employed for their detection and to assess the intracellular region, where the nanomaterials are located.

4.1. Cellular uptake, co-localization and cytotoxicity of Poly(lactide-*co*-glycolide) Nanoparticles

In Chapter 3, it has been shown that PLGA NPs can be prepared employing PEI or BSA as surface stabilizers *[96-98]*. It was demonstrated by Flow Cytometer and CLSM, that the uptake of NPs is influenced by the nature of the surface of the PLGA NPs. Large uptake was observed for PLGA NPs coated with PEI and BSA. A coating with polyelectrolyte multilayers or a pegylation reduced the uptake significantly. Subsequent modification with folic acid facilitated again uptake by specific cell targeting *[96-98]*.

It is nevertheless difficult to differentiate whether the NPs have been internalized in the cells or remained attached to the cell membrane. Flow cytometry measures the fluorescence per cell and does not provide further information about localization of

labeled NPs, whether attached to or indeed taken up by the cells under study. Visualization of the NPs by CLSM is not a straightforward task because it is not always possible to distinguish between NPs that have been internalized in the cell and NPs attached to the cell membrane, which in many cases needs to be labeled for cell visualization. Also, the encapsulated dye may be released and accumulated in the cell interior even though the PLGA NPs remained in the bulk phase. In the case that PLGA molecules are labeled covalently, PLGA could eventually degrade and incorporated in the cell together with the marker. In these situations, one could arrive to the false conclusion that the particles have been incorporated in the cells when it is not the case *[260]*.

Xu P., et al. *[260]*, have been demonstrated by means of coherent anti-Stokes Raman scattering (CARS) microscopy, that PLGA NPs stabilized with poly(vinyl alcohol) (PVA) were not taken up by cells, although CLSM and flow cytometry indicated that they were. Notwithstanding with this observation, Chernenko T., et al., showed by CRM that NPs stabilized with Pluronic F 108 are incorporated within cells and could be found in the Golgi associated vesicles of the late endosomes *[302]*. The localization of PLGA NPs was also recently studied with immune fluorescence techniques in epithelial cells *[265]* demonstrating an association with different intracellular compartments as a function of time. These results demonstrate that the chemical properties of the surface of the NPs play a decisive role regarding internalization and uptake of PLGA NPs.

CRM is a well-suited technique to study the uptake of NPs into culture cells. CRM does not require labeling and can therefore be used for studying a large variety of NPs without having the requisite of labeling them. This is an important advantage because authentic NP can be probed. In this chapter, the cellular uptake of PLGA NPs with PEI or BSA as surface coatings has been studied by CRM and compared with data from CLSM and flow cytometry. In addition, the cytotoxicity of these two kinds of PLGA NPs was determined, to evaluate the possible use of surface-modified nanocarriers for intracellular delivery.

4.1.1. PLGA NPs cellular uptake by means of Flow Cytometer and Confocal Laser Scanning Microscopy

Flow cytomerter and CLSM studies of the cellular uptake of PLGA NPs stabilized with either PEI or BSA, were described in detail in Chapter 2. Briefly, in Chapter 2 it was presented that the uptake of BSA and PEI stabilized NPs labeled with rhodamine reaches a plateau during the first hours of incubation. For BSA the uptake was faster than for PEI stabilized NPs reaching a plateau value corresponding to about 90 % of the cell population within 6 h (*Figure 4.1a*). For PEI stabilized NPs the uptake ratio increased more gradually and did not reach the values observed for BSA stabilized NPs. The cell uptake ratio was defined as the percentage of cells, which are associated with NPs, having them either internalized or attached to the cell membrane.

The fluorescence intensity was also taken as a measure of uptake. When comparing the net fluorescence of BSA and PEI stabilized PLGA NPs it has to be taken into account that these two particle preparations have a priori different fluorescence intensities per NP. The fluorescence distribution of the BSA and PEI stabilized PLGA NPs was measured with the flow cytometer, employing the same settings as the experiments with cells (*Appendix Figure E*). The result was that the PEI stabilized PLGA NPs have fluorescence intensity almost three times the intensity of the BSA stabilized PLGA NPs, implying that the latter had a lower degree of labeling than the PEI stabilized NPs. In *Figure 4.1b*, consequently, it is displayed the normalized intensity curves of PEI stabilized PLGA NPs, taking the BSA stabilized labeled particles as the reference. The data in *Figure 4.1b* thus provide a measure of the number of particles taken up by a single cell. In the case of BSA stabilized PLGA NPs the intensity reached a maximum within 3 h and then decreased. The uptake of PEI stabilized NPs increased; on the contrary, more steadily reaching finally values comparable to BSA stabilized particles. These results are consistent with the cell uptake ratio, where it is observed that the percentage of cells with NPs associated increases faster for BSA modified NPs than for PEI stabilized PLGA NPs.

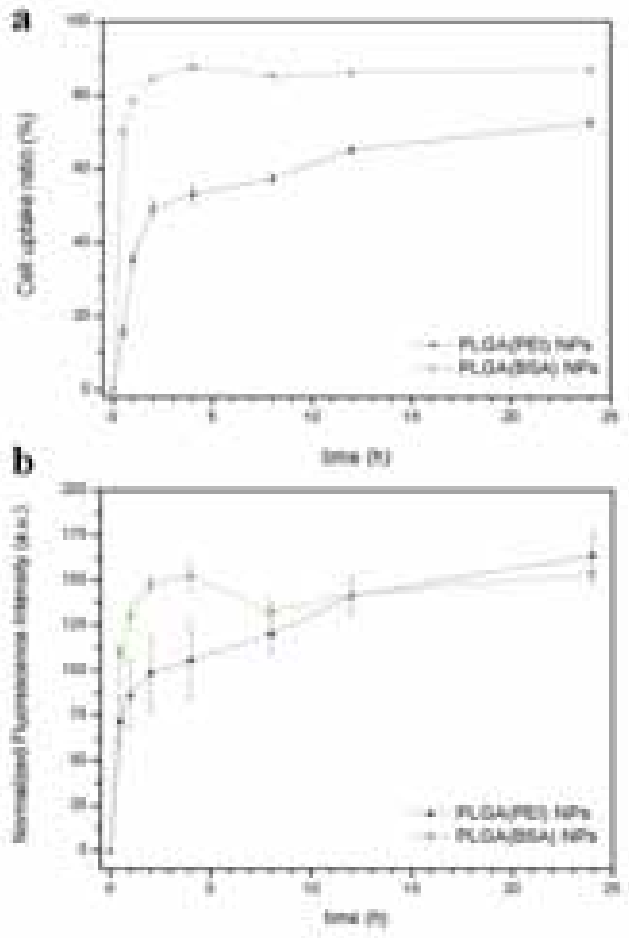

Figure 4.1. *(a) Cellular uptake ratio and (b) normalized fluorescence intensity maximum for PLGA (PEI) NPs as function of the incubation time.*

CLSM was used to have a direct visualization of the association of NPs with HepG2 cells, again this has been already presented in Chapter 2. In *Figure 4.2a,* the confocal image shows that PLGA NPs stabilized with PEI are associated with the cells. This follows from the red color indicating the rhodamine labeled NPs distributed around the blue stained nucleus. Similar images can be obtained for the PLGA NPs stabilized with BSA, shown in *Figure 4.2b*. Because of the intrinsic difference in fluorescence between the PEI and BSA stabilized particles the intensity of the red fluorescence in *Figure 4.2b* is weaker than in *Figure 4.2a*, however, the normalized plot in *Figure 4.1b* shows that the uptake of BSA stabilized PLGA NPs per cell is not smaller than the uptake of PEI stabilized PLGA NPs.

Although flow cytometry proves the association of both BSA and PEI modified PLGA NPs with cells, it is not clear if the NPs are really incorporated into the cell and have crossed the membrane barrier or if they remain only attached to the cell membrane. The CLSM images in *Figure 4.2*, where the nucleus and NPs have been labeled with DAPI (blue) and Rd6G (red), are representative of the behavior of the NPs in contact with Hep2G cells. The images clearly show that the NPs do not reach the nucleus, but an unambiguous conclusions about the environment in which the NPs are located within the cell or if they simply remained attached to the cell membrane cannot be drawn.

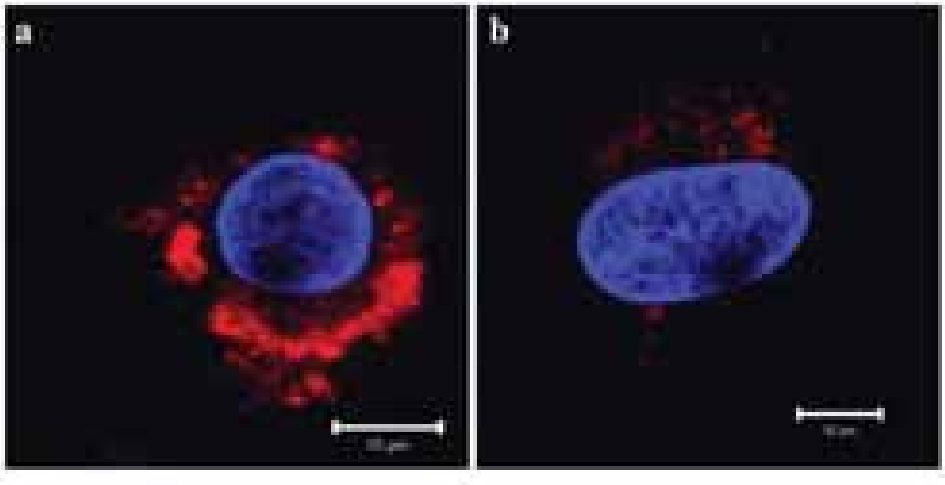

Figure 4.2. *CLSM images of HepG2 cells after being co-cultured with (a) PLGA NPs stabilized with PEI and (b) PLGA NPs stabilized with BSA.*

4.1.2. Cell internalization and NPs co-localization and distribution by means of Confocal Raman Microscopy

The internalization of the NPs as a function of their surface modification is certainly a key issue regarding their potential use as delivery devices. Therefore, alternative methods capable of proving internalization and intracellular location are highly desirable. As it was mention above, Xu P., et al. *[260]*, showed that PLGA NPs stabilized with PVA are not internalized by the cells. Employing CARS, they did not

find the typical signal of PLGA at 2940 cm^{-1} within the cell cytoplasm, where the spectra of lipid bodies can be well detected. They concluded that although experiments with fluorescently labeled NPs hint the uptake of PLGA NPs, the latter remained attached to the cell membrane and did not enter the cytoplasm.

Instead of using CARS and looking at defined Raman bands within the cell, spontaneous Raman confocal microscopy was applied to imagine the NPs at different planes of the cell and at different spots in a plane. The advantage of spontaneous confocal Raman microscopy is that at each spot the whole spectrum is recorded. The disadvantage of this technique compared to CARS is that it takes much longer time.

In order to perform cellular internalization studies via Raman Spectroscopy, samples were prepared as follow. When cell confluence of HepG2 cells reached around 70 %, the culture was trypsinized and 100000 cells were seeded in a glass bottom Petri dish for Raman experiments. After 24 h, the cells were incubated with UV sterilized NPs at a concentration of 150 μg/mL of PLGA NPs for 12 h. Afterwards, the plate was rinsed with PBS several times and the cells were fixed with 3.7 % formaldehyde in PBS during 30 min and rinsed again. Micro-Raman analyses were performed using a Renishaw inVia Raman Microscope. Measurements were performed using the 532 nm laser excitation wavelength with a grating of 1800 mm^{-1}. Spectra were taken using a 40× water immersion objective. The size of the focal spot was approximately 1 μm. Raman spectra were recorded in the region 300-3600 cm^{-1} with a resolution of approximately 7 cm^{-1}. The system was calibrated to the spectral line of crystalline silicon at 520.7 cm^{-1}. At least 8-15 accumulation scans at different spots in the various cell compartments: lipid bodies (LB), cytoplasm and nucleus, were taken to reduce the spectral noise. Control spectra of the different cell compartments were taken in cells not exposed to NPs. All spectra were corrected taking into account the PBS solution and glass coverslip baseline.

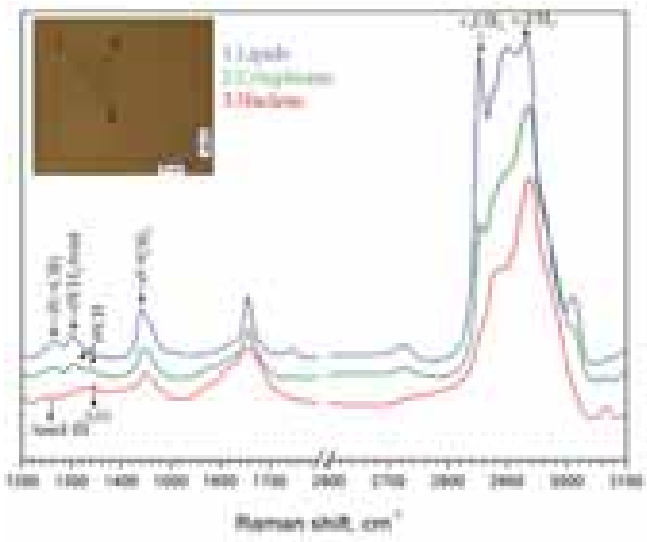

Figure 4.3. *Raman spectrum recorded at different positions within a cell from the HepG2 line (ν indicates stretching and δ deformation vibration modes; (l) denote vibrations of lipids and (p) of proteins). The inset corresponds to the image of the cell under study. The numbers together with the color indicates the location in the cell at which the Raman spectra were recorded.*

The nucleus, cytoplasm, and lipid bodies can be identified by the chemical signature of proteins, lipids and nucleotides provided by the Raman spectrum. HepG2 cells have characteristic multilamellar lipid inclusions within the cytoplasm that are called lipid bodies. In the high frequency region, the intensity ratio of the symmetric stretch bands of CH_2 (2850 cm^{-1}) to CH_3 (2935 cm^{-1}) is observed to be much higher in lipid bodies than in the cytoplasm. This can be explained by the higher density of CH_2 groups more abundant in the lipids from the lipid bodies, than in the cytoplasm. In the cytoplasm the signal corresponding to CH_3 increases as the amount of proteins, which present more CH_3 than CH_2 groups. The nucleus region, with high protein contain, reveals the smallest intensity ratio of CH_2 to CH_3 bands, and specific bands assigned as vibration of DNA bases of adenine (A) and guanine (G). *Figure 4.3* displays the changes in the Raman Spectra at different positions within the cell.

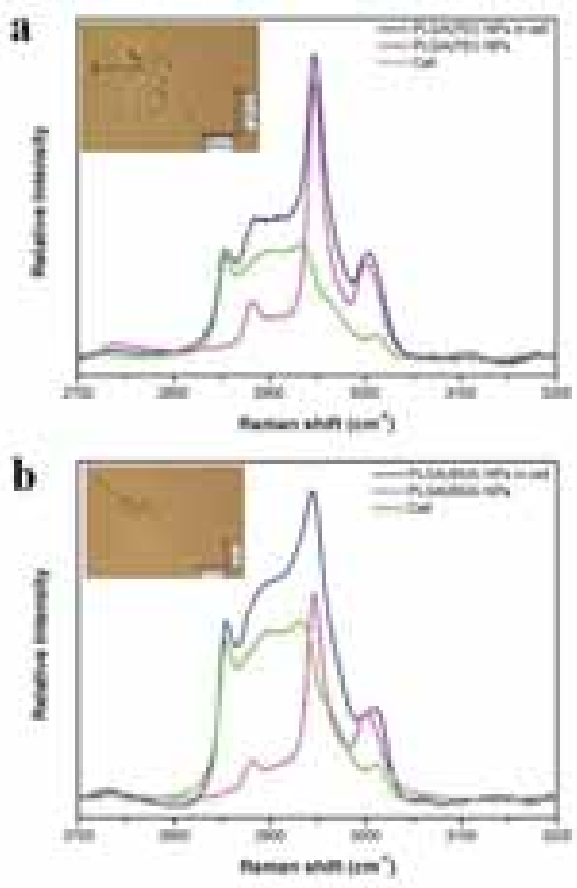

Figure 4.4. *Spot Raman spectra (blue) in cells exposed to PLGA NPs covered with PEI (a) and BSA (b). In both cases, pink and green lines denote the component spectra of PLGA NPs and of the cells, respectively. The insets correspond to the image of the cell under study.*

Then, cells incubated with PLGA NPs, which were either coated with PEI or BSA were studied with CRM. The blue curves in *Figure 4.4a*, corresponding to PEI stabilized PLGA NPs and in *Figure 4.4b*, corresponding to BSA stabilized PLGA NPs, display features from the region of the lipid bodies as it is deduced from the relation of the bands between 2850 and 2900 cm^{-1}, but they also show new bands in the methyl-methylene stretching region. These bands correspond to the characteristic CH_2 and CH_3 vibrations of PLGA NPs. For comparison, the spectra of the pure PLGA NPs and of the lipid bodies region have been included in *Figure 4.4a* and *4.4b* (pink and green lines

denote the spectra of PLGA NPs and the lipid body environment, respectively). It is clear that the dark blue curve displays the main bands of both the pure PLGA NPs and the lipid body region. From *Figure 4.4* it can be concluded that it is possible to prove the co-localization of the PGLA NPs and lipid bodies within the dimensions of the confocal spot.

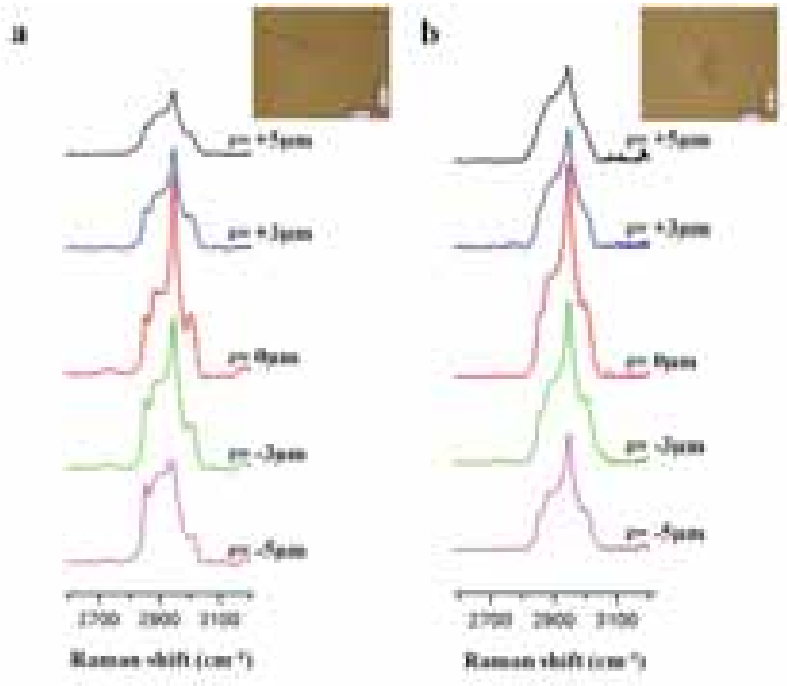

Figure 4.5. *Z scans of HepG2 cells treated with PLGA NPs covered with PEI (a) and with BSA (b). The height level z=0, refers to the plane where the intensity at 2950 cm^{-1} referring to the PLGA NPs is maximal. The transmission images in the inset correspond to the scanned cells, the arrow points out the position where the measurement has been performed in the cell.*

Figure 4.5 displays Raman spectra of two spots taken at different z positions in cells which were exposed to PLGA NPs stabilized with either PEI or BSA. While moving away from the zero plane, the relative intensity of the signals of PLGA to that of the lipid bodies diminishes as it is can observed for both the BSA and the PEI coated NPs.

For the PEI coated NPs, when moving downward, a region rich of lipid bodies is reached, where, however, NPs have not been detected as can be seen in *Figure 4.5a*. For the BSA stabilized PLGA the cytoplasm is reached 5 μm below the zero plane and again NPs were not detected. The z scanning provides an ambiguous proof of internalization of the NPs because the depth analysis is done in distances of micrometers inside the cell, where the detection of PLGA attached to the cell membrane from the outside is very unlikely.

The analysis of the Raman spectra revealed a co-localization of both PEI and BSA stabilized NPs with lipid bodies in the sense that the PLGA NPs were always found together with lipid bodies. However, the reverse conclusion cannot be drawn. Furthermore, a co-localization of the PLGA NPs and the nucleus region was never observed.

The reason, why BSA and PEI stabilized NPs were internalized, while the PVA stabilized NPs reported in *[260]* were not, is most likely related to the particular surface coating employed. It is known that polyelectrolytes carrying cationic amines like PEI can interact with lipid membranes crossing the membrane barrier. PEI for example, is a widely used vector for DNA delivery in cell culture *[303, 304]*. Most likely, the PEI molecules around the PLGA NPs form a spherical brush, with chains protruding out of the surface of the NPs *[96, 97]*. These chains will have some conformational freedom, which can facilitate their interaction with the plasma membrane. It is also well-known that the positive charge of the NPs will attract proteins of the media, mostly BSA but also others like the apolipoprotein E, which can bind to a specific receptor in liver cells and this could facilitate uptake *[233, 236]*. For BSA stabilized NPs protein adsorption has to be less. Their negative surface charge will diminish the binding to the generally negatively charged cell surface. Therefore, a priori a smaller interaction with the cell surface as compared with PEI can be expected. Nevertheless, it is possible to observe that the number of cells, which have incorporated NPs is higher for BSA modified NPs than for the PEI modified ones. It is difficult to give a proper explanation to this

observation at this point but it is probably related to a mechanism of uptake linked to a receptor *[303, 305]*.

In principle, the confocal raman microscope, allows for the recording of Raman spectra in all three dimensions with an accuracy limited by the resolution of the device. However, since the signal intensity is small, a multidimensional spectral mapping would require a rather long time. Therefore the spatial mapping was restricted to line scans. Raman spectra were recorded along lines crossing through cells, which had been exposed to PLGA NPs with a distance increment of 0.5 μm. The relative integral intensities of the PLGA NP contribution in the Raman spectrum across the cell after spectra decomposition was determined as described above in the NPs co-localization. The lipid CH_2 symmetrical stretching band at 2852 cm^{-1} was chosen as the reference band to obtain the lipid distribution across the scanned line. The integral intensities of $\nu_s(CH_2)$ was plotted as a function of the distance along the line. The lipid distribution across the cell reflects the presence of lipid bodies, cytoplasmic lipid inclusions and lipids in intracellular membranes. A well pronounced maximum in the lipid distribution would indicate the presence of lipid bodies at a particular location. The distributions of PLGA and lipids in a cell exposed to PEI stabilized PLGA NPs are shown in *Figure 4.6a*. The component intensities of PLGA and lipids were weighted to the maximum of intensity. The transmission image of the selected cell and the line along which the PLGA intensity distribution was mapped is displayed in *Figure 4.6b* as a rainbow color presentation. Red corresponds to the maximum and black to the minimum of the PLGA NPs signal.

The analysis of the Raman spectra of representative cells reveals two maxima along the selected line scan (*Figure 4.6*). This means that there are two regions within the particular cell, where PEI stabilized PLGA NPs have been accumulated. The uptake of PLGA NPs with different distribution inside the cell was also observed for other cells. It was therefore confirmed that, PEI stabilized PLGA NPs are being readily taken up by HepG2 cells.

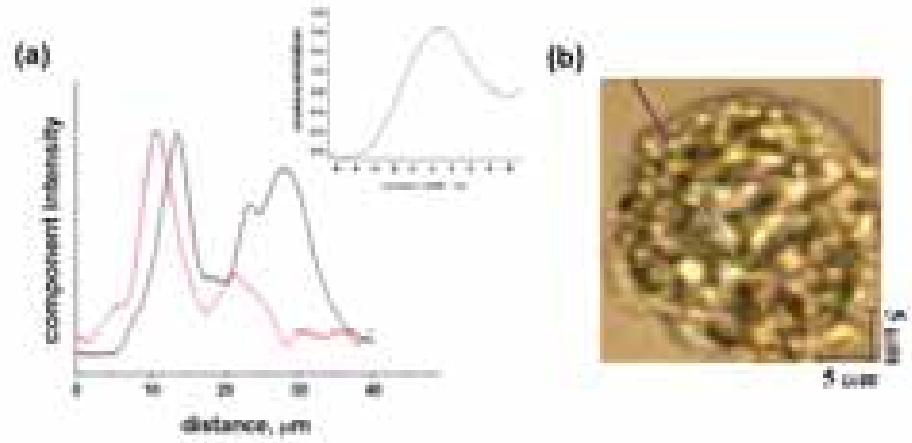

Figure 4.6. *(a) PLGA (black line) and lipid (red line) distributions across a cell exposed to PEI stabilized PLGA NPs. The figure insert represent the spatial cross-correlation function between the two component distributions. (b) Transmission image of the cell. The line reflects the PLGA intensity distribution in rainbow presentation. The red colour corresponds to the maximum intensity of the bands corresponding to the NPs.*

A remarkable issue to mention is that the major PLGA NPs fraction at the distance of about 12 µm almost coincides with the maximum of the lipid bodies apart from a small spatial shift (*Figure 4.6a*), which suggest the tendency of the PEI stabilized PLGA NPs to follow the distribution of the lipid components. This tendency for co-localization can be quantified by a spatial cross-correlation analysis. The Pearson product-moment correlation coefficient ($\rho_{X,\,Y}$) can been used to measure the correlation between two variables *X* and *Y,* giving a value between +1 and −1. It is a measure of the strength of the linear dependence between X and Y. The value 1 refers to 100 % linear dependence, and the 0 value is found when the two variables are independent. The Pearson product-moment correlation coefficient can be calculated by:

$$\rho_{X,Y} = \frac{\operatorname{cov}(X,Y)}{\sigma_X \sigma_Y} \qquad (Eq.\ 4.1)$$

where cov(X,Y) is the covariance of the two variables, and σ_X σ_Y is the product of their standard deviations. The two variables in the line Raman mapping are the distance dependent component intensities of PLGA NPs and lipids. $\rho_{X,Y}$ is calculated as a function of a spatial shift, Δ. The spatial cross-correlation function is then defined as $\rho_{X,Y}(\Delta)=cov(X(r),Y(r\pm\Delta))/(\sigma_X\rho_Y)$, and it is presented in the inset of *Figure 5.6a*. $\rho_{X,Y}(\Delta)$ has a maximum value at Δ^{max}=2.7 μm with a correlation coefficient of 0.65, which demonstrates a correlation between the lipid and the PLGA NPs distribution. A simple geometric interpretation of the spatial shift, Δ^{max}, would be the distance between the centre of the lipids distribution maximum (radius about 0.5-1 μm) and the centre of PLGA NPs accumulation This simple view is only meaningful if there is not more than one pronounced spot where both kinds of particles co-associate. If there are many centres of association Δ^{max} should assume a value close to zero since association on either site should be equally probable. Similar results were obtained for the line mapping analysis of cells treated with BSA stabilized PLGA NPs.

4.1.3. Cell viability

HepG2 cell viability was studied with the MTT assay. First, around 5000 HepG2 cells were planted into each well of 96-well plates, and after 24 h, PLGA NPs covered with PEI or BSA were added into culture media at different concentrations (0, 20, 50, 100, 200 μg/mL). After 3 days of co-incubation, 20 mL of MTT solution (5 mg/mL in 10 mM PBS) was added into each well of the plates and incubated for 3 h. The absorbance was measured by means of a plate reader at 550 nm.

In *Figure 4.7* is shown the HepG2 cell viability results of PLGA NPs stabilized with PEI and BSA after 3 days of co-incubation. For both, PEI and BSA stabilized PLGA NPs, the cell viability decreased with higher NPs concentrations. At the highest concentration of NPs (100 μg/mL), cell viability was around a 50 % for PEI stabilized PLGA NPs and almost 60 % for BSA stabilized PLGA NPs, indicating that PEI stabilized PLGA NPs produce a higher cytotoxic effect than BSA stabilized PLGA NPs.

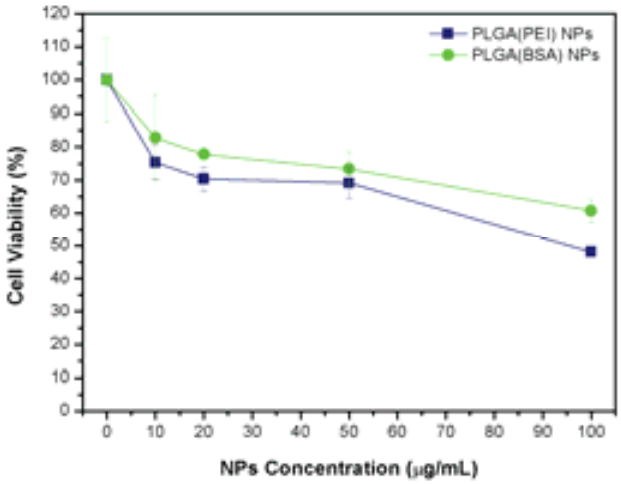

Figure 4.7. *Viability of HepG2 cells incubated with PLGA NPs covered with PEI and BSA after 3 days of co-incubation.*

Cell toxicity is a critical aspect regarding the use of NPs in drug delivery. Therefore, cell viability experiments have been extended to several lines, applying other different tests than MTT *[306]*. Four different human tumor cell lines were used for the cell viability study: Lymphoblastoid B (Hmy2), acute T lymphoblastic leukemia (Jurkat), myeloid-monocytic lymphoma (U937), and prostate adenocarcinoma (PC3). Quick cell proliferation testing solution was used to evaluate the cell viability and proliferation. All cell lines were maintained in RPMI medium supplemented with 10 % heat inactivated FBS, penicillin (100 U/mL), streptomycin (100 μg/mL), and glutamine (2 mM) at 37 °C in a humidified atmosphere containing 5 % CO_2. When culture confluence was around 70 %, cells were seeded in 96-well plates in different amounts, depending on their proliferation rate as follows: PC3, 25000 cells/well; Jurkat, 10000 cells/ well; Hmy, 10000 cells/well; and U937, 20000 cells/well. After 24 h, NPs were added until a final concentration of 50 μg/mL was obtained, with the exception of the control, and incubated for 24 and 48 h. Then, the cell suspension from the plate was centrifuged 1 min at 1000 g and 100 μL of supernatant was removed. A total of 50 μL of Quick Cell Counting Solution was added to each well and incubated for 3 h. The reaction product was estimated by measuring its absorbance at 425 nm in a microplate reader.

Results are shown as percent of viability (V%) according to the following formula:

$$V\% = \frac{absorbance(cell + medium + NPs) - absorbance(medium + NPs)}{absorbance(cell + medium)} x100 \quad (Eq.\ 4.2)$$

The cell viability for NPs stabilized with PEI and BSA for four different cell lines are compared in *Figure 4.8*. Cell viability was measured after 1 day of exposure to the NPs (*Figure 4.8a*), and after 2 days of exposure (*Figure 4.8b*). It is interesting to notice how the viability changes for the different cell types. For example, the cell viability of the Hmy line was not affected by the NPs while the cell viability of PC3 was around 90 % for BSA stabilized NPs (*Figure 4.8a*). Also, it can be seen that for PEI stabilized NPs the viability of the Jurkat line is close to 80 %, while in Hmy is less than 40 %. For each cell line the viability in presence of NPs stabilized with PEI is always lower than for NPs stabilized with BSA. For the Hmy and U937 lines this difference is most pronounced. After a day of exposure to NPs it is observed viabilities of less than 40 % for PEI coated NPs and over 100 % for BSA coated NPs.

The smallest difference in viability within a cell line is observed for the PC3 line, where the viability for the PEI stabilized NPs is close to 90 % and the viability of the BSA stabilized NPs is close to 100 %. Cell viability behavior after two days of exposure of the cells to NPs differed in some cases from what is observed after a day of exposure, but no particular correlation can be established between one and two days exposure of the cells to NPs. To resume cell viability of PEI stabilized PLGA NPs was always lower than that of BSA stabilized PLGA NPs for all cell lines, which means that the cytotoxicity of these NPs was higher than the toxicity of the NPs stabilized with BSA. PEI molecules are cytotoxic even condensed with DNA *[306, 307]*, therefore, it is understandable that the PEI coating on the surface of PLGA presents certain toxicity within the cell lines tested. On the other hand, albumin, as the most abundant protein in serum, has excellent cytocompatibility for most of cell types. This would explain that when the NPs stabilized with BSA were added into the cell culture medium, almost no cytotoxicity could be found. BSA coated NPs seem to have a positive effect on cellular viability, which reaches values over the 100 % for several cell lines. From their

moderate to low toxicity, the PLGA NPs fabricated, especially those stabilized with BSA, are excellent candidates for intracellular drug delivery, as has been proved by CRM that can be internalized within cells.

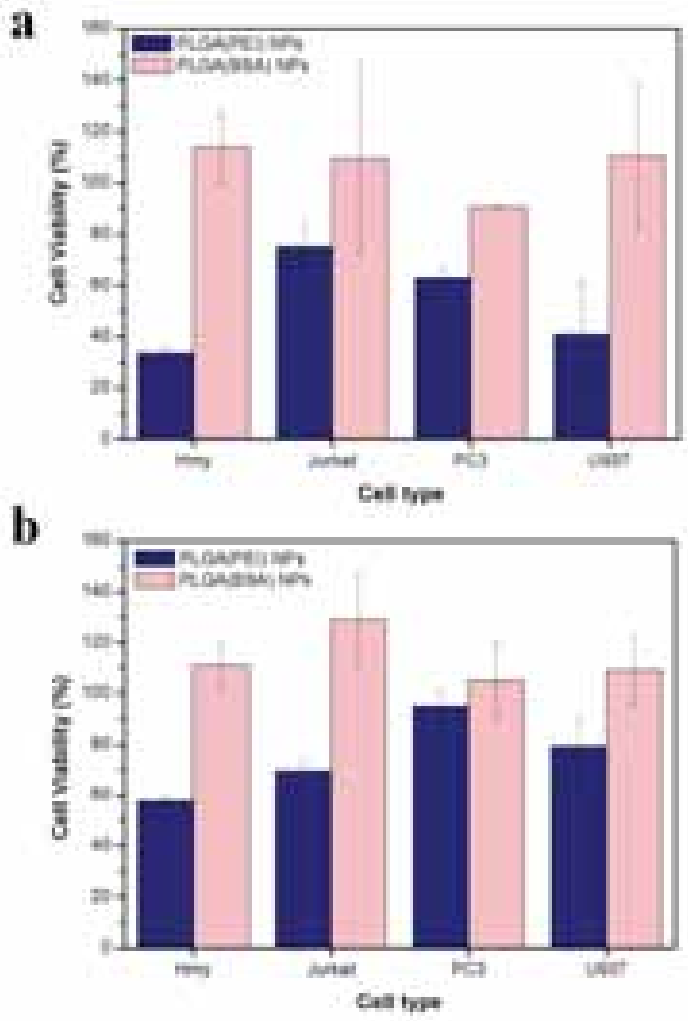

Figure 4.8. *Viability of different cell lines incubated with PLGA NPs prepared by PEI or BSA as stabilizers after (a) 1 day and (b) 2 days of co-incubation.*

4.2. Uptake, intracellular distribution and *"in vitro"* toxicity of Carbon Nanotubes

In Chapter 3, it has been shown the stepwise surface tailoring of CNTs with polyelectrolyte brushes and lipid layers. Lipid coated CNTs could be an attempt alternative to reduce CNTs toxicity for their possible biomedical applications. CNTs with a soft interface based on a polyelectrolyte cushion and a lipid bilayer may affect their distribution within cells and their cytotoxicity.

In this section, the interaction of CNTs with cells will be studied. Understanding how the interaction of CNTs with biological matter can be tuned by their surface modification it is very important issue to be studied. Most of the present applications of CNTs are as composite materials, where the CNTs are imbedded in matrixes and could be in contact with cells. Therefore, it is quite important regarding commercial applications of CNTs to know how a biocompatible coating, in this case a lipid layer, may affect their toxicity.

4.2.1. Cellular uptake and intracellular distribution of surface modified CNTs by means of CRM and TEM

CRM can be applied for uptake studies of any kind of NPs or nanomaterials provided that have a Raman Spectra. We have extended the work with PLGA NPs to the CNTs bearing different surface functionalization presented in Chapter 3.

In order to study cellular uptake and intracellular distribution of surface modified CNTs by means of CRM, samples were prepared following the same procedure described in section 4.1.2 for PLGA NPs. In *Figure 4.9a*, it is possible to observe the Raman spectra recorded in a HepG2 cell, which has been cultured in the presence of oxidized CNTs. For comparison the Raman Spectra of the pure CNTs is also provided in the figure.

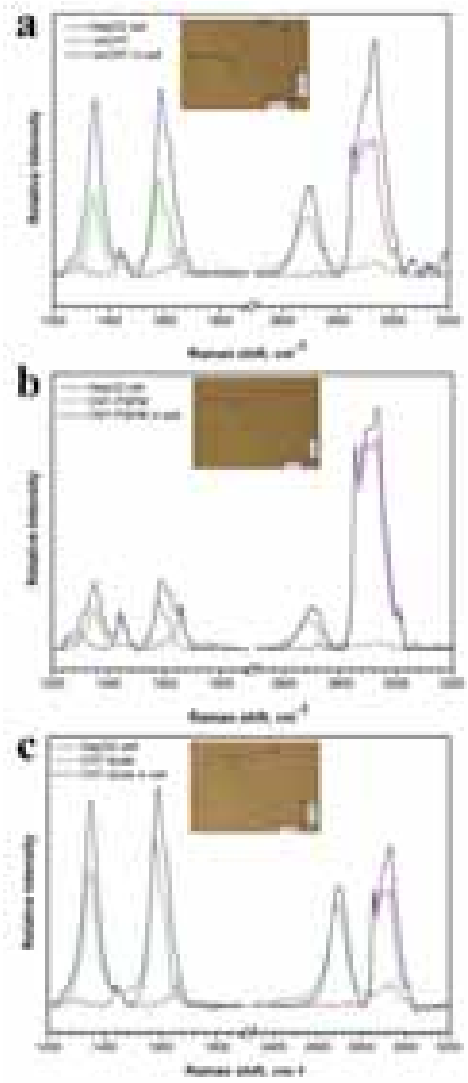

Figure 4.9. *Raman spectra of oxidized CNTs (a), PSPM coated CNTs (b) and lipid coated CNTs (c). The blue lines correspond to the spectra of CNTs exposed to cells, the green lines represent the Raman Spectra of the different surface modified CNTs and the pink line corresponds to the control cells in the region of the lipid bodies. The insets are the optical images of the scanned cell in the scanned position.*

When looking at the spectra within the cell, two prominent bands of CNTs were observed in the exposed cells at 1350 cm^{-1} (D-band) and 1585 cm^{-1} (G-band). The D-band is an indicator for disorder in the graphene sheet and is called ‘‘disorder-included’’ band. The G-band is a tangential mode originating from tangential oscillations of the

carbon atoms in the CNTs *[308-310]*. These clearly defined bands allow for the decomposition of the total spectrum into the CNT signal and the spectrum of the cell. The latter represents the chemical signature of the cell in the presence of CNTs. The characteristic peaks of this spectrum are very similar to those of the spectra taken in the lipid rich region of cells as shown in *Figure 4.3*. Clearly pronounced symmetric bands can be observed in the CH_2 stretching region. From the comparison of these spectra follows that lipid bodies and CNTs are both present in the 1 μm in diameter confocal spot of the laser beam. Therefore, the spectra do not only provide information on the presence of the CNTs but also on the intracellular environment in the vicinity of the CNTs like for PLGA NPs. Oxidized CNTs were always found in close vicinity to lipid bodies or in the cytoplasm.

Figure 4.9b shows the Raman spectra for HepG2 cells co-cultured with PSPM coated CNTs. The spectral decomposition clearly demonstrated that PSPM coated CNTs were taken up by HepG2 cells and, as same as oxidized CNTs, CNTs-PSPM are located in the lipid rich region of the cell. Moreover, the Raman spectra recorded for lipid coated CNTs co-incubated with HepG2 cells, and their subsequent spectral decomposition (*Figure 4.9c*), also revels the cell internalization of CNTs-lipids in the close vicinity of the lipid bodies of the cell. The coating with polyelectrolytes and then with lipids had no effect on the position of the characteristic bands of the CNTs but affected their relative intensities.

In order to confirm cellular internalization of CNTs, Raman spectra were measured at different planes in cells exposed to CNTs as shown in *Figure 4.10*. The intracellular plane where the signals of the D and G bands from the CNTs were the strongest was denoted by zero. Then, spectra were recorded at higher and lower planes. As it can be seen the relation between the signal of the CNTs and those coming from the cell changed progressively, showing an inhomogeneous distribution of the CNTs in the cells. The Raman z-scanning proved that all the surface modified CNTs were internalized into the cell and preferentially found in the lipid rich region of the cells.

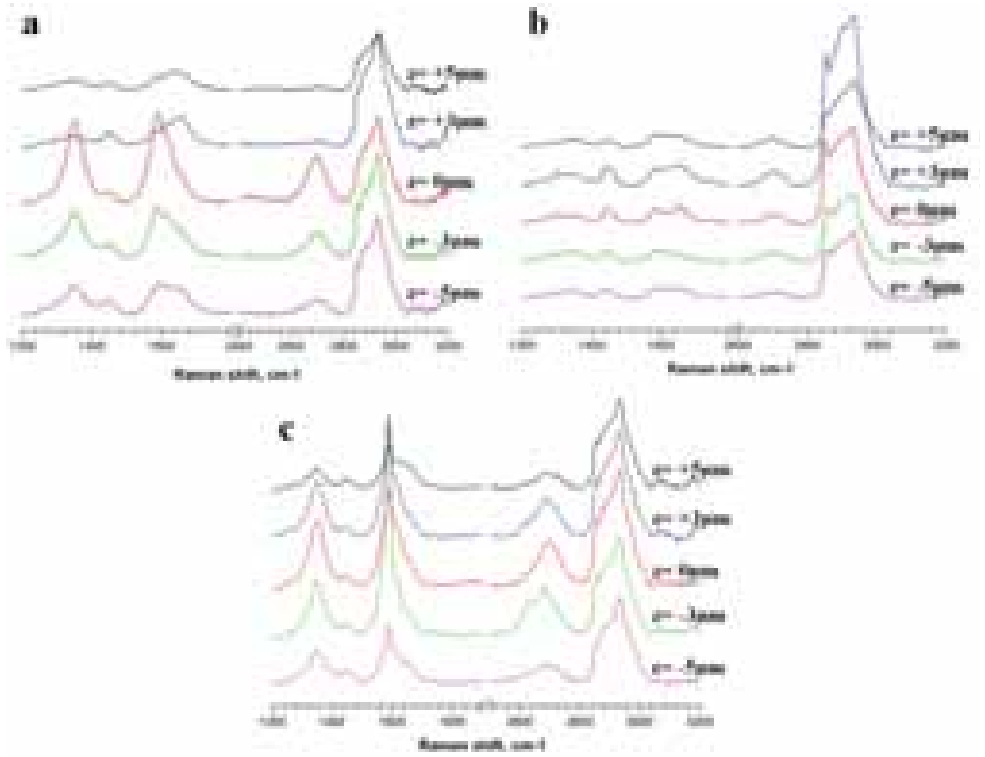

Figure 4.10. *Raman spectra taken at different planes in HepG2 cells incubated with: oxidized CNTs (a), PSPM coated CNTs (b) and lipid coated CNTs (c).*

Nevertheless, PSPM coated CNTs were also observed in the region close to the nucleus of the cell. The fingerprints from the cell in *Figure 4.11a* show that the CNTs are located in a region with a very small intensity of the CH_2 band to the CH_3 band, which is characteristic of the nucleus. From all the CNTs coatings studied, CNTs-PSPM was the only kind of nanotubes found in the close vicinity of the nucleus. The z-scan spectra of the PSPM coated CNTs co-localizated in the cell nucleus are shown in *Figure 4.11b*.

To have an independent probe of the internalization of the CNTs in the cell, TEM imaging of the cells after exposition to the CNTs were performed in the same conditions as for Raman microscopy.

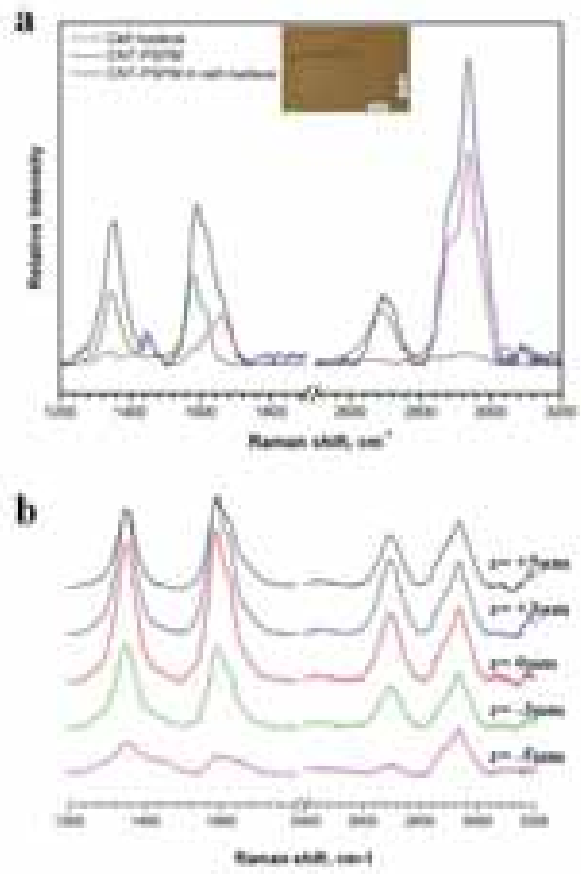

Figure 4.11. *(a) Spectra of PSPM coated CNTs (green), control cells in the cell nucleus (pink) and cells exposed to CNTs-PSPM co-localized in the nucleus of the cell (blue). (b) Raman spectra taken in nucleus at different planes in HepG2 cells incubated with CNTs-PSPM. The inset corresponds to the optical image of the scanned cell.*

A total of $2.5x10^6$ cells were seeded into a 100 mm diameter cell culture Petri dish. The different modified CNTs were added into the culture medium 24 hours later. The final concentration of CNTs was adjusted to 50 µg/mL. After 24 hours of co-culture, cell were trypsinized, washed with PBS, fixed in solution with 3.7 % formaldehyde and resuspended in PBS. For the TEM visualization the sample was previously washed with PBS and fixed with 1 % of osmium tetroxide. Then, the sample was infiltrated in acetone at different concentrations (from 50 to 100%) at different times, followed by an inclusion process in EPO resin. And finally, the resin blocks were cut by an

ultramicrotome into ultrafine cuts of 70 nm. Each cut was placed on a copper grid and contrasted by Reynolds technique for proper visualization.

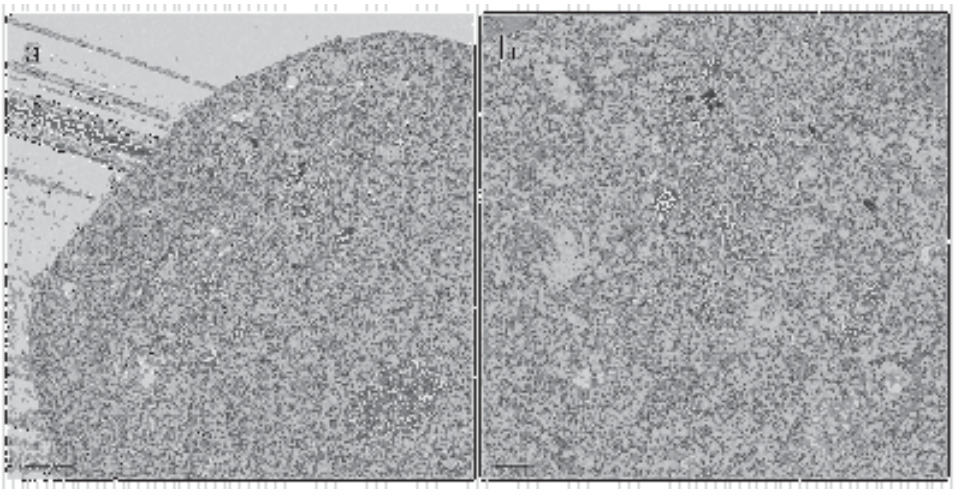

Figure 4.12. *(a) TEM micrographs of HepG2 cells treated with oxidized CNTs; (b) the corresponding magnified micrograph of the region of CNTs in cell.*

In *Figure 4.12* can be observed the cells which had been exposed to oxidized CNTs. In the images the CNTs can be recognized inside vacuoles from their cylindrical shape showing lengths of approximately 500 nm. A closer inspection to the cell in *Figure 4.12b* proves that the CNTs are inside a vacuole in the cytoplasm, and shows clearly the CNTs tendency to associate into bundles. This particular vacuole presents a high concentration of CNTs. No CNTs could be detected in the nucleus. Although the use of TEM gives a visual proof of the presence of the CNTs in the cells, which is absent in Raman, confocal Raman has the enormous advantage for uptake studies of not being invasive and that the cells can be imagined being still alive. In this way any artifact that could come from the sample preparation is avoided. Besides that, Raman allows for fast detection and to recognize the environment of the CNT in the cell.

TEM images in *Figure 4.13* show the presence of PSPM CNTs in a HepG2 cell. The amount of CNTs present seems to be less than that for the oxidized CNTs. *Figure 4.13b*

and *4.13*c are magnifications of *Figure 4.13a* in the region where the CNTs are observed. Although the amount of the CNTs is smaller than the oxidized it can be clearly seen that they tend to associate and also their characteristic shape tubular and curved can be recognized. In the magnified images it is clear that the CNTs are in the cytoplasm. The presence of CNTs in the nucleus could not be observed in these images.

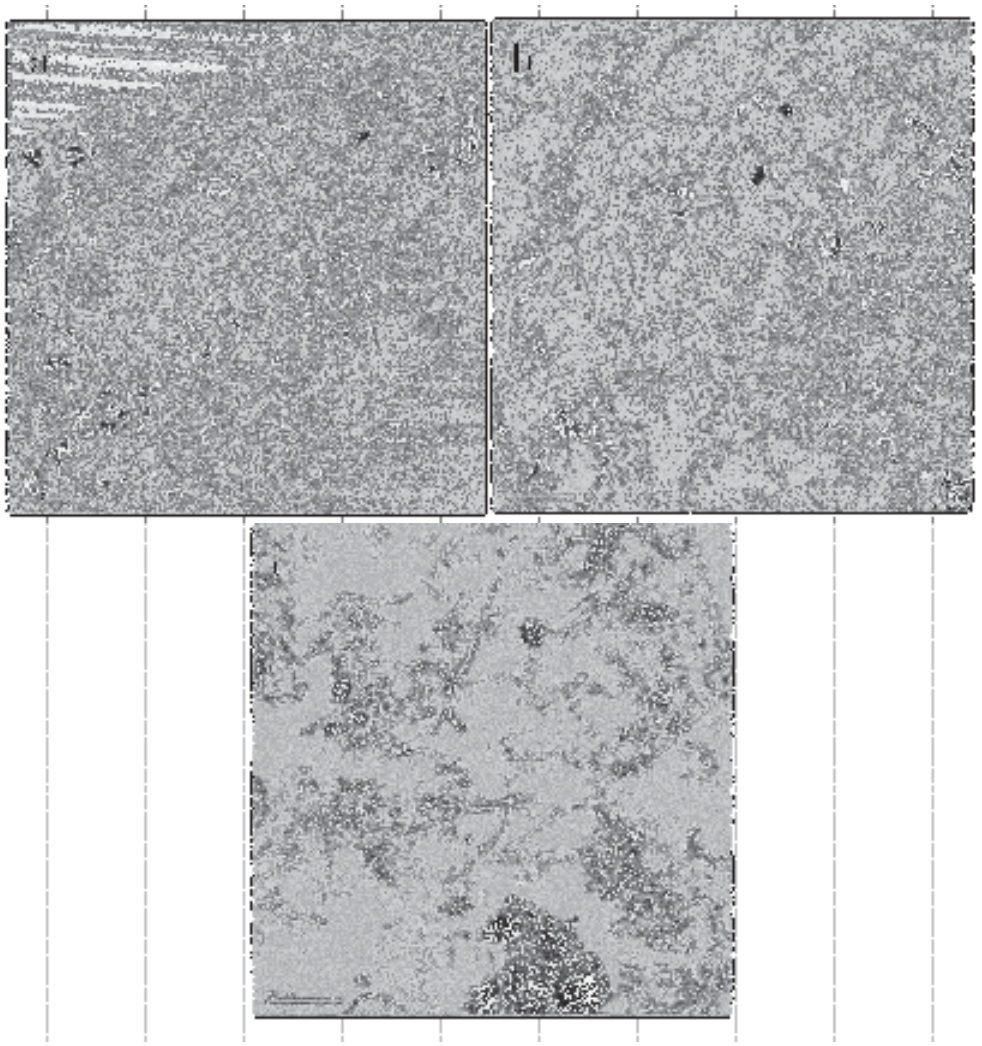

Figure 4.13. *TEM micrographs of HepG2 cells treated with PSPM coated CNTs. Magnified micrographs (b) and (c) correspond to the cell showed in (a).*

For the lipid coated CNTs, TEM images also corroborate the uptake by the HepG2 cells. From all the samples studied this is the one with the highest uptake observed. In *Figure 4.14a* it is appreciated the TEM image of a cell exposed to lipid coated CNTs.

The lipid coated CNTs accumulate inside the cytoplasm forming a dense arrangement with a size in the μm range. The aggregate shown in *Figure 4.14b* is more than 10 μm long and 2 μm wide. The aggregate does not seem to be inside vacuoles; at least these cannot be clearly detected with TEM.

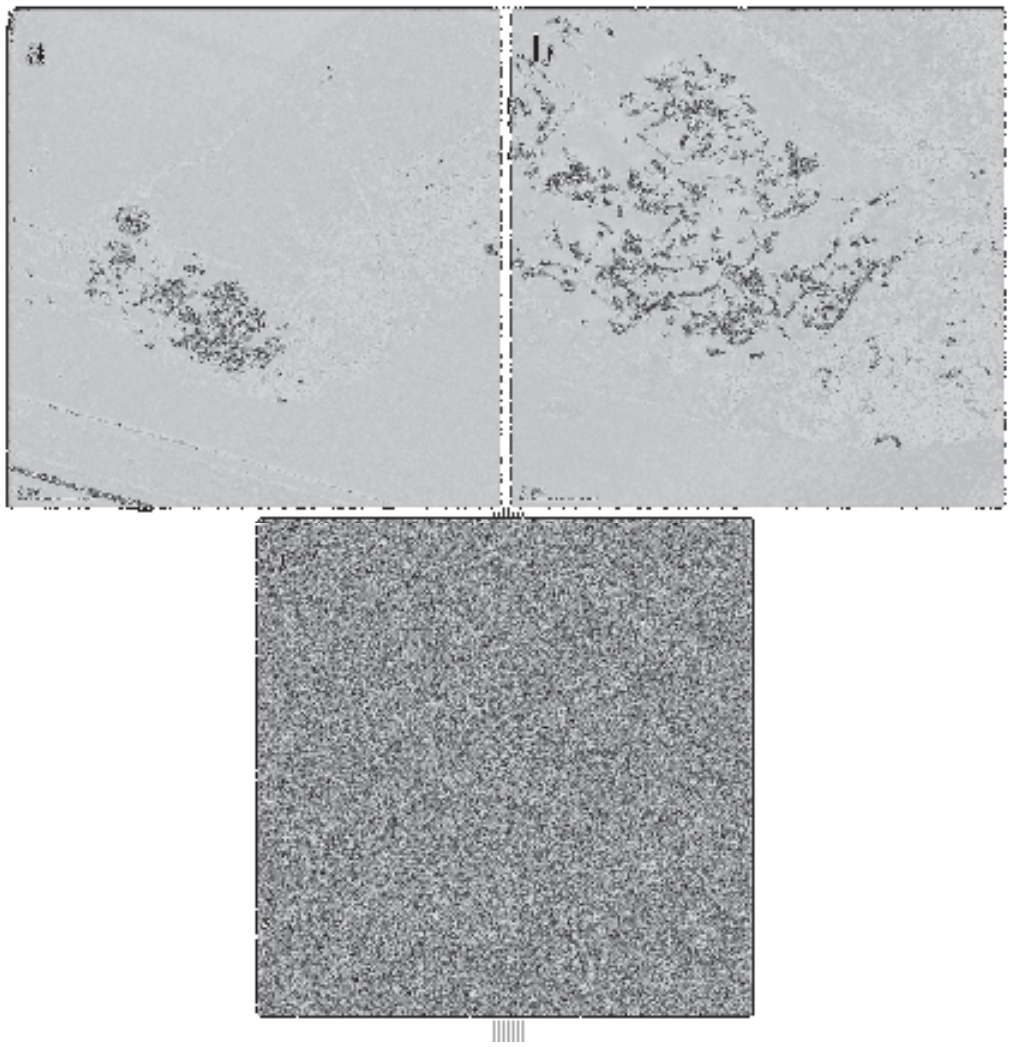

Figure 4.14. *TEM micrographs of HepG2 cells treated with lipid coated CNTs. Magnified micrographs (b) and (c) correspond to the cell showed in (a).*

The z scan done with CRM (*Figure 4.10c*) confirms the internalization of the CNTs-lipids and from the strong 2850 cm^{-1} band (CH_2), compared to the 2935 cm^{-1} band (CH_3), would indicate that the CNTs are in a region of lipid bodies. In TEM the lipid bodies cannot be recognized but it could be that they are associated to the CNTs. Also,

the signals from the lipids coating the CNTs in such a dense arrangement could contribute to the band at 2850 cm^{-1}. In *Figure 4.14c* a higher magnification of the aggregates is provided where it can be observed that they are associated forming sort of networks. The formation of these structures with CNTs in the cell and if they are due to a previous aggregation of the CNTs in the cell culture media need of deeper understanding.

As it was showed above for PLGA NPs, Raman spectra were recorded along lines crossing through cells, which had been exposed to CNTs with a distance increment of 0.5 μm. In this case, the relative integral intensities of the CNTs contribution in the Raman spectrum across the cell after spectra decomposition was determined with the D-band and G-band signals coming from CNTs. In *Figure 4.15* the distributions and cross-correlation functions in the cases of CNTs-PSPM and lipid coated CNTs are represented. The observed behaviour is strikingly different. In the case of CNTs-PSPM a spatial correlation between the localization of lipid bodies and the nanomaterials is not observed as revealed by a correlation coefficient of about zero at $\Delta = 0$. The increase of correlation at $\Delta = -7$ μm to 0.6 can be interpreted as a tendency of the PSPM coated CNTs to avoid the site where the lipid bodies are preferentially located. This follows from the lipid body intensity distributions (*Figure 4.15a*), which has a maximum, where the CNT signal has its minimum. The opposite behaviour is found in the case of the lipid coated CNTs, *Figure 4.15b*. A well pronounced maximum of the cross correlation coefficient of about 0.7 at $\Delta^{max} = 0.4$ μm was found. This value reveals a relatively strong correlation of the distribution of the CNTs with that of the lipid bodies and cellular lipids. Line Raman mappings analysis shows that lipid coated CNTs tend to localize, within cells, in close proximity of accumulations of lipid bodies. This tendency can be due to either a lipid associated mechanism of uptake, or to a retrospective arrangement of the CNTs with the lipid rich compartments in HepG2 cells. Nonetheless, the Raman line scanning strongly suggests that the nature of the CNTs surface is important concerning their possible effects on cells.

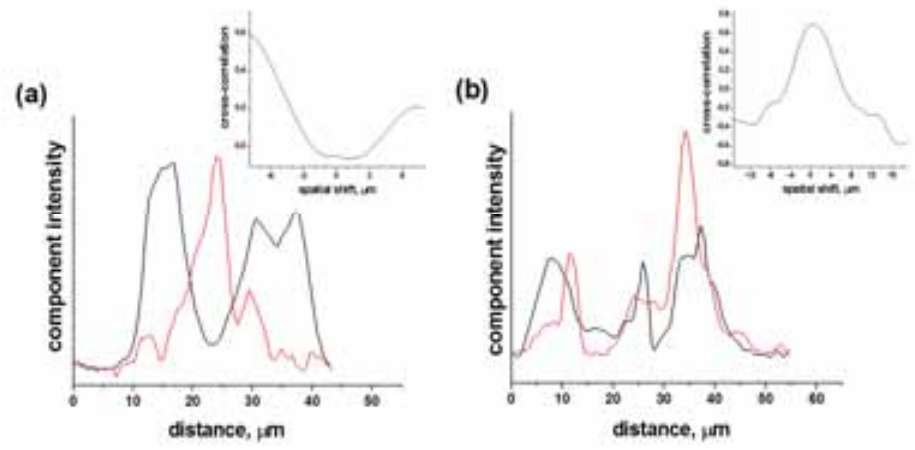

Figure 4.15*. (a) CNT-PSPM and (b) CNT-lipids (black lines) and lipid bodies of the cell (red lines) distributions across CNTs treated cells. The figure inserts represent the spatial cross-correlation function between the two component distributions.*

4.2.2. *"In vitro"* toxicity of surface modified CNTs

A key aspect regarding the interaction of CNTs with cells is their toxicological effect. To have an independent proof of the toxicity of the modified CNTs, MTT assays for the different surface coatings employed have been performed. HepG2 cells were exposed to oxidized CNTs, CNTs-PSPM and lipid coated CNTs with concentrations varying between 10 and 100 μg/mL. Cell proliferation was measured at the end of the first day after exposure to the CNTs, and at the end of the second, third and fourth day. The MTT assay was carried out following the same procedure described above in section 4.1.3 for PLGA NPs.

From proliferation data, shown in *Figure 4.16*, it follows that toxicity of oxidized and polyelectrolyte coated CNTs are always higher than that of the lipid coated CNTs. Indeed, oxidized CNTs cause a reduction in proliferation of around a 50 % after the first day, and to around a 35 % after the fourth day of incubation. A similar value for the proliferation as in the presence of oxidized CNTs is observed for PSPM coated CNTs after the first day but proliferation decreases significantly to less than 30 % the second day and to less than 10 % the fourth day of exposition. The CNTs coated with lipids

only induce a reduction in proliferation to values between 80 and 90%. Proliferation does not change pronouncedly in the following days; after the fourth day cell proliferation reaches a value of 70 %; this value is significantly higher than that for any of the other surface functionalization after a first day of exposure to the CNTs.

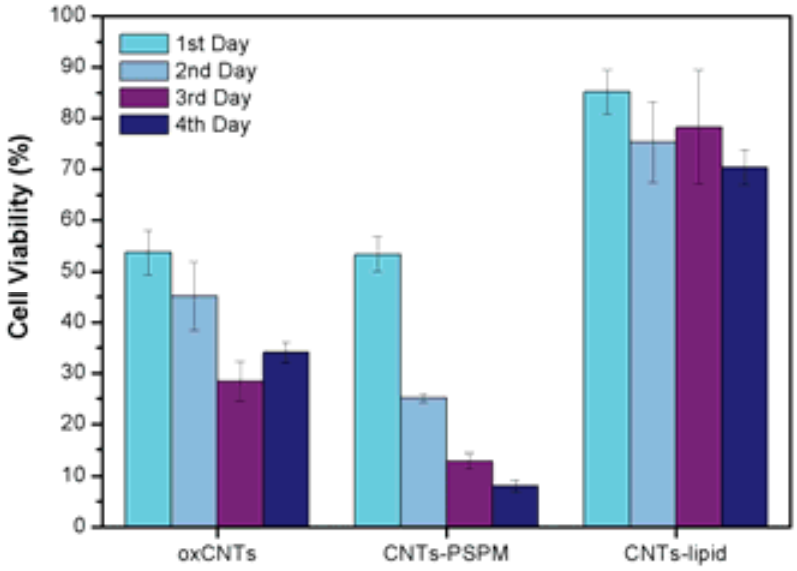

Figure 4.16. *Proliferation of HepG2 cells incubated with CNTs at a concentration of 100 µg/mL after 1, 2, 3 and 4 days of exposure.*

The toxicity of sulfate group is well known *[309, 311]*. This might be an additional factor to explain the dramatic decrease in the proliferation rate in the presence of PSPM coated CNTs. From these data follows that concerning practical applications both, the toxic impact of the CNTs *[312]* itself, as well as the effect of the coating which is often required to ensure colloidal stability of CNTs in aqueous solutions, have to be considered. Indeed, the protecting effect of the lipid layer is such that it reduces the toxicity of the CNTs, preventing the action of the CNT walls and polyelectrolyte molecules in the time frame of the *''in vitro''* experiments.

4.2.2.1 *"In vitro"* Raman studies of surface modified CNTs impact on cell functions

CRM was also applied to study how the present of the CNTs impact on the cell machinery looking at the evolution of the signals of DNA and proteins (Amide III band) in the cell nucleus after the presence of the CNTs. The ratio of the adenine and guanine bands to the protein bands in the nucleus can indeed be used as a measure of toxicity *[313-315]*. Raman spectra in the cell nucleus were recorded for control HepG2 cells and for cell exposed to the different surface modified CNTs. CNTs spectra were subtracted from the total spectrum to avoid the overlapping of Raman signals in the amid III and nucleic acid region. Differences in the Raman spectra in the nucleus region were found between control cells and cells exposed to CNTs. The corresponding spectral region was deconvoluted into five components (inset *Figure 4.17*). From the deconvoluted signal it was possible to calculate the integral peak ratio between the peak related to A, G (1338 cm^{-1}) and the peaks of the protein amid III bands, consisting of random coil, β-sheet and α-helical contributions (1200-1290 cm^{-1}).

Figure 4.17a demonstrates that the relative intensity of the Raman peak at 1338 cm^{-1}, associated with the nucleotide signal, to that of the amid III peak decreased in cells treated with modified CNTs. The ratio of the bands of DNA to proteins diminishes in cells exposed to the oxidized and PSPM coated CNTs to approximately a 30 and 50 % respectively of its value for control cells non-exposed to CNTs. The ratio for the cells exposed to lipid coated CNTs increases again to the values of the control cells. The calculated DNA/protein ratio can be taken as a measure for the damage in cell nucleus induced by the toxic effect of the respective CNTs. Like for the cytotoxic assay, the coating of the CNTs with lipids seems to have a protective effect. Indeed, biomimetic lipid layers *[185, 316]* on nanomaterials designed for delivery might be a good strategy to reduce toxic side effects. The peak ratios, calculated for the surface modified CNTs, are summarized and compared with the control in *Figure 4.17b*.

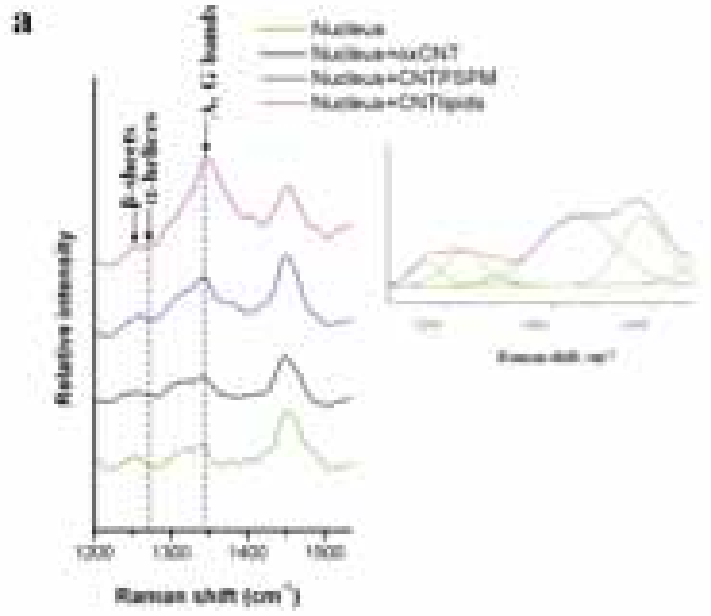

Figure 4.17. *(a) Average Raman spectra from the nucleus of HepG2 cells treated with surface modified CNTs compared with the spectrum of the nucleus of untreated cells. The inset graph shows the peak fitting analysis of a Raman spectrum from the untreated cell nucleus. (b) Summary of the integral intensity ratios between A, G nucleobases and amide III protein bands.*

Different cellular process can change the DNA/protein ratio in response to cytotoxic effects of CNT; first of all cytotoxicity often results in cell cycle delay, decreasing the quantity of cells with duplicated genome (4 N) in phases S- or G- in the cell cycle. Just taken into account the quiescent cells or G1-cells with (2 N) non-duplicated genome the reduced DNA/protein ratio could be consequence of partial loss of DNA due to the activation of endogenous nucleases and diffusion of low-molecular weight DNA outside

the nucleus in apoptotic cells *[317]*. In response to DNA damage, over expression of DNA associated proteins like histones or heat shock proteins *[318]* will also result in reduction of the ratio of DNA to protein bands through the increase of the proteins proportion in the nucleus when earlier apoptosis.

Chapter 5

Poly(lactide-*co*-glycolide) Nanoparticles as potential carriers for the "*in vitro*" release of antiTNF-α and doxorubicin

5.1. Poly(lactide-*co*-glycolide) nanoparticles Layer by Layer engineered for the sustainable delivery of antiTNF-α

In recent years, biomedical research has highly focused in the development of effective and specific therapeutic agents. Among the novel therapeutic agents, the current sales volume of therapeutic monoclonal antibodies is the largest, underlining their great importance for curing complex diseases, such as autoimmune diseases and cancer *[315, 319]*. Adalimumab, also known as Humira or anti tumour necrosis factor alpha (antiTNF-α), has been one of the first monoclonal antibodies in the market. This antibody binds to the tumour necrosis factor alpha (TNF-α), thereby down regulating inflammatory reactions in autoimmune diseases *[320]*. Meanwhile, there are more than hundred different antibodies or antibody fragments undergoing trials or even on the market. The administration of therapeutic antibodies is generally done by means of injection or infusion, since oral administration is not possible. The drawbacks of this systemic administration route are that they include non-specific off-target binding resulting in adverse effects, caused by the required high doses of the antibodies. Any reduction in the doses by controlling the release on the targeted site would decrease adverse effects and also the costs of these comparatively high priced medications. Local delivery systems with prolonged controlled release are thus highly desirable. In addition, it is necessary to find ways of protecting the antibodies from proteolytic enzymes active at inflammation sites.

Although the encapsulation of an antibody into PLGA NPs is possible, its release would depend on the degradation of the NP, which is a slow process of several days or even weeks. Therefore, one could think as alternative to carry the antibody on the surface of the NPs. This could be done covalent binding or self assembly. Antibodies can be assembled on top of PLGA on the basis of the LbL technique *[167, 168]*. Both, synthetic and natural polyelectrolyte molecules can be used for LbL assembly. The loaded material will be released from the PEM, or the PEMs will be eventually peeled off liberating the entrapped material *[60]*. In addition, an important advantage of the LbL protocol is that the doses, the amount of encapsulated material, can be controlled by the number of layers assembled.

Here it is shown the use of PEMs for the encapsulation of an antibody. A strategy based on the antibody complexation with natural polyelectrolytes and LbL assembly will be developed for the loading of PLGA NPs with antiTNF-α. A complex will be formed in solution with antiTNF-α and an excess of the biopolyelectrolyte alginate (Alg). The complex will be assembled in a PEM carrying antiTNF-α. It will be shown that in this way the resulting PEM will be stable and only degrade in PBS progressively. The strategy developed here can be extended to other antibodies and can be applied for the development of carriers for sustainable delivery with multiple possible market applications.

5.1.1. Characterization of the LbL assembling and antiTNF-α encapsulation process

To confirm and monitor the LbL assembly, this was first conducted on a silicon oxide coated quartz crystal in a QCM-D chamber. The antibody antiTNF-α is positively charged and it could be assembled as polycation together with a negative charged polyelectrolyte. Initial experiments were performed with different combinations of natural polyelectrolytes. Several polyelectrolyte combinations of antiTNF-α and biodegradable polyelectrolytes like with carboxymethylcellulose (CMC), chondroitin sulfate, hyluronan, gelatin B, BSA and alginate, were tried. For the direct assembly of

antiTNF-α as polyelectrolyte layer it was observed in all cases that the PEMs assembled were not stable enough to remain attached onto the surface after flushing a PBS solution; not even after the building up of more than 40 layers. Therefore, as alternative it was decided to form a complex of antiTNF-α with polyelectrolyte in excess in bulk. Having the antiTNF-α entrapped in a polyelectrolyte the charges of the polyelectrolyte will be employed for the assembly in the PEM and the stability of the multilayer will be determined by the interaction between the negative charge polyelectrolyte in the complex and the polycation used for the LbL, and not involving antiTNF-α. Complexes were formed between the different polyanions and antiTNF-α. For complex formation an optimal combination was found for Alg and antiTNF-α with a molar ratio 2:1 Alg/antiTNF-α in 0.2 M NaCl at pH 4. The complex with this stoichiometry has a hydrodynamic size of around 4.7 ± 0.2 nm in diameter and a ζ-potential value of ~ -46.6 ± 2.4 mV (*Figure 5.1*). At this molar ratio the complex was stable and did not precipitate. For PEM formation the complex was used as polyanion with poly(L-lysine) (PLL) as polycation.

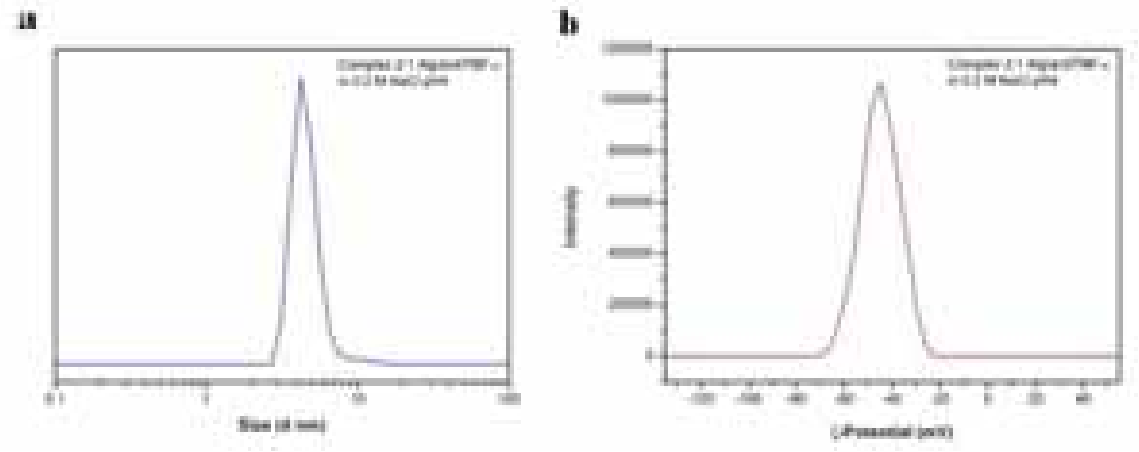

Figure 5.1. *(a) Size distribution by DLS and (b) ζ-Potential of the complex formed by Alg/antiTNF-α with a molar ratio 2:1 in 0.2 M NaCl at pH 4.*

The complex and PLL in 0.2 M NaCl were LbL assembled on a silicon oxide coated quartz crystal in a QCM-D chamber. The pH of all the polyelectrolyte solutions was adjusted to 4 by addition of either 1M HCl or NaOH. The incubation time of each polyelectrolyte layer was 15 min, and a 0.2 M NaCl solution was used to rinse the crystal after each layer deposition.

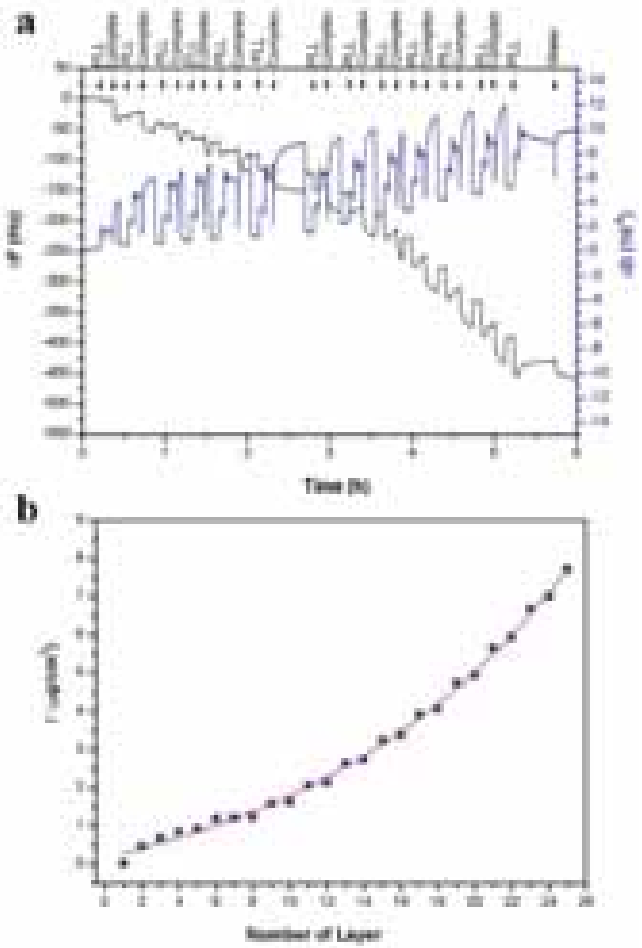

Figure 5.2. *(a) QCM-D frequency and dissipation changes during the 25 PLL/Complex multilayer assembly process. (b) Mass increase as function of the layer number, calculated employing the Sauerbrey equation.*

Figure 5.2a shows the variation in frequency (ΔF) and in dissipation (ΔD) during the deposition of 25 multilayers of PLL/Complex. The mass deposited on the crystal was calculated using Sauerbrey equation and in *Figure 5.2b* the increase of mass is plotted per each layer deposited. A negative variation in frequency (ΔF) of ~ -427 Hz for the whole PLL/Complex multilayers assembly is observed, revealing that the mass was also continuously increasing up to a final mass of 7.72 μg/cm^2 for 25 layers. The increment of mass per layer during the assembling of 25 layers shows an exponential growth profile. Concerning the changes in dissipation, it is possible to observe in *Figure 5.2a*

an increase of ~10X10^{-6} units confirming that the assembled film is densely packed. Moreover, the ratio of dissipations and frequency changes (ΔD/-ΔF) is 2.34×10^{-8}/Hz, an smaller value than 0.2×10^{-6}/Hz, which justifies the application of Sauerbrey equation to calculate the mass deposited *[321]*.

In the design of a drug delivery system the burst release is normally not desired but a progressive release of the encapsulated material. The release of antiTNF-α, encapsulated between PEMs will depend on the stability of the deposited layers. For a progressive or sustainable release of antiTNF-α, the PEMs should have certain stability and should not degrade at simple contact with the PBS solution but at the same time they have not to be very stable and gradually start to peel off with time, delivering in this way the antibody.

To study the stability of the system after LbL deposition of 25 layers of PLL/Complex, either PBS or a solution of 1 mg/mL of lysozyme in PBS at 37 ºC was flushed through the QCM-D crystal and the frequency and dissipation changes were monitored. In *Figure 5.3a* the frequency and dissipation changes when PBS at 37 ºC was flushed through the 25 PLL/Complex assembled multilayers are shown. Immediately after the PBS injection into the chamber, an increment in ΔF of around 100 Hz was detected; nevertheless, the ΔF recovers the same value that before PBS exposition after 1 hour of flushing, and this frequency remains constant for the next 16 h. The fast increment in the frequency when the PEMs were exposed to PBS indicates a loss in the mass that may be due to a rearrangement of the PEM in presence of the phosphate salts or to the increase of the ionic strength. This change is however revesible and the PEM recovers its original frequency after passing through the 25 PLL/Complex multilayers PBS at 37 ºC, meaning that no polymer is released. This result suggests that the interaction between PLL and the Complex is strong enough not to be degraded by the PBS flushing. In the case of the dissipation monitoring, a decrease of around 11 units can be observed when PBS pass through the system, this dissipation value hold over the next hours until the water rinse when the dissipation drops again to their value before PBS flushing.

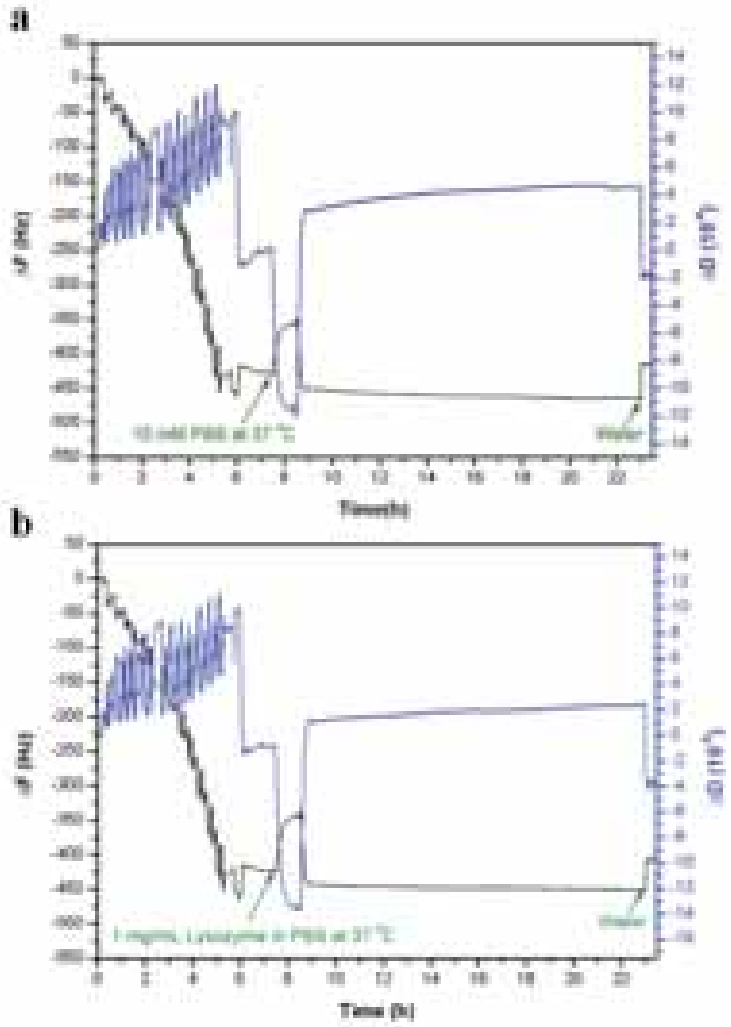

Figure 5.3. *QCM-D frequency and dissipation changes during the (a) PBS and (b) lysozyme solution flushing through the 25 PLL/Complex multilayers film at 37 ºC.*

In order to expose the PEMs to more aggressive conditions than PBS at 37 ºC, and taking into account the possible use of the delivery system for biomedical applications, a solution of 1 mg/mL lysozyme in PBS was passed through the preassembled multilayers film at 37 ºC. The frequency and dissipation change monitored in the QCM-D for the flushing of the lysozyme solution through 25 PLL/Complex multilayers is represented in *Figure 5.3b*. As same as observed when PBS was flushed through the system, an increase in the frequency and a decrease in the dissipation were observed at the beginning of the flushing, and as well, after 1 hour of flushing, the frequency and dissipation, return to their original values. Not even lysozyme in solution at 37 ºC is

able to disrupt PLL-Complex interaction and cause the peeling off of the 25 preassembled PEMs.

The building up and the release experiments performed by QCM-D suggest that the PLL/Complex PEMs, form a highly stable film that cannot be easily disrupted. PLL/Complex multilayers with antiTNF-α entrapped in the Complex layers do not have the drawback of fast peel off and burst release, and with the advantage of controlling the amount of antibody encapsulated by the number of multilayers deposited.

5.1.2. Layer by Layer encapsulation of antiTNF-α onto PLGA NPs surface and release profiles in PBS

For the fabrication of the actual carrier, the antibody antiTNF-α was assembled on PLGA NPs using LbL technique. Polyelectrolyte solutions were prepared as mentioned above for the characterization of the LbL assembling process onto planar surfaces. The incubation time of each polyelectrolyte layer was 15 min, and the NPs were washed with a 0.2 M NaCl pH 4 solution three times between each layer, until reaching 11 or 25 layers of PLL/Complex onto PLGA NPs, being in both cases PLL at the outmost layer.

The PEMs deposition onto PLGA NPs was followed via ζ-potential measurements (*Figure 5.4*). The alternative assembly of polyelectrolytes of opposite charge induces surface recharging and the consequent change in the sign of the potential. BSA stabilized PLGA NPs displayed a ζ-potential of -25.5 mV. During the LbL assembly of PLL/Complex the ζ-potential oscillated between +13 ± 2 mV and _-25 ± 2 mV, for either PLL or the Alg/ antiTNF-α complex as the outmost layer

After LbL assembly and antiTNF-α encapsulation onto PLGA NPs, the release of the antibody was study in PBS at 37 ºC and 60 ºC for NPs containing either 11 or 25 PLL/Complex multilayers. A solution of 1 mg/mL in 10 mM PBS of PLGA NPs with encapsulated antiTNF-α, was prepared. Then, the NPs were incubated in a thermostatically controlled shaker at 100 rpm at 37 ºC or 60 ºC. In designed time intervals, samples of the NPs suspension were taken out and centrifuged at 10 000 g for

3 min. After centrifugation the remaining PLGA NPs with encapsulated antibody were hydrolyzed with 1 mL of 0.1 M NaOH solution at 60 ºC for 30 min, and then the solution was adjusted to pH 7.4 by adding 1 M HCl. The amount of antiTNF-α released and not released from the PLGA NPs coating was quantified by using the Q-ADA Kit. The released samples were exposed to Q-ADA solutions that specifically react with antiTNF-α, and then the UV absorption of the generated compounds was measured with a plate reader recording at 450 nm. To calculate the concentration of the antibody released, a calibration curve was previously made by testing with Q-ADA Kit antiTNF-α solutions in PBS at different known concentrations.

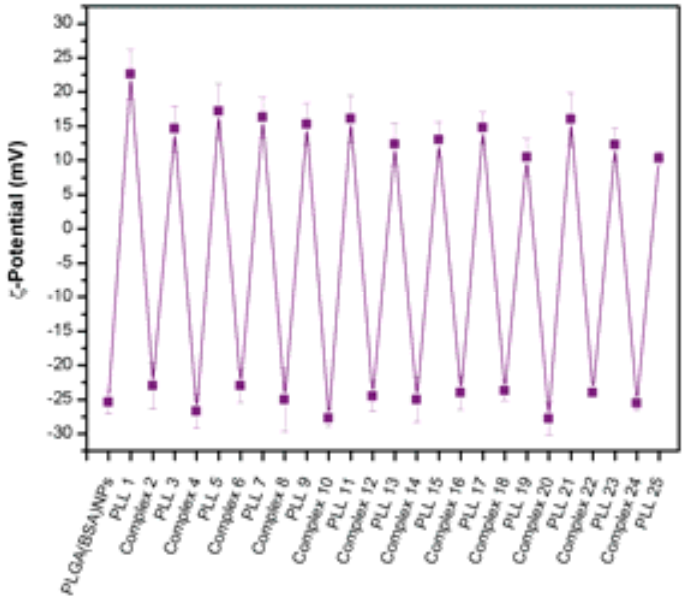

Figure 5.4. *Variation of the ζ-Potential of BSA stabilized PLGA NPs during PLL/Complex LbL assembly.*

The amount of antiTNF-α encapsulated between the PEMs was obtained by hydrolyzing a known amount of PLGA NPs coated with PLL/Complex layers and afterwards testing the remaining solution by Q-ADA text as well. PLGA NPs coated with 11 layers can load close to 53 µg of antibody per 1 mg of PLGA NPs, while PLGA NPs coated with 25 PEMs load up to 177 µg per each mg of PLGA NPs.

The release of antiTNF-α from the PLGA NPs in presence of PBS was studied over 5 days. The antibody release curves for PLGA NPs coated with 11 PLL/Complex layers are shown in *Figure 5.5a and 5.5c*. It is observed that the release of antiTNF-α is very fast at the beginning, and then became substantially slower after 8 h, resembling a first order release model although the data cannot be fitted by Higuchi model because of the burst release at the beginning of the profile.

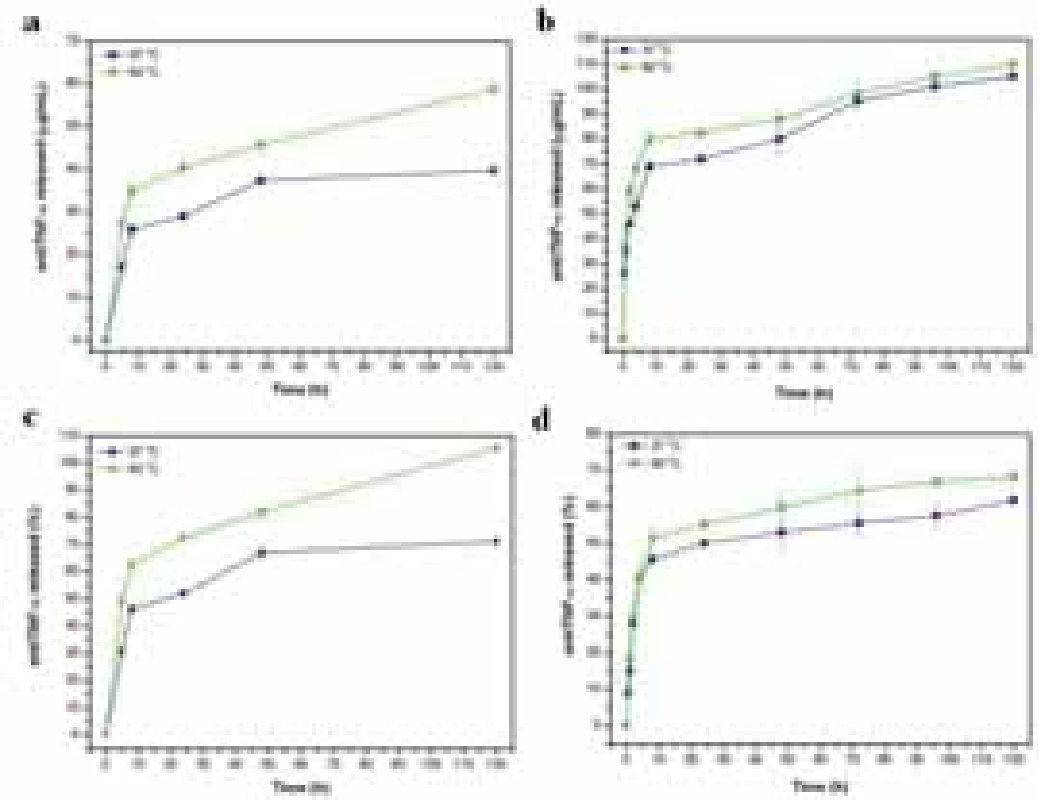

Figure 5.5. *Release profiles at 37 ºC and 60 ºC of antiTNF-α from the PLGA NPs represented in: (a) concentration in µg of antiTNF-α per mL of PBS and (c) released ratio for PLGA NPs coated with 11 layers of PLL/Complex, and (b) concentration in µg of antiTNF-α per mL of PBS and (d) released ratio for PLGA NPs coated with 25 layers of PLL/Complex.*

The release profile of antiTNF-α from the PEMs was measured at 60 ºC, to study the effect of temperature on in the delivery. Comparing the antiTNF-α at different temperatures, the final release rate is slower at 37 ºC than at 60 ºC. After 24 h ~29

µg/mL (50 %) of antiTNF-α was released from PLGA NPs coating at 37 ºC, while at 60 ºC up to 40 µg/mL (70 %) of antibody was delivered. After 5 days, the release of antiTNF-α from the 11 layers LbL coating almost reached close to 40 µg/mL (70%) at 37 ºC, while at 60 ºC all the antibody seems to be completely liberated (58 µg/mL).

The release of antiTNF-α from the 25 layers PEMs assembled on PLGA NPs, was also characterized in PBS using Q-ADA assay. The release profiles are represented *Figure 5.5b and 5.5d*. Similar as for 11 layers, with 25 PLL/Complex layers antiTNF-α is released relatively fast in the first hours of NPs exposure to PBS either 37 or 60 ºC, and after 8 h the liberation of the antibody became slower. Comparing the antiTNF-α release at different temperatures, it is possible to see that release rate at 37 ºC is slightly slower than at 60 ºC. After 24 h ~72 µg/mL (50 %) of antiTNF-α was released from the 25 layers coating at 37 ºC, while at 60 ºC up to 82 µg/mL (55 %) of antibody was released. After 5 days, the release of antiTNF-α from the 25 layers coating reached 105 µg/mL (60%) at 37 ºC, and at 60 ºC almost 110 µg/mL (70 %) of the antibody was liberated. The release profile when antibody is liberated from the 25 layers coating can be compared with a first order release model, but as in the profile for 11 layers, due to the burst release at the beginning of exposure, the data cannot be fitted by Higuchi model.

Comparing the results profiles obtained for the release of antiTNF-α from PLGA NPs LbL coated with 11 and 25 PLL/Complex layers in PBS at 37 and at 60 ºC, it is possible to observe that in both cases the release curves have similar tendencies, a burst release at the beginning that becomes slower after 8 h. In addition, it is possible to confirm that the amount of encapsulated antiTNF-α can be controlled by the number of layers deposited onto PLGA NPs surface, almost the double of antibody was released for the NPs coated with 25 layers as with the ones coated with only 11 layers.

5.1.3. *"In vitro"* release of antiTNF-α from PLGA NPs

The amount of antiTNF-α present in HepG2 cells after co incubation with PLGA NPs was quantified with the Q-ADA Kit. The HepG2 cell line was cultured in DMEM with 10 % FBS and 1000 U penicillin, 10 mg/mL streptomycin at 37 ºC and in 5 % CO_2.When the cell confluence was around 70 %, all the cells were trypsinized. 10^6 cells were seed into each well of a 12-well plate. 24 h later, PLGA NPs with antiTNF-α encapsulated in 11 or 25 PLL/Complex multilayers coating, were added into the culture medium at a final concentration of 100 µg/ mL following different incubation times. Finally, the cells were washed with PBS twice, trypsinized and lysed.

In *Figure 5.6a* the amount in ng/mL of antiTNF-α in one million cells has been displayed as a function of the incubation time for both, PLGA NPs, with 11 and 25 coating layers. In *Figure 5.6b* the release ratio of antiTNF-α has been plotted as function of the time for PLGA NPs coated with 11 and 25 PEMs. It is observed that for both cases 11 or 25 layers, the increase in concentration of antiTNF-α inHepG2 cells resemble a first order release profiles in a similar way as for the release profiles in PBS showed in *Figure 5.5*.

When HepG2 cells were exposed to PLGA NPs coated with 11 layers, a gradual increase of the antibody inside 10^6 cells over time is shown. After 4 days of co-incubation, the antibody uptake reaches the 22 ng/mL, which represents the 80% of the encapsulated antibody. For the cells exposed to PLGA NPs coated with 25 layers, a burst uptake of the antibody can be observed at the beginning of the profile. After 5 hours the release becomes slower liberating close to 32 ng/mL of antiTNF-α after 4 days; this amount represents the 95% of the antibody encapsulated for the given sample of PLGA NPs. The encapsulation of antiTNF-α between the PEMs coating onto PLGA NPs seems to be effective for the gradually release of the antibody inside the cells. Nevertheless, these experiments only prove the presence of the antibody in the cell population.

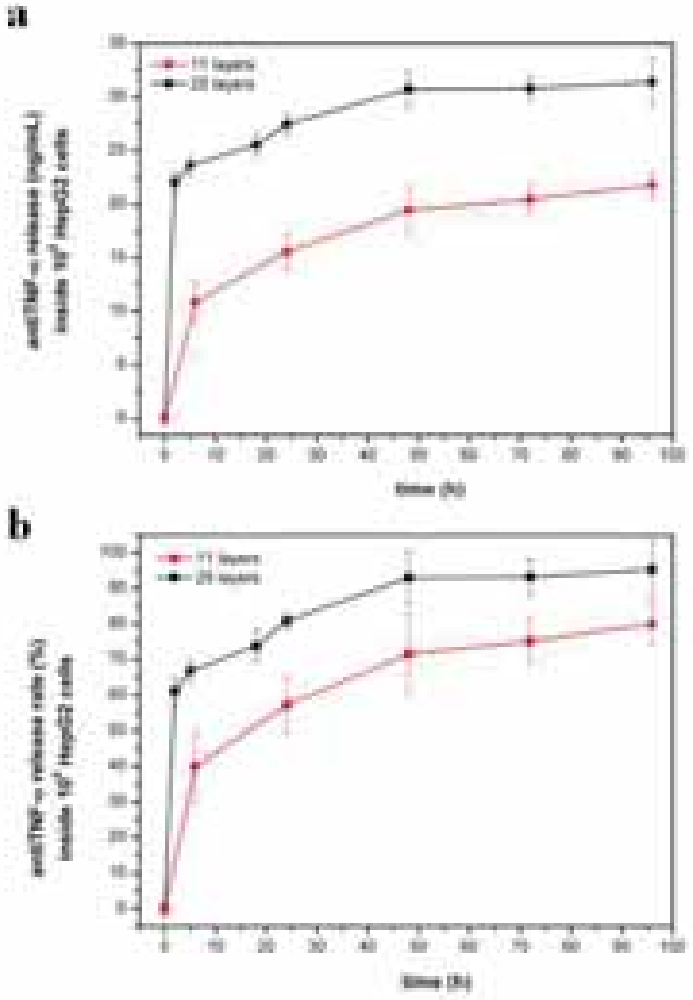

Figure 5.6. *Release profiles of antiTNF-α liberated inside 10^6 HepG2 cells from the 11 and 25 LbL coatings of PLGA NPs. The release profiles are represented for: (a) concentration in ng/mL and (b) released ratio.*

To effectively prove the intracellular liberation of antiTNF-α CRM experiments were performed. In Chapter 4 it has been shown that CRM can be used to study the uptake of carbon nanotubes (CNTs) *[155, 317]*, and PLGA NPs *[99, 322]* into cells. CRM provides both information on the CNTs or PLGA NPs localization within cells, internalization and co-localization within cell components. CRM allows differentiating regions within a cell from their Raman signals as it can be appreciated in *Figure 4.3*. The nucleus, the cytoplasm and lipid bodies by their chemical signature can be recognized from their signature in the Raman spectra. The nucleus region, for example,

reveals the smallest intensity ratio of CH_2 to CH_3 bands and specific bands assigned as vibration of DNA bases of adenine (A) and guanine (G).

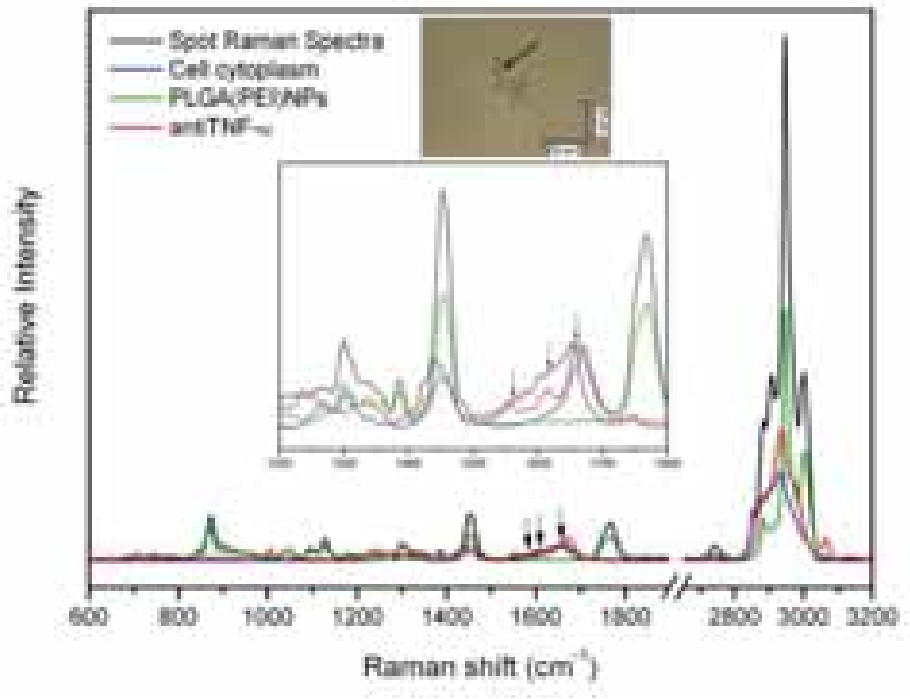

Figure 5.7. *Spot Raman spectra (black) in cells exposed to PLGA NPs with antiTNF-α. Encapsulated on their surface Green, red and blue curves denote the component spectra of PLGA NPs, antiTNF-α and cell. The insets correspond to a zoom in the spectra for the region of the antibody signals.*

In *Figure 5.7* it is observed the Raman spectra recorded in a HepG2 cell, which has been cultured in the presence of PLGA NPs with a 25 layers PLL/Complex. The Raman spectra recorded (black) displays features from the region of the cell cytoplasm as it is deduced from the relation of the bands between 2850 and 2900 cm^{-1} (*Figure 4.3*), but also presents new bands in the methyl-methylene stretching region. These bands correspond to the characteristic CH_2 and CH_3 vibrations of PLGA NPs. Moreover, it is also possible to visualize three characteristic bands between 1500 and 1700 cm^{-1} (*inset Figure 5.7*), which correspond to proteins and C=O stretching modes signals coming from antiTNF-α. For comparison the spectra of pure PLGA NPs (green), antiTNF-α (red) and of the cell cytoplasm (blue) have been included in *Figure 5.7*. From the spot Raman spectra recorded can be concluded that it is possible to prove the colocalization

of the PLGA NPs, antiTNF-α and cell cytoplasm within the dimensions of the confocal spot.

Raman spatial spectra mappings were recorded within cells, which had been exposed to NPs and contain antibody entrapped in their surface with a distance increment of 0.7 μm. The relative integral intensities of the NPs and antiTNF-α contribution in the Raman spectrum within the cell after spectra decomposition were obtained as described above. The lipid CH_2 symmetrical stretching band at 2852 cm^{-1} was chosen as reference band to obtain the cell signal distribution across the scanned map. An arbitrary line in the middle of the cell in the x direction was chosen to analyze the components distribution across the cell. The integral intensities of $\nu_s(CH_2)$ were plotted as a function of the distance along the line. The lipid distribution across the cell reflects the presence of lipid bodies, cytoplasmic lipid inclusions and lipids in intracellular membranes. A well pronounced maximum in the lipid distribution would indicate the presence of lipid bodies at a particular location.

The distributions of PLGA NPs, antibody and lipids in the cell are shown in *Figure 5.8a*. The individual intensities of all components were weighted to the maximum of intensity. The transmission image of the selected cell map and the line along which the NPs and antibody distributions were studied is shown in *Figure 5.8b* as a rainbow color presentation. The analysis of the Raman spectra of representative cells reveals that the major antibody fraction almost coincides with the maximum of the lipid signal of the cell, and a very small fraction of the antibody maximum signal is coincident with the intensities distribution of PLGA NPs. These results suggest that major part of the antibody encapsulated onto PLGA NPs is released inside the cell, and this liberated material preferentially co-localize in the lipid rich region or in the cytoplasm of the cell. Nevertheless, the distribution of intensities across the selected line also showed that part of antiTNF-α is coincident with PLGA NPs, revealing the presence of NPs with encapsulated material. PLGA NPs with entrapped antibody are present as well in the lipid bodies region and the cytoplasm of the cell.

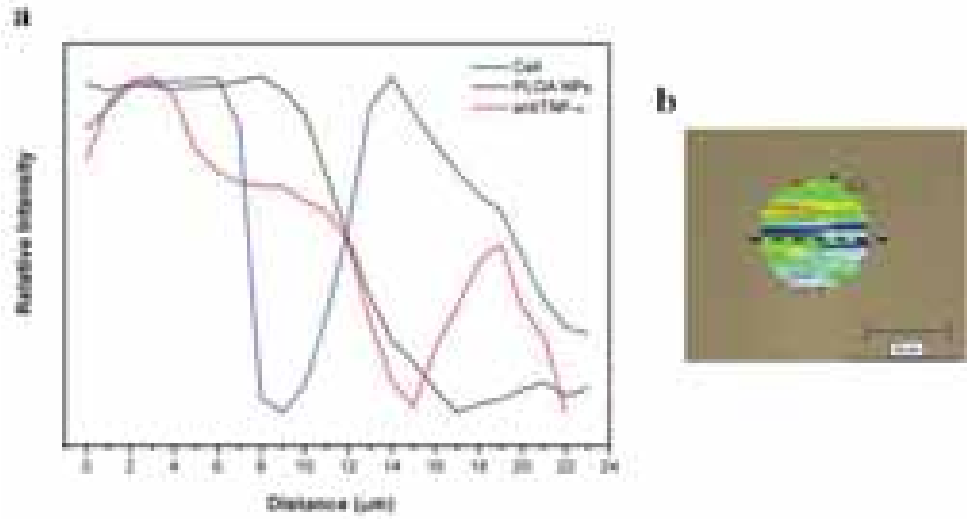

Figure 5.8. *(a) PLGA (black line), antiTNF-α (red line) and cell lipids (blue line) distributions across a cell exposed to PLGA NPs. (b) Transmission image of the cell. The map reflects the antibody intensity distribution in rainbow presentation. The red colour corresponds to the maximum intensity of the protein bands corresponding to antiTNF-α. The dash line is the arbitrary line chosen for the distribution analysis showed in (a).*

CRM mapping demonstrates the release of antiTNF-α from PLGA NPs inside the cell. As it can be observed in *Figure 5.8*a in the line analysis, in which there are some areas where bands from the antibody are not coincident with that of the PLGA NPs, meaning that the antiTNF-α is present in areas where no PLGA NPs can be detected This proves that the antiTNF-α has been released from the PLGA NPs at least partially.

5.2. Study of intracellular delivery of doxorubicin from Poly(lactide-*co*-glycolide) Nanoparticles

Controlling and monitoring the release of an encapsulated drug, is an important factor in designing more effective drug carriers. Although, release kinetics are easy to monitor in

the laboratory in biological fluids, it is quite difficult to track the liberation of an encapsulated drug at the cellular level. For example, Doxorubicin (Dox) is one the most frequently used drugs for cancer treatment and is also one of the anticancerigens most commonly used as a model drug for delivery due to its intrinsic fluorescence which makes it suitable for different characterization techniques. Dox acts by intercalating itself in the DNA chains and, in this way, inhibits the strand replication process. Nevertheless, typical fluorescence techniques, such as flow cytometry or confocal laser scanning microscopy, are frequently limited when applied to *"in vitro"* characterization of Dox release from a carrier, since it is very difficult to distinguish between fluorescence due to the released drug and the encapsulated drug. Dai X. and co-workers *[323]*, showed for the first time that fluorescence lifetime imaging microscopy (FLIM) can be applied for measuring drug delivery inside cells and permits the environment of the drug in the cell to be determined. FLIM produces contrast images based upon the lifetime of the fluorophores. The lifetime of a fluorophore is the average time the fluorophore remains in the excited state before emitting a fluorescence photon. Interactions between the fluorophore and its local environment can affect the lifetime and, thus, can be used to probe the local environment within which the fluorophore resides, e.g. inside the cell. As a result, lifetime data provides information about the intramolecular interactions, such as protein binding *[324]*, pH changes *[325]*, local viscosities *[326]*, presence of quenchers *[327, 328]*, and many others which are also helpful in drug delivery detection.

The drug delivery can finally be assessed by monitoring the effects of the cargo on the cell function, once released. In the case of Dox this can be done by measuring how cell viability is affected by the release of the drug with standard methods for measuring proliferation. Also, Confocal Raman Microscopy (CRM) provides a means to monitor alterations in the cell machinery due to the drug liberation. CRM can detect DNA damage by measuring variations in the intensity of the DNA bases, adenine and guanine bands. The ratio of the adenine and guanine bands to the protein bands (Amide III band) in the nucleus has been proposed as a means to evaluate the toxicological end points and cell response to drugs and nanomaterials*[155, 313]*.

In this section is dedicated to study the effectiveness of the PLGA NPs for intracellular drug delivery. For this purpose Dox has been encapsulated as a model drug into PLGA NPs. The drug was encapsulated during NP preparation via double emulsion-solvent evaporation method. The release of Dox from NPs was studied in PBS. The kinetics of NP and Dox uptake *"in vitro"* were then measured by using flow cytometry. Dox release at the single cellular level was measured by fluorescence life time microscopy (FLIM). Cell viability experiments were conducted to assess the capacity of the PLGA carriers with Dox to decrease cell viability. In parallel, DNA defragmentation due to the presence of Dox was measured by CRM.

5.2.1. Doxorubicin release from PLGA NPs in PBS

PLGA NPs with encapsulated doxorubicin (Dox) were prepared by the W/O/W double emulsion–solvent evaporation method using BSA as a stabilizer *[98, 99]*. The Dox loading efficiency was determined by measuring the UV absorption of a known quantity of hydrolyzed PLGA NPs with encapsulated Dox. Dox encapsulation preformed in combination with PLGA NPs fabrication via the double emulsion–solvent evaporation method has a loading efficiency of approximately 80%.

The release behavior of the PLGA NPs with encapsulated doxorubicin (PLGA(Dox) NPs) was first studied in PBS. A 1 mg/mL solution of PLGA(Dox) NPs in 10 mM PBS was prepared, following this, the NPs were incubated in a thermostatically controlled shaker at 100 rpm at 37 ºC. In the designed time intervals, samples of the NPs suspension were taken and centrifuged at 10 000 g for 3 min. The absorption at 480 nm of the supernatant was recorded using a Varian spectrophotometer (Cary-500). After centrifugation the remaining PLGA(Dox) NPs were hydrolyzed with 1 mL of 0.1 M NaOH solution at 60 ºC for 30 min, and then the solution was adjusted to pH 7.4 by adding 1 M HCl. The absorption at 480 nm of the hydrolyzed NPs was also measured using the spectrophotometer. Release experiments in PBS were also performed at 60 ºC. To estimate the amount of Dox released, a calibration curve was created by measuring the absorption at 480 nm of Dox in PBS at different concentrations. The release curves are shown in *Figure 5.9*. The rate of Dox release was initially rapid, before reducing

substantially after 2 h. Although the release profiles resemble a first order release model, the data cannot be fit to a Higuchi model. This is probably due to the burst release shown at the beginning of the profiles.

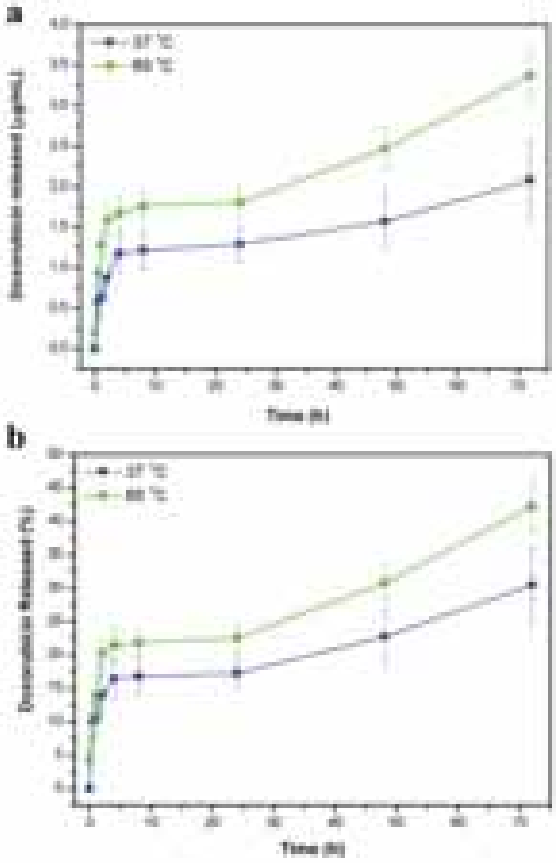

Figure 5.9. *Release profiles of doxorubicin from PLGA NPs in PBS at 37 ºC and 60 ºC, plotted for (a) µg/mL of doxorubicin released and (b) percentage of doxorubicin released, from 1 mg of PLGA NPs in PBS.*

In order to study the impact of temperature on the release, a temperature higher than that of the glass transition temperature (Tg) of the PLGA (55–58 ºC) was chosen. In contrast to the glassy state, in which the polymer chains are hardly mobile, the segments of the PLGA chains have increased mobility, leading to easier diffusion of molecules in the polymer matrix *[116, 329]*. The release curves at 60 ºC are also shown in *Figure 5.9*. Comparing the Dox release at different temperatures it can be seen that the release rate is slower at 37 ºC than at 60 ºC. After 8 h 17 % of Dox was released from PLGA NPs at

37 ºC, while at 60 ºC around 22 % of the drug was released. After 3 days, the release of Dox from PLGA NPs approached 30% at 37 ºC and 42 % at 60 ºC. The slow release of Dox from PLGA NPs either at 37 ºC or 60 ºC in PBS can be explained by the Dox positive electrostatic charge *[330]* that may form a strong complex with the negatively charged BSA present in the surface of PLGA NPs.

5.2.2. *"In vitro"* release of doxorubicin from PLGA NPs

Taking advantage of the intrinsic fluorescence emission of Dox at 588 nm, for an excitation wavelength of 480 nm, Dox release inside HepG2 cells can be characterized via fluorescent techniques. Therefore, flow cytometry was used to investigate, in parallel, cellular uptake of the NPs and Dox by monitoring both fluorescence intensities, from Dox and from PLGA NPs. NPs were prepared with fluorescein labeled PLGA. The HepG2 cell line was cultured in DMEM with 10% FBS and 1000 U penicillin, 10 mg/mL streptomycin at 37 ºC and in 5 % CO_2.When the cell confluence was around 70 %, all the cells were trypsinized. 100 000 cells were seeded into each well of a 24-well plate. 24 h later, fluorescent PLGA NPs with encapsulated Dox, were added into the culture medium to give a final concentration of 100 µg/ mL, following different incubation times. Finally, the cells were washed with PBS twice, trypsinized and studied with flow cytometry.

In *Figure 5.10a* the mean fluorescence per cell has been displayed as a function of incubation time while *in Figure 5.10b* the cellular uptake ratio has been plotted as a function of time for the PLGA NPs and for Dox. In both cases, fluorescence intensity and cellular uptake, it can be seen that the amount of PLGA NPs associated with the cell increases rapidly in the first hours of incubation, and then after 2 hours both values stabilize, reaching, after 24 hours of incubation, a fluorescence intensity of ~242 a. u., which represents a cellular uptake ratio of almost 90 %.

On the other hand, from the Dox fluorescence intensity and cellular uptake ratio it is possible to observe that the amount of Dox associated with HepG2 cells quickly increases in the first 4 hours of exposure, and then stabilizes for the next 4 hours with a

fluorescence intensity value close to 230 a. u. (cellular uptake ratio of 66 %). Moreover, after 8 hours the fluorescence intensity of Dox inside the cell begins to gradually decrease, reaching a value of ~117 a. u. after 24 hours. The unexpected decrease in the fluorescence intensity and cellular uptake ratio of Dox could be interpreted as quenching of the Dox. This could be because Dox reaches the cell nucleus and stops the replication process by intercalating between the DNA strands *[331, 332]*, or simply due to lower emission intensities of Dox inside the cell when compared to encapsulated in the NPs.

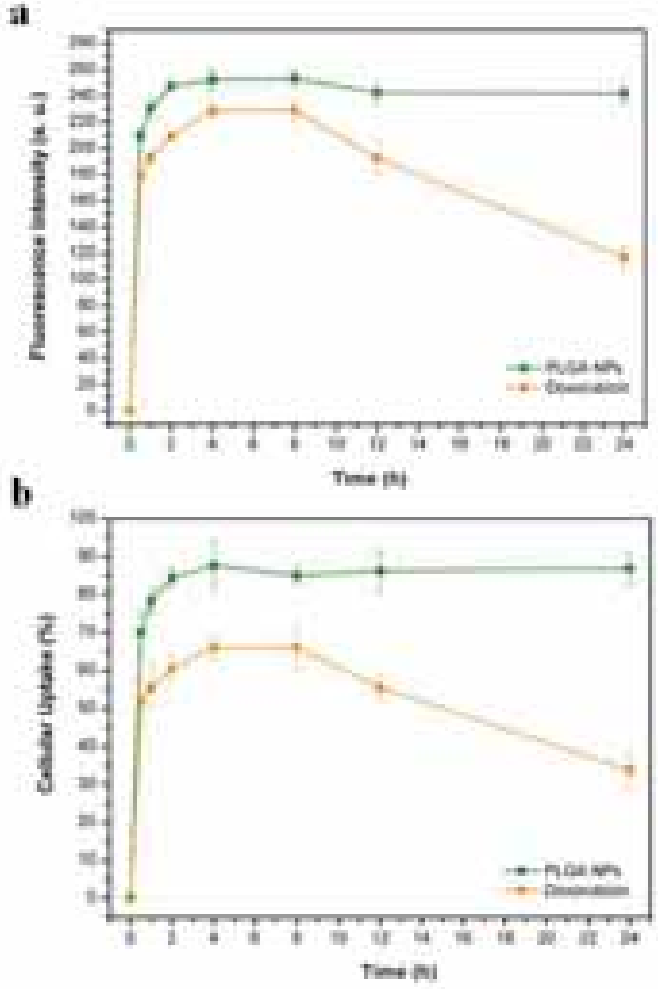

Figure5.10. *(a) Fluorescence intensity of PLGA NPs and Dox inside HepG2 cells and (b) percentage of doxorubicin and PLGA NPs taken up by HepG2 cells.*

Flow cytometry clearly shows PLGA NPs and Dox association within the cell; nevertheless, it is not possible to distinguish if Dox has been released from PLGA NPs or if it is still loaded in PLGA NPs. This can only be determined after a few hours due to the decrease in fluorescence intensity of Dox while the values for PLGA remain constant.

In order to probe the intracellular release of Dox from PLGA NPs FLIM was employed. Confocal laser scanning microscopy (CLSM, Carl-Zeiss LSM 10 META) combined with fluorescence lifetime imaging microscopy (TCSPC FLIM, Becker&Hickl Gmbh) equipped with a pulsed diode laser (405 nm) were used to image the cells after incubation with fluorescent PLGA(Dox) NPs. 100 000 cells were seeded on a coverslip which was placed in a 3.5 cm culture plate. 24 h later, PLGA NPs were added into the culture medium to give a final concentration of to 50 μg /mL. After 4 hours of incubation, the culture medium was removed and the cells were rinsed three times with sterilized PBS. The cells were subsequently fixed with 3.7 % formaldehyde solution in PBS for 30 min. Finally, the coverslip was sealed with Mounting Medium for fluorescence and observed under CLSM employing a 63X oil objective.

Water solutions of Dox and Dox loaded into PLGA NPs were first characterized by FLIM. Dox in water excited by a 405 nm laser, was found to have a lifetime of 1.15 ns (*Figure 5.11b*) with a homogeneous distribution, as can be seen in its lifetime image and lifetime histogram (*Figure 5.11a and c*). Unlike the free drug, Dox encapsulated in PLGA NPs displays a longer lifetime, with a value of 3.12 ns (*Figure 5.11d-f*). It can be expected that the lifetime of Dox increases following encapsulation when compared to free Dox in water, due to the fact that encapsulation reduces exposure to possible quenchers, such as dissolved oxygen in water.

As it has been shown by using flow cytometry in PBS, Dox release from PLGA NPs occurs rapidly. To avoid a high concentration of Dox in the media, PLGA NPs with encapsulated Dox were incubated with HepG2 cells for a relatively short time of 4 h and then studied by FLIM. In *Figure 5.11g* it is seen the lifetime image of HepG2 cells exposed to PLGA(Dox) NPs, also shown is the lifetime distribution within the cell

cytoplasm (*Figure 5.11i*). The lifetime distribution is relatively narrow, indicating that there is only one fluorescent species of Dox present inside the cell.

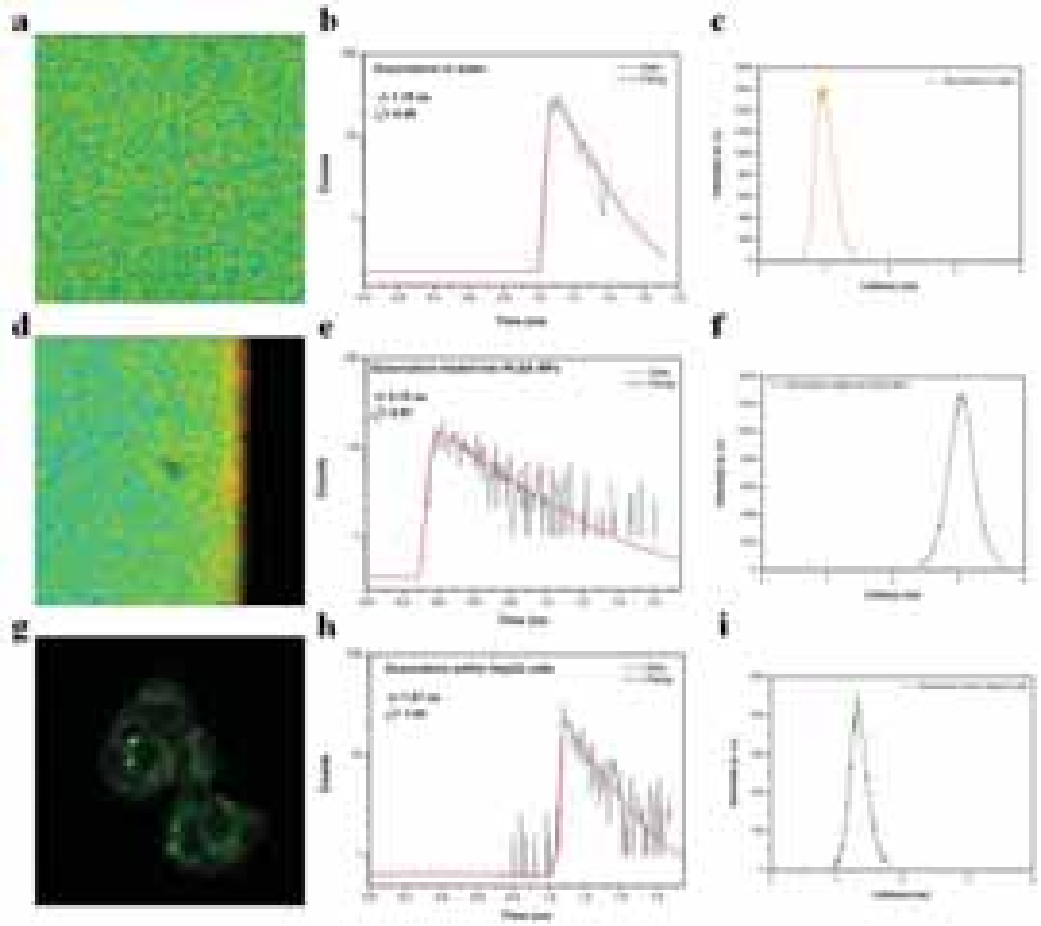

Figure 5.11. *Lifetime images and corresponding lifetime decay curves and lifetime distributions of Doxorubicin in water (a-c), Doxorubicin loaded into PLGA NPs (d-f) and HepG2 cells incubated with doxorubicin loaded PLGA NPs (g-i).*

The lifetime value for Dox inside the cell was measured to be 1.61 ns, as can be seen in *Figure 5.11h and 5.11i*, this is not consistent with the lifetime of free Dox in water or PLGA(Dox) NPs. Nevertheless, it very well known that the lifetime of a fluorescent molecule strongly depends on its environment. Dox tends to form π-π stacks with aromatic groups of biological compounds, which again reduce Dox exposure to external quenchers resulting in an increase of the lifetime value *[323, 333]*. In addition, the Dox lifetime obtained inside the cytoplasm of HepG2 cells is comparable with the lifetime

value obtained by Dai X. and co workers in the cytoplasm of HeLa cells *[323]*. The results obtained by FLIM for HepG2 cells co-cultured with PLGA(Dox) NPs, suggest that after 4 hours of incubation, Dox is completely released from PLGA NPs and preferentially locates in the cell cytoplasm. No measurable lifetime could be recorded inside the nucleus, however, the small aggregates of DOX in the proximity of the nucleus that could be observed in the lifetime image (*Figure 5.11g*), correspond to free Dox. The fact that Dox could not be detected inside the nucleus in the experiments may be because when Dox enters the nucleus the cell will immediately die. In all the experiments performed here, alive cells were used and therefore the possibility of Dox being present inside the nucleus is likely to be minimal.

5.2.3. Cell viability studies

Cell proliferation was also studied to indicate Dox release since is well known that this anticancer drug is able to kill cancer cells such as the HepG2 cell line. The cell proliferation was studied with the MTT assay. Initially, approximately 5000 HepG2 cells were planted into each well of a 96-well plate, and after 24 h, PLGA(Dox) NPs were added into culture media at different concentrations (0, 20, 50,100, 200 μg/mL). After different time intervals of co-incubation, 20 mL of MTT solution (5 mg/mL in 10 mM PBS) was added into each well of the plates and incubated for 3 h. The absorbance was measured by means of a plate reader at 550 nm.

The graph in *Figure 5.12*, clearly shows that the cell viability after incubation with PLGA(Dox) NPs decreases with higher NP concentrations and increasing incubation time. In the first 2 h at 10 μg/mL, the lowest concentration of NPs, cell viability was around 68 % and close to 34 % for the same concentration following 24 h of incubation. In case of the higher concentration of NPs (100 μg/mL) cell viability was almost 50 % in the first 2 h of incubation, decreasing to approximately 8 % after 24 h of incubation. MTT results shows that cell viability decreases considerably after 24 h of incubation with PLGA(Dox) NPs. It was previously shown that PLGA NPs stabilized with BSA, as prepared here, have no toxic effect in HepG2 cells *[99]*; therefore, the low viability of the cells can be related directly to the presence of Dox.

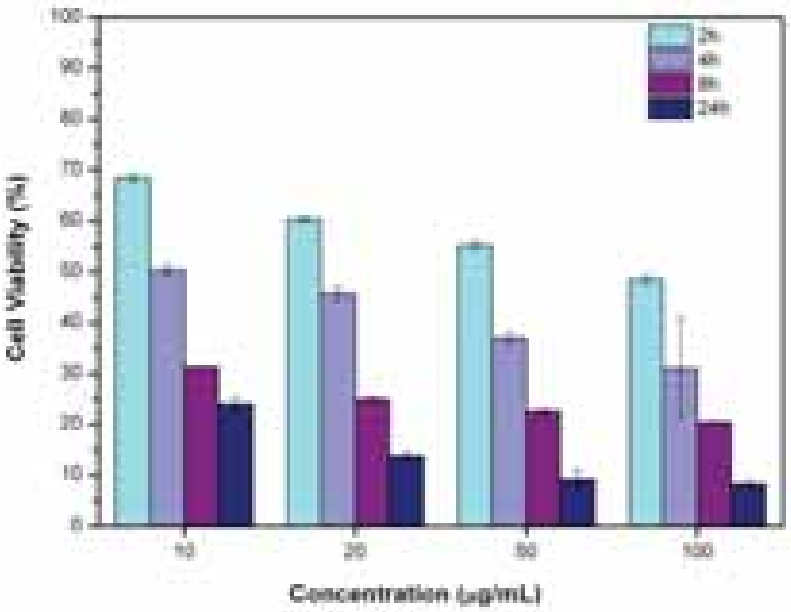

Figure 5.12. *Cell viability of HepG2 cells after co-incubation with PLGA(Dox) NPs at various concentrations over 4 days.*

Since the action of Dox is due to its intercalation in the DNA strands inhibiting the replication process, CRM experiments were conducted to study the impact of the delivery of Dox in cell physiology. As for FLIM, CRM allows us to look at individual cells. Differences in the Raman spectra of the nucleus region were found between control cells and cells exposed to PLGA(Dox) NPs. Spectra were deconvolved into the cellular and the respective NP components. The signal of the PLGA NPs and Dox were subtracted from the total spectrum to remove the overlapping Raman signals in the region of amide III and nucleic acids. *Figure 5.13a* shows the changes in intensity of the Raman peak at 1338 cm^{-1}, associated with a nucleotide signal and in the amide III peak for cells treated with empty or Dox loaded NPs. The corresponding spectral region was deconvoluted into six components (inset of *Figure 5.13a*), from the resulting signal it was possible to calculate the integral peak ratio between the peak related to A, G (1338 cm^{-1}) and the peaks of the protein amide III bands, consisting of random coils, β-sheet and α-helical contributions (1200-1290 cm^{-1}). The ratio of the A G bands to the amide III bands are summarized and compared with the control in the table in *Figure 5.13b*.

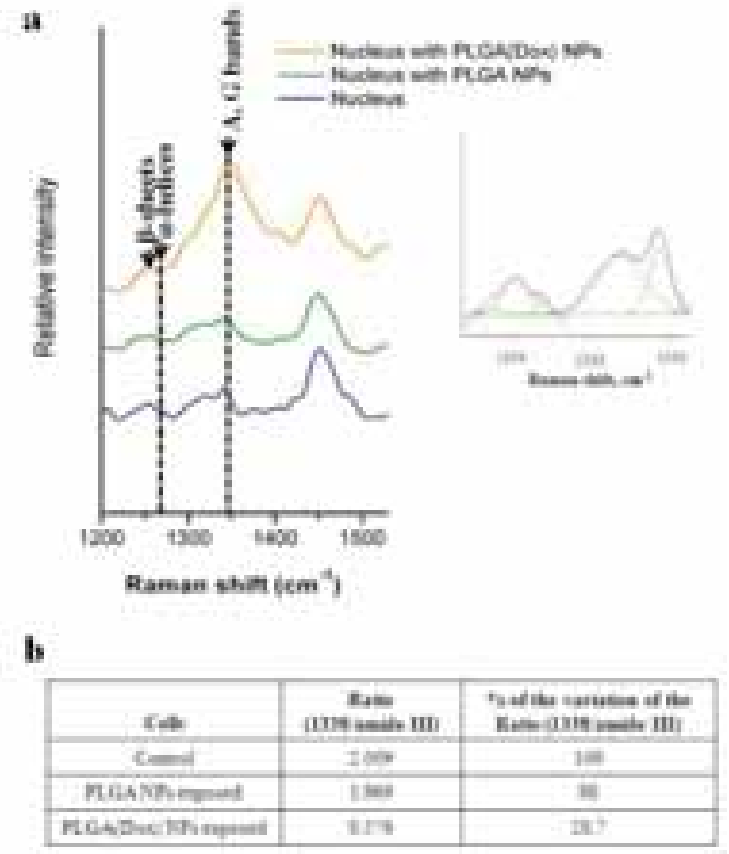

***Figure 5.13**. (a) Averaged Raman spectra from the nucleus of cells treated with PLGA NPs (green line) and PLGA(Dox) NPs (orange line) compared with the spectrum of the nucleus of untreated cells (blue line). The inset figure shows the peak fitting analysis of a Raman spectrum from the nucleus of untreated cells. The arrows denote β-sheets, α-helices and A, G bands from left to right. (b) Summary table of the integral intensity ratio between A, G bases and amide III protein bands.*

The calculated DNA/protein ratio can be taken as a measure of the damage in the cell nucleus induced by the toxic effect of external molecules. When HepG2 cells were exposed to PLGA NPs there was a minimal change observed in the DNA/protein ratio compared with the ratio of the control cells, revealing that there is almost no effect detected in the nucleus of the cells as a result of PLGA NPs co-culturing. In contrast to the PLGA NPs, a dramatic decrease of the DNA/protein ratio can be detected, in the case of Dox loaded PLGA NPs the ratio drops to approximately 29% of the

DNA/protein ratio of the control sample. The results prove the acute toxicity of Dox since PLGA NPs alone do not show any toxic effect on HepG2 cells. One possible explanation of the decrease of the DNA/protein ratio is fragmentation of DNA as a result of Dox intercalation into DNA strands and enzymes inhibition. Moreover, conformational changes of the secondary structure of proteins can be observed from *Figure 5.13a* in the spectra of cells treated with PLGA(Dox) NPs. The intensities of α-helix associated peaks at 1270 cm^{-1} are reduced compared with those resulting from β-sheets at 1256 cm^{-1}. The deconvolution of amide III bands revealed the same tendency. The protein fraction with random coils and α-helical conformations are reduced and conformational transformation to β-sheets occurred in cells exposed to NPs containing Dox.

Raman experiments were also performed using living cells and cells exposed to PLGA NPs for 4 hours. The observed effects on cells may be due to the presence of the Dox in cytoplasm before coming into the nucleus since, as already mentioned for the FLIM experiments, cells with Dox outside the nucleus could be seen to be alive.

Chapter 6
Conclusions

This PhD thesis work presented the design, fabrication and surface engineering of PLGA NPs and CNTs as potential nanocarriers for targeted delivery. The surface modification of both nanomaterials was carried out on the basis of polyelectrolyte molecules through LbL films and polyelectrolyte brushes, combined with covalent chemistry, and on the self assembly of lipid vesicles. It has been demonstrated that through the proper surface modification of PLGA NPs or CNTs it is possible to control their interactions with the cells such as, uptake, localization, biological fate and toxicity. Moreover, it has been shown that there is a potential use of PLGA NPs as drug delivery carriers through the encapsulation and *"in vitro"* release of different molecules. The main results of the thesis are summarized below:

- PAA/PEI multilayers were successfully built up on positively charged PLGA NPs, and were used for further surface engineering through the covalent attachment of PEG and PEG-FA molecules. The PAA/PEI multilayer coating and pegylation provide a simple and stepwise procedure to define the surface properties of the NPs especially regarding their interaction with proteins and cells. Co-culture of the engineered NPs with HepG2 cancer cells revealed that the cellular uptake of the NPs decreased significantly after pegylation. However, a higher cellular uptake was obtained for the NPs whose surface was engineered with PEG-FA. It is known that the tumor cells such as HepG2 overexpress folate receptors on their membranes, thus the PEG-FA coated NPs can be potentially used as the specific targeting carriers for anticancer drugs.

- Chitosan (Chi) and alginate (Alg) were LbL assembled on top of the BSA stabilized PLGA NPs. The PEMs also provided a stable coating for further functionalization with specific recognition functions by means of covalent

binding of FA and PEG–FA. The Chi/Alg multilayers, with either Alg or Chi at the outermost layer, displayed very low interaction with albumin, with minimal deposition on the multilayer and display a very low association with cells. These results allow us to envisage the use of Chi/Alg multilayers as antifouling coatings to avoid interactions with proteins and to decrease cell uptake. A higher cellular uptake has been achieved after FA or PEG–FA was covalently bound to the multilayer.

The results obtained for PLGA NPs engineered with either, PEI/PAA or Chi/Alg multilayers, show that the LbL approach combined with covalent binding of PEG and FA, can tune the surface properties of the NPs to reduce unspecific interactions and to achieve targeted delivery in cancer cell lines.

- PLGA NPs have been surface modified with lipid layers assembled on top of a polyelectrolyte coating. The cellular uptake and the co-localization of PLGA NPs inside HepG2 cells can be controlled by proper engineering of their surface with mixed lipid layers of DOPC and DOPS. Lipid coated PLGA NPs are taken up by cells, forming vesicle-like aggregates in the proximity of the nucleus, more specifically they co-localize with the ER in the HepG2 cells. Increasing the molar ratio of DOPC in the lipid coating of the NPs, results in more vesicle-like aggregates with a clear co-localization in the ER of the cell, although fewer NPs are taken up. Regarding the uptake mechanism, lipid coated PLGA NPs were not taken up via fusion of their lipid coatings with the cell membrane. The internalization mechanism of unmodified PLGA NPs follows clathrin-mediated endocytosis, macropinocytosis and internalization through the cell cytoskeleton, while the PLGA NPs coated with lipids, either with 65:35 or 95:5 DOPC/DOPS, were found to be internalized into the cell mainly via macropinocytosis, clathrin-mediated and caveolae-mediated endocytosis.

  The strategy presented for the engineering of PLGA NPs with lipid layers with a variable composition of DOPC and DOPS represents a simple but effective way of targeting NPs towards the ER as well as controlling the amount of NPs

assimilated by the cells. Therefore, PLGA NPs engineered with lipid layers could potentially be used for the treatment of different diseases in which the synthesis and transport of proteins in the ER play an important role, such as the intracellular delivery of some proteins as cancer vaccinations, or for the delivery of specific sugars that are known to inhibit glycoproteins folding, useful in antiviral human pathogens treatments.

- CNTs have been successfully coated with a negatively charged polyelectrolyte brush of PSPM by *in situ* polymerization employing ATRP from initiating silanes attached onto the CNTs surface. The covalently bonded polymer brush forms an organic layer around the CNTs and provides colloidal stabilization in aqueous media. The polymer shell also serves as a scaffold for the synthesis of nanoparticles such as: quantum dots or magnetite to form hybrid organic–inorganic CNT–polymer–NP structures. The fabrication strategy followed results in water stable, hybrid CNTs nanocomposite structures that could have applications in the design of more complex systems and devices. The synthesized nanoparticles, endow CNTs with magnetic or fluorescence properties. The procedures developed could be applied to the synthesis of other nanoparticles as cargo to broaden the usefulness or functionality of the CNTs.

- The PSPM shell surrounding the CNTs was also used for the assembly of lipid layers on top of the CNTs. The strategy followed comprised the assembly of an oppositely charged polyelectrolyte layers on top of CNTs-PSPM, and, finally, the assembly of lipid vesicles composed of 1,2-dioleoyl-sn-glycero-3-choline and 1,2-dioleoyl-sn-glycero-3-phospho-L-serine on top of the polymer cushion. The whole procedure was performed in an aqueous environment resulting in a stable colloidal dispersion. The proposed strategy of functionalization could be used for the coating of surfaces where CNTs are present as part of composites and biocompatibility is required.

- By means of CRM it has been shown that PLGA NPs either stabilized with PEI or with BSA can be internalized in HepG2 cells. The Raman data unambiguously prove the interpretation given by flow cytometry and confocal laser scanning microscopy that the NPs were internalized. PEI stabilized NPs were taken over a longer period of time compared with BSA stabilized PLGA NPs. CRM proves that both kinds of PLGA NPs are found in the region of the lipid bodies. Cell viability studies shows that PEI stabilized NPs are moderately toxic, while BSA stabilized NPs display very good biocompatibility, resulting in cell viability percentages comparable or better than the control. These results indicate the potential use of PEI/BSA coated PLGA NPs for intracellular delivery.

- The interaction of the stepwise modified CNTs with HepG2 cells has been studied by means of CRM based on spontaneous Raman emission, TEM and cell toxicity assays. It has been found that oxidized and polyelectrolyte coated CNTs have a higher toxicity than lipid coated CNTs. The lipid coating significantly reduces the toxic effect of CNTs. The results suggest the use of lipid coated CNTs for biological applications, delivery or sensing, where a moderate toxic response in vitro is acceptable. Also, the proposed strategy of functionalization could be used for the coating of surfaces where CNTs are present as part of composites, reducing their possible toxic effects.

  Spontaneous CRM has been successfully applied to identify PLGA NPs and CNTs with different surface modification in single hepatocarcinoma cells. The obtained results prove that CRM, being a label-free technique, is a powerful tool to study the uptake of nanomaterials in cells. For either, PLGA NPs or CNTs, CRM confirms the internalization and co-localization within different environments of the cell (cytoplasm, lipid bodies and nucleus). CRM was also used as a tool to measure toxicity, since is possible to analyze the signals coming from DNA and proteins of the cell nucleus.

- A strategy for the encapsulation of antiTNF-α in PEMs has been developed on the basis of the complexation of antiTNF-α with an excess of Alginate, and the

assembly of this complex in the PEMs. It has been proved by means of QCM-D that a stable multilayer can be built up by the complex and PLL. PEMs with up to 25 layers of antiTNF-α /Alg and PLL were fabricated which, suffer little degradation in the presence of PBS or lysozyme.

The assembly of the antiTNF-α /Alg complex was performed on PLGA NPs. For the particles the antiTNF-α is released following an approximate first order release mechanism in PBS, which is not temperature dependent. Uptake experiments at intracellular level displayed the same tendency of an increasing presence of antiTNF-α in the cell population as the antiTNF-α is released in PBS. To prove the liberation of the antiTNF-α complex inside the cell CRM experiments were performed. It was shown that the Raman bands from antiTNF-α can be detected alone in some areas within the cells, not correlating with the signal coming from the PLGA. This situation is only possible when the PEMs have been dissociated from the particle. The procedure shown here can be extended to any other antibody or therapeutic with a moderate charge that can be first, complexed and then, assembly in LbL fashion.

- Doxorubicin was encapsulated inside the PLGA matrix during NPs fabrication via emulsion methods. The intracellular delivery of Dox encapsulated in PLGA NPs to HepG2 cells has been shown. Flow cytometry proves that PLGA NPs and Dox follow, initially, the same kinetics. However, after 8 hours the intensity of Dox significantly decreases while that of the PLGA remains constant. This indicates that Dox is being released from the NPs. FLIM studies show that the lifetime of Dox inside the cell has a value of 1.61 ns, lower than inside the PLGA NPs and higher than in water. The presence of only one lifetime implies that the Dox has been completely released inside the cells after 4 h.

  The effectiveness of Dox delivery in reducing cell proliferation was assessed by the MTT assay. For all concentrations of loaded Dox studied, from 10 to 100 mg/ml, cell viability decreased to values below 25 % after 24 hrs. The action of Dox in cells was also measured from the defragmentation of DNA that could be

determined with CRM at the single cell level. PLGA NPs stabilized with BSA and fabricated by emulsion-solvent evaporation technique can be used for intracellular delivery of anticancer drug such as Dox. Further work will be required in order to control the release of the encapsulated drug to achieve a more sustainable release.

Appendix

Figure A

FIRT spectra of Folic Acid (FA), Poly(ethylene glycol) (PEG) and PEG modified FA.

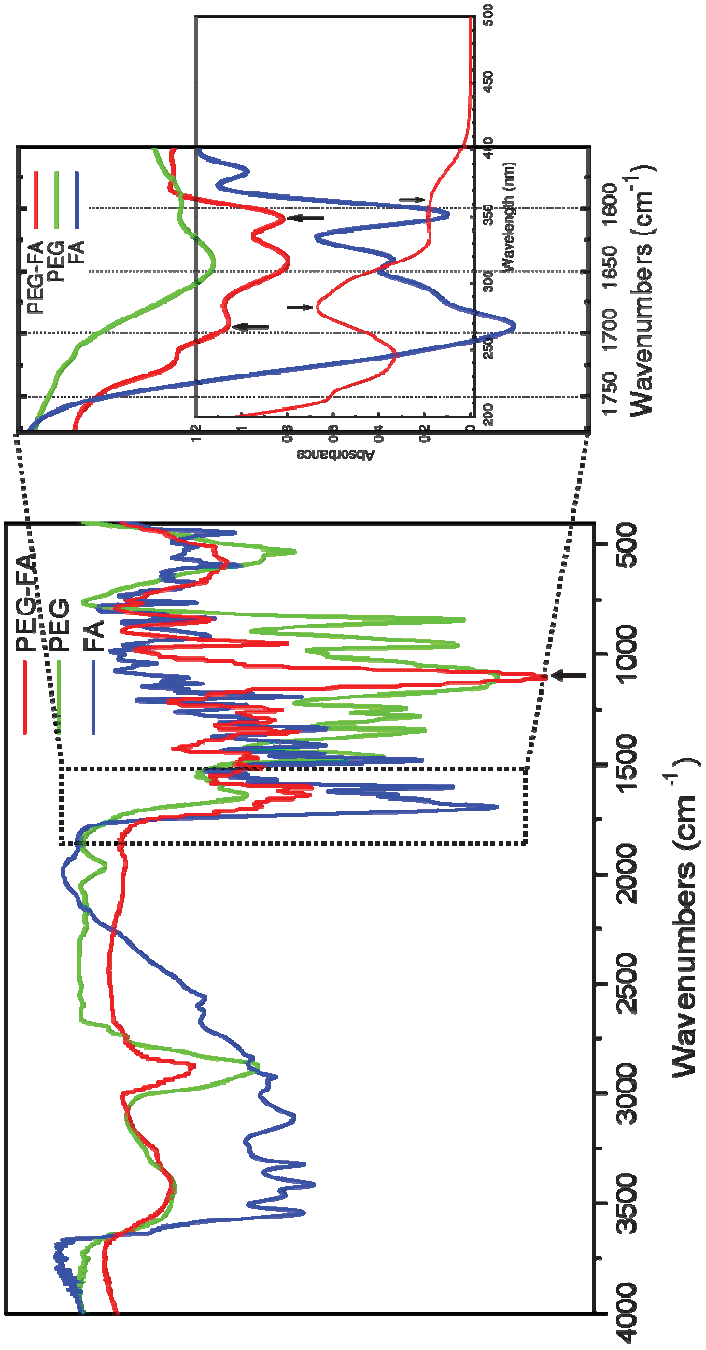

Figure B

1H NMR spectra of PEG modified FA (500M in D_2O)

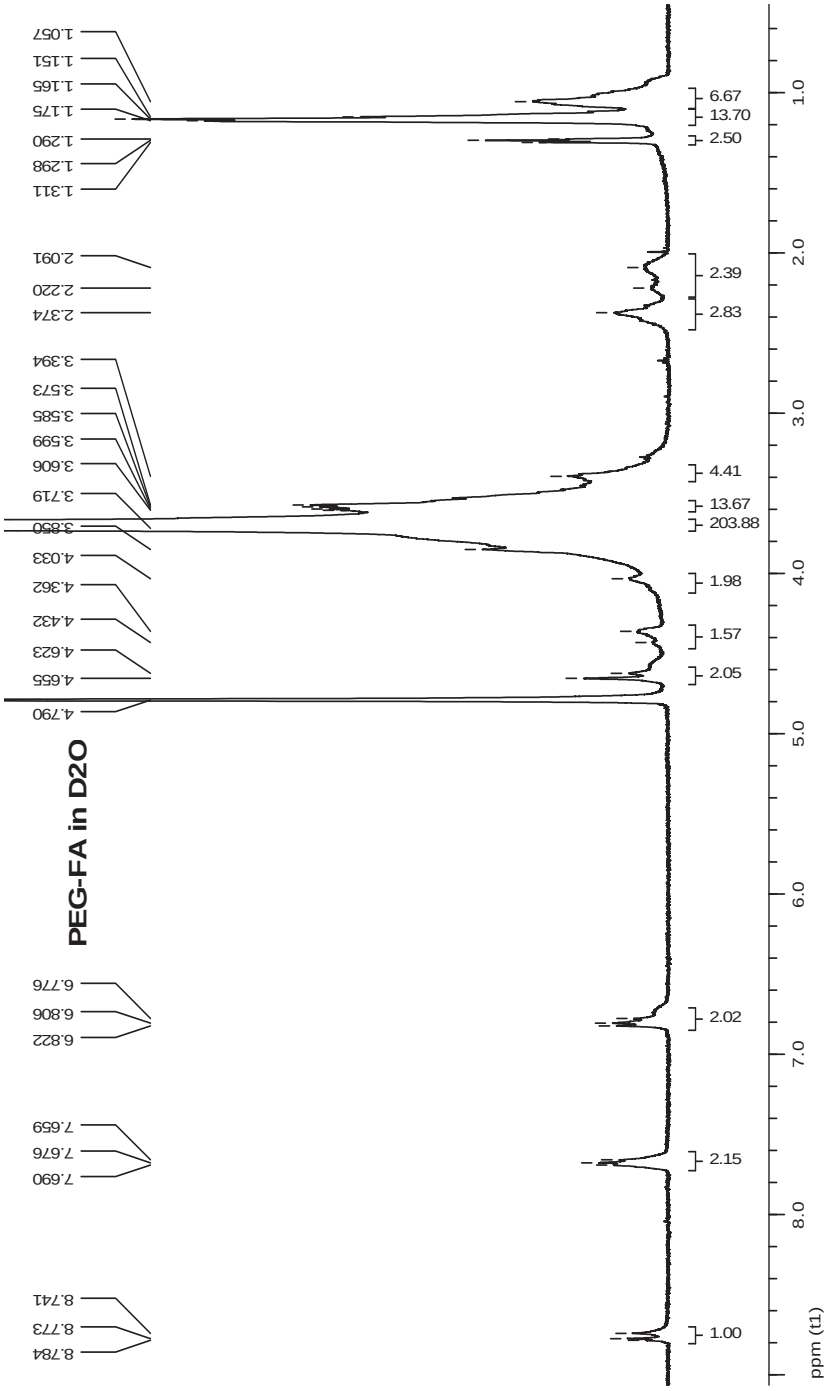

Figure C

FCS vs Fluorescence Intensity dotplot graphs of (1) HepG2 cells without NPs as control sample and (2) HepG2 exposed to PEG-FA grafted NPs after 0.5h incubation.

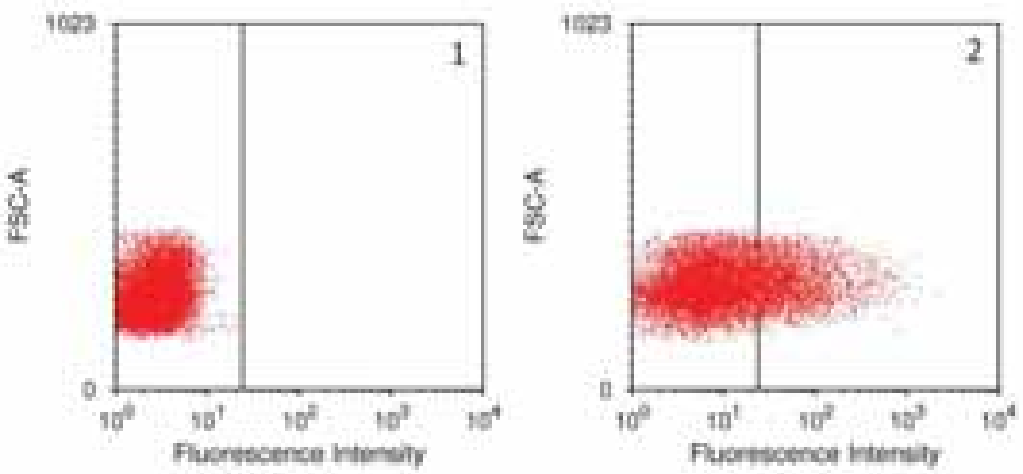

Figure D

PLGA NPs size variation during surface modification (1) and DLS size distribution (2).

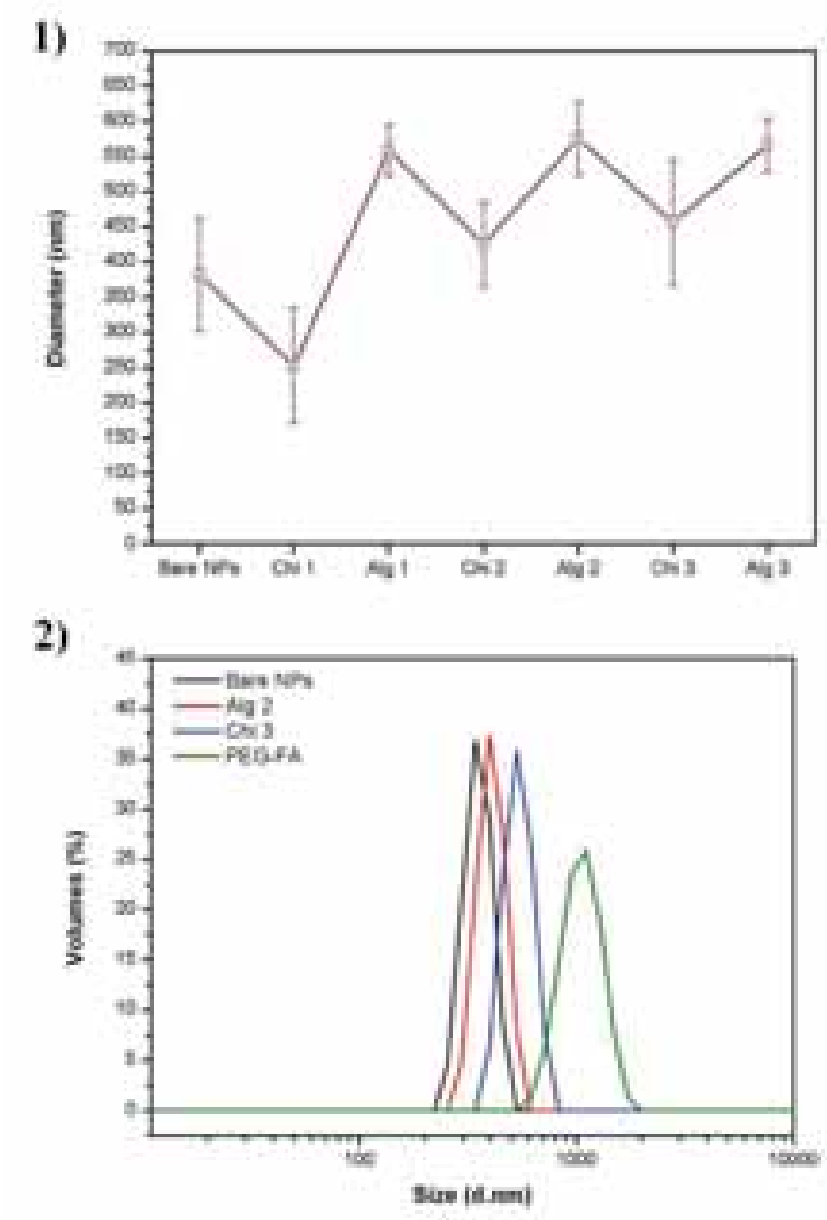

Figure E

Fluorescence Intensity of Rd6G labeled PLGA NPs stabilized with : (1) PEI and (2) BSA.

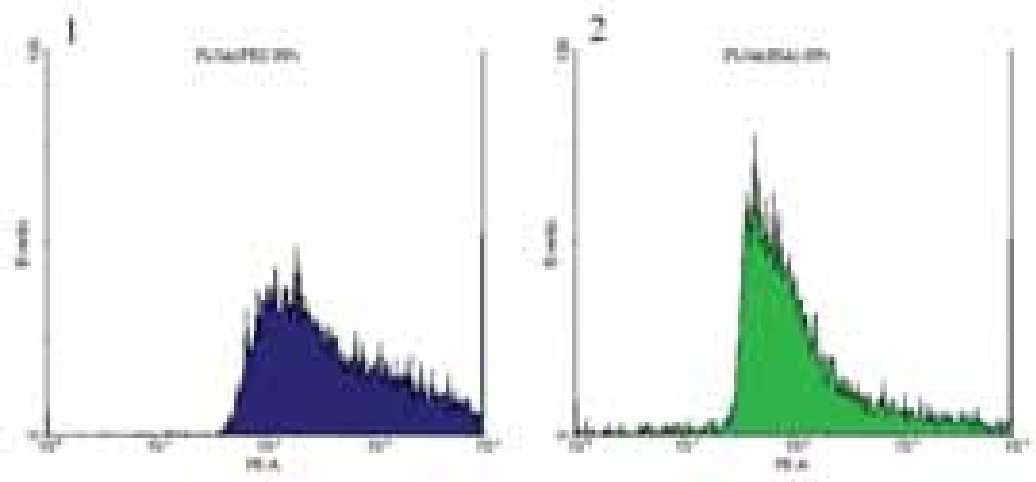

References

[1] E. Hutter, D. Maysinger, *Microscopy Research and Technique* **2011**, *74*, 592.

[2] H. C. Huang, S. Barua, G. Sharma, S. K. Dey, K. Rege, *Journal of Controlled Release* **2011**, *155*, 344.

[3] J. L. Vivero-Escoto, Y. T. Huang, *International Journal of Molecular Sciences* **2011**, *12*, 3888.

[4] S. Jain, D. G. Hirst, J. M. O'Sullivan, *British Journal of Radiology* **2012**, *85*, 101.

[5] M. Mahmoudi, V. Serpooshan, S. Laurent, *Nanoscale* **2011**, *3*, 3007.

[6] M. De, S. S. Chou, H. M. Joshi, V. P. Dravid, *Advanced Drug Delivery Reviews* **2011**, *63*, 1282.

[7] K. H. Bae, H. J. Chung, T. G. Park, *Molecules and Cells* **2011**, *31*, 295.

[8] F. Sonvico, C. Dubernet, P. Colombo, P. Couvreur, *Current Pharmaceutical Design* **2005**, *11*, 2091.

[9] X. Luo, A. Morrin, A. J. Killard, M. R. Smyth, *Electroanalysis* **2006**, *18*, 319.

[10] R. Brayner, Vol. 2, **2006**, 241.

[11] T. Asefa, C. T. Duncan, K. K. Sharma, *Analyst* **2009**, *134*, 1980.

[12] X. N. Wang, P. A. Hu, *Frontiers of Materials Science* **2012**, *6*, 26.

[13] K. Balasubramanian, T. Kurkina, A. Ahmad, M. Burghard, K. Kern, *Journal of Materials Research* **2012**, *27*, 391.

[14] S. Hyun, T. H. Park, *Biotechnology Journal* **2011**, *6*, 1310.

[15] M. S. Artiles, C. S. Rout, T. S. Fisher, *Advanced Drug Delivery Reviews* **2011**, *63*, 1352.

[16] T. Premkumar, K. E. Geckeler, *Progress in Polymer Science (Oxford)* **2012**, *37*, 515.

[17] T. Kuila, S. Bose, P. Khanra, A. K. Mishra, N. H. Kim, J. H. Lee, *Biosensors and Bioelectronics* **2011**, *26*, 4637.

[18] M. Pumera, *Materials Today* **2011**, *14*, 308.

[19] M. Vallet-Regí, E. Ruiz-Hernández, *Advanced Materials* **2011**, *23*, 5177.

[20] M. Deng, S. G. Kumbar, K. W. H. Lo, B. D. Ulery, C. T. Laurencin, *Recent Patents on Biomedical Engineering* **2011**, *4*, 168.

[21] C. V. Rahman, A. Saeed, L. J. White, T. W. A. Gould, G. T. S. Kirby, M. J. Sawkins, C. Alexander, F. R. A. J. Rose, K. M. Shakesheff, *Chemistry of Materials* **2012**, *24*, 781.

[22] A. O. El-Sadik, A. El-Ansary, S. M. Sabry, Vol. 2, **2010**, 9.

[23] L. Yang, T. J. Webster, *Expert Opinion on Drug Delivery* **2009**, *6*, 851.

[24] M. Elfinger, S. Üzün, C. Rudolph, *Current Nanoscience* **2008**, *4*, 322.

[25] L. Zhang, T. J. Webster, *Nano Today* **2009**, *4*, 66.

[26] S. L. Edwards, J. A. Werkmeister, J. A. M. Ramshaw, *Expert Review of Medical Devices* **2009**, *6*, 499.

[27] K. Sahithi, M. Swetha, K. Ramasamy, N. Srinivasan, N. Selvamurugan, *International Journal of Biological Macromolecules* **2010**, *46*, 281.

[28] H. Haniu, N. Saito, Y. Matsuda, T. Tsukahara, Y. Usui, N. Narita, K. Hara, K. Aoki, M. Shimizu, N. Ogihara, S. Takanashi, M. Okamoto, S. Kobayashi, N. Ishigaki, K. Nakamura, H. Kato, *Journal of Nanomaterials* **2012**, *2012*.

[29] E. Amstad, M. Textor, E. Reimhult, *Nanoscale* **2011**, *3*, 2819.

[30] R. R. Arvizo, S. Bhattacharyya, R. A. Kudgus, K. Giri, R. Bhattacharya, P. Mukherjee, *Chemical Society Reviews* **2012**, *41*, 2943.

[31] S. Bhattacharyya, R. A. Kudgus, R. Bhattacharya, P. Mukherjee, *Pharmaceutical Research* **2011**, *28*, 237.

[32] C. S. S. R. Kumar, F. Mohammad, *Advanced Drug Delivery Reviews* **2011**, *63*, 789.

[33] S. Rana, A. Bajaj, R. Mout, V. M. Rotello, *Advanced Drug Delivery Reviews* **2012**, *64*, 200.

[34] M. Ding, J. Li, H. Tan, Q. Fu, *Soft Matter* **2012**, *8*, 5414.

[35] S. P. Egusquiaguirre, M. Igartua, R. M. Hernández, J. L. Pedraz, *Clinical and Translational Oncology* **2012**, *14*, 83.

[36] T. Patel, J. Zhou, J. M. Piepmeier, W. M. Saltzman, *Advanced Drug Delivery Reviews* **2012**, *64*, 701.

[37] C. Prabhakar, K. Bala Krishna, *Research Journal of Pharmacy and Technology* **2011**, *4*, 496.

[38] J. Gong, M. Chen, Y. Zheng, S. Wang, Y. Wang, *Journal of Controlled Release* **2012**, *159*, 312.

[39] X. B. Xiong, Z. Binkhathlan, O. Molavi, A. Lavasanifar, *Acta Biomaterialia* **2012**, *8*, 2017.

[40] J. Liu, W. D. Gray, M. E. Davis, Y. Luo, *Interface Focus* **2012**, *2*, 307.

[41] M. Sun, A. Fan, Z. Wang, Y. Zhao, *Soft Matter* **2012**, *8*, 4301.

[42] I. A. Syed, Y. M. Rao, *Research Journal of Pharmacy and Technology* **2012**, *5*, 307.

[43] R. E. Wang, F. Costanza, Y. Niu, H. Wu, Y. Hu, W. Hang, Y. Sun, J. Cai, *Journal of Controlled Release* **2012**, *159*, 154.

[44] K. Buyens, S. C. De Smedt, K. Braeckmans, J. Demeester, L. Peeters, L. A. Van Grunsven, X. De Mollerat Du Jeu, R. Sawant, V. Torchilin, K. Farkasova, M. Ogris, N. N. Sanders, *Journal of Controlled Release* **2012**, *158*, 362.

[45] M. R. Micheli, R. Bova, A. Magini, M. Polidoro, C. Emiliani, *Recent Patents on CNS Drug Discovery* **2012**, *7*, 71.

[46] C. Puglia, F. Bonina, *Expert Opinion on Drug Delivery* **2012**, *9*, 429.

[47] J. L. Cuellar, F. Meinhoevel, M. Hoehne, E. Donath, *Journal of General Virology* **2010**, *91*, 2449.

[48] M. Fischlechner, U. Reibetanz, M. Zaulig, D. Enderlein, J. Romanova, S. Leporatti, S. Moya, E. Donath, *Nano Letters* **2007**, *7*, 3540.

[49] D. A. Gomez-Gualdrón, J. C. Burgos, J. Yu, P. B. Balbuena, Vol. 104, **2011**, 175.

[50] Z. Liu, J. T. Robinson, S. M. Tabakman, K. Yang, H. Dai, *Materials Today* **2011**, *14*, 316.

[51] N. Mali, S. Jadhav, M. Karpe, V. Kadam, *International Journal of Pharmacy and Pharmaceutical Sciences* **2011**, *3*, 45.

[52] S. Prakash, M. Malhotra, W. Shao, C. Tomaro-Duchesneau, S. Abbasi, *Advanced Drug Delivery Reviews* **2011**, *63*, 1340.

[53] L. Brannon-Peppas, J. O. Blanchette, *Advanced Drug Delivery Reviews* **2004**, *56*, 1649.

[54] J. C. Leroux, E. AllÃ©mann, F. De Jaeghere, E. Doelker, R. Gurny, *Journal of Controlled Release* **1996**, *39*, 339.

[55] G. Storm, S. O. Belliot, T. Daemen, D. D. Lasic, *Advanced Drug Delivery Reviews* **1995**, *17*, 31.

[56] V. P. Torchilin, V. S. Trubetskoy, *Advanced Drug Delivery Reviews* **1995**, *16*, 141.

[57] Y. Cheng, A. C. Samia, J. Li, M. E. Kenney, A. Resnick, C. Burda, *Langmuir* **2010**, *26*, 2248.

[58] Y. Liu, S. Franzen, *Bioconjugate Chemistry* **2008**, *19*, 1009.

[59] G. F. Paciotti, L. Myer, D. Weinreich, D. Goia, N. Pavel, R. E. McLaughlin, L. Tamarkin, *Drug Delivery: Journal of Delivery and Targeting of Therapeutic Agents* **2004**, *11*, 169.

[60] U. Reibetanz, C. Claus, E. Typlt, J. Hofmann, E. Donath, *Macromolecular Bioscience* **2006**, *6*, 153.

[61] C. M. Jewell, D. M. Lynn, *Advanced Drug Delivery Reviews* **2008**, *60*, 979.

[62] G. B. Sukhorukov, H. Möhwald, *Trends in Biotechnology* **2007**, *25*, 93.

[63] Y. Ikeda, Y. Nagasaki, Vol. 247, **2012**, 115.

[64] R. H. Müller, S. Gohla, C. M. Keck, *European Journal of Pharmaceutics and Biopharmaceutics*, *78*, 1.

[65] J. P. Rolland, E. C. Hagberg, G. M. Denison, K. R. Carter, J. M. De Simone, *Angewandte Chemie International Edition* **2004**, *43*, 5796.

[66] J. P. Rolland, B. W. Maynor, L. E. Euliss, A. E. Exner, G. M. Denison, J. M. DeSimone, *Journal of the American Chemical Society* **2005**, *127*, 10096.

[67] P. H. Nelson, G. C. Rutledge, T. A. Hatton, *Journal of Chemical Physics* **1997**, *107*, 10777.

[68] G. r. Riess, *Progress in Polymer Science* **2003**, *28*, 1107.

[69] J. Zhu, Z. Zhou, C. Yang, D. Kong, Y. Wan, Z. Wang, *Journal of Biomedical Materials Research Part A*, *97A*, 498.

[70] U. Kedar, P. Phutane, S. Shidhaye, V. Kadam, *Nanomedicine: Nanotechnology, Biology and Medicine*, *6*, 714.

[71] T. S. Davies, A. M. Ketner, S. R. Raghavan, *Journal of the American Chemical Society* **2006**, *128*, 6669.

[72] T. Imura, H. Yanagishita, J. Ohira, H. Sakai, M. Abe, D. Kitamoto, *Colloids and Surfaces B: Biointerfaces* **2005**, *43*, 115.

[73] M. J. Hope, M. B. Bally, L. D. Mayer, A. S. Janoff, P. R. Cullis, *Chemistry and Physics of Lipids* **1986**, *40*, 89.

[74] L. A. Maguire, H. Zhang, P. A. Shamlou, *Biotechnol. Applied Biochemistry* **2003**, *37*, 73.

[75] S. Šegota, Đ. Težak, *Advances in Colloid and Interface Science* **2006**, *121*, 51.

[76] S. Camelo, L. Lajavardi, A. Bochot, B. Goldenberg, M. C. Naud, N. Brunel, *J. Ocul. Pharmacol. Ther.* **2009**, *25*, 9.

[77] D. E. Discher, F. Ahmed, *Annual Review of Biomedical Engineering* **2006**, *8*, 323.

[78] D. A. Christian, S. Cai, D. M. Bowen, Y. Kim, J. D. Pajerowski, D. E. Discher, *European Journal of Pharmaceutics and Biopharmaceutics* **2009**, *71*, 463.

[79] N. A. Christian, M. C. Milone, S. S. Ranka, G. Li, P. R. Frail, K. P. Davis, F. S. Bates, M. J. Therien, P. P. Ghoroghchian, C. H. June, D. A. Hammer, *Bioconjugate Chemistry* **2006**, *18*, 31.

[80] H. Ringsdorf, *Journal of Polymer Science: Polymer Symposia* **1975**, *51*, 135.

[81] R. Duncan, M. J. Vicent, F. Greco, R. I. Nicholson, *Endocrine-Related Cancer* **2005**, *12*, S189.

[82] R. Haag, F. Kratz, *Angewandte Chemie International Edition* **2006**, *45*, 1198.

[83] M. a. J. Vicent, R. Duncan, *Trends in Biotechnology* **2006**, *24*, 39.

[84] R. Duncan, H. Ringsdorf, R. Satchi-Fainaro, R. Satchi-Fainaro, R. Duncan, Vol. 192, Springer Berlin / Heidelberg, **2006**, 1.

[85] B. Klajnert, M. Bryszewska, *Acta biochimica Polonica* **2001**, *48*, 199.

[86] E. R. Gillies, J. M. J. FrÃ©chet, *Drug Discovery Today* **2005**, *10*, 35.

[87] C. Dufès, I. F. Uchegbu, A. G. Schätzlein, *Advanced Drug Delivery Reviews* **2005**, *57*, 2177.

[88] J. M. Oliveira, A. n. J. Salgado, N. Sousa, J. o. F. Mano, R. L. s. Reis, *Progress in Polymer Science*, *35*, 1163.

[89] E. Donath, G. B. Sukhorukov, F. Caruso, S. A. Davis, H. Möhwald, *Angewandte Chemie International Edition* **1998**, *37*, 2201.

[90] F. Caruso, R. A. Caruso, H. Möhwald, *Science* **1998**, *282*, 1111.

[91] E. Donath, S. Moya, B. Neu, G. B. Sukhorukov, R. Georgieva, A. Voigt, H. Bäumler, H. Kiesewetter, H. Möhwald, *Chemistry – A European Journal* **2002**, *8*, 5481.

[92] C. Gao, E. Donath, S. Moya, V. Dudnik, H. Möhwald, *European Physical Journal E* **2001**, *5*, 21.

[93] C. Gao, S. Leporatti, S. Moya, E. Donath, H. Möhwald, *Langmuir* **2001**, *17*, 3491.

[94] C. Gao, S. Moya, E. Donath, H. Möhwald, *Macromolecular Chemistry and Physics* **2002**, *203*, 953.

[95] S. Moya, E. Donath, G. B. Sukhorukov, M. Auch, H. BÃ¤umler, H. Lichtenfeld, H. Möhwald, *Macromolecules* **2000**, *33*, 4538.

[96] J. Zhou, S. Moya, L. Ma, C. Gao, J. Shen, *Macromolecular Bioscience* **2009**, *9*, 326.

[97] J. Zhou, G. Romero, E. Rojas, S. Moya, L. Ma, C. Gao, *Macromolecular Chemistry and Physics* **2010**, *211*, 404.

[98] J. Zhou, G. Romero, E. Rojas, L. Ma, S. Moya, C. Gao, *Journal of Colloid and Interface Science* **2010**, *345*, 241.

[99] E.-L. I. Romero G., Zhou J., Rojas E., Franco A., Sanchez Espinal C., González Fernández A., Gao C., Donath E. and Moya S., *Biomacromolecules* **2010**, *11*, 2993.

[100] E. Allémann, R. Gurny, E. Doelker, *International Journal of Pharmaceutics* **1992**, *87*, 247.

[101] E. Allémann, J. C. Leroux, R. Gurny, E. Doelker, *Pharmaceutical Research* **1993**, *10*, 1732.

[102] M. F. Zambaux, F. Bonneaux, R. Gref, E. Dellacherie, C. Vigneron, *Journal of Controlled Release* **1999**, *60*, 179.

[103] Z. Wang, C. Tiruppathi, R. D. Minshall, A. B. Malik, *ACS Nano* **2009**, *3*, 4110.

[104] C. Pinto Reis, R. J. Neufeld, A. n. J. Ribeiro, F. Veiga, *Nanomedicine: Nanotechnology, Biology and Medicine* **2006**, *2*, 8.

[105] M. F. Zambaux, F. Bonneaux, R. Gref, P. Maincent, E. Dellacherie, M. J. Alonso, P. Labrude, C. Vigneron, *Journal of Controlled Release* **1998**, *50*, 31.

[106] L. L. Yuan X. D., Rathinavelu A., Hao J. S., Narasimhan M., He M., Heitlage V., Tam L., Viqar S. and Salehi M., *Journal of Nanoscience and Nanotechnology* **2006**, *6*, 2821.

[107] G. Crotts, H. Sah, T. G. Park, *Journal of Controlled Release* **1997**, *47*, 101.

[108] J. Panyam, V. Labhasetwar, *Advanced Drug Delivery Reviews* **2003**, *55*, 329.

[109] P. D. Scholes, A. G. A. Coombes, L. Illum, S. S. Davis, M. Vert, M. C. Davies, *Journal of Controlled Release* **1993**, *25*, 145.

[110] B. Weiss, M. Schneider, L. Muys, S. Taetz, D. Neumann, U. F. Schaefer, C. M. Lehr, *Bioconjugate Chemistry* **2007**, *18*, 1087.

[111] R. C. Mundargi, V. R. Babu, V. Rangaswamy, P. Patel, T. M. Aminabhavi, *Journal of Controlled Release* **2008**, *125*, 193.

[112] I. Bala, S. Hariharan, M. N. V. R. Kumar, *Critical Reviews in Therapeutic Drug Carrier Systems* **2004**, *21*, 387.

[113] T. G. Park, *Journal of Controlled Release* **1994**, *30*, 161.

[114] K. A. Athanasiou, G. G. Niederauer, C. M. Agrawal, *Biomaterials* **1996**, *17*, 93.

[115] J. Panyam, M. M. Dali, S. K. Sahoo, W. Ma, S. S. Chakravarthi, G. L. Amidon, R. J. Levy, V. Labhasetwar, *Journal of Controlled Release* **2003**, *92*, 173.

[116] N. Faisant, J. Akiki, F. Siepmann, J. P. Benoit, J. Siepmann, *International Journal of Pharmaceutics* **2006**, *314*, 189.

[117] J. Siepmann, N. Faisant, J. Akiki, J. Richard, J. P. Benoit, *Journal of Controlled Release* **2004**, *96*, 123.

[118] Y. Liu, H. Miyoshi, M. Nakamura, *International Journal of Cancer* **2007**, *120*, 2527.

[119] H. Fessi, F. Piusieux, J. P. Devissaguet, N. Ammoury, S. Benita, *International Journal of Pharmaceutics* **1989**, *55*, R1.

[120] P. B. O'Donnell, J. W. McGinity, *Advanced Drug Delivery Reviews* **1997**, *28*, 25.

[121] A. L. Doiron, K. A. Homan, S. Emelianov, L. Brannon-Peppas, *Pharmaceutical Research* **2009**, *26*, 674.

[122] C. D. Anderson, E. S. Daniels, *Rapra Rev. Rep.* **2003**, *14*, 3.

[123] T. Trimaille, C. Pichot, A. Elaïssari, H. Fessi, S. Briançon, T. Delair, *Colloid & Polymer Science* **2003**, *281*, 1184.

[124] J. Liu, Z. Qiu, S. Wang, L. Zhou, S. Zhang, *Biomedical Materials* **2010**, *5*, 065002.

[125] S. Schubert, J. J. T. Delaney, U. S. Schubert, *Soft Matter*, *7*, 1581.

[126] Y. Cirpanli, F. Yerlikaya, K. Ozturk, N. Erdogar, M. Launay, C. Gegu, T. Leturgez, E. Bilensoy, S. Calis, Y. Capan, *Pharmazie* **2010**, *65*, 867.

[127] S. A. Galindo-Rodriguez, F. Puel, S. Briancon, E. Allemann, E. Doelker, H. Fessi, *European Journal of Pharmaceutical Science* **2005**, *25*, 357.

[128] L. E. van Vlerken, Z. Duan, S. R. Little, M. V. Seiden, M. M. Amiji, *Molecular Pharmaceutics* **2008**, *5*, 516.

[129] L. Mu, S. S. Feng, *Journal of Controlled Release* **2003**, *86*, 33.

[130] V. Bhardwaj, D. Ankola, S. Gupta, M. Schneider, C. M. Lehr, M. Kumar, *Pharmaceutical Research* **2009**, *26*, 2495.

[131] T. Musumeci, C. A. Ventura, I. Giannone, B. Ruozi, L. Montenegro, R. Pignatello, G. Puglisi, *International Journal of Pharmaceutics* **2006**, *325*, 172.

[132] J. Cheng, B. A. Teply, I. Sherifi, J. Sung, G. Luther, F. X. Gu, E. Levy-Nissenbaum, A. F. Radovic-Moreno, R. Langer, O. C. Farokhzad, *Biomaterials* **2007**, *28*, 869.

[133] G. Mattheolabakis, E. Taoufik, S. Haralambous, M. L. Roberts, K. Avgoustakis, *European Journal of Pharmaceutics and Biopharmaceutics* **2009**, *71*, 190.

[134] R. Manchanda, A. Fernandez-Fernandez, A. Nagesetti, A. J. McGoron, *Colloids and Surfaces B: Biointerfaces*, *75*, 260.

[135] T. Betancourt, B. Brown, L. Brannon-Peppas, *Nanomedicine* **2007**, *2*, 219.

[136] A. Mukerjee, J. K. Vishwanatha, *Anticancer Research* **2009**, *29*, 3867.

[137] M. M. Yallapu, B. K. Gupta, M. Jaggi, S. C. Chauhan, *Journal of Colloid and Interface Science* **2010**, *351*, 19.

[138] R. Dinarvand, N. Sepehri, S. Manoochehri, H. Rouhani, F. Atyabi, *International journal of nanomedicine* **2011**, *6*, 877.

[139] M. Zeisser-Labouèbe, N. Lange, R. Gurny, F. Delie, *International Journal of Pharmaceutics* **2006**, *326*, 174.

[140] E. Ricci-Júnior, J. M. Marchetti, *International Journal of Pharmaceutics* **2006**, *310*, 187.

[141] L. Hong, X. Chuan, N. Srivastava, K. Banerjee, *Electron Devices, IEEE Transactions on* **2009**, *56*, 1799.

[142] M. Sharon, *Defence Science Journal* **2008**, *58*, 460.

[143] Z. Liu, J. T. Robinson, S. M. Tabakman, K. Yang, H. Dai, *Materials Today* **2011**, *14*, 316.

[144] K. P. Loh, Q. Bao, K. P. Ang, J. Yang, *Journal of Materials Chemistry* **2010**, *20*, 2277.

[145] D. Tasis, N. Tagmatarchis, A. Bianco, M. Prato, *Chemical Reviews* **2006**, *106*, 1105.

[146] H. W. Kroto, J. R. Heath, S. C. O'Brien, R. F. Curl, R. E. Smalley, *Nature* **1985**, *318*, 162.

[147] S. Iijima, *Nature* **1991**, *354*, 56.

[148] K. S. Novoselov, A. K. Geim, S. V. Morozov, D. Jiang, Y. Zhang, S. V. Dubonos, I. V. Grigorieva, A. A. Firsov, *Science* **2004**, *306*, 666.

[149] M. Foldvari, *http://science.uwaterloo.ca/~foldvari/research_program/index.html* **April 2012**.

[150] A. Ilie, J. S. Bendall, O. Kubo, J. Sloan, M. L. H. Green, *Physical Review B - Condensed Matter and Materials Physics* **2006**, *74*.

[151] M. Uo, T. Akasaka, F. Watari, Y. Sato, K. Tohji, *Dental Materials Journal* **2011**, *30*, 245.

[152] G. Jia, H. Wang, L. Yan, X. Wang, R. Pei, T. Yan, Y. Zhao, X. Guo, *Environmental Science & Technology* **2005**, *39*, 1378.

[153] A. Magrez, S. Kasas, V. Salicio, N. Pasquier, J. W. Seo, M. Celio, S. Catsicas, B. Schwaller, L. Forró, *Nano Letters* **2006**, *6*, 1121.

[154] R. H. Hurt, M. Monthioux, A. Kane, *Carbon* **2006**, *44*, 1028.

[155] G. Romero, I. Estrela-Lopis, P. Castro-Hartmann, E. Rojas, I. Llarena, D. Sanz, E. Donath, S. E. Moya, *Soft Matter* **2011**, *7*, 6883.

[156] W. Yang, K. R. Ratinac, S. P. Ringer, P. Thordarson, J. J. Gooding, F. Braet, *Angewandte Chemie International Edition* **2010**, *49*, 2114.

[157] H.-C. Wu, X. Chang, L. Liu, F. Zhao, Y. Zhao, *Journal of Materials Chemistry* **2010**, *20*, 1036.

[158] A. Bianco, M. Prato, *Advanced Materials* **2003**, *15*, 1765.

[159] H. Jiang, *Small* **2011**, *7*, 2413.

[160] P. Wick, M. J. D. Clift, M. Rösslein, B. Rothen-Rutishauser, *ChemSusChem* **2011**, *4*, 905.

[161] J. V. Veetil, K. Ye, *Biotechnology Progress* **2009**, *25*, 709.

[162] D. Pantarotto, R. Singh, D. McCarthy, M. Erhardt, J.-P. Briand, M. Prato, K. Kostarelos, A. Bianco, *Angewandte Chemie International Edition* **2004**, *43*, 5242.

[163] D. Jagadeesan, M. Eswaramoorthy, *Chemistry – An Asian Journal* **2010**, *5*, 232.

[164] S. Banerjee, S. S. Wong, *The Journal of Physical Chemistry B* **2002**, *106*, 12144.

[165] K. Balasubramanian, M. Burghard, *Small* **2005**, *1*, 180.

[166] J. Q. Liu, T. Xiao, K. Liao, P. Wu, *Nanotechnology* **2007**, *18*.

[167] G. Decher, J. D. Hong, J. Schmitt, *Thin Solid Films* **1992**, *210-211*, 831.

[168] G. Decher, *Science* **1997**, *277*, 1232.

[169] S. T. Dubas, J. B. Schlenoff, *Macromolecules* **1999**, *32*, 8153.

[170] J. B. Schlenoff, S. T. Dubas, *Macromolecules* **2001**, *34*, 592.

[171] X. Arys, A. Laschewsky, A. M. Jonas, *Macromolecules* **2001**, *34*, 3318.

[172] B. Schoeler, G. Kumaraswamy, F. Caruso, *Macromolecules* **2002**, *35*, 889.

[173] N. G. Balabushevitch, G. B. Sukhorukov, N. A. Moroz, D. V. Volodkin, N. I. Larionova, E. Donath, H. Mohwald, *Biotechnology and Bioengineering* **2001**, *76*, 207.

[174] G. Berth, A. Voigt, H. Dautzenberg, E. Donath, H. Möhwald, *Biomacromolecules* **2002**, *3*, 579.

[175] X. Su, B.-S. Kim, S. R. Kim, P. T. Hammond, D. J. Irvine, *ACS Nano* **2009**, *3*, 3719.

[176] T. Mauser, C. Déjugnat, G. B. Sukhorukov, *Macromolecular Rapid Communications* **2004**, *25*, 1781.

[177] S. Moya, L. DÃ¤hne, A. Voigt, S. Leporatti, E. Donath, H. MÃ¶hwald, *Colloids and Surfaces A: Physicochemical and Engineering Aspects* **2001**, *183â€“185*, 27.

[178] M.-K. Park, C. Xia, R. C. Advincula, P. SchÃ¼tz, F. Caruso, *Langmuir* **2001**, *17*, 7670.

[179] A. B. Artyukhin, A. Shestakov, J. Harper, O. Bakajin, P. Stroeve, A. Noy, *Journal of the American Chemical Society* **2005**, *127*, 7538.

[180] M. Delcea, A. Yashchenok, K. Videnova, O. Kreft, H. Möhwald, A. G. Skirtach, *Macromolecular Bioscience* **2010**, *10*, 465.

[181] D. V. Volodkin, A. I. Petrov, M. Prevot, G. B. Sukhorukov, *Langmuir* **2004**, *20*, 3398.

[182] O. Shchepelina, V. Kozlovskaya, E. Kharlampieva, W. Mao, A. Alexeev, V. V. Tsukruk, *Macromolecular Rapid Communications* **2010**, *31*, 2041.

[183] D. I. Gittins, F. Caruso, *Advanced Materials* **2000**, *12*, 1947.

[184] F. Cuomo, F. Lopez, M. G. Miguel, B. Lindman, *Langmuir* **2010**, *26*, 10555.

[185] S. Moya, E. Donath, G. B. Sukhorukov, M. Auch, H. Bäumler, H. Lichtenfeld, H. Möhwald, *Macromolecules* **2000**, *33*, 4538.

[186] S. S. Balkundi, N. G. Veerabadran, D. M. Eby, G. R. Johnson, Y. M. Lvov, *Langmuir* **2009**, *25*, 14011.

[187] S. T. Milner, *Science* **1991**, *251*, 905.

[188] K. Matyjaszewski, J. Xia, *Chemical Reviews* **2001**, *101*, 2921.

[189] J. Pyun, T. Kowalewski, K. Matyjaszewski, *Macromolecular Rapid Communications* **2003**, *24*, 1043.

[190] R. J. Hunter, *London, Academic Press* **1981**.

[191] W. B. Russel, D. A. Saville, W. R. Schowalter, *Cambridge Univerity Press* **1989**, *1*.

[192] M. von Smoluchowski, *Bull. Int. Acad.. Sci. Cracovie* **1904**, 182.

[193] W. Licht, *T. Allen, Chapman and Hall, London* **1976**, *22*, 202.

[194] R. Erni, M. D. Rossell, C. Kisielowski, U. Dahmen, *Physical Review Letters* **2009**, *102*, 096101.

[195] M. A. O'Keefe, L. F. Allard, *DOE Scientific and Technical Information by OSTI* **2010**.

[196] S. Skujins, *Agilent Technologies, Varian A. G.* **1986**, *1, 2*.

[197] J. R. Lakowicz, *Kluwer Academic/Plenium Publishers* **1999**.

[198] S. Weiss, *Science* **1999**, *283*, 1676.

[199] A. Domack, O. Prucker, J. r. RÃ¼he, D. Johannsmann, *Physical Review E* **1997**, *56*, 680.

[200] M. V. V. a. M. R. a. M. J. a. B. Kasemo, *Physica Scripta* **1999**, *59*, 391.

[201] G. Sauerbrey, *Zeitschrift für Physik* **1959**, *155*, 206.

[202] C. V. Raman, K. S. Krishnan, *Nature* **1928**, *121*, 501.

[203] W. A. P. Luck, *Berichte der Bunsengesellschaft für physikalische Chemie* **1990**, *94*, 1047.

[204] T. I. Sideroudi, N. M. Pharmakakis, G. N. Papatheodorou, G. A. Voyiatzis, *Lasers in Surgery and Medicine* **2006**, *38*, 695.

[205] P. Vesely, *Scanning* **2007**, *29*, 91.

[206] T. J. Fellers, M. W. Davidson, *Olympus Coorporation* **2009**.

[207] N. S. Claxton, T. J. Fellers, M. W. Davidson, in *Encyclopedia of Medical Devices and Instrumentation*, John Wiley & Sons, Inc., **2006**.

[208] G. Cox, C. J. R. Sheppard, *Microscopy Research and Technique* **2004**, *63*, 18.

[209] A. L. Givan, in *Chapter 3 to 5*, John Wiley & Sons, Inc., **2001**.

[210] J. P. Robinson, *Wiley* **1993**.

[211] M.-B. A. Ashour, S. J. Gee, B. D. Hammock, *Analytical Biochemistry* **1987**, *166*, 353.

[212] T. Mosmann, *Journal of Immunological Methods* **1983**, *65*, 55.

[213] C. M. Stoscheck, P. D. Murray, in *Methods in Enzymology*, Vol. 182, Academic Press, **1990**, 50.

[214] H. M. Lorenz, *Curr. Opin. mol. Ther.* **2002**, *4*, 185.

[215] L. Costantino, F. Gandolfi, G. Tosi, F. Rivasi, M. A. Vandelli, F. Forni, *Journal of Controlled Release* **2005**, *108*, 84.

[216] A. Ambruosi, S. Gelperina, A. Khalansky, S. Tanski, A. Theisen, J. r. Kreuter, *Journal of Microencapsulation* **2006**, *23*, 582.

[217] J. M. Koziara, P. R. Lockman, D. D. Allen, R. J. Mumper, *Journal of Controlled Release* **2004**, *99*, 259.

[218] S. Pollock, R. Antrobus, L. Newton, B. Kampa, J. Rossa, S. Latham, N. B. Nichita, R. A. Dwek, N. Zitzmann, *The FASEB Journal* **2010**.

[219] P. B. Fischer, M. Collin, G. B. Karlsson, W. James, T. D. Butters, S. J. Davis, S. Gordon, R. A. Dwek, F. M. Platt, *Journal of Virology* **1995**, *69*, 5791.

[220] E. Steinmann, T. Whitfield, S. Kallis, R. A. Dwek, N. Zitzmann, T. Pietschmann, R. Bartenschlager, *Hepatology* **2007**, *46*, 330.

[221] T. M. Block, X. Lu, F. M. Platt, G. R. Foster, W. H. Gerlich, B. S. Blumberg, R. A. Dwek, *Proceedings of the National Academy of Sciences* **1994**, *91*, 2235.

[222] H. Sneh-Edri, D. Stepensky, *Biochemical and Biophysical Research Communications* **2011**, *405*, 228.

[223] P. Kocbek, N. Obermajer, M. Cegnar, J. Kos, J. Kristl, *Journal of Controlled Release* **2007**, *120*, 18.

[224] P. A. McCarron, W. M. Marouf, D. J. Quinn, F. Fay, R. E. Burden, S. A. Olwill, C. J. Scott, *Bioconjugate Chemistry* **2008**, *19*, 1561.

[225] B. Sun, B. Ranganathan, S.-S. Feng, *Biomaterials* **2008**, *29*, 475.

[226] N. Zhang, C. Chittasupho, C. Duangrat, T. J. Siahaan, C. Berkland, *Bioconjugate Chemistry* **2007**, *19*, 145.

[227] Z. Zhang, S. Huey Lee, S.-S. Feng, *Biomaterials* **2007**, *28*, 1889.

[228] H. Zhao, L. Y. L. Yung, *International Journal of Pharmaceutics* **2008**, *349*, 256.

[229] S.-W. Choi, J.-H. Kim, *Journal of Controlled Release* **2007**, *122*, 24.

[230] F. Meng, G. H. M. Engbers, J. Feijen, *Journal of Biomedical Materials Research Part A* **2004**, *70A*, 49.

[231] E. Donath, A. Budde, E. Knippel, H. Bäumler, *Langmuir* **1996**, *12*, 4832.

[232] J.-C. Leroux, P. Gravel, L. Balant, B. Volet, B. M. Anner, E. Allémann, E. Doelker, R. Gurny, *Journal of Biomedical Materials Research* **1994**, *28*, 471.

[233] J.-C. Leroux, F. De Jaeghere, B. Anner, E. Doelker, R. Gurny, *Life Sciences* **1995**, *57*, 695.

[234] E. Allémann, P. Gravel, J. C. Leroux, L. Balant, R. Gurny, *Journal of Biomedical Materials Research* **1997**, *37*, 229.

[235] D. Lechardeur, A. S. Verkman, G. L. Lukacs, *Advanced Drug Delivery Reviews* **2005**, *57*, 755.

[236] H. Mokuno, N. Yamada, H. Shimano, S. Ishibashi, N. Mori, K. Takahashi, T. Oka, T. H. Yoon, F. Takaku, *Biochimica et Biophysica Acta - Lipids and Lipid Metabolism* **1991**, *1082*, 63.

[237] W. Zauner, N. A. Farrow, A. M. R. Haines, *Journal of Controlled Release* **2001**, *71*, 39.

[238] T. Blunk, D. F. Hochstrasser, J.-C. Sanchez, B. W. Müller, R. H. Müller, *ELECTROPHORESIS* **1993**, *14*, 1382.

[239] E. Donath, S. Moya, B. Neu, G. B. Sukhorukov, R. Georgieva, A. Voigt, H. Baumler, H. Kiesewetter, H. Möhwald, *Chemistry - A European Journal* **2002**, *8*, 5481.

[240] N. Kohler, G. E. Fryxell, M. Zhang, *Journal of the American Chemical Society* **2004**, *126*, 7206.

[241] C. Sun, R. Sze, M. Zhang, *Journal of Biomedical Materials Research Part A* **2006**, *78A*, 550.

[242] F. Sonvico, S. p. Mornet, S. b. Vasseur, C. Dubernet, D. Jaillard, J. Degrouard, J. Hoebeke, E. Duguet, P. Colombo, P. Couvreur, *Bioconjugate Chemistry* **2005**, *16*, 1181.

[243] J. A. Rowley, G. Madlambayan, D. J. Mooney, *Biomaterials* **1999**, *20*, 45.

[244] K. Smetana Jr, *Biomaterials* **1993**, *14*, 1046.

[245] L. A. Maguire, H. Zhang, P. A. Shamlou, *Biotechnology and Applied Biochemistry* **2003**, *37*, 73.

[246] S. Camelo, L. Lajavardi, A. Bochot, B. Goldenberg, M. C. Naud, N. Brunel, B. Lescure, C. Klein, E. Fattal, F. Behar-Cohen, Y. De Kozak, *Journal of Ocular Pharmacology and Therapeutics* **2009**, *25*, 9.

[247] D. D. Lasic, *Handbook of Biological Physics* **1995**, *1*, 491.

[248] M. Reza Mozafari, C. Johnson, S. Hatziantoniou, C. Demetzos, *Journal of Liposome Research* **2008**, *18*, 309.

[249] J. C. Vuillemard, *Journal of Microencapsulation* **1991**, *8*, 547.

[250] K. de Meijere, G. Brezesinski, H. Möhwald, *Macromolecules* **1997**, *30*, 2337.

[251] C. Heibel, S. Maus, W. Knoll, J. Rühe, in *Organic Thin Films*, Vol. 695, American Chemical Society, **1998**, 104.

[252] G. Brezesinski, H. Möhwald, *Advances in Colloid and Interface Science* **2003**, *100-102*, 563.

[253] S. Moya, R. Georgieva, H. Bäumler, W. Richter, E. Donath, *Medical and Biological Engineering and Computing* **2003**, *41*, 504.

[254] M. Fischlechner, E. Donath, *Angewandte Chemie - International Edition* **2007**, *46*, 3184.

[255] M. Fischlechner, L. Toellner, P. Messner, R. Grabherr, E. Donath, *Angewandte Chemie International Edition* **2006**, *45*, 784.

[256] M. Fischlechner, O. Zschörnig, J. Hofmann, E. Donath, *Angewandte Chemie International Edition* **2005**, *44*, 2892.

[257] L. Toellner, M. Fischlechner, B. Ferko, R. M. Grabherr, E. Donath, *Clinical Chemistry* **2006**, *52*, 1575.

[258] P. Watson, A. T. Jones, D. J. Stephens, *Advanced Drug Delivery Reviews* **2005**, *57*, 43.

[259] J.-M. Oh, S.-J. Choi, S.-T. Kim, J.-H. Choy, *Bioconjugate Chemistry* **2006**, *17*, 1411.

[260] P. Xu, E. Gullotti, L. Tong, C. B. Highley, D. R. Errabelli, T. Hasan, J.-X. Cheng, D. S. Kohane, Y. Yeo, *Molecular Pharmaceutics* **2008**, *6*, 190.

[261] S. Park, S. J. Lee, H. Chung, S. Her, Y. Choi, K. Kim, K. Choi, I. C. Kwon, *Microscopy Research and Technique* **2010**, *73*, 857.

[262] A. A. Tokarev, A. Alfonso, N. Segev, *Landes Biosciences and Springer Science+Business Media* **2009**, *1*, 3.

[263] L. M. Bareford, P. W. Swaan, *Advanced Drug Delivery Reviews* **2007**, *59*, 748.

[264] M. G. Qaddoumi, H. J. Gukasyan, J. Davda, V. Labhasetwar, K. J. Kim, V. H. L. Lee, *Molecular Vision* **2003**, *9*, 559.

[265] M. S. Cartiera, K. M. Johnson, V. Rajendran, M. J. Caplan, W. M. Saltzman, *Biomaterials* **2009**, *30*, 2790.

[266] A. G. Ostermeyer, J. M. Paci, Y. Zeng, D. M. Lublin, S. Munro, D. A. Brown, *The Journal of Cell Biology* **2001**, *152*, 1071.

[267] Y. Zhang, L. Hu, D. Yu, C. Gao, *Biomaterials* **2010**, *31*, 8465.

[268] S. Hong, S. Myung, *Nat Nano* **2007**, *2*, 207.

[269] I. Takesue, J. Haruyama, N. Kobayashi, S. Chiashi, S. Maruyama, T. Sugai, H. Shinohara, *Physical Review Letters* **2006**, *96*, 057001.

[270] P. Avouris, Z. Chen, V. Perebeinos, *Nat Nano* **2007**, *2*, 605.

[271] M.-F. Yu, O. Lourie, M. J. Dyer, K. Moloni, T. F. Kelly, R. S. Ruoff, *Science* **2000**, *287*, 637.

[272] X. Lei, T. Natsuki, J. Shi, Q.-Q. Ni, *Journal of Nanomaterials* **2011**, *2011*, 805313.

[273] I. W. Frank, D. M. Tanenbaum, A. M. van der Zande, P. L. McEuen, *Journal of Vacuum Science and Technology B: Microelectronics and Nanometer Structures* **2007**, *25*, 2558.

[274] A. Ilie, J. S. Bendall, O. Kubo, J. Sloan, M. L. H. Green, *Physical Review B* **2006**, *74*, 235418.

[275] E. N. Konyushenko, J. Stejskal, M. Trchová, J. Hradil, J. Kovárová, J. Prokes, M. Cieslar, J. Y. Hwang, K. H. Chen, I. Sapurina, *Polymer* **2006**, *47*, 5715.

[276] G. Mountrichas, S. Pispas, N. Tagmatarchis, *Small* **2007**, *3*, 404.

[277] S. E. Moya, A. Ilie, J. S. Bendall, J. L. Hernandez-Lopez, J. Ruiz-García, W. T. S. Huck, *Macromolecular Chemistry and Physics* **2007**, *208*, 603.

[278] G. Guo, D. Yang, C. Wang, S. Yang, *Macromolecules* **2006**, *39*, 9035.

[279] Y.-L. Liu, W.-H. Chen, *Macromolecules* **2007**, *40*, 8881.

[280] P. C. Ma, J.-K. Kim, B. Z. Tang, *Composites Science and Technology* **2007**, *67*, 2965.

[281] N. Zhang, J. Xie, M. Guers, V. K. Varadan, *Smart Materials and Structures* **2003**, *12*, 260.

[282] I. Haller, *Journal of the American Chemical Society* **1978**, *100*, 8050.

[283] X. Kong, T. Kawai, J. Abe, T. Iyoda, *Macromolecules* **2001**, *34*, 1837.

[284] M. Döbbelin, G. Arias, I. Loinaz, I. Llarena, D. Mecerreyes, S. Moya, *Macromolecular Rapid Communications* **2008**, *29*, 871.

[285] S. Wang, R. Liang, B. Wang, C. Zhang, *Chemical Physics Letters* **2008**, *457*, 371.

[286] C. Gao, Y. Z. Jin, H. Kong, R. L. D. Whitby, S. F. A. Acquah, G. Y. Chen, H. Qian, A. Hartschuh, S. R. P. Silva, S. Henley, P. Fearon, H. W. Kroto, D. R. M. Walton, *The Journal of Physical Chemistry B* **2005**, *109*, 11925.

[287] L. Tang, Y. Zhu, X. Yang, J. Sun, C. Li, *Biosensors and Bioelectronics* **2008**, *24*, 319.

[288] B. H. Juárez, C. Klinke, A. Kornowski, H. Weller, *Nano Letters* **2007**, *7*, 3564.

[289] S. F. Wuister, A. Meijerink, *Journal of Luminescence* **2003**, *102-103*, 338.

[290] P. K. Khanna, N. Singh, *Journal of Luminescence* **2007**, *127*, 474.

[291] C. W. Wang, M. G. Moffitt, *Langmuir* **2004**, *20*, 11784.

[292] C. W. Wang, M. G. Moffitt, *Langmuir* **2005**, *21*, 2465.

[293] J. Wang, G. Liu, M. R. Jan, Q. Zhu, *Electrochemistry Communications* **2003**, *5*, 1000.

[294] M. A. Correa-Duarte, M. Grzelczak, V. Salgueiriño-Maceira, M. Giersig, L. M. Liz-Marzán, M. Farle, K. Sierazdki, R. Diaz, *Journal of Physical Chemistry B* **2005**, *109*, 19060.

[295] D. Yang, F. Yang, J. Hu, J. Long, C. Wang, D. Fu, Q. Ni, *Chemical Communications* **2009**, 4447.

[296] M. Uo, T. Akasaka, F. Watari, Y. Sato, K. Tohji, *Dental Materials Journal* **2011**, *30*, 245.

[297] G. Jia, H. Wang, L. Yan, X. Wang, R. Pei, T. Yan, Y. Zhao, X. Guo, *Environmental Science & Technology* **2005**, *39*, 1378.

[298] A. Magrez, S. Kasas, V. r. Salicio, N. Pasquier, J. W. Seo, M. Celio, S. Catsicas, B. Schwaller, L. s. ForrÃ³, *Nano Letters* **2006**, *6*, 1121.

[299] D. Cui, C. S. Ozkan, S. Ravindran, Y. Kong, H. Gao, *Mechanics & chemistry of biosystems : MCB.* **2004**, *1*, 113.

[300] T. Kaneko, T. Okada, R. Hatakeyama, *Contributions to Plasma Physics* **2007**, *47*, 57.

[301] M. Fischlechner, M. Zaulig, S. Meyer, I. Estrela-Lopis, L. CuÃ©llar, J. Irigoyen, P. Pescador, M. Brumen, P. Messner, S. Moya, E. Donath, *Soft Matter* **2008**, *4*, 2245.

[302] T. Chernenko, C. Matthäus, L. Milane, L. Quintero, M. Amiji, M. Diem, *ACS Nano* **2009**, *3*, 3552.

[303] H. L. Jiang, Y. K. Kim, R. Arote, J. W. Nah, M. H. Cho, Y. J. Choi, T. Akaike, C. S. Cho, *Journal of Controlled Release* **2007**, *117*, 273.

[304] T. Chernenko, C. MatthÃ¤us, L. Milane, L. Quintero, M. Amiji, M. Diem, *ACS Nano* **2009**, *3*, 3552.

[305] Y. Cu, C. LeMoëllic, M. J. Caplan, W. M. Saltzman, *Nanomedicine: Nanotechnology, Biology, and Medicine* **2010**, *6*, 334.

[306] B. Díaz, C. Sánchez-Espinel, M. Arruebo, J. Faro, E. de Miguel, S. Magadán, C. Yagüe, R. Fernández-Pacheco, M. R. Ibarra, J. Santamaría, Á. González-Fernández, *Small* **2008**, *4*, 2025.

[307] A. Beyerle, O. Merkel, T. Stoeger, T. Kissel, *Toxicology and Applied Pharmacology* **2010**, *242*, 146.

[308] S. M. Bose, S. Gayen, S. N. Behera, *Physical Review B - Condensed Matter and Materials Physics* **2005**, *72*, 1.

[309] A. M. Keszler, L. Nemes, S. R. Ahmad, X. Fang, *Journal of Optoelectronics and Advanced Materials* **2004**, *6*, 1269.

[310] H. Kuzmany, B. Burger, M. Hulman, J. KÃ¼rti, A. G. Rinzler, R. E. Smalley, *Europhysics Letters* **1998**, *44*, 518.

[311] H. Niknahad, P. J. O'Brien, *Chemico-Biological Interactions* **2008**, *174*, 147.

[312] Y. Zhang, B. Wang, X. Meng, G. Sun, C. Gao, *Annals of Biomedical Engineering* **2011**, *39*, 414.

[313] G. Perna, M. Lastella, M. Lasalvia, E. Mezzenga, V. Capozzi, *Journal of Molecular Structure* **2007**, *834–836*, 182.

[314] A. A. Shvedova, V. Castranova, E. R. Kisin, D. Schwegler-Berry, A. R. Murray, V. Z. Gandelsman, A. Maynard, P. Baron, *Journal of Toxicology and Environmental Health - Part A* **2003**, *66*, 1909.

[315] D. Cui, F. Tian, C. S. Ozkan, M. Wang, H. Gao, *Toxicology Letters* **2005**, *155*, 73.

[316] M. Fischlechner, M. Zaulig, S. Meyer, I. Estrela-Lopis, L. Cuellar, J. Irigoyen, P. Pescador, M. Brumen, P. Messner, S. Moya, E. Donath, *Soft Matter* **2008**, *4*, 2245.

[317] Z. Darzynkiewicz, S. Bruno, G. Del Bino, W. Gorczyca, M. A. Hotz, P. Lassota, F. Traganos, *Cytometry* **1992**, *13*, 795.

[318] M. Ahamed, R. Posgai, T. J. Gorey, M. Nielsen, S. M. Hussain, J. J. Rowe, *Toxicology and Applied Pharmacology* **2010**, *242*, 263.

[319] F. C. Breedveld, *Lancet* **2000**, *355*, 735.

[320] J. Kempeni, *Annals of the Rheumatic Diseases* **1999**, *58*, I70.

[321] J. J. Iturri Ramos, S. Stahl, R. P. Richter, S. E. Moya, *Macromolecules*, *43*, 9063.

[322] G. Romero, E. Rojas, I. Estrela-Lopis, E. Donath, S. Moya, *Nanoscale Research Letter* **2011**, *6*, 1.

[323] X. Dai, Z. Yue, M. E. Eccleston, J. Swartling, N. K. H. Slater, C. F. Kaminski, *Nanomedicine: Nanotechnology, Biology, and Medicine* **2008**, *4*, 49.

[324] V. Calleja, S. M. Ameer-Beg, B. Vojnovic, R. Woscholski, J. Downward, B. Larijani, *Biochem. J.* **2003**, *372*, 33.

[325] H.-J. Lin, P. Herman, J. R. Lakowicz, *Cytometry Part A* **2003**, *52A*, 77.

[326] A. H. A. Clayton, Q. S. Hanley, D. J. Arndt-Jovin, V. Subramaniam, T. M. Jovin, *Biophysical Journal* **2002**, *83*, 1631.

[327] A. Campbell, D. Uttamchandani, *IEE Proceedings: Science, Measurement and Technology* **2004**, *151*, 291.

[328] Q. S. Hanley, V. Subramaniam, D. J. Arndt-Jovin, T. M. Jovin, *Cytometry* **2001**, *43*, 248.

[329] Y. Aso, S. Yoshioka, A. Li Wan Po, T. Terao, *Journal of Controlled Release* **1994**, *31*, 33.

[330] L. Gallois, M. Fiallo, A. Garnier-Suillerot, *Biochimica et Biophysica Acta (BBA) - Biomembranes* **1998**, *1370*, 31.

[331] S. Zarzhitsky, H. Rapaport, *Journal of Colloid and Interface Science*, *360*, 525.

[332] S. Chandra, S. Mehta, S. Nigam, D. Bahadur, *New Journal of Chemistry*, *34*, 648.

[333] S. A. Akman, J. H. Doroshow, T. G. Burke, M. Dizdaroglu, *Biochemistry* **1992**, *31*, 3500.

List of Piblications

Irantzu Llarena, Gabriela Romero, Ronald F. Ziolo and Sergio E. Moya. Carbon nanotube surface modification with polyelectrolyte brushes endowed with quantum dots and metal oxide nanoparticles through in situ synthesis. *Nanotechnology*, 21, **2010**, 055605-005613.

Jie Zhou, Gabriela Romero, Elena Rojas, Sergio Moya, Lie Ma, Changyou Gao. Folic Acid Modified Poly(lactide-co-glycolide) Nanopareticles, Layer-by-Layer Surface Engineered for Tergeted Delivery. *Macromolecular Chemestry and Physics*, 211, **2010**, 404- 411.

Jie Zhou, Gabriela Romero, Elena Rojas, Sergio Moya, Lie Ma, Changyou Gao. Layer by layer chitosan/alginate coatings on poly(lactide-co-glycolide) nanoparticles for antifouling protection and Folic acid binding to achieve selective cell targeting. *Journal of colloid and Interfaces* Science, 345, **2010**, 241-247.

Gabriela Romero, Irina Estrela-Lopis, Jie Zhou, Elena Rojas, Ana Franco, Christian Sánchez Espinel, Africa Gonzalez Fernandez, Changyou Gao, Edwin Donath and Sergio Moya. Surface Engineered Poly(lactide-co-glycolide) Nanoparticles for Intracellular Delivery: Uptake and Cytotoxicity—A Confocal Raman Microscopic Study. *Biomacromolecules*, 111, **2010**, 2993-2999.

Gabriela Romero, Irina Estrela-Lopis, Edwin Donath and Sergio Moya. Spontaneus Confocal Raman Microscopy- a tool to study the uptake of nanoparticles and carbon nanotubes into cells. *Nanoscale Research Letters*, 6, **2011**, No. 429.

Gabriela Romero, Irina Estrela-Lopis, Pablo Castro Hartman, elena Rojas, Irantzu Llarena, David Sanz, Edwin Donath and Sergio Moya. Stepwise Surface Tailoring of Carbon nanotubes with Polyelectrolyte Brushes and Lipid Layers to Control their Intracellular Distribution and "in vitro" Toxicity. *Soft Matter*, 7, **2011**, 6883-6890.

Irina Estrela-Lopis, Gabriela Romero, Elena Rojas, Sergio Moya and Edwin Donath. Nanoparticle uptake and their co-localization with cell compartments- a confocal Raman microscopy study at single cell level. *Journal of Physics: Conference Series*, 304, **2011**, No.012046.

Gabriela Romero, Irina Estrela-Lopis, Elena Rojas, Irantzu Llarena, Edwin Donath and Sergio Moya. Lipid/Polyelectrolyte Coatings to Control Carbon Nanotubes Intracellular Distribution. *Journal of Nanoscience and Nanotechnology*, 12, **2012**, 4836-4842.

Gabriela Romero and Sergio Moya. Chapter 4: Synthesis of Organic Nanoparticles. Nanobiotechnology: Inorganic Nanoparticles vs Organic. *Elsevier*, **2012**, 115-141.

Gabriela Romero and Sergio Moya. Soft matter engineering of Carbon Nanotubes: polyelectrolytes as tools for surface tailoring, templation of hybrid nanostructures and self-organization. *Soft Matter*, Highlight Article, **2012**, DOI: 10.1039/C2SM25425E.

Gabriela Romero, David José Sanz, Dahai Yu, Mao Zhengwei, Changyou Gao and Sergio Moya. Lipid layer engineering of Poly(lactide-co-glycolide) Nanoparticles to control their uptake and intracellular targeting towards the endoplasmic reticulum. Submitted.

Gabriela Romero, Yuan Qiu, Richard A. Murray and Sergio Moya. Study of Intracellular Delivery from Poly(lactide-co-glycolide) Nanoparticles by Means of Fluorescence lifetime Imaging and Confocal Raman Microscopy. Submitted.

Gabriela Romero, Olaia Ochoteco, David José Sanz, Irina Estrela-Lopis, Edwin Donath and Sergio Moya. Poly(lactide-co-glycolide) Nanoparticles Layer by Layer engineered for the sustainable delivery of antiTNF-α. Manuscript in preparation.

Gabriela Romero, María Echeverría, Richard A. Murray and Sergio Moya. Intracellular degradation of Poly(lactide-co-glycolide) Nanoparticles in HepG2 cells by flow cytometry. Manuscript in preparation.